Creation and distribution of cold plasma in gas giants' magnetospheres through in situ and remote observations

Georgios Xystouris

Supervisors: Dr. Christopher Arridge, Dr. Sarah Badman

This thesis is submitted for the degree of

Doctor of Philosophy

Space and Planetary Physics

Department of Physics

Lancaster University

December 2024

‘Η αστρονομία αναγκάζει την ψυχή να κοιτάξει ψηλά,
και μας οδηγεί από αυτόν τον κόσμο σε έναν άλλο.’
— ΠΛΑΤΩΝΑΣ

‘Astronomy compels the soul to look upwards
and leads us from this world to another.’
— PLATO

To my parents, Nicos and Olga.
For everything they have provided for me
and for all of their support.

Abstract

Georgios Xystouris

Creation and distribution of cold plasma in gas giants' magnetospheres through in situ and remote observations.

This thesis focused on studying the production and distribution of neutrals and plasma in the magnetospheres of Saturn and Uranus, using data from several instruments that provided both in-situ and remote observations. These specific planets were selected because they are expected to have similarly cold and water-like plasma: Saturn has Enceladus as the main neutral provider, and Uranus has its 5 biggest moons: Ariel, Umbriel, Titania, Oberon and Miranda. While the existence of a water-group plasma is studied thoroughly for Saturn with the Cassini Mission, it is still a topic of debate for Uranus, as no heavy ion plasma was observed during Voyager 2 flyby.

For Uranus I searched for the existence of a water neutral torus using observations from Herschel/HIFI. Although models predict such a torus, the data were inconclusive: there was a feature on the data hinting at the existence of a torus, but it was not potent enough to confirm without further study.

For Saturn I focused on the factors affecting the cold plasma measurements, particularly the photoelectrons, as they have the same properties as the cold electron plasma. I studied how data from the Cassini/LP and CAPS evolve when Cassini goes into Saturn's shadow, where the photoelectron generation stops, and I found that data from both instruments exhibited clear changes. Moreover, I calculated the transparency of the main rings based on photoelectrons variations when Cassini was in the rings' shadow.

Lastly, as the sunlight or the plasma flow can be important to an instruments' measurements, I developed algorithms that use a spacecraft 3D model to: (i) calculate the field-of-view of an instrument mounted on a spacecraft, and (ii) search for any intersections of a vector with any part of a spacecraft. This work can be adapted to any spacecraft.

Contents

List of Tables

List of Figures

Acknowledgements

First of all I would like to thank my family, especially my mum, dad, and brother. They supported all my crazy dreams in any way they could. Mum, you will be missed...

I would also like to thank my two supervisors, Dr. Chris Arridge and Dr. Sarah Badman. They were great advisors, guiding me through this work, and helping whenever needed. I definitely learned a lot from them.

Special thanks go to Dr. David Teyssier and Dr. Fran Bagenal, for two wonderful collaborations during my PhD. Results of those projects should be coming soon!

I would also like to thank my colleagues and the rest of the people in the Space and Planetary Group, who they made it nice to work there. Special thanks go to Dr. Leela Koutsantoniou, Dr. Aggela Adamaki, Dr. Rob Wilson, Krystal Juvrud, and Alex Stjärnfelt. Each one helped in a different way, and often their help was crucial.

A huge help on proofreading this thesis goes to Lummi Bruhn - even though I'm sure there still are some mitsakes here and there...

Lastly, thank yous go to people from all over the world who were inspiring me to keep on going, and showing me that I'm doing something cool. Yes, space **is** cool! Around $-270°$C to be exact [Fixsen, 2009].

"At Loss for Words"

So! *[...pause...]* This is the part where I would like to express some of my thoughts and concerns, and some more acknowledgments that did not make it to the formal, serious section - consider this like the "kids table" at a dinner. It doesn't mean they're not special though! This is going to be like the end titles of a movie that lasted over 3.5 years, so brace yourselves! Here we go.

Names go here: Krystal, Λευτέρης, Joseph, Ωρίωνας, Εκάβη, Μαρίνος, Mario, Χρυστάλλα, Φλωρεντία, Βίκτωρ, Κώστας, Μαρία, Καλλιστώ, Ορσούλα, Ιάκωβος, Leela, Lummi, Sabina, Markus, Zoi, Elizabeth, Elias, Annika, Sigrid, Mostafa, Ismael, Adeline, Paulina, Jenny, Arvid, Johan, Alex, Svante, Mathias, Mikael, Kristian, Roger & Jenny, Ulli, Γιώργος, Georgia, Georgia, Kaitlin (Kaytlheene?), Ματίνα, Βασίλης, Κώστας, Madde, Δημήτρης, Rachel, Josh, Chris, Joe, Wayne, Diego, Maria, George, Freya, Licia, Alexi, Kristen, Lisa, Jonas, Kurt, Scottie, Laila and many more from people from Cyprus, Greece, Sweden, UK, Austria, USA and almost all over the world. Apologies to any names that are not there. I was told to say that "I accidentally missed them", but on a more serious note though I *did* miss them. You know who you are.

During my PhD years I listened to tens of thousands hours of music, so thank you: Novarupta, Bell Witch, Grand Cadaver, sunn o))), The Moth Gatherer, Dark Tranquillity, At the Gates, In Flames, Slayer, Lamb of God, mgła, 1000mods, Planet of Zeus, NONE, SKRCKVLDET, Dream Theater, The Ocean, LLNN, Grift, Panopticon, Meshuggah, Monster Magnet, Forndom, Iron Maiden, Slipknot, Korn, Akhlys, Amenra, БАТЮШКА, Rammstein, Electric Wizard, Karma to Burn, OM, Tool, and so many more. Also, special thanks go to the podcasts BANANAS! (who would have thought that they would have been an educational podcast), Heavy Hops, and Welcome to Night Vale, as they were a nice distraction from everything.

I feel that I need to thank Atkinsons and Lindvall's coffee roasters, as well Spreesso Coffee & More (thank you chief Christos!), and acknowledge Nescafé, and Red Bull for all the provided energy. I initially attempted to keep track of my coffee consumption, keeping it strictly to coffee consumed while working. But COVID and lockdowns happened, work was interwoven with life, everything felt the same, so I lost track of it. For reference, in

the first 5 months I consumed $\sim$ 6kg of coffee. Since coffee consumption tends to grow exponential during one's PhD, according to my calculations by the time I am submitting this thesis I would have consumed $\sim$ 12.3t (metric tonnes), with an additional $\sim$ 50kg of the very last day. While plausible, this estimate looks slightly exaggerated. Alternatively, there is a possibility that the consumption follows a linear trend, in which case I would have consumed $\sim$ 66kg, with $\sim$ 0.4kg on the final day. This estimate also looks plausible. Clearly, more data were needed for this experiment.

Uplands Nation was also a big help on having something else to work on and worry about besides my thesis... But the people there did help with keeping me sane and happy. *Var ligger landet?*. Beer at Svantes Källare after this!

Also some breweries, that their beers helped with celebrations, drowning sorrows, and sparking science conversations: Tempel Brygghus, The Northern Monk, Nøgne Ø, Thornbridge, Accidental Brewery, Rodenbach, 3 Fonteinen, and so many more.

TTT

I thank you all for all the energy, the panic attacks, the support, the trust, the joy, the tears, the emotions, the music, the endless conversations, the inarticulate sounds, the screams, the travelling, the beer. It was a fun ride. I'm not sure I want to do it again anytime soon. As "At the Gates" said: *we are blind to the worlds within us waiting to be born.*

PS: The names above are not in any particular order.

I'm tired...

Declaration of Authorship

I, Georgios Xystouris, declare that this thesis titled "Creation and distribution of cold plasma in Gas Giants magnetospheres through in situ and remote observations", and the work presented in it are my own.
I further confirm that:

- This work was done wholly while in I was a candidate for a research degree at this university.

- It is clearly stated in sections of the thesis where any part has previously been submitted for a degree or any other qualification at Lancaster University or any other institution.

- Two papers have been published in peer reviewed journals as a result of this thesis:

  ☐ G. Xystouris, C. S. Arridge, M. M. Morooka, and J.-E. Wahlund. Estimating the optical depth of Saturn's main rings using the Cassini Langmuir Probe. *MNRAS*, 526(4):5839-5860, Dec. 2023. doi:10.1093/mnras/stad2793

  ☐ G. Xystouris, O. Shebanits, and C. S. Arridge. A simple spacecraft - vector intersection methodology and applications. *RAS Techniques and Instrum.*, 3(1): 166–173. doi:10.1093/rasti/rzae012

  These papers are discussed in section 4.6 and chapter 5 respectively.

- Where I have consulted the published work of others, this is always clearly attributed.

- Where I have used and / or reproduced any material from other studies, published or not, I have acquired the necessary permissions.

- Where I have quoted from the work of others, the source is always given. With the exception of such quotations, this thesis is entirely my own work.

- Where the thesis is based on work done by myself jointly with others, I have made clear exactly what was done by others and what I have contributed myself.

- I have acknowledged all main sources of help.

Signed: Georgios Xystouris, PhD candidate

Date: 23 May 2024

1. Introduction

> **"Space is big. You just won't believe how vastly, hugely, mind-bogglingly big it is."**
>
> — Douglas Adams, *The Hitchhiker's Guide to the Galaxy*

1.1. Overview

In this thesis I will present my studies on plasma creation and distribution in the gas giants' magnetospheres, focusing on Saturn and Uranus. It is mostly a data analysis work, where I also focused on instrumentation and parameters that affected the measurements made by instruments. Chapter 1 gives an introduction of the studies to follow, along with some required basic plasma physics elements. Chapter 2 gives an overview of the instruments whose data were used in this thesis. Chapter 3 presents the work done focusing on Uranus, chapter 4 respectively is focused on Saturn. Chapter 5 shows the work on how the field of view (FOV) on an instrument can be calculated and how to assert whether a vector 'hits' the spacecraft. Lastly, chapter 6 presents the conclusions of this thesis, along with ideas for future work on the projects discussed.

Two publications came out of this thesis. The first publication is an interdisciplinary study of how I calculated the transparency of Saturn's rings while studying the parameters affecting plasma measurements [Xystouris et al., 2023a] and it is part of chapter 4. The second publication is a technical paper based on chapter 5 [Xystouris et al., 2024].

All the scalar variables in this thesis are noted in italic and the vectors in bold italic. Also, some symbols are used for different things in different chapters, e.g. α is used to define the pitch angle in chapter 1 and the attack angle in chapter 3. Therefore each symbol will always be defined in advance in each chapter, and no two quantities using the same symbol will be used together throughout the thesis.

In this chapter all the elements in sections 1.2, 1.3, 1.4, 1.5, 1.6, and 1.7 are from Baumjohann and Treumann [2022], unless otherwise stated.

1.2. Plasma definition

Plasma is a gas consisting of equal numbers of free ions and electrons. If the ions are the same number as the electrons in the same volume element it makes the plasma *quasineutral*. Such a volume element must be large enough to contain a sufficient number of particles, and small enough compared to the variations of macroscopic parameters, e.g. density and temperature. On average the plasma macroscopically is neutral, as the randomness in the particle distribution cancels their individual electric charge, but also each particle is not affected by other charges in the plasma (Debye shielding - to be discussed in the next section). A particle is free when its motion is free from the influence of its neighbouring particles, i.e. has no direct collisions with them. For this to happen its potential energy due to its nearest neighbour must be less than its random thermal (kinetic) energy.

Over 99% of all the known ordinary matter is in plasma state, and in space it can be found in a range of energies: from very cold, e.g. the interstellar medium has a temperature of $\mathcal{O}\left(10^{-2}\text{eV}\right)$ [Gibbon, 2020], to very hot, e.g. the hottest star has a temperature of $\sim 5 \cdot 10^{4}\text{eV}$ [Brands et al., 2022].

1.3. Debye shielding, Debye length, L-shells, & plasma parameters

The Coulomb potential field of every point charge, q, is defined as:

$$\Phi_C = \frac{q}{4\pi\epsilon_0 r} \tag{1.1}$$

where ϵ_0 is the electric permittivity in vacuum and r is the distance from the particle (assuming that the particle is a point in space). If there are no other charges in space the particle's field will drop to zero at infinity. In the case of plasma though, where there are other charges around, those charges will move around to 'shield' a 'naked' potential (i.e. the potential of a single charge). This movement of charges to shield the naked potential is called *Debye shielding*. It will cause the attenuation of the Coulomb potential of the 'naked' charge, and the total potential of the charge will drop much faster than if it was naked. The distance where the naked potential is shielded is controlled by the *Debye length*, λ_D, which depends on the temperature and density of the particles. The Debye length can also be defined as the characteristic length where a balance is obtained between the

thermal energy of the particles and the electrostatic potential energy. The thermal energy is responsible for perturbing the electrical neutrality of the plasma, while the electrostatic potential energy tends to restore the charge neutrality. The hotter the plasma particles, the faster they move, and the less efficient they are at shielding the potential. Also, a lower density population will also be less effective at shielding the potential due to their small number.

The Debye potential is in the form of

$$\Phi_C = \frac{q}{4\pi\epsilon_0 r} \exp\left[-\frac{r}{\lambda_D}\right] \tag{1.2}$$

The exponent cuts off the potential at distances where $r > \lambda_D$. For the plasma to be quasineutral, the physical dimension of the system, D, must be much larger than the Debye length

$$D \gg \lambda_D \tag{1.3}$$

otherwise there will not be enough space for the shielding of each particle to occur, and the system will simply be a neutral gas with some ionised particles. This requirement is called *the first plasma criterion*.

Assuming that the temperature between electrons and ions are approximately equal, $T_e \simeq T_i$, as is their number density (assuming singly charged ions), $n_e \simeq n_i$, the Debye length is given as

$$\lambda_D = \left(\frac{\epsilon_0 k_B T_e}{n_e e^2}\right)^{1/2} \tag{1.4}$$

where k_B is the Boltzmann constant and e is the electron charge. We can also find the number of particles, N, inside a Debye sphere, i.e. a sphere of radius λ_D

$$N_{e,Debye\ sphere} = \frac{4\pi}{3} n_e \lambda_D^3 \tag{1.5}$$

In a dipolar magnetosphere the L-shell parameter, or L value, can be defined as

$$L = \frac{r_{eq}}{R_{pl}} \tag{1.6}$$

where R_{pl} is the planetary radius and r_{eq} is the distance at the magnetic equator. This parameter is particularly important because a planet's magnetic dipole is not necessarily

aligned with its rotation axis. Since plasma follows magnetic field lines, the L-shell (or L value) indicates the specific magnetic field line along which a particle is located. Calculating the L in simpler, dipole-like magnetospheres, such as Saturn's, is straight-forward by simply following eq. 1.6, where the locus of constant L creates a shell around the planet. In more complex magnetospheres with more poles and a complicated configuration, such as Uranus', an L can still be defined, provided that the magnetosphere can be approximated as a dipole at larger distances. Once the L values for these shells are calculated, they can be extrapolated to smaller distances. However, unlike at larger distances, the L at closer distances will not for a shell but will instead represent regions of constant magnetic field strength, similar to contour maps.

Fig. 1.1 shows the Coulomb and Debye potentials for the Kronian plasma in two regions: close to Enceladus orbital distance, at $L \approx 4$, and away from it, at $L \approx 7$. The x-axis of the figure show the distance between the particles, while the y-axis shows the potential of the particles. For $L = 4$ a density of $n_e \approx 50\text{cm}^{-3}$ and temperature of $T \approx 10\text{eV}$ were used, while for $L = 7$ those values were $n_e \approx 20\text{cm}^{-3}$ and $T \approx 5\text{eV}$ respectively (values from Xystouris [2016] and Persoon et al. [2020]). As Enceladus is the main plasma source for the Kronian magnetosphere, these distances show typical Debye lengths for a hotter, denser plasma, right at the source, and a more tenuous, colder plasma, away from any sources. The figure shows clearly the faster drop of the Debye potential than the Coulomb potential. Also, comparing the density and temperature, the denser the plasma, the shorter the λ_D, and the faster the Debye potential drops. As those two values can be considered two extreme values for the plasma, dense and hot versus tenuous and cold, we see that the Debye length for Saturn's inner magnetospheric plasma is $\sim 3.5\text{m}$.

The term $n_e\lambda_D^3$ is called *plasma parameter*, Λ, and it shows (approximately) the number of charges inside a sphere. The second criterion of plasma says:

$$\Lambda = n_e\lambda_D^3 \gg 1 \tag{1.7}$$

meaning that the plasma must be densely populated inside the Debye sphere. Combining eq. 1.4 and 1.7 we get:

$$k_B T_e \gg \frac{n_e^{1/3} e^2}{\epsilon_0} \tag{1.8}$$

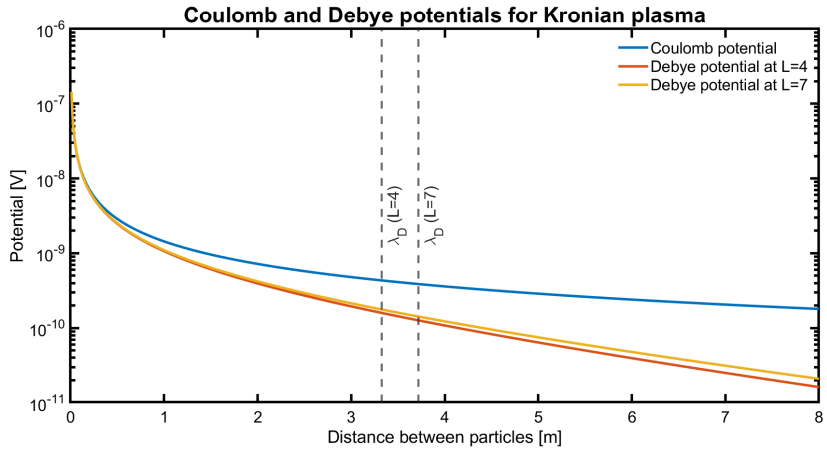

Figure 1.1: Coulomb and Debye potentials for the Kronian magnetospheric plasma. The Debye length for the Kronian plasma is ~ 3.5m.

which implies that a particle's mean potential energy due to its nearest neighbour must be much smaller than its mean thermal energy. Hence some combination of high temperature and low density is expected.

Fig. 1.2 shows examples of various plasmas' temperature and energy. The Debye length and particles in the Debye sphere are also presented on the plot with the dashed and solid line respectively. For planetary magnetospheres the Debye lengths can be from less than 1m to hundreds of meters, while a Debye sphere contains from $\sim 10^7$ to over $\sim 10^{15}$ particles. For comparison, the plasma density and temperature for Saturn and Uranus, as both are studied in this work, are added on the plot. The orange circle is the plasma conditions range for Saturn: Persoon et al. [2020] calculated the water group ion density close to Enceladus to be $\sim 1-50\text{cm}^{-3}$ with a temperature of $\sim 0.4-80$eV, while the hydrogen ion density is $\sim 1-10\text{cm}^{-3}$ with a temperature of $\sim 5-45$eV. Xystouris [2016] showed that the electrons follow the same parameters as the water group, with slightly lower temperatures, ~ 10eV. These conditions give Debye lengths of $\sim 1-10$m, with $\sim 10^{10}$ particles inside a Debye sphere. The blue circle is the plasma conditions reported in Uranus: McNutt et al. [1987] calculated the cold hydrogen ion density is $\sim 0.5-2\text{cm}^{-3}$ with a core temperature of $\sim 5-10$eV, but they also reported a hot component with density and of $\sim 0.1-0.8\text{cm}^{-3}$ and a temperature of $\sim 400-6000$eV. Sittler et al. [1987]

calculated electron parameters similar to the cold hydrogen: density $\sim 0.02 - 1\text{cm}^{-3}$, and temperatures $\sim 50 - 5\text{eV}$ respectively. Therefore, the Uranian magnetospheric has Debye lengths $\sim 10 - 100\text{m}$, with $\sim 10^7 - 10^{15}$ particles inside each Debye sphere.

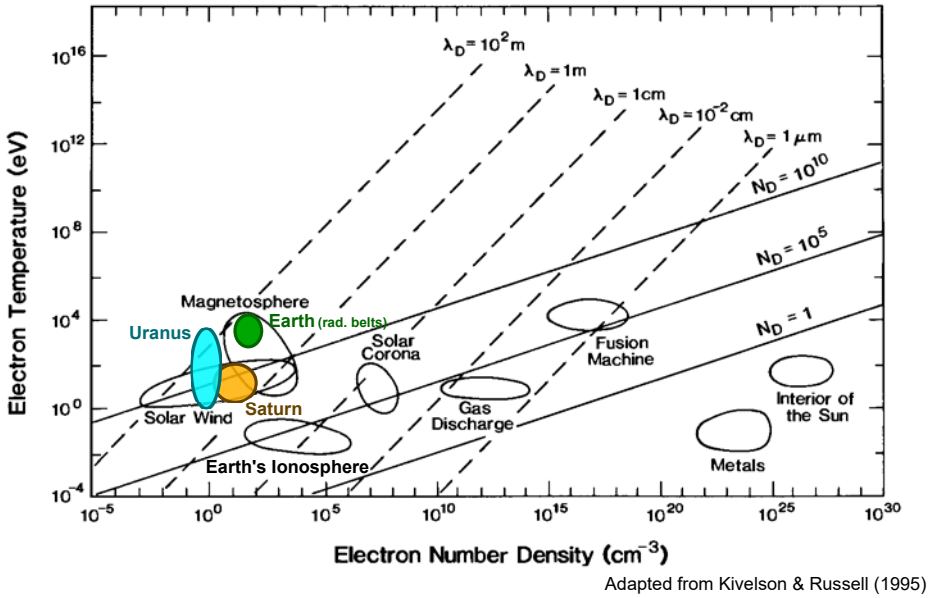

Figure 1.2: Example of various plasmas temperature and energy. The Debye length (dashed line), and charges in a Debye sphere (solid line) are also shown. For comparison the Uranian and Kronian plasma, that this work uses, and the Earth Van Allen radiation plasma are marked with the blue, orange, and green circles respectively. Figure adapted from Kivelson and Russell [1995]

While it looks that the two magnetospheres are not fully within the textbook region of a magnetospheric plasma parameters, each planet has its unique configuration of magnetospheric plasma density and temperature. As an example of showing how diverse magnetospheric plasma environments can be the green circle shows the plasma environment of the Earth's Van Allen radiation belts [Li and Hudson, 2019], where the plasma has higher density ($\sim 10 - 100\text{cm}^{-3}$) and temperature ($\sim 10^3 - 10^4\text{eV}$) than Saturn and Uranus.

1.4. Plasma beta

The plasma beta, β, can be defined as the ratio of the thermal pressure to the magnetic pressure of a plasma:

$$\beta = \frac{nk_BT}{B^2/2\mu_0} \tag{1.9}$$

where n is the particle number density, T is their temperature, k_B is the Boltzmann constant, B is the magnetic field strength, and μ_0 is the magnetic permeability in vacuum. β is an indicator of whether the particles are being driven by the magnetic field (low β), or whether they drag the magnetic field due to their thermal energy (high β).

A cold (i.e. low energy) plasma has $\beta \ll 1$, while a warm (i.e. high energy) plasma has $\beta \geq 1$ [Kivelson and Russell, 1995]. Examples of plasma β: the solar interior has $\beta \gg 1$, the solar corona has $\beta \ll 1$, and the solar wind at the earth's neighbourhood has $\beta \sim 1$. The magnetospheres of the outer planets can have a wide range of values, depending on the combination of the local plasma conditions. For example, Kanani et al. [2010] presented modelling indicating that β can vary from 10^{-4} to 10^3 in Saturn's magnetosheath (fig. 5d in their work).

1.5. Stationary dipole magnetospheres

The internal magnetic field of gas giants are mostly dipoles, but also have moments of higher order. Those can be minimal, such as Saturn's case [Smith et al., 1980], weak, such as Jupiter's case [Connerney et al., 1987], or stronger, such as Uranus and Neptunes' moments [Connerney et al., 1991, Connerney, 1993]. Despite these higher order moments, the fields are approximately dipolar within a few planetary radii of the surface. Beyond this, they are radially stretched into a magnetodisk configuration (e.g. Achilleos et al. [2021]).

The dipole strength at a specific location, r, can be calculated using the equation

$$B = \frac{\mu_0}{4\pi}\frac{M_{pl}}{r^3}\left(1 + 3\sin^2\lambda\right)^{1/2} \tag{1.10}$$

where M_{pl} is the planetary dipole moment, and λ is the magnetic latitude.

The dipole magnetic field lines equation is

$$r = r_{eq} \cos^2 \lambda \tag{1.11}$$

For any point on the equator, $\lambda = 0 \Rightarrow r = r_{eq}$; this is also the greatest distance of the line.

By combining eq. 1.6 and eq. 1.11, and setting the distance on the surface of the planet, $r = R_{pl}$, we can find the intersection latitude on the planet, λ_{pl}, of a line with an L-shell value:

$$\cos^2 \lambda_{pl} = L^{-1} \tag{1.12}$$

Eq. 1.10 can be parametrised to the L-shell value and λ using eq. 1.11 and eq. 1.6:

$$B(\lambda, L) = \frac{B_{pl}}{L^3} \frac{\left(1 + 3\sin^2 \lambda\right)^1 / 2}{\cos^6 \lambda} \tag{1.13}$$

where B_{pl} is the planetary equatorial magnetic field strength on the planet's surface, given by the equation

$$B_{pl} = \frac{\mu_0 * M_{pl}}{4\pi R_{pl}^3} \tag{1.14}$$

1.6. Trapped charged particle motions

Assuming that the plasma particles created in the processes described in section 1.7 are in an empty space, each particle that is at rest creates an electrostatic field, $\boldsymbol{E}$. The force each particle feels due to the electrostatic field of another particle is the *Coulomb force*

$$\boldsymbol{F_C} = q\boldsymbol{E} \tag{1.15}$$

If a particle moves through a magnetic field $\boldsymbol{B}$ with a velocity $\boldsymbol{u}$ it experiences a force, called *Lorentz force*

$$\boldsymbol{F_L} = q\left(\boldsymbol{u} \times \boldsymbol{B}\right) \tag{1.16}$$

While the plasma is in an environment with a magnetic field, such as a planetary magnetosphere, the charged particles will be accelerated by the electric and magnetic field in the magnetosphere, leading to a number of fundamental motions. If the magnetic field

has the shape of a dipole, the particles will be subjected into three major motions: (i) the gyration around a magnetic line, (ii) the curvature drift along the magnetic line and eventually the magnetic mirroring (i.e. the bounce between the two poles of the dipole), and (iii) the drift around the equator of the dipole.

1.6.1. Gyration

The equation of motion (Newton's second law) for a particle can be written as

$$\boldsymbol{F} = m\frac{d\boldsymbol{u}}{dt} \tag{1.17}$$

where m is the particle mass and $\boldsymbol{u}$ its velocity. If that particle is charged with a charge q, the forces applied on it are the Coulomb and Lorentz forces. Hence using eq. 1.15, eq. 1.16, and eq. 1.17 we have

$$m\frac{d\boldsymbol{u}}{dt} = q\left(\boldsymbol{E} + \boldsymbol{u} \times \boldsymbol{B}\right) \tag{1.18}$$

In a planetary magnetosphere though we can assume (for now) that there are solely magnetic lines, without electric fields. Therefore essentially we only have the Lorentz force applied to the particle. Eq. 1.18 becomes

$$m\frac{d\boldsymbol{u}}{dt} = q\left(\boldsymbol{u} \times \boldsymbol{B}\right) \tag{1.19}$$

Taking the dot product of eq. 1.19 with $\boldsymbol{u}$, and using the property $\boldsymbol{u} \cdot (\boldsymbol{u} \times \boldsymbol{B}) = 0$, we get

$$m\frac{d\boldsymbol{u}}{dt} \cdot \boldsymbol{u} = \frac{d}{dt}\left(\frac{mu^2}{2}\right) = 0 \tag{1.20}$$

which shows that the kinetic energy and the magnitude of the velocity of a particle that moves in a static magnetic field are constant.

Placing the magnetic field direction on the z-axis, $\boldsymbol{B} = B\hat{\boldsymbol{e_z}}$, and at this point assuming that and $u_z = u_{\parallel} = 0$, we get from eq. 1.19

$$\begin{aligned} m\dot{u_x} &= qBu_y \\ m\dot{u_y} &= -qBu_x \\ m\dot{u_z} &= 0 \end{aligned} \tag{1.21}$$

which shows that the motion of the particle takes place only the XY plane, that is perpendicularly to the magnetic field direction. In other words $u_\perp \neq 0$. As the perpendicular motion is largely circular the centre where the particle orbits around is called *guiding centre*.

Taking the second derivative of eq. 1.21 we have

$$\begin{aligned} m\ddot{u_x} &= -\left(\frac{qB}{m}\right)^2 u_x \\ m\ddot{u_y} &= -\left(\frac{qB}{m}\right)^2 u_y \end{aligned} \tag{1.22}$$

which look like the equations of a harmonic oscillator

$$u_i = u_0 \cos(\omega t) \Rightarrow \ddot{u_i} = -u_0 \omega^2 \cos(\omega t) \tag{1.23}$$

The coefficient ω is the frequency of oscillation, or *gyrofrequency* and it stays constant over time. Combining 1.22 and 1.23 we get

$$\omega_g = \frac{qB}{m} \tag{1.24}$$

which is the gyrofrequency of a particle rotating around a magnetic line.

Since the rotation of the particle is circular, we can express its displacement from the guiding centre, (x_0, y_0) as follows:

$$\begin{aligned} x - x_0 &= A \sin(\omega_g t) \\ y - y_0 &= A \cos(\omega_g t) \end{aligned} \tag{1.25}$$

where A is the amplitude of the displacement from the equilibrium position (i.e. the guiding centre), which is essentially the radius of the orbit, i.e. the *gyroradius*. Deriving and squaring eq. 1.25, and combining with eq. 1.24 we get

$$r_g^2 = \frac{u_x^2 + u_y^2}{\omega_g^2} \Rightarrow r_g = \frac{u_\perp}{|\omega_g|} = \frac{m u_\perp}{|q| B} \tag{1.26}$$

While the gyroradius is independent of the particle charge sign, it is included in the gyrofrequency solely for showing the direction of rotation.

This motion is very fast compared to the rest of the motions that will be discussed, as an electron completes an orbit around a magnetospheric magnetic line in times of $\mathcal{O}\left(10^{-6}\right)$ s.

1.6.2. Curvature drift & magnetic mirroring

If the moving particle has a z-component, i.e. $u_{\parallel} \neq 0$, this will allow the particle to move parallel to the magnetic lines. As the magnetic lines of the dipole are curved, the particle will also be subjected to a curvature drift, that is described below.

The *pitch angle*, α, of a particle can be defined as

$$\alpha = \arctan\left(\frac{u_{\perp}}{u_{\parallel}}\right) \tag{1.27}$$

which can be used to show which component, parallel or perpendicular, contributes more to the movement. From eq. 1.27 we can also get the following equations for each of the individual components

$$\begin{aligned} u_{\perp} &= \sin\alpha \\ u_{\parallel} &= \cos\alpha \end{aligned} \tag{1.28}$$

As $u_{\parallel} \neq 0$, the particles will also experience a centrifugal force, $\boldsymbol{F}_R$

$$\boldsymbol{F}_R = m u_{\parallel}^2 \frac{\boldsymbol{R}_c}{R_c^2} \tag{1.29}$$

where $\boldsymbol{R}_c$ is the vector of the local radius of curvature.

If the gyroradius of a particle varies over a gyration, then a rotational drift starts developing, with a drift force $\boldsymbol{F}$. The general equation for the guiding centre drift velocity is

$$\boldsymbol{u}_F = \frac{1}{\omega_g}\left(\frac{\boldsymbol{F}}{m} \times \frac{\boldsymbol{B}}{B}\right) \tag{1.30}$$

Plugging eq. 1.30 to eq. 1.29, we get the curvature drift velocity:

$$\boldsymbol{u}_R = \frac{m u_{\parallel}^2}{q}\left(\frac{\boldsymbol{R}_c \times \boldsymbol{B}}{R_c^2 B^2}\right) \tag{1.31}$$

From eq. 1.31 we see that the curvature drift is perpendicular to both the magnetic field and its curvature. Also the drift is proportional to the parallel energy of the particle, $W_{\parallel} = (1/2) m u_{\parallel}^2$.

The magnetic moment of a particle that moves along a magnetic field is expressed as

$$\mu = \frac{m u_{\perp}^2}{2B} \tag{1.32}$$

and it is connected with the gyration of the particle around the magnetic field. When the particle moves to a stronger or weaker magnetic field, its gyroradius and gyrofrequency change, but its magnetic moment is not affected by their changes - given the changes are small - hence the magnetic moment can be considered invariant.

Combining eq. 1.32 and eq. 1.28 we get the relationship between the magnetic moment and pitch angle

$$\mu = \frac{m \sin^2 \alpha}{2B} \tag{1.33}$$

The only parameters that are changing in the equation are the pitch angle of the particle and the magnetic field strength of the region it currently is at. As the magnetic moment is adiabatic we can connect the parameters of two regions, e.g. region 1 and region 2, as eq. 1.28

$$\frac{\sin^2 \alpha_2}{\sin^2 \alpha_1} = \frac{B_2}{B_1} \tag{1.34}$$

The magnetic field of a dipole though is becoming stronger towards the pole. Therefore, as a particle moves towards the poles there will be a point, B_m, where the magnetic field will be strong enough that its pitch angle will reach $\alpha = 90°$, which will stop it from continuing travelling, and eventually it will be reflected. This point is the *mirror point*. At the mirror point the particle's energy shift solely to its perpendicular component, $u_\perp \Rightarrow u_\parallel = 0$, and, due to the parallel component of the gradient force

$$\boldsymbol{F}_{\boldsymbol{\nabla}_\parallel} = -\mu \nabla_\parallel B \tag{1.35}$$

it is pushed backwards. This force is called *mirror force*.

Seeing the dipole from afar, if no more forces are applied to the particle, the particle will eventually become trapped in a bouncing motion from pole to pole, as the same process will be repeated on the other pole of the dipole. In this case its pitch angle at a specific location can be found using the equation

$$\sin \alpha = \left(\frac{B}{B_m} \right)^{1/2} \tag{1.36}$$

The minimum strength of a magnetic field is on the equatorial plane, and can be calculated as

$$B_{eq} = \frac{B_{pl}}{L^3} \tag{1.37}$$

Combining eq. 1.13 and eq. 1.36 an equatorial pitch angle, α_{eq} can be defined as

$$\sin^2 \alpha_{eq} = \frac{B_{eq}}{B_m} = \frac{\cos^6 \lambda_m}{\left(1 + 3\sin^2 \lambda_m\right)^{1/2}} \tag{1.38}$$

where λ_m is the magnetic latitude of the particle's mirror point. This equation shows that the α_{eq} depends solely of the magnetic latitude of its mirroring point, and not at all from its L-shell value.

The bounce period of a particle is calculated as

$$\tau_b \approx \frac{LR_{pl}}{(W/m)^{1/2}} \left(3.7 - 1.6 \sin \alpha_{eq}\right) \tag{1.39}$$

where W is the particle's energy. The period of this motion is in the hours range. For Earth the bounce period of a proton with energy 1eV ranges from $\sim$ 1.5h to $\sim$ 10h, depending on its L-shell value, while for an electron with the same energy the period is $\sim$ 5s to $\sim$ 10s. Vogt et al. [2014], using simulations, calculated that on Jupiter, the bounce period for a heavy ion with mass of 20 proton masses, for energies 100eV to 50keV, and for α_{eq} between 20° and 80°, is from $\sim$ 1h to $\sim$ 10h.

1.6.3. Equatorial drift

There are three sources of equatorial drift for the magnetospheric particles: the planetary magnetic field, the corotational electric field, and the solar-wind-generated electric field. This drift is perpendicular to the planetary equatorial magnetic field lines, forcing the particles to drift along the equator. Here are presented some major processes resulting to an equatorial drift.

Corotation electric field & $\boldsymbol{E} \times \boldsymbol{B}$ drift

As a planet rotates with an angular velocity Ω_{pl}, the particles, following the magnetic lines, will corotate. This corotation of particles will create a corotating electric field:

$$\boldsymbol{E_{cr}} = -\left(\Omega_{pl} \times \boldsymbol{r}\right) \times \boldsymbol{B} \tag{1.40}$$

Combining eq. 1.40 with eq. 1.13, the strength of the corotating electric field on the equator is

$$E_{cr} = \frac{\Omega_{pl} B_{pl} R_{pl}}{L^2} \tag{1.41}$$

which shows that the electric field strength decreases with the square of the L value.

This corotating current will also affect the particles. Taking eq. 1.18, and this time including the electric field, we can separate it to parallel and perpendicular components.

The parallel component describes an electric field along the magnetic field

$$m\ddot{u}_{\parallel} = qE_{\parallel} \tag{1.42}$$

which though cannot be sustained due to the high mobility of electrons, that create an counter-acting electric field, and the plasma quasi-neutrality, that forces the plasma to maintain a quasi-neutral state.

The perpendicular component, assuming that the perpendicular electric field is parallel to the x-axis, $\boldsymbol{E}_{\parallel} = E_x\hat{e_x}$ gives the following velocity components for a particle

$$\begin{aligned} \dot{u_x} &= \omega_g u_y + \frac{q}{m}E_x \\ \dot{u_y} &= -\omega_g u_x \\ \dot{u_z} &= 0 \end{aligned} \tag{1.43}$$

Taking the second derivative we have

$$\begin{aligned} \ddot{u_x} &= -\omega_g^2 u_x \\ \ddot{u_y} &= -\omega_g^2\left(u_y + \frac{E_x}{B}\right) \end{aligned} \tag{1.44}$$

Which, similarly to section 1.6.1, eq. 1.44 describes a gyration around a guiding centre with an extra drifting term that forces the guiding centre to drift to the -y direction.

The general form of the $\boldsymbol{E} \times \boldsymbol{B}$ drift is

$$\boldsymbol{u_E} = \frac{\boldsymbol{E} \times \boldsymbol{B}}{B^2} \tag{1.45}$$

This drift is independent of the particles sign, hence both electrons and ions move towards the same direction. The path they will follow will be a helical movement: an ion / electron is accelerate towards / away from the direction of the electric field, increasing its gyroradius. But during its second half of its orbit it is decelerated, hence its gyroradius is decreased. This increase and decrease of the gyroradius shift the position of the guiding centre, causing the drift.

General force drift

By combining eq. 1.15, eq. 1.45, and eq. 1.24 we get the equation

$$\boldsymbol{u_F} = \frac{1}{\omega_g}\left(\frac{\boldsymbol{F}\times\boldsymbol{B}}{mB}\right) \tag{1.46}$$

where applies for any force acting on a particle in a magnetic field: Coulomb, polarisation, gradient, and gravitational. As the ω_g carries the particles sign, for any force other than Coulomb force, the particles will drift to opposite directions. For Coulomb force, since it also carries the particles sign, those will cancel each other out, showing that the particles are moving towards the same direction.

Magnetic gradient drift

Any inhomogeneity of a magnetic field, such as the multipolar nature of a planetary magnetic field, the magnetospheric plasma movement, the planetary rotation etc., will lead to a magnetic drift of the particles. In a quasi-dipolar magnetosphere a primary inhomogeneity is the gradient in the magnetic field, in both the radial and latitudinal directions. Any strong variations of the magnetic field will create an electric field (based on the Faraday law, $\nabla\times\boldsymbol{E} = -d\boldsymbol{B}/dt$) causing the $\boldsymbol{E}\times\boldsymbol{B}$ drift that was discussed previously. Any weak variations though will limit the effects of the $\boldsymbol{E}\times\boldsymbol{B}$ drift, but creating a drift solely due to the magnetic field. The gradient drift of the guiding centre is

$$\boldsymbol{u_\nabla} = \frac{mu_\perp^2}{2qB^3}\left(\boldsymbol{B}\times\nabla B\right) \tag{1.47}$$

and the motion is perpendicular to both the magnetic field and its gradient. Also, since the gradient drift depends on the charge of the particle, ions and electrons will drift in different directions.

As the gyration and bounce motions are much faster than the drift motion, in order to accurately calculate the drift period one must first integrate over the first two, and then focus on the drift motion. By ignoring any contribution of drifts due to the electric field, the particle will experience a perfect and purely azimuthal magnetic drift, u_d. The velocity of the drift can be found by dividing the angular drift that occurs during one bounce cycle, $\Delta\psi$, by the bounce period, τ_b.

The angular drift, $\Delta\psi$, is calculated by integrating $u_d/r\cos\lambda$ over one bounce cycle. Also, we have $dt = ds/u_{\parallel}$. Hence the angular drift is calculated as

$$\Delta\psi = 4\int_0^{\lambda_m} \frac{u_d}{r\cos\lambda}\frac{ds}{u_{\parallel}} \tag{1.48}$$

The angular drift velocity, $2\pi\langle\Omega_d\rangle$, over a cycle with a drift period, τ_d, is given as

$$2\pi\langle\Omega_d\rangle = \frac{\Delta\psi}{\tau_b} \tag{1.49}$$

where the τ_b is the bounce period, as shown in eq. 1.39. The right side of eq. 1.49 is essentially the bounce frequency, f_b.

The average drift period, $\langle\tau_d\rangle = \langle\Omega_d\rangle^{-1}$ for a particle in a dipole magnetic field is given by the equation

$$\langle\tau_d\rangle \approx \frac{\pi q B_{pl} R_{pl}^2}{3LW}\left(0.35 + 0.15\sin\alpha_{eq}\right)^{-1} \tag{1.50}$$

The numerical values in the parenthesis are a result of an approximation for the integral of $\Delta\psi$, which while it can be solved numerically, the approximation is adequate for the purposes of this section. As the average drift velocity is

$$\langle u_d\rangle = \frac{2\pi L R_{pl}}{\langle\tau_d\rangle} \tag{1.51}$$

combining eq. 1.50 and eq. 1.51 we get the average magnetic drift velocity

$$\langle u_d\rangle = \frac{2\pi L R_{pl}}{\tau_d} \approx \frac{6L^2 W}{q B_{pl} R_{pl}}\left(0.35 + 0.15\sin\alpha_{eq}\right)^{1/2} \tag{1.52}$$

As the drift velocity depends on the charge of the particle, electrons and ions will move to different directions. For Saturn, as the north magnetic pole is parallel to the north rotating pole, the ions will drift eastwards and the electrons westwards. This is the opposite to what happens on Earth, as the antiparallel direction between the magnetic and rotation axes force the ions to drift westwards and the electrons eastwards. This movement of the plasma creates the *ring current* around a planet. Both the average magnetic drift period and velocity are independent of the particle mass, hence ions and electrons with the same energy have the same drift period. An interesting feature is that since the velocity scales with L^2, a particle's velocity increases with distance, which is opposite to a Keplerian motion where its velocity decreases with distance.

Mauk et al. [1999] mentions that due to magnetic drifts the high-energy electrons lag behind the lower-energy electrons, but for ions this picture is reversed, as the high-energy ions drift faster than the lower-energy ions.

This is the slowest of all the drift motions. As an example, Gray [2018], based on the works of Lew [1961], Hamlin et al. [1961], Mauk et al. [1999], calculated that for particles in the Jovian magnetosphere with energy $10 - 1000$eV, $L = 10 - 20$, and $\alpha_{eq} = 10^\circ - 90^\circ$, the period for a full rotation around the planet due to the equatorial magnetic drift is ~ 9.5 to ~ 1700 Jovian days (a drift rate of $0.02^\circ - 3.82^\circ$/h).

Fig. 1.3 shows all the drift motions of a charged particle that were discussed above. The top row shows the case of a particle in a magnetic field outwards of the page, where it simply gyrates around a magnetic line, while the next three rows show a different disturbance acting on the particle simultaneously with the magnetic field: a homogenous electric field (second row), a force (third row), and a gradient of the magnetic field (fourth row). The figure shows the drift for both ions (left column, in blue) and electrons (right column, in red). As seen from the figure, the simultaneous existence of a magnetic field and an electric field, i.e. $\boldsymbol{E} \times \boldsymbol{B}$, creates a drift, forcing the ions and electrons to drift towards the same direction. The force and magnetic gradient though force them to drift to opposite directions.

Curvature drift

As the magnetic lines of a dipole are curved, they are introducing the curvature drift. As the particles have a parallel velocity, $u_{\parallel}$, they will experience a centrifugal force around the local curvature radius, $\boldsymbol{R_C}$, given in 1.29. Combining eq. 1.46 and eq. 1.29 we get the curvature drift

$$\boldsymbol{u_R} = \frac{m u_{\parallel}^2}{q} \left(\frac{\boldsymbol{R_C} \times \boldsymbol{B}}{R_C^2 B^2} \right) \tag{1.53}$$

The curvature drift is proportional to the parallel particle energy, $W_{\parallel} = (1/2)\, m u_{\parallel}^2$ and perpendicular to the magnetic field and its curvature.

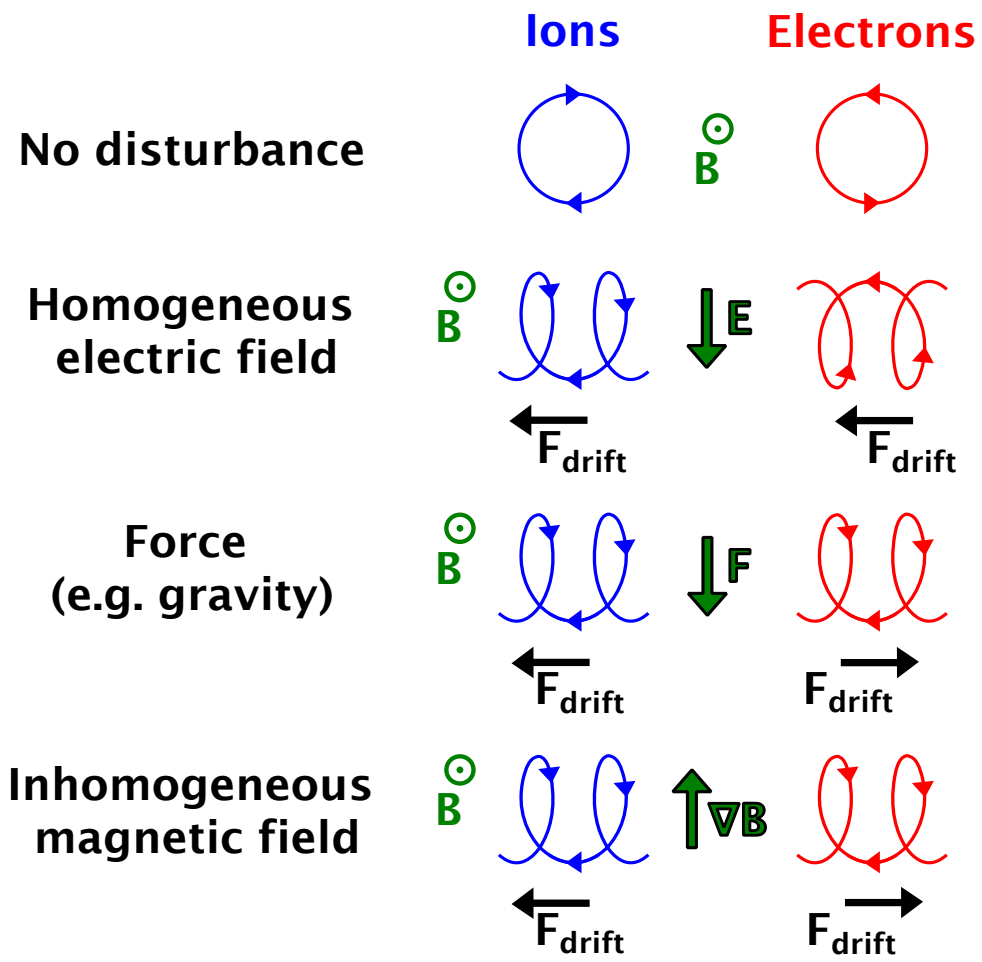

Figure 1.3: Charged particle drifts, under different disturbances. *Top row*: case of a particle in a magnetic field outwards of the page, with no additional disturbances. *Second raw*: a homogenous electric field acts on the particles as an additional disturbance, simultaneously with the magnetic field. *Third row*: same as second raw, with a general case of a force (e.g. gravity). *Fourth row*: same as the second row, with a gradient of the magnetic field. The direction of each disturbance is marked with the arrow, and the drift of each particle (left column, in blue, for ions and right column, in red, for electrons) is marked with the black arrow. The $\boldsymbol{E} \times \boldsymbol{B}$ forces the particles in drifting in the same direction, while the other disturbances force them to drift in opposite directions.

Solar wind induced electric drift

The solar wind generates an electric field inside a magnetosphere (for example, at Jupiter this field is directed from dusk to dawn along the equatorial plane). Hence, all the charged particles are subject to a $E \times B$ drift, which will draw them towards the Sun. The equatorial drift velocity of a particle due to the electric drift is

$$u_E = \frac{E_{eq}}{B_{eq}} = \frac{E_{eq} L^3}{B_{pl}} \tag{1.54}$$

This drift does not depend on the charge of the particle, hence all the particles will be drawn towards the Sun.

So far all the drifts that a charged particle can be subjected to have been presented. For the cold plasma case though, due to the particles low energy the magnetic gradient drift and the curvature drift are weak compared to the gyration, the magnetic mirroring, and the $E \times B$ drift.

1.7. Plasma creation & loss

Fig. 1.4 shows the processes of how the inner magnetospheric plasma is being created, from the sources to the plasma torus. The neutral sources are usually the planets, the moons surface or interior, and special structures like planetary rings.

Neutrals can be extracted/expelled from a surface via photosputtering (e.g. Harrison and Schoen [1967]), sputtering from charged particles, corotating ions, or energetic particles (e.g. [Bar-Nun et al., 1985, Shi et al., 1995]), impact of micrometeorites [Haff and Eviatar, 1986], geological activities (e.g [Morabito et al., 1979, Hansen et al., 2006]), or simply due to overcoming the gravitational pull of a planet or a moon. These processes creates a neutral torus on the orbital path of the body. The torus then gets ionised through solar UV ionisation, electron impact, charge exchange with protons, or even CRAND (cosmic-ray albedo neutral decay) energetic particles [Cheng, 1984], creating the plasma torus.

The neutral torus is formed on the orbital plane of the body and it is subjected to the gravitational forces, i.e. it follows Keplerian orbits. The plasma torus though, while it is still formed on the orbital plane of the body, it will eventually follow the magnetic fields

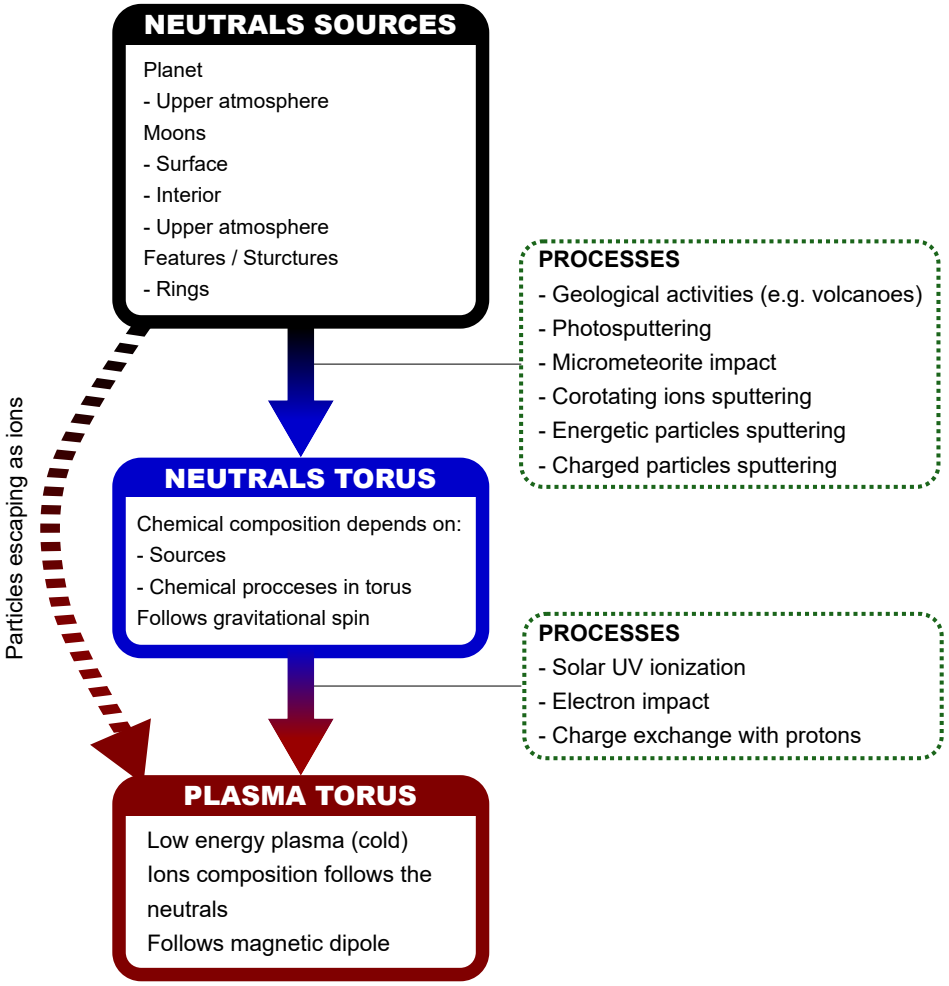

Figure 1.4: Creation processes of the inner magnetospheric plasma, from the neutral sources to the plasma torus.

of the region.

The planetary plasma composition is associated with the composition of the source: the Jovian plasma, due to the volcanic activity of Io, consists mainly of sulphur and oxygen, while the Kronian plasma, due to deposition of water from Enceladus, consists mainly of water-products [Achilleos et al., 2021]. For Uranus the consistency of the plasma is still under investigation: while a water-product, Saturn-like, environment was expected, due to

the water in the higher atmosphere of the planet (e.g. Teanby et al. [2022]), but also its icy moons (e.g. Cheng et al. [1986]), Voyager 2 observations found a pure hydrogen plasma, with no traces of water-products (Bridge et al. [1986], McNutt et al. [1987]). For Neptune, if a planetary plasma environment exists, we expect it to have hydrogen and helium, from the planet's higher atmosphere (e.g. Lindal et al. [1990]), and nitrogen, water, methane and carbon dioxide from Triton [McKinnon and Kirk, 2014].

A main ion sink is the ring current. There, the ions (e.g. A^+) interact with neutral molecules and atoms (e.g. B). The latter take the charge from the ion, leaving it neutral; this is the *charge exchange* process

$$A^+ + B \rightarrow A + B^+ \tag{1.55}$$

Even if the ring current density is too low to allow a significant number of direct collisions between ions and neutrals, a charge exchange will take place due to some resonance effect if there is enough energy difference between the two (e.g. cold a atom meeting a hot ring current ion). The produced neutral will keep the original high energy of the ion, becoming an energetic neutral atom (ENA), and it will eventually escape the magnetosphere, as, in these conditions, it is moving faster than the planetary escape speed.

There are also processes that can accelerate the particles along the field lines, moving their magnetic mirror point inside the planet's atmosphere. The magnetospheric particles will then interact with the atmospheric particles, and the particles scattering can produce planetary aurora. As those variations are altering the particles' pitch angles, it is called *pitch angle scattering*. The field-aligned acceleration can be caused by shear Alfvén waves, (i.e. a type of a wave - or, equally, electromagnetic oscillation - that propagates perpendicularly to both the direction of the magnetic field and the direction of the wave propagation), or field-aligned potential drops. Fig. 1.5 shows an example of this process: the main auroral oval.

Fig. 1.5 also shows another exciting auroral feature associated with a moon: the auroral footprints of a Io, Ganymede, and Europa. They appear as bright spots close to the magnetic poles, each with a small trailing tail. The auroral footprint is produced by more complicated interactions of a moon with the magnetic field, such as the Alfvén wings: an interaction between a sub-Alfvénic plasma flow (i.e. flow velocity lower than the local

Alfvén speed) and a conducting obstacle. As the plasma flows towards the object, it is slowed down and diverted around it, creating Alfvén waves that propagate away from the obstacle, along the magnetic field lines. The field-aligned currents generated by these waves close through perpendicular currents near the obstacle. This process essentially forces the field lines to bend back, creating a loop. The region which this process is taking place is called Alfvén wings [Jia et al., 2010]. This is presented schematically in fig. 1.6.

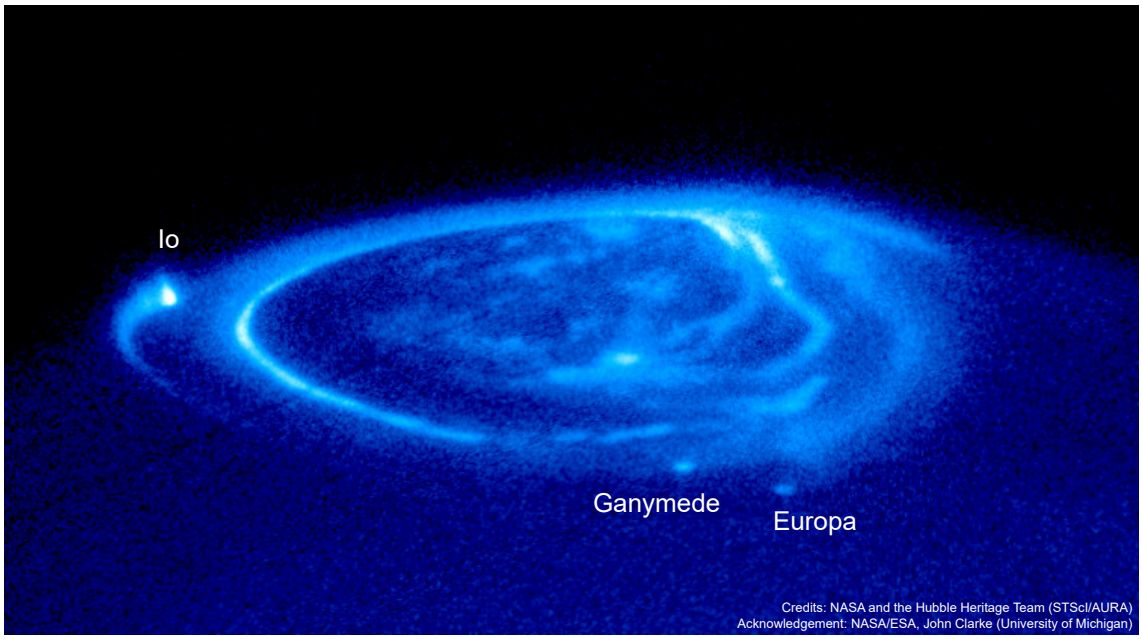

Figure 1.5: Main emission and auroral footprints of Io, Ganymede, and Europa on Jupiter's north pole. The main emission is a result of the magnetic mirroring point of a trapped magnetospheric particle moving inside the atmosphere of the planet, where it causes the particle to interact with atmospheric particles and produce aurora. This movement is due to acceleration of the particles along the field lines. Image credits: NASA/ESA and Hubble Heritage Team (STScI/AURA) and Clarke J. (University of Michigan) [2001]

We can calculate the pitch angles of the particles that will be lost due to interaction with the atmosphere by using the equatorial pitch angle (eq. 1.38) and setting the magnetic field of the mirroring point to be the magnetic strength of the planetary dipole, $B_m \rightarrow B_{pl}$.

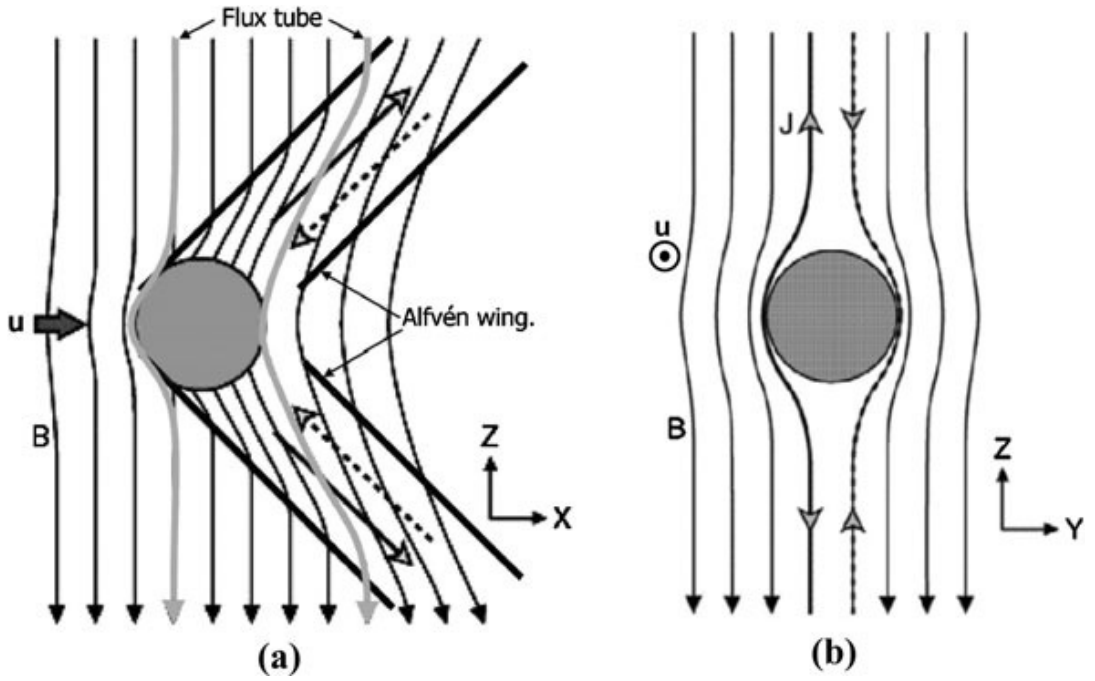

Jia et al. (2010); Adaptation of figure in Kivelson et al. (2004)

Figure 1.6: Schematic of an Alfvén wing, formed by the interaction between a sub-Alfvénic plasma flow and a conducting obstacle, such a magnetospheric moon. *Left*: a view of the system in the XZ plane, where +X is the plasma flow direction (with velocity $\boldsymbol{u}$) and -Z is the direction of the magnetic field, $\boldsymbol{B}$, which is perpendicular to X. As the plasma flows past the moon, the moon acts as an obstacle, causing the magnetic lines to stretch around and beyond it. This stretch creates currents (depicted by solid and dashed lines in the +Y and -Y directions), which, as they are forced to close near the moon, they form a loop. The region where this process takes place is the Alfvén wing, marked in bold black lines. Flux tubes are shown as grey bold lines. *Right*: the same process shown in the YZ plane, i.e. viewed from the plasma flow direction, with the currents labelled as J. Fig. from Jia et al. [2010], adapted from Kivelson et al. [2004].

So we have

$$\sin^2 \alpha_l = \frac{B_{eq}}{B_{pl}} = \frac{\cos^6 \lambda_{pl}}{\left(1 + 3\sin^2 \lambda_{pl}\right)^1 / 2} \tag{1.56}$$

All the particles with $\alpha < \alpha_l$ will be lost in the atmosphere. Also, due to the symmetric bounce motion, particles with $\alpha > 180 - \alpha_l$ will be also lost on the atmosphere in the other hemisphere.

Combining eq. 1.56 with eq. 1.37 we get

$$\sin^2 \alpha_l = \left(4L^6 - 3L^5\right)^{1/2} \tag{1.57}$$

which shows that the pitch angle depends only on the field line radius.

In reality α_l is the loss angle around a magnetic line, hence in three dimensions this will be a cone with an opening angle of α_l, which is called *loss cone*.

1.8. Magnetospheres & solar wind

As plasma particles and magnetic field co-exist in a region, under the right they can convect together. In a convection dominated plasma the magnetic field is *frozen-in* amongst the particles, resulting the two to move as one body. In a frozen-in plasma, the parameter β (defined and discussed in section 1.4) is important, as it shows whether the plasma particles drag the frozen-in magnetic field (high plasma pressure - high β), or whether the field confines the frozen-in plasma (high magnetic pressure - low β).

Both the magnetospheric plasma and the solar wind contain frozen-in plasma, but as the conditions in each region is different (β, magnetic field orientation, particles energy and density etc.) it is very hard for convected plasmas to mix. Therefore a planetary magnetosphere can be consider an obstacle in the path of the solar wind, where the solar wind will slow down and flow around the magnetosphere. This interaction will compress the front of the magnetosphere, and stretch the back, creating the magnetotail. The locus where the magnetospheric pressure is equal to the solar wind pressure is called *magnetopause*. Outside the magnetopause, as a result of the solar wind deceleration, a region of slow, heated, and dense solar wind is created, which is called *magnetosheath*. Fig. 1.7 shows schematically the above.

The connection of the magnetosphere with the solar wind magnetic field is also visible on this figure. This interaction is one of the basic features of a rotating magnetosphere, as it will be discussed in section 1.9.

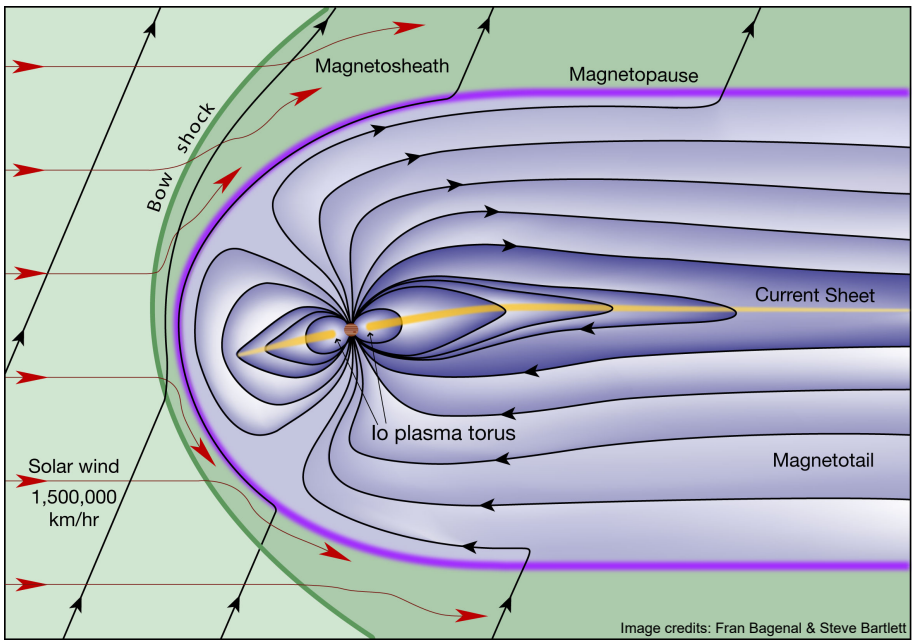

Figure 1.7: Example of the interaction of the solar wind with a magnetosphere of a gas giant - in the specific example with Jupiter. The red arrows are the solar wind flow, while the black arrows are the magnetic lines orientation. Image credits: Bagenal and Bartlett

If the solar wind hits the magnetosphere in an angle, i.e. for an angle between the magnetic dipole axis and the solar wind flow (which is the *attack angle*, as it will be further discussed in section 3.2) different than 90°, besides compressing the sunward part of the magnetosphere it can also distort it. Such an example is presented in fig. 1.8 (from Arridge et al. [2008]), where it shows the solar wind hitting the Kronian magnetosphere from below the Kronian equatorial plane. The left panel shows the distorted magnetic lines and plasma/current sheet, and the right panel shows the same effect in 3D, which, in this case, the magnetosphere took a bowl-shape plasma/current sheet.

1.9. Rotational magnetospheres

As the planet rotates, the magnetic lines are stretched outwards due to centrifugal force and plasma pressure gradient forces. This effect is more potent at the equator though, as the force is largest there. This creates a disk-like structure of stretched magnetic lines,

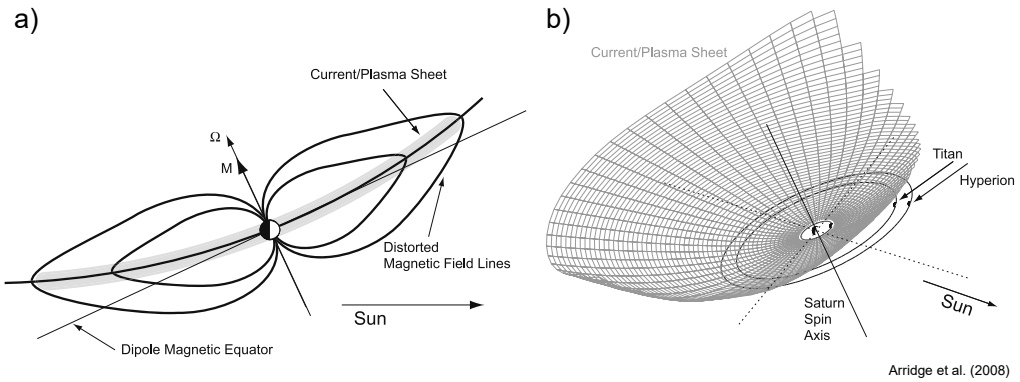

Figure 1.8: Example of the distortion of a magnetosphere when the solar wind is not parallel to the planetary equatorial plane. *Left*: the distorted magnetic lines and plasma/current sheet. *Right*: same, for 3D. In these conditions the magnetosphere takes a bowl-shape. Fig. from Arridge et al. [2008]

often referred to as *magnetodisk*, (e.g. Gledhill [1967], Kivelson [2015]). The magnetic lines though also carry plasma, hence, the region can also be called the *plasma disk*. This section is based on Achilleos et al. [2021], unless otherwise noted.

The magnetodisk affects the global morphology of the planetary magnetosphere, as, in the outer equatorial magnetosphere the total magnetic field strength will be a sum of the dipole magnetic field on that point plus the field from the magnetodisk current, caused by the moving plasma. The carried plasma is usually hot plasma and its β can reach high values, well above 1. For example, ions in the Jovian magnetosphere with energies over 20keV can reach values ~ 50 [Mauk et al., 2004] (where these populations carry so much energy that are not strongly affected by centrifugal forces), while ions in the Kronian magnetosphere with energies over 3keV can reach values ~ 10 [Sergis et al., 2009]. This hot plasma also expands the magnetopause distance; for Jupiter, for example, it can stretch the magnetopause from 42 Jupiter radii to $65 - 90$ Jupiter radii [Joy et al., 2002, Bagenal and Delamere, 2011]

Additionally, this rotation can create phenomena on the interface between the magnetosphere and solar wind. On Earth, the Kelvin-Helmholtz instability can be observed as the ocean waves: fast air, that can be considered liquid, blows over slow water, creating the waves. Such instabilities can occur in a rotating magnetosphere, in regions where the

magnetosphere and the flow of the solar wind are moving in opposite directions. Kelvin-Helmholtz instabilities have been observed in the dawn-side of Earth's magnetosphere (e.g. Rice et al. [2022]), and in dawn-side of Saturn's [Masters et al., 2010]. While on Earth the length of those structures can be couple of tens of meters high, the structure size that was observe at Saturn was over $33,000$km long. This is an impressive demonstration of scaling of physics, as the same mechanism can create structures that are scaled over more than three orders of magnitude.

1.9.1. Vasyliūnas cycle

The gas giants' magnetospheres have some differences on how they interact with the solar wind versus to the rocky planets. The Earth is a slow rotator, so the magnetic field is controlled by the solar wind. This makes corotational electric field dominant only very close to Earth. The interaction between the solar wind and the terrestrial magnetosphere is described by the *Dungey cycle* [Dungey, 1961]: on the dayside magnetopause the planetary magnetic lines (re)connect with the interplanetary magnetic field (IMF), creating a series of open magnetic lines coming from the ionosphere and extending to the flowing solar wind. The magnetospheric end of those lines is rotating with the planet, while the open end is being swept and stretched towards the magnetotail with the solar wind, where they eventually close there. As they close, due to being stretched and under tension, they will contract back towards the Earth. Meanwhile, the disconnected part of the magnetotail (where the magnetic line closed, away from the Earth) will accelerate away from the Earth, taking some of the magnetodisk plasma with it.

On the other hand on a magnetosphere much stronger and much faster rotating than the Earth's, the internal processes dominate while the solar wind interaction, i.e. the Dungey cycle, is marginally important. Such an example is Jupiter, where the corotational electric field is much stronger than the solar wind electric field. Additionally, Io loads heavily the system with plasma. This combination of the strong magnetic field with high density plasma makes the magnetic field and the plasma to move as one body. As the planet rotates, the magnetic lines are stretched beyond the corotation distance, where, in those distances the magnetic line will continue moving until something stops it. The

obstacle on the dayside is the magnetopause, where it will force the lines to move along the magnetopause boundary in a corotation motion. On the nightside though the plasma will move towards the (low-pressure) magnetotail, creating a situation where on one end the magnetic lines are attached to the ionosphere, while on the other end are constantly stretched towards the magnetotail. Eventually there will be a reconnection on the magnetotail, that will cause the planetary side of the loop to pull towards the planet, and the far side to move towards the magnetotail. Due to centrifugal force the plasma on this line will be concentrated in the very far end of the magnetic line, and with the reconnection it will be released moving away from the planet; this is a *plasmoid*. The described process is the *Vasyliūnas cycle* [Vasyliūnas, 1983].

Fig. 1.9 shows a sketch of the Vasyliūnas cycle. The left panel shows the equatorial plasma movement, while the right panel shows the process of a plasmoid creation in 4 snapshots on specific areas on the magnetosphere. The white arrows show the plasma movement, and the black lines on the right show the local magnetic field. The $\times$ on the left panel is where the magnetic reconnection happens, and the $\bigcirc$ is the centre of the disconnected plasmoid.

While Jupiter is the best example of Vasilyūnas cycle, not all gas giants have the same characteristics. Saturn, for example, while is a fast rotator, it has a magnetic field strength comparable to the Earth's, and the mass loading of the system due to Enceladus is not as prominent as is at Jupiter. This creates a unique situation where both the Dungey and Vasilyūnas cycles exist simultaneously: the corotation electric field is dominant closer to the planet, hence following the Vasyliūnas cycle, while on the magnetopause distances it is following the Dungey cycle [Achilleos et al., 2021].

1.10. Brief history of missions to the gas giants

The first in-situ data from the outer planets of our solar system came in the 1970s from Pioneer 10 and 11, and Voyager 1 and 2. While those missions yielded a plethora of discoveries, such as Saturn's faint F-ring [Simpson et al., 1980], Uranus' black rings [Curtis and Ness, 1985], Jupiter's magnetic dipole tilt [Smith et al., 1974], and Neptune's dramatic magnetic axis tilt [Krimigis, 1992], they were only designed for a single fly-by of each

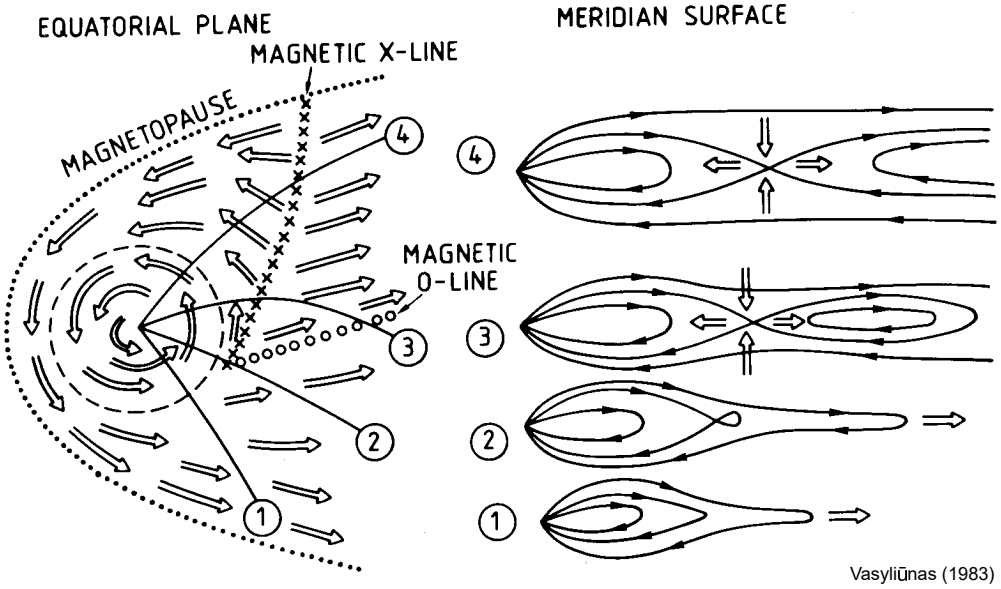

Figure 1.9: Example of the Vasyliūnas cycle. *Left*: plasma movement due to Vasyliūnas cycle (arrows). *Right*: magnetic lines in 4 snapshots on specific areas on the magnetosphere, showing the creation of a plasmoid. Fig. from Vasyliūnas [1983]

planet. So, in practice, the entire scientific community was trying to extract results from a handful of data.

The first orbiter to an outer planet was launched 20 years later, where Galileo started its journey around Jupiter in 1995 and stayed in orbit for almost 8 years studying the Jovian system [Johnson et al., 1992]. For Saturn, the first orbiter to Saturn arrived more than 20 years after the last contact with the planet by Voyager 2. Cassini–Huygens arrived to the planet in July 2004, and stayed in orbit for 13 years studying in depth the Kronian system [Lebreton and Matson, 1992]. To this date no orbiters have been sent to the Ice Giants, but the NASA Planetary Decadal Survey [National Academies of Sciences, Engineering, and Medicine, 2023] and ESA Voyage 2050 [Tacconi et al., 2001] reports set the exploration of Uranus as a high priority. This has also been suggested to the NASA Heliophysical Decadal Survey with a whitepaper that I participated [Arridge, Xystouris et al. 2023].

2. Instrumentation

> **"Matter and energy had ended and with it space and time. Even A[utomatic]C[omputer] existed only for the sake of the one last question that it had never answered. [...] The consciousness of AC encompassed all of what had once been a Universe and brooded over what was now Chaos. Step by step, it must be done.**
> **And AC said, 'LET THERE BE LIGHT'**
> **And there was light –"**
> — Isaac Asimov, *The Last Question*

2.1. Instruments overview

For this work I used data from the Langmuir probe and Cassini Plasma Spectrometer onboard the Cassini orbiter, as well as from the Heterodyne Instrument for Far Infrared on the Herschel space observatory. In this chapter, I will give a description of the instruments and their operation.

2.2. Cassini–Huygens mission

Cassini-Huygens Mission was a two-module spacecraft that was sent to study the Kronian system in a joint collaboration of the National Aeronautics and Space Administration (NASA), the European Space Agency (ESA) and the Italian Space Agency (ASI). It was composed of the Cassini orbiter, designed to study Saturn's system, and the Huygens probe, designed to study Titan's atmosphere and surface through its landing on the moon. It was launched on 15 October 1997, from Cape Canaveral, USA, and was captured by Saturn's gravitational pull (i.e. Saturn's sphere of influence) on 18 May 2004. A couple of months later on 1 July 2004 it conducted Saturn Insertion Orbit (SOI), and it stayed in Saturn's system until 15 September 2017, where it dived into Saturn after 294 orbits around it. [NASA's Jet Propulsion Laboratory (JPL), 2023]

The mission's objectives were the planet itself (study of the clouds, atmospheric composition, temperatures, internal structure, rotation etc.), the ring system (structure, com-

position, dynamical processes etc.), the icy satellites (characteristics, geological histories, surface composition, internal structure etc.), the planet's magnetosphere (composition, particles sources and sinks, electric currents, dynamics, interaction with solar wind etc.), and Titan (distribution of gases and aerosols, winds, temperatures etc.)[Matson et al., 2002]. Overall it carried 12 instruments: imagers, microwave remote sensors, and instruments focused on fields, particles, and waves. For this work two of the instruments were used: the Cassini Radio and Plasma Wave Investigation [Gurnett et al., 2004] Langmuir Probe and the Cassini Plasma Spectrometer [Young et al., 2004].

2.2.1. Cassini Langmuir Probe (LP)

A Langmuir probe is an ideal instrument for measuring and characterising the properties of a low pressure, low energy ionised gas, such as the magnetospheric plasma. Its operation is quite straight forward: when a collector (probe) submerged in an ionised gas (plasma) is charged, the same-charge particles around it are repelled while the opposite-charge particles are attracted. A space will therefore be created around the probe, containing only the opposite-charge particles; this is referred to a *sheath*. The attracted particles are accelerated towards the probe, and by hitting it they generate a current, which provides these particles' properties (mass, temperature, density). To avoid disturbances from the spacecraft, the Debye length of the plasma must be smaller than the distance of the probe from the spacecraft. The LP onboard Cassini was spherical. The left panel of fig. 2.1 shows all the possible interactions between a LP and an electron, an ion, and the sunlight, and the right panel shows an example of a the LP under a positive bias. The sunlight impact will be discussed later in the study.

This was first described in Mott-Smith and Langmuir [1926], for an *orbital motion limiting (OML)* case, i.e. the gas pressure is sufficiently low so there are no collisions between the particles, hence the particles motion is purely described by their orbit. In reality though there are always collisions; the number of collisions though is sufficiently small to be considered that it is negligible. Also the assumption was made that there are no same-charge particles reaching the probe, which could be challenged if the particles are energetic enough; again though their number is negligible compared to the bulk of

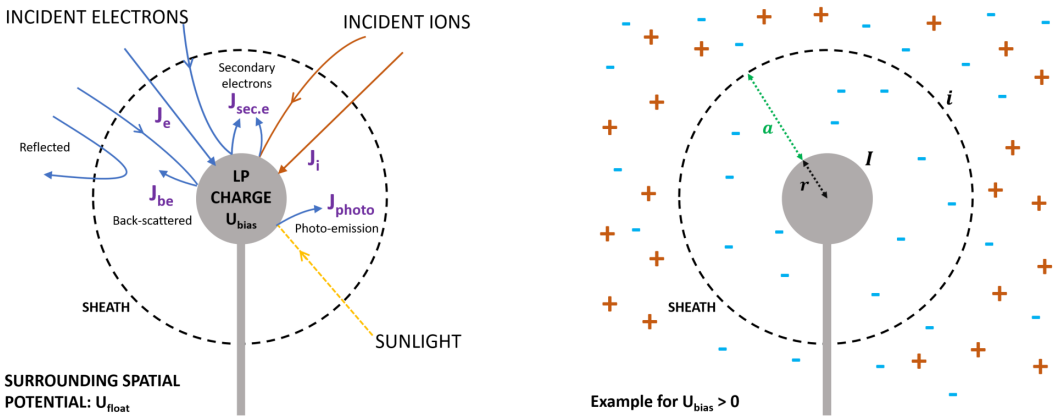

Figure 2.1: *Left*: The possible interaction between a charged probe and particles/light. *Right*: an example of the LP being under positive bias.

the opposite-charge particles reaching the probe. In addition no reflections are assumed on the probe: all particles reaching the probe are depositing their charge on it. Lastly, a sharp transition is assumed at the edge of the sheath. This is unnatural as there is a drop of potential region, which, though, is small compared to the region of steady potential, and therefore the assumption is valid.

Let a particle velocity in spherical coordinates $u = (u_r, u_\phi, u_\theta)$ (where r the radial, ϕ the azimuthal, and θ the polar components), r the probe radius, and a the sheath radius. Due to the spherical shape of the probe, hence spherical symmetry of the problem, the only velocity components that are relevant to the problem is the radial component, u_r, and the tangential to the surface of the sphere, $u_\parallel$, that lies on the $u_\phi u_\theta$ plane. We define $u_\parallel^2 = u_\phi^2 + u_\theta^2$, and an angle ψ normal to the radial direction so that $u_\theta = u_\parallel \sin\psi$ and $u_\phi = u_\parallel \cos\psi$.

We can get a velocity distribution function in any coordinates:

$$f\left(u_r, u_\phi, u_\theta\right) \;=\; f\left(u_\parallel, u_\parallel \sin\psi, u_\parallel \cos\psi\right) \tag{2.1}$$

which we can then integrate to find the velocity distribution in 2D:

$$g\left(u_r, u_\parallel\right) = \int_0^{2\pi} f\left(u_\parallel, u_\parallel \sin\psi, u_\parallel \cos\psi\right) d\psi \tag{2.2}$$

We then need to know how the variables $\left(u_r, u_\parallel\right)$ relate at the end of the sheath and the probe, and hence integrate the velocity distribution and calculate the current. For this we are conserving the angular momentum and the kinetic energy from the probe radius, r, to the sheath radius a:

$$\frac{1}{2}m\left(u_{r,r}^2 + u_{\parallel,r}^2\right) = \frac{1}{2}m\left(u_{r,a}^2 + u_{\parallel,a}^2\right) + qV \tag{2.3}$$

$$ru_{\parallel,r} = au_{\parallel,a} \tag{2.4}$$

where $\left(u_{r,r}, u_{\parallel,r}\right)$ and $\left(u_{r,a}, u_{\parallel,a}\right)$ are the velocity components at the probe and sheath respectively, q is the particle charge and V is the potential. Solving for $u_{r,r}$ and $u_{\parallel,r}$:

$$u_{r,r}^2 = u_{r,a}^2 - \left(\frac{a^2}{r^2} - 1\right)u_{\parallel,r}^2 + \frac{2qV}{m} \tag{2.5}$$

$$u_{\parallel,r} = \frac{a}{r}u_{\parallel,a} \tag{2.6}$$

Only if $u_{r,r}^2 \geq 0$ a physical solution exists, hence we are only looking for combination of $u_{r,a}$, $u_{\parallel,a}$, a/r, q/m and V that satisfy the condition. This can be seen schematically in fig. 2.2 (figure adapted from Mott-Smith and Langmuir [1926]). The plot on the left is for potential greater or equal to zero, and the one on the right is for potential less than zero. For both plots solutions exist only in the shaded area. The solutions for potential equal or greater than zero are between $\pm u_{\parallel,1}$ where

$$u_{\parallel,1} = \left(\frac{2qV/m}{(a^2/r^2) - 1}\right)^{1/2} \tag{2.7}$$

where the solutions for negative potential are

$$u_{r,1} \geq -\frac{2qV}{m} \tag{2.8}$$

At the boundary $r = a$ where $u_{\parallel,a} = 0$ we get:

$$u_{r,r}^2 = u_{r,a}^2 + \frac{2qV}{m} \;\Leftrightarrow\; u_{r,a}^2 = u_{r,r}^2 - \frac{2qV}{m} \tag{2.9}$$

We can only have a solution if $u_{r,a} > 0$, so we can define the limit as $u_{r,lim}$, and we have solutions for:

$$u_{r,lim}^2 \geq u_{r,r}^2 - \frac{2qV}{m} \tag{2.10}$$

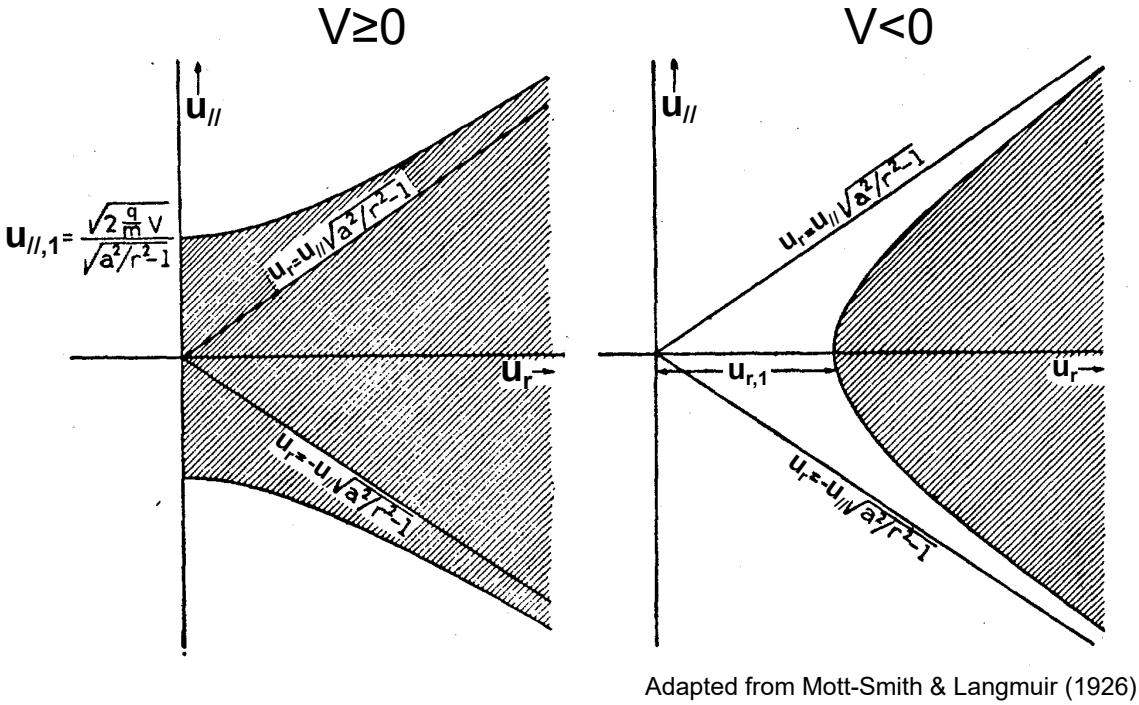

Figure 2.2: Solution regions (in grey) of a spherical collector for moving particles, for negative (*left*) and positive (*right*) applied potential. The combination of $u_{r,a}$, $u_{\parallel,a}$, a/r, q/m and V must lay inside the grey areas. Figure adapted from Mott-Smith and Langmuir [1926] (©American Physical Society)

To calculate the current generated by the incident particles at the probe we integrate the distribution function of eq. 2.1. The number of particles crossing a unit area in unit time is the number flux:

$$N = \vec{v} f\left(\vec{v}\right) d^3\vec{v} \tag{2.11}$$

By integrating the number flux over the entire space and multiplying with the charge, q, of the particles we get the current density, i.e. the charge crossing a unit area in unit time:

$$j = \int q\vec{v} f\left(\vec{v}\right) d^3\vec{v} \tag{2.12}$$

Lastly we get the current by multiplying the current density with the area of the detector:

$$I = Aj \;\Leftrightarrow\; I = Aq \int \vec{v} f\left(\vec{v}\right) d^3\vec{v} \tag{2.13}$$

The area in our case, of the sheath distance is $A = 4\pi a^2$.

Combining eq. 2.2 2.13 and integrating for the entire space we can find the current reaching a spherical detector

$$\text{for } V > 0: \quad I = 4\pi a^2 qN \int_0^{\infty} \int_0^{u_{\parallel,1}} u_{r,a} u_{\parallel,a} g\left(u_{r,a} u_{\parallel,a}\right) du_{r,a} du_{\parallel,a} \tag{2.14}$$

$$\text{for } V < 0: \quad I = 4\pi a^2 qN \int_{u_{r,1}}^{\infty} \int_0^{u_{\parallel,1}} u_{r,a} u_{\parallel,a} g\left(u_{r,a} u_{\parallel,a}\right) du_{r,a} du_{\parallel,a} \tag{2.15}$$

Lastly we are substituting with the distribution function of the gas. Although space plasmas are rarely Maxwellian (e.g. Hoegy and Brace [1999]) we can express these in terms of the properties of a Maxwellian distribution

$$f\left(u_r, u_\theta, u_\phi\right) = \left(\frac{m}{2\pi k_B T}\right)^{3/2} \exp\left[-\frac{m\left(u_r^2 + u_\theta^2 + u_\phi^2\right)}{2k_B T}\right] \tag{2.16}$$

Eq. 2.16 can also be expressed a specific 2D space as the example in eq. 2.2:

$$g\left(u_r, u_\parallel\right) = \frac{1}{\sqrt{2\pi}} \left(\frac{m}{k_B T}\right)^{3/2} \exp\left[-\frac{m\left(u_r^2 + u_\parallel^2\right)}{2k_B T}\right] \tag{2.17}$$

and substituting in eq. 2.15 we get the current on the LP surface:

$$\text{for } \eta > 0: \quad I = 4\pi a^2 A \left(1 - \frac{a^2 - r^2}{a^2} \exp\left[-\eta \frac{a^2}{a^2 - r^2}\right]\right) \tag{2.18}$$

$$\text{for } \eta < 0: \quad I = 4\pi r^2 A \exp\left[-\eta\right] \tag{2.19}$$

where

$$A = Nq\sqrt{\frac{k_B T}{2\pi m}} \qquad \text{and} \qquad \eta = \frac{qV}{k_B T} \tag{2.20}$$

Cassini's LP (fig. 2.3) had a diameter of 5cm and it was made of titanium with a titanium nitride coating. It was located on the edge of a 0.8m boom, that when extended as part of the launch sequence it placed the probe 1.5m away from the body of the spacecraft. The last 10.9cm of the mountain boom, called the stub, were very thin (6.35cm in diameter), kept in the same potential as the LP, and coated with the same titanium nitride as the probe [Jacobsen et al., 2009]. This was done to minimise the impact of the photoelectrons that are coming from the stub. The upper energetic threshold of particles the LP could detect is 10eV [Gustafsson and Wahlund, 2010], and the noise floor is 100pA. This noise, was mostly coming from the electronics of the instrument, and it is often called thermal

noise, electronic noise, or Johnson-Nyquist noise. Essentially it is disturbances or noise in a signal, coming from the thermal agitation of the electrons inside the devices' electronics [Motchenbacher and Connelly, 1993]

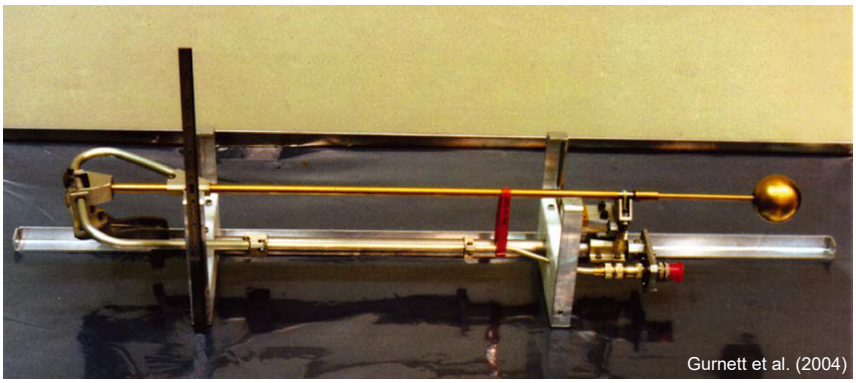

Figure 2.3: The LP onboard Cassini, as photographed pre-flight. Image from Gurnett et al. [2004].

A bias voltage from −32V to +32V was applied over 256 points, each done twice to allow the bias potential to settle and currents to readjust, producing 512 points. This is called a *sweep*, and its product is a *current-voltage* (I-V) curve. This is done rapidly over the course of 0.5 seconds and carried out periodically to provide a sampling of the plasma at different locations. The typical period is around 10 minutes, but it can vary for some special orbits, e.g. for targeted moon flybys the sweep frequency drops down to 10 seconds and the bias voltage is reduced from −5V to +5V. Due to the electrons moving faster than the ions the produced currents are usually largest under positive bias. Also in some few cases the bias voltage was applied 3 times, aiming to study any possible delays on the settling of the surrounding plasma.

Due to the plasma charge neutrality a quasineutrality between electrons and ions is assumed for the inner Kronian magnetosphere. The spacecraft though is being charged due to the rapid movement of the electrons compared to the ions, hence, in dense plasma regions, more electrons are hitting the spacecraft charging it negatively, which is the potential relative to the surrounding plasma. The LP, as it is close and connected to the spacecraft, will be under the *floating potential*, U_{fl}, i.e. a potential to maintain zero current. Hence, as long as no bias voltage is applied to the LP, its the U_{fl} will vary to

whatever potential is necessary for the LP to maintain zero net current [Merlino, 2007]. In the area of our study, i.e. the inner Kronian magnetosphere, the spacecraft potential is typically negative. However at very low and very high altitudes, and when the spacecraft is in sunlight the photoemission may dominate over the rate which electrons are hitting the spacecraft, resulting to a positive spacecraft potential [Fahleson, 1967].

When the LP is charged, the total potential that it is under is sum of the floating potential plus the applied bias voltage, U_b:

$$U_{total} = U_b + U_{fl} \tag{2.21}$$

When the applied U_b is equal to the $-U_{fl}$, the total voltage the LP is under is equal to 0; this is the 'changing' point for the attracted particles species. The LP is negatively charged in the interval -32V to $-U_{fl}$ attracting ions, hence this can be called the *ion current* and symbolise it as I_-, and positively charged in the interval $-U_{fl}$ to $+32$V attracting electrons, with this being the *electron current*, symbolised as I_+. It must also be noted that when Cassini is in sunlight there is always a photoelectron current from the LP, regardless of the probe charge – the probe charge though changes whether the photoelectrons return to the probe or not. As the photoemission removes negative charges from the LP, it is equivalent as adding positive charges to it, and therefore the photocurrent, I_{ph}, will be mapped in the ion current.

While in dense plasma regions ($\sim 10^7 \mathrm{m}^{-3}$) the I-V curve can be modelled with currents, giving estimates of the surrounding plasma properties (as shown in e.g. Gustafsson and Wahlund [2010], Holmberg et al. [2012]). This method though is reliable only if the Debye length of the surrounding plasma is large compared with the probe radius [Laframboise, 1966], which is valid in our case as the median of the Debye length of the measurements is ~ 2.5m. Fig. 2.4 shows an example of an I-V curve for the sweep between 2005-05-02 23:28:48.093 - 23:28:48.604UT. The top panel shows the I-V curve in linear scale, the middle panel shows the same curve in logarithmic scale, and the bottom panel shows the current gradient with respect to the applied bias voltage. The blue and red bars on the top are a visual aid to make clearer when the applied bias voltage is negative or positive. Also the LP floating potential, U_{fl} is marked with the yellow dashed line on the bottom panel. Here follows the methodology for calculating the ion and electron plasma parameters.

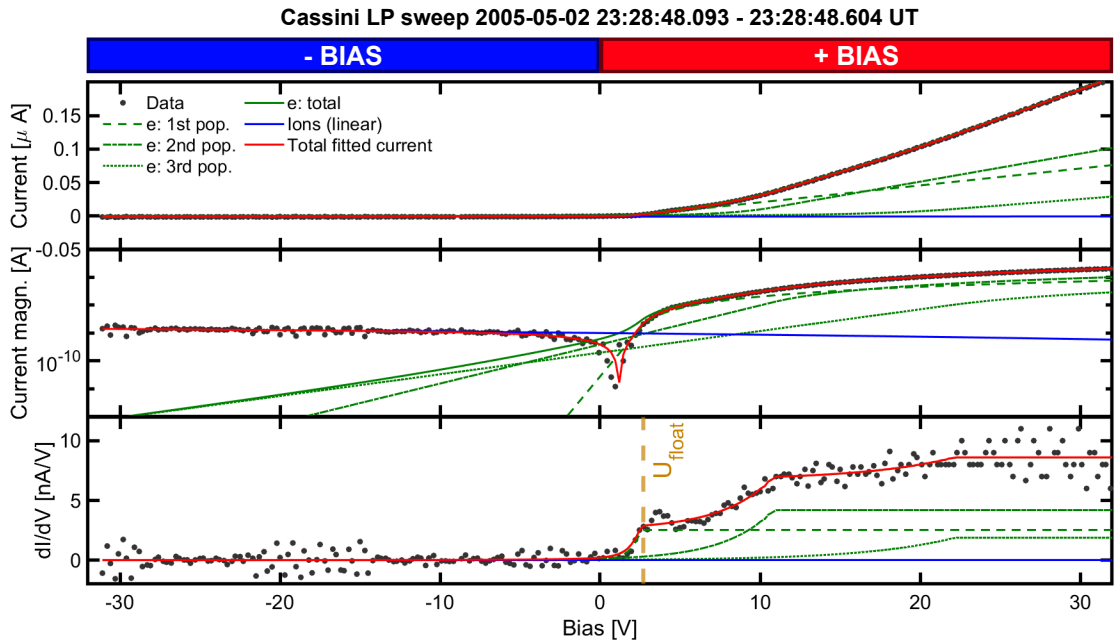

Figure 2.4: Example of an LP sweep. The I-V curve is shown in linear (top panel) and logarithmic (middle panel) scale. The bottom panel shows the current gradient with respect to the applied bias voltage. The blue and red bars on the top are a visual aid to make clear when the applied bias voltage is negative or positive.

2.2.2. Ion parameters

For the ion parameters the Fahleson [1967] approximation is used. The ion current can be expresses as

$$I_i = I_{i,0}\left(1 - \frac{q_i\left(U_{fl} + U_b\right)}{\frac{m_i u_i^2}{2} + k_B T_i}\right) \tag{2.22}$$

where

$$I_{i,0} \approx -A_{LP} n_i q_i \left(\frac{u_i^2}{16} + \frac{k_B T_i}{2\pi m_i}\right)^{1/2} \tag{2.23}$$

and q_i / m_i / T_i / u_i are the ion charge / mass / temperature / bulk ion speed, A_{LP} is the surface area of the LP, k_B is the Boltzmann constant, U_b is the applied bias voltage, and U_{fl} is the floating potential of the probe. Introducing the photoelectron current, I_ph

to eq. 2.22 and replacing with

$$m = I_{i,0}\left(1 - \frac{q_i U_{fl}}{\frac{m_i u_i^2}{2} + k_b T_i}\right) + I_{ph}, \qquad b = \frac{I_{i,0} q_i}{\frac{m_i u_i^2}{2} + k_b T_i} \tag{2.24}$$

we get the linear equation

$$I_i = bU_b + m \tag{2.25}$$

As the region from about -5V to $-U_{fl}$ is not linear (due to additional current sources, such as secondary electrons and energetic electrons that can overcome the negative potential and interact with the probe) we apply the eq. 2.25 to the $-32V$ to -5V region. We will also further discuss the photoelectrons and photocurrent in section 2.2.5.

2.2.3. Electron parameters

For the electron parameters a multiple-electron-population model is used, as described in Gustafsson and Wahlund [2010]: the electron density can be described by a superposition of multiple electron populations, each one following a Maxwellian distribution. There can be up to three populations, and the total electron density is the sum of each of the lateral densities:

$$n_{e,tot} = \sum n_{e,j} \ , \ j \in 1, 2, 3 \tag{2.26}$$

The number of the populations that must be used for the analysis of the I-V curve is given from the shape of the gradient of the current with respect to the voltage (bottom panel of 2.4). Each of the 'knees'/'break', i.e. where the current changes gradient non-smoothly at $U_{fl.}$ and around 10V and 22V, correspond to a population; in the given example the analysis must be done with 3 electron populations. If the LP is sunlit photoelectrons will be produced due to the photoelectric effect. Earlier works often assumed that the first population corresponded to photoemission, but this assumption collapses when the best fit gives us an one-population model, as the LP measures both the magnetospheric plasma and the photoelectrons.

2.2.4. Cassini Plasma Spectrometer (CAPS)

CAPS was an instrument designed to make a full 3D map of the Kronian plasma, in order to understand deeper the sources of ionisation, and the means which is accelerated, transported, and lost [Young et al., 2004, Blanc et al., 2002]. It had three sensors: the Electron Spectrometer (ELS), the Ion Beam Spectrometer (IBS), and the Ion Mass Spectrometer (IMS). Fig. 2.5 shows a photograph of the complete instrument, and the arrangement of the three sensor heads.

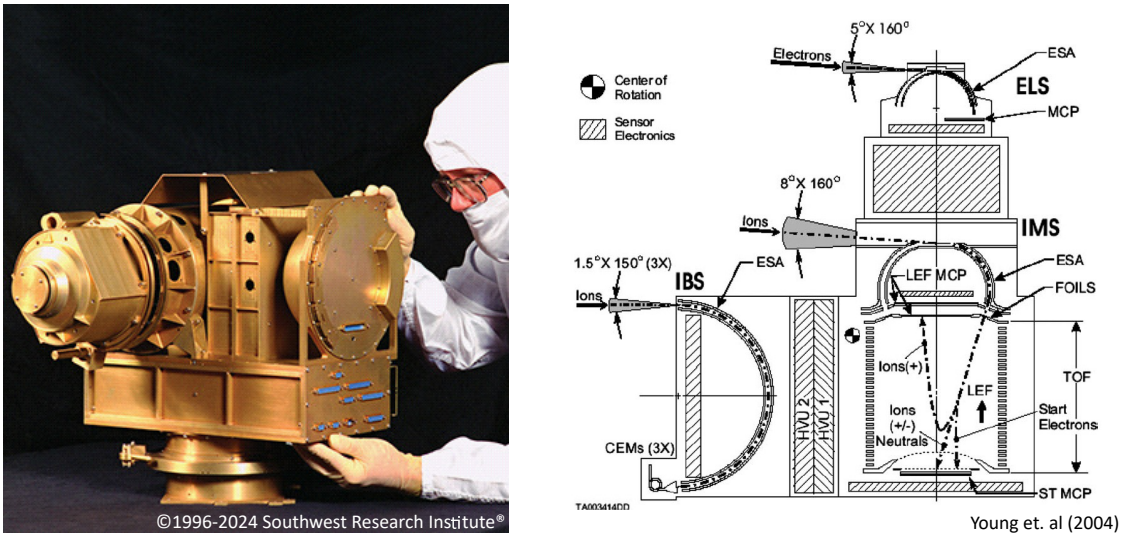

Figure 2.5: *Left*: CAPS as photographed pre-flight (Image credits Soutwest Research Institute (SwRI), ©1996-2024 Southwest Research Institute®). *Right*: Configuration of the detectors on CAPS. More information on each acronym and further details on the instrument can be found in Young et al. [2004], where this image is also taken from.

The energy per charge (E/q) range for ELS was from 0.6eV to 28.25keV, the IBS could measure the velocity distribution of ions with E/q from 1eV to 49.8keV, and lastly the IMS could measure the composition of hot plasmas and ion species with E/q from 1eV to 50.28keV. Also as a mass spectrometer IMS was capable to separate atomic species and to identify isobaric molecular species, e.g. CH_4^+, NH_2^+, O_2^+, all with mass to charge ratio of 16. In general assumptions must be made about the charge of the detected ions

in order to define the species, but for the electrons it can simply be assumed that all the measurements are coming purely from electrons, and not negative ions. This is almost always true, but one must still be careful when Cassini is in dusty regions (as the dust is negatively charged), or in regions with negative ions.

IMS had 8 pixels (anodes), vertically aligned, each having $8.3^\circ \times 20^\circ$ resolution (azimuth by elevation), giving the sensor a total Instantaneous field of view (IFOV) of $8.3^\circ \times 160^\circ$. Similarly ELS had 8 pixels with $5.2^\circ \times 20^\circ$ resolution and an IFOV of $5.2^\circ \times 160^\circ$, and IBS had 3 pixels, where due to their placement they created an IFOV of $1.4^\circ \times 150^\circ$ with a resolution of $1.4^\circ \times 1.5^\circ$. The detectors are mounted on a motor–driven actuator that rotates from -80° to $+104^\circ$ azimuthal angle every 3 minutes. This movement also increases each sensor's total FOV: for IMS it creates a FOV of $\sim 184^\circ \times 160^\circ$, for ELS $\sim 184^\circ \times \sim 160^\circ$ and for IBS $\sim 184^\circ \times \sim 150^\circ$. More details on CAPS can be found in Young et al. [2004].

In my work I used data from the ELS, which is a hemispherical top-hat electrostatic analyser (similar to the descriptions of Carlson et al. [1982] and Johnstone et al. [1997]). Fig. 2.6 shows a cut-through of a top-hat hemispherical analyser, such as ELS (top part of the schematic of fig. 2.5). Two hemispherical shells are placed within each other with a small gap between them. One of the shells can be charged with a voltage, V, creating an electric field

$$E = -\nabla V \tag{2.27}$$

and since we have a constant distance, d, between the shells, we can reduce the equation to 1 dimension:

$$E = -\frac{V}{d} \tag{2.28}$$

The incident particles, with mass m and charge q, are experiencing a Lorentz force due to the electric field of strength E:

$$F_L = qE \tag{2.29}$$

Since the electric field changes direction, following the curvature of the sphere (with a

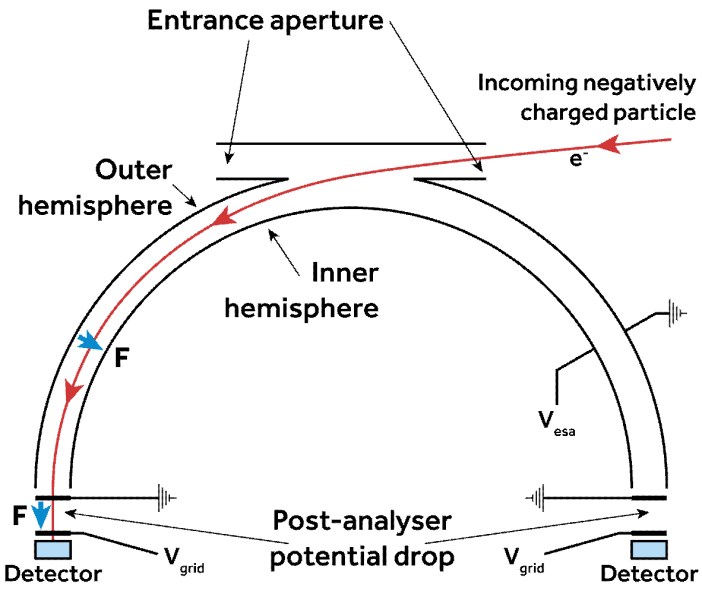

Figure 2.6: Schematic of the operation of ELS. Diagram provided by Arridge

radius r), the force can be considered to be centripetal acceleration:

$$F_c = \frac{mu^2}{r} \tag{2.30}$$

Combining eq. 2.28, 2.29 and 2.30 we can get the speed the particles should have in order to reach the detector:

$$\frac{mu^2}{r} = q\frac{V}{d} \tag{2.31}$$

Taking into consideration that a moving particle has kinetic energy

$$E = \frac{1}{2}mu^2 \tag{2.32}$$

and combining eq. 2.31 and 2.32 we get:

$$\frac{E}{q} = \frac{Vr}{2d} \tag{2.33}$$

The quantity $r/2d = k$ is a dimensionless constant called the *analyser constant* and it connects the potential between the shells with the incoming particles, e.g. if there is a potential drop of 5V between the plates, only the particles with energy per charge, E/q,

equal to $5k$ will pass through. The process of the instrument going through all the energies (0.6eV to 28.25keV) is called a *scan*, and it lasts for 2 seconds.

It must be noted that E/q has units of volts, since eV/e equals to V; however, in the literature the units of 'energy' on a spectrogram are described as volts.

2.2.5. Photoelectrons and photocurrents

A major process affecting measurements of low energy plasmas is photoemission, i.e., the emission of electrons from spacecraft and instrument surfaces, due to sunlight. The sunlight has enough energy to surpass the work function, i.e. the energy required to remove an electron from a the surface of a solid, of either the spacecraft or the instrument surfaces, freeing electrons from the surface. This is a process that happens in every sunlit surface on a spacecraft. The photocurrent appears in the EUV region of the spectrum, from $10 - 120$nm (e.g. Whipple [1981], and references therein).

This current though varies, depending on the surface material and how the surface was processed (e.g. quenching, tempering, heat treating etc.), the intensity and spectral distribution of sunlight, and the angle and polarisation of the incident sunlight (examples in Grard [1973], Diaz-Aguado et al. [2018]).

The photoemission process impacts plasma measurements in two ways:

1. It changes the spacecraft potential. As said earlier the spacecraft is being charged due to the surrounding electrons impact, resulting to a negatively charged spacecraft. The photoemission removes negative charge from the spacecraft. Eventually the electrons impact current and the photoemission current will bring the spacecraft to a charge balance, i.e. the spacecraft potential $U_{s/c}$. If the spacecraft is in a region of thin plasma, the photoemission may dominate over the electrons impact current, resulting to a spacecraft positively charged.

2. It can contaminate the electron plasma measurements. The photoelectrons have temperatures around 2eV (e.g. Hinteregger et al. [1959], Grard [1973], Gustafsson and Wahlund [2010]). While their energy can be affected by the material of which they were generated from, it will only be by a handful of eV. Hence their temperature

are similar to that of the cold energy plasma, it makes very difficult, if not impossible, to differentiate the two.

While Cassini is in an eclipse, i.e. in the shadow of Saturn, the rings, or a moon, the photoelectron production drops drastically due to the lack of sunlight. The spacecraft, due to the lack of electrons removal becomes more negatively charged, which can repulse cold plasma electrons, but also affect some instruments. Also, the position of an instrument can be such that the spacecraft itself can shadow it while in specific orientations, stopping any photocurrent from that instrument.

Unfortunately, while the instruments can be well-calibrated on Earth, it was impossible to recreate the conditions it met at Saturn (e.g. the placement of an instrument on the spacecraft, the geometry of the spacecraft, the photoelectrons impact etc.). As a result, some parameters that can affect any instrument's measurements are impossible to be calculated, or even predicted, hence a fuller understanding of their operation during the mission is needed. Both Cassini instruments that were described are affected by the photoelectrons in the lower energy plasma measurements, each one in a different way.

Impact on LP

The LP is generating photoelectrons from its entire surface, as it is made of metal. If it is negatively charged, the photoelectron cloud around the probe will be repelled, creating a current away from the probe, while if the probe is positively charged, it will attract a fraction of those electrons back to the probe as a photoelectron current. Grard [1973] showed that if the probe is small compared to the plasma Debye length the photoelectrons have a Maxwellian distribution and the photocurrent from the probe can be expressed as:

$$I = \begin{cases} I_0 & \text{for } \phi \geq 0 \\ I_0 \left(1 - \frac{e\phi}{kT} \exp\left[e\phi/kT\right]\right) & \text{for } \phi \leq 0 \end{cases} \tag{2.34}$$

where I_0 is a constant determined by the measurements, and ϕ is the potential difference between the plasma potential and the applied bias voltage on the probe:

$$\phi = U_{plasma} - U_{bias} \tag{2.35}$$

However, the constant I_0 cannot be calculated that easily on Cassini's LP due to additional parameters affecting the generation of photoelectrons. One of them is the stub, which when sunlit can be a source of photoelectrons itself (red trapezium in fig. 2.7). A current variability due to an LP - rod connection of potential was studied and confirmed when Cassini was in the solar wind close to Saturn (see fig. 2 in Jacobsen et al. [2009]). The extreme thinness of the stub minimises the photoelectrons contribution from it. When Cassini is in shadow the initial balance between $U_{s/c}$ and U_{fl} is thrown off. This

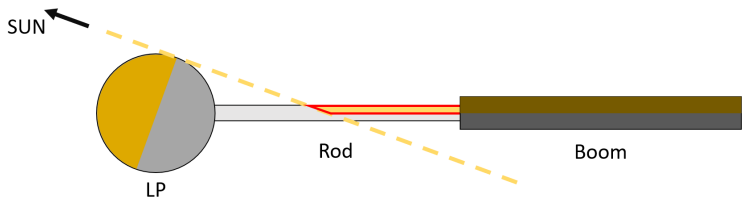

Figure 2.7: Sketch of the connection between the LP boom and the LP. Besides the LP generating photoelectrons, the rod connecting the LP boom and the LP also generates photoelectrons (red trapezium). Figure adapted from Jacobsen et al. [2009].

shift towards an even more negative potential combined with the disappearance of the photocurrent from the LP affects both the ions and electrons measurements: much less ion current is registered and fewer electrons are measured.

The LP can also be affected by being in the shadow of the spacecraft, where the photoemission only from the instrument will stop. This, again, will result in registering less ion current and counting fewer electrons. The main difference though between the LP photoemission stopping due to the instrument being in the spacecraft's shadow, and due to the spacecraft being in the shadow of a body is that in the first case the $U_{s/c}$ does not change at all, hence the balance between $U_{s/c}$ and U_{fl} does not change as dramatically as in the latter case. Therefore, any variation in the LP electron density measurements are tied to the change of the number of photoelectrons coming from the instrument.

Impact on CAPS

For CAPS the measured photoelectrons will appear as a higher measured electron density on the ELS measurements. The source of the photoelectrons are solely the spacecraft, as the hemispherical design of ELS does not allow sunlight to hit the detector directly, which would produce photoelectrons inside the instrument. When the spacecraft goes into an eclipse the low energy electrons measurements are expected to drop.

As it will be shown in chapter 4 I attempted to study the effect of the photoelectrons on both the LP and CAPS measurements, and I also used the variation of the measurements to calculate Saturns' main rings opacity. Also in chapter 5 I will show how an instrument's field of view can be calculated, but also how to look for any intersection between a spacecraft and a vector, e.g. the sunlight.

2.2.6. Plasma wake

Another factor that could potentially affect the plasmas measurements is any wakes that are introduced by the spacecraft, i.e. the orientation of the spacecraft is such that it blocks the plasma flow towards the instrument. For studying any wakes effects I created a methodology where one can check whether a vector (such as the plasma flow, or the sunlight) intersects any part of a given 3D model of a spacecraft. This work is published at the RAS Techniques and Instruments journal [Xystouris et al., 2024]. The full work is presented in chapter 5.

2.3. Herschel Space Observatory

The Herschel Space Observatory [Pilbratt et al., 2010] (fig. 2.8) was an ESA space observatory with science instruments provided by European-led Principal Investigator consortia and with important participation from NASA. It was designed, built, tested, and launched under a contract to ESA managed by the Herschel/Planck Project team by an industrial consortium under the overall responsibility of the prime contractor Thales Alenia Space (Cannes), and including Astrium (Friedrichshafen) responsible for the payload module and for system testing at spacecraft level, Thales Alenia Space (Turin) responsible for the service module, and Astrium (Toulouse) responsible for the telescope, with in excess of a

hundred subcontractors [ESA].

Herschel was operating in the infrared part of the spectrum. It was launched on 14 May 2009 and was operating until 29 April 2013, when the liquid helium coolant, needed for the cooling of the instruments, boiled off. It was located on the Lagrangian point L2. Its primary mirror had a diameter of 3.5m and there were three different instruments on-board: the Heterodyne Instrument for Far Infrared (HIFI) [de Graauw et al., 2010], the Photodetector Array Camera and Spectrometer (PACS) [Poglitsch et al., 2010], and the Spectral and Photometric Imaging Receiver (SPIRE) [Griffin et al., 2010], seen on the right panel of fig. 2.8; combined they covered a big part of the infrared and far-infrared domains: from $\sim 60\mu$m to $\sim 672\mu$m. Everything presented here is from Teyssier et al. [2017] unless otherwise stated.

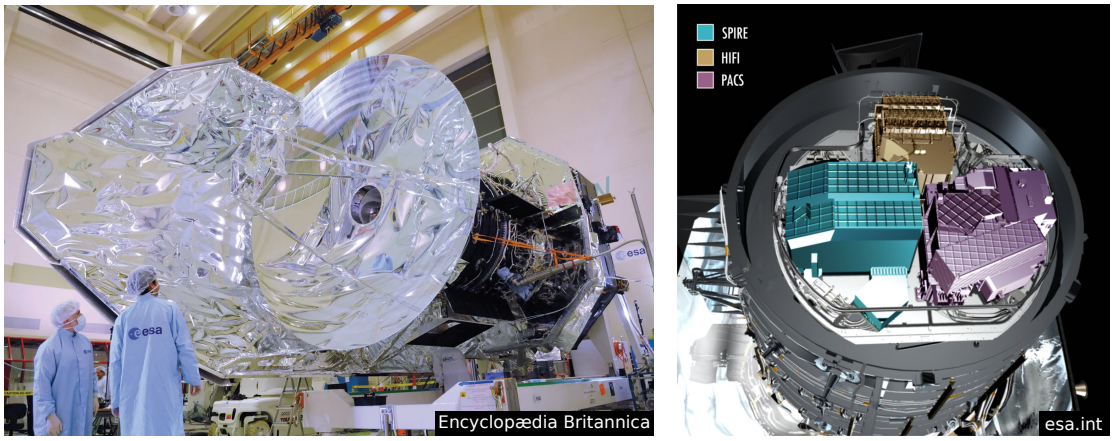

Figure 2.8: *Left*: Herschel in the assembly phase. (Image credits Encyclopædia Brittanica [2019]) *Right*: Configuration of the three instruments on Herschel. (Image credits ESA [2007a], ©ESA)

2.3.1. Herschel Interactive Processing Environment (HIPE)

Herschel engineers developed the software Herschel Interactive Processing Environment (HIPE) [Ott, 2010] in order to easily obtain Herschel observations, focus on them in any data level, and apply functions and filters, such as removing standing waves, calculating the background noise etc. This way all the required constants and parameters are applied

automatically, and all the known issues are addressed, without the need of a manual input by the user.

2.3.2. Herschel Heterodyne Instrument for the Far Infrared (HIFI)

For this work I used data from HIFI, which was a high-to-very-high resolution spectrometer, operating in ranges of approximately $480-1250$GHz and $1490-1910$GHz ($625-240\mu$m and $208-157\mu$m respectively). The detector was a bolometer, i.e. a sensor measuring radiant heat, as it is the ideal detector for that range. The temperature was then translated to integrated intensity.

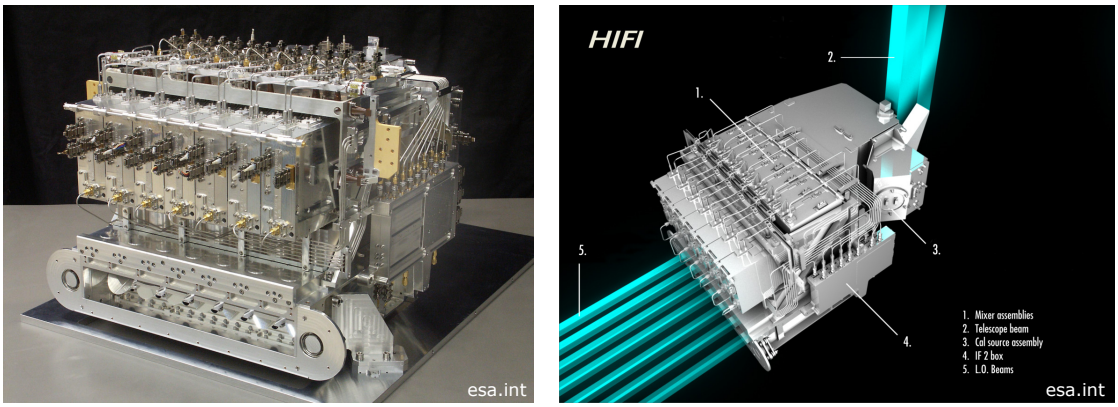

Figure 2.9: *Left*: the HIFI before it was placed on the telescope, viewed from its focal plane. (Image credits SRON Netherlands Institute for Space Research [2007]; ©SRON - Netherlands Institute for Space Research) *Right*: A sketch of the beam path inside HIFI. Details for each of the numbered parts can be found in the text or in the HIFI Handbook [Teyssier et al., 2017]. (Image credits ESA [2007b])

HIFI was using the heterodyne technique: the signal is mixed with an additional frequency, which is very close to the frequency of interest, resulting to the signal shifting to a lower or higher frequency but keeping the original spectral resolution, amplitude, and phase. HIFI, using a Local Oscillator (LO) frequency, was operating as Double Sideband (DSB), i.e. it was mixing two frequencies: one higher (the upper sideband – USB), and one lower (the lower sideband – LSB) from the LO frequency. The two ranges overlap,

resulting in a single spectrum. The USB and the LSB are symmetric around the LO frequency. The product of mixing a specific frequency of interest with the LO produces the intermediate frequency (IF). The advantages of this method are (a) since two spectra are essentially combined into one, more information can be embedded in that single spectrum, which saves on transmission data from the telescope, and (b) the spectra are mixed to a known intermediate frequency, which make the analysis easier.

An example of the heterodyne technique for the HIFI is presented in fig. 2.10. The top panel shows a part of the temperature over a range of frequencies; the temperature can be considered to be the signal intensity at the specific frequency. The LO frequency is at 500GHz, so the LSB range is between $492 - 496$GHz (in red) and the USB range (in blue) is between $504 - 508$GHz. The two bands are combined (shown in lower left panel), and the final spectrum, shown in the lower right panel, shows the combination, i.e. the sum, of the respective USB and LSB spectra. The process of the beam calibration involves some normalisation to the emission of the emission of the black bodies continuum one the telescope, which reduces the spectral intensity to half as their Single Sideband value (further details about this process can be found in section 4.1.2 in Teyssier et al. [2017]). The minimum frequency accuracy (i.e. how accurate the frequency is after a frequency conversion) is 250kHz for the Wide-band Acousto-optical Spectrometer (WBS) band 7. The minimum frequency resolution for any of the elements or operating modes is 1.19MHz

The telescope beam goes through the mixer assembly, where it passes through the 7 mixer bands. The IF ranges from 4GHz to 8GHz for mixers 1-5 (4GHz bandwidth), and 2.4GHz to 4.8GHz for mixers 6 and 7 (2.4GHz bandwidth). So the USB will be from ν_{LO}+4GHz to ν_{LO}+8GHz (in ascending frequency), while the LSB will be from $\nu_{LO}-4$GHz to $\nu_{LO} - 8$GHz (in descending frequency). The mixers are kept in a temperature of around 4K in order to minimise the thermal noise introduced to the signal.

There were two spectrometers on board HIFI: a Wide-band Acousto-optical Spectrometer (WBS) and a High Resolution Autocorrelation Spectrometer (HRS). The WBS was able to cover the full IF range available (4GHz) at a single resolution (1.1MHz), while the HRS was able to cover up to half of the IF range at several available resolutions (0.125MHz

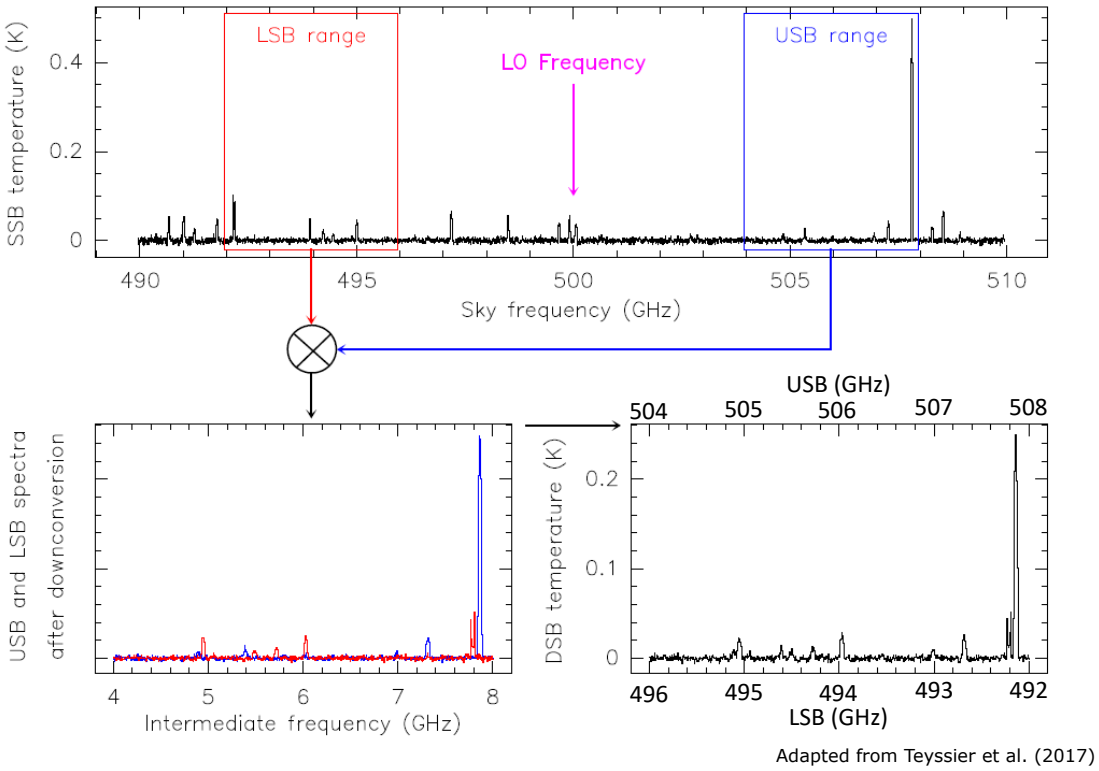

Figure 2.10: Example of the heterodyne technique on a HIFI spectrum. *Top*: a range of frequencies of a target. The LO frequency is at 500GHz, and both the LSB and USB are marked. *Bottom left*: IF spectrum where the USB and LSB are combined. *Bottom right*: The final combined spectrum, with the corresponding frequencies for USB and LSB. The object of the spectrum is IRC+10216. (Image adapted from Teyssier et al. [2017]).

to 1.00MHz). Each spectrometer could separately distinguish signals with two different polarisations: a horizontal (H) and a vertical (V) polarisation. Their profiles intensity agreed to within 7%. This dual polarisation was also a 'safety' feature of the instrument: in case the signal or data of one of the polarisations was lost, the other polarisation would still be operational and return data. An advantage of combining the two channels was the reduction of the noise of the spectrum. Also HIFI did not respond exactly linearly to any radiation fields; pre-flight calibration showed that the non-linearity was around 1% or less, and it can be corrected in the data processing.

The background noise can be measured using a *flat image* of the spectrum. This is achieved using the Focal Plane Chopper (FPC): a mirror that was able to rotate by 3arcmin in one direction, moving the field of view of the telescope to the OFF position, i.e. off the target. Hence by taking a spectrum on an empty space of the sky right next to the object after each step of observation, the background noise level can be measured; this is called *chopping*. The noise, that, due to diffraction comes from the entire sky (4π) rather than the observation FOV, then can be subtracted from the spectrum. This blank sky calibration (OFF calibration) can give information on the difference in standing waves patterns (mentioned later in the section) that occur between the astronomical observation and the load measurement. There are two chopper speeds: a fast chop (up to 4Hz) and a slow chop (typically around 0.125Hz if all 4 spectrometers are operating simultaneously, and twice as fast if two of them were operating, e.g. the WBS was switched off). The settling time of the FPC is under 20ms.

The main contribution in the OFF position on a blank sky is the dust emission in the Milky Way, but this is negligible unless the OFF position is taken directly in the direction of the galactic centre. For a typical OFF position 4-5 degrees away from the Galactic plane, at 500GHz, the continuum intensity corresponds to just 10^{-3}K. Additional parameters taken into account for the calibration in the OFF position (i.e. OFF calibration) are the telescope forward efficiency, i.e. the efficiency of each band for the H and V spectra, and the temperature of the telescope.

Another factor that needs to be addressed during the signal processing are standing waves created inside the instrument. There are two types of standing waves on Herschel/HIFI: the optical standing waves, which are caused by resonances created in the cavity between two optical components of the instrument or the telescope, and electrical standing waves, which are caused by reflections inside the coaxial cable between the mixer and the first signal amplifiers [Higgins and Kooi, 2009, Higgins, 2011]. That reflection can eventually generate a detectable artificial signal. The standing waves are very visible on the background noise where instead of having a background of the same intensity over all the frequencies, it varies. They can be broken down to three contributing areas: standing waves that add to the receiver noise (e.g. sine waves), standing waves changing

the coupling to the telescope, and standing waves changing the overall gain (shown as enhanced spectral baseline ripples when the telescope observes strong continuum sources). An example of standing waves removal on a spectrum is presented in fig. 2.11. The top panel shows the raw data of the horizontally polarised WBS spectrum for observation 1342198318, while the bottom panel shows the same spectrum with the standing waves removed. The standing waves removal not only made the spectrum how much less 'wavy', but also increased the intensity of the emission line (the intensity increase at $\sim$ 557GHz).

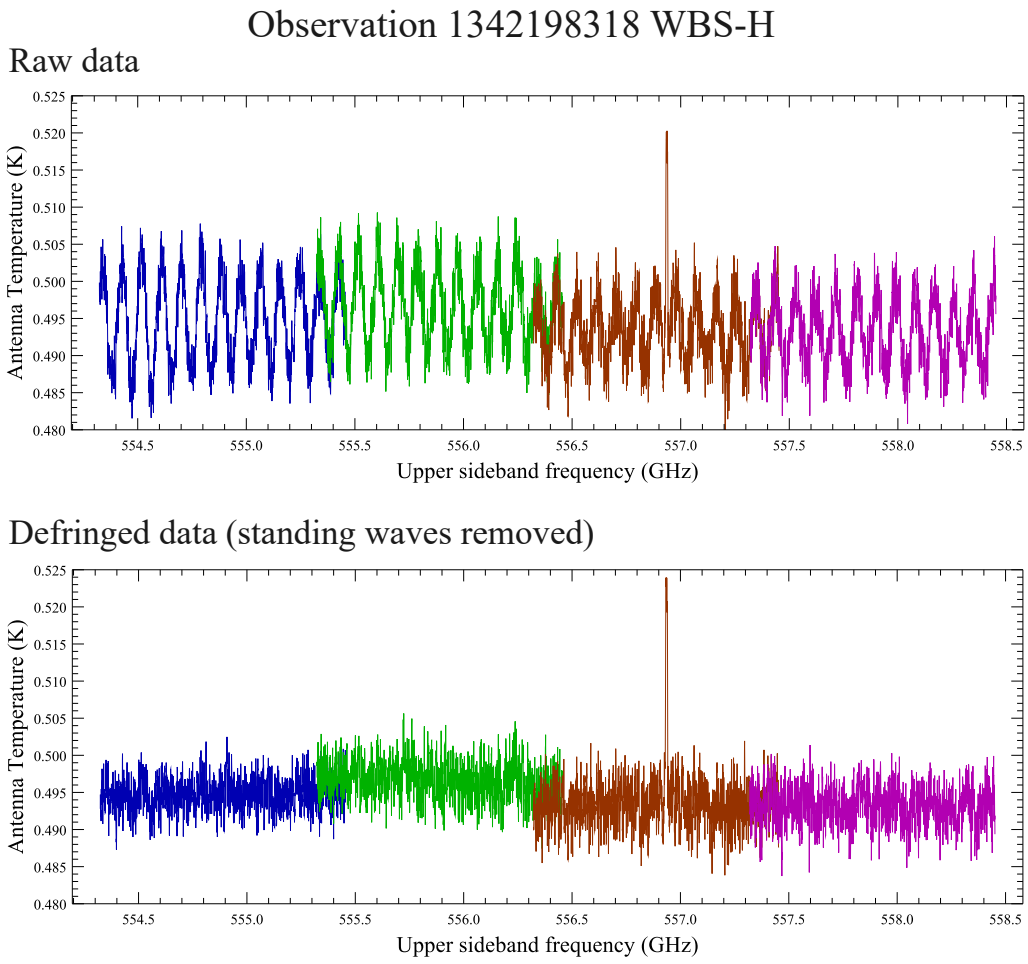

Figure 2.11: Example of standing waves removal. *Top*: The raw data of the horizontally polarised WBS spectrum for observation 1342198318. *Bottom*: The defringed (i.e. having the standing waves removed) spectrum.

The periods of the optical standing waves are well defined and they depend on the size of the cavity, but their amplitude depend on several parameters, such as the instrument gain drift magnitude, the intensity of the signals etc. The most common optical standing wave in the HIFI data has a period of around $100MHz$, but this can slightly change depending on the frequency of interest, e.g. in low frequencies it can appear between $92 - 98MHz$. Another optical standing wave with a $645MHz$ period originates from the beam combiner unit. These can be addressed by fitting sine wave models to the baseline and removing them from the signal.

The electrical standing waves mostly affect the bolometer mixers and they cannot be defined analytically by a single period or amplitude; in the Fourier space though they show at a period of $\sim 320MHz$, which is a good first-order approximation for their removal. Also their continuum scales together with the amplitude and phase of the signal, and when the phase is negative they actually become negative. Kester et al. [2014] developed an algorithm to correct the electric standing waves, and it is applied within the data pipeline.

Lastly, the spurious responses (*spurs*) coming from the LO that can degrade the quality of the spectra. With pre-flight calibration the frequencies that could suffer from spurs were identified, hence can be avoided during the data process.

2.3.3. Temperature - flux conversion and calibration

As mentioned the telescope is a bolometer, detecting temperature, which needs to be calibrated before being processed. Here are given some calibration basics - the full calibration concept is described in detail in Ossenkopf [2003].

For cancelling out the instrument response drift the mentioned blank sky (OFF calibration) is used. For calibrating the instrument bandpass (i.e. the spectral response function) HIFI uses two different internal black bodies (called *hot load* and *cold load*). This calibration puts the source as if it was located next to the instrument internal loads. The measured counts are tied into an antenna temperature scale, T_A^*, (commonly used in radio-telescopes, e.g. Kutner and Ulich [1981]), which is tied to an instrument (in our case the HIFI). As the T_A^* does not take into consideration the optics between the instrument focal plane and the sky (i.e. the prime and secondary telescope mirrors) it needs to be

converted to a more physical scale that can be used for a scientific analysis. Often this scale is Janksy (Jy), which shows the flux density of a source.

Let the telescope beam intensity gain pattern be $P(\phi,\theta)$ and the flux distribution of the source for a specific wavelength, λ, be $T(\phi,\theta,\lambda)$. The antenna temperature, T_A^*, for a specific position (ϕ_0,θ_0) on the sky is the convolution of the beam pattern with the source flux distribution:

$$T_A^*(\phi_0,\theta_0) = \frac{\iint_{4\pi} P(\phi-\phi_0,\theta-\theta_0)\,T(\phi,\theta,\lambda)\,d\Omega}{\iint_{4\pi} P(\phi,\theta)\,d\Omega} = \frac{P\otimes T}{\eta_l\Omega_a} \tag{2.36}$$

where η_l is the forward beam coupling efficiency ($\eta_l = 0.96$ for all HIFI bands and frequencies), Ω_a is the antenna solid angle, and the symbol $\otimes$ simply denotes a convolution of the beam pattern with the flux distribution of the source.

The *antenna theorem* combines the Ω_a with the wavelength in order to define the effective area of the telescope, A_e:

$$A_e\Omega_a = \lambda^2 \tag{2.37}$$

The aperture efficiency, η_A, which depends on the frequency, can be defined as

$$\frac{A_e}{A_g} \tag{2.38}$$

where A_g is the geometric area of Herschel ($A_g = 4\pi r^2$).

Using equations 2.36, 2.37 and 2.38 we get:

$$T_A^*(\phi_0,\theta_0) = \frac{\eta_A}{\eta_l}\frac{A_g}{\lambda^2}\iint_{source} P(\phi-\phi_0,\theta-\theta_0)\,T(\phi,\theta,\lambda)\,d\Omega \tag{2.39}$$

The relation between flux density, S_v, and brightness temperature, T_B, where the Rayleigh-Jeans approximation ($hv \ll kT$) applies is:

$$S_v = \frac{2k_B}{\lambda^2}\int T_B(\Omega)\,d\Omega \tag{2.40}$$

where k_B is the Boltzmann constant. Hence, combining equations 2.39 and 2.40 the conversion between antenna temperature scale, T_A^*, and flux density in Jy is:

$$S_{v,tot}(Jy) = \frac{\eta_l}{\eta_A}\frac{2k}{A_g}\frac{1}{K}T_A^* \tag{2.41}$$

where K is the *flux dilution factor*, which accounts for the temperature reduction when the source does not fully fill the beam. For point sources $K = 1$ while for non-point sources $K < 1$. Ultimately, when all constants are merged we get the expression:

$$\frac{S_{v,tot}}{T_A^*} = \frac{313}{\eta_A K} \tag{2.42}$$

As an example, for a source that is fully inside the beam there are typically $470 - 560$Jy per measured Kelvin. This is also the case of Uranus and part of the neutral torus. This will be further discussed in chapter 3.

3. Uranus

> **‘Και η Γη γέννησε πρώτα ίσον μ᾽ αυτή τον Ουρανό που ᾽ναι γεμάτος άστρα, να την καλύπτει από παντού τριγύρω και να ᾽ναι έδρα των μακαρίων θεών παντοτινά ασφαλής.’**
>
> — Ισίοδος, *Θεογονία*

> **“And Gaia first bore starry Ouranos, equal to herself, to cover her on every side, and to be an ever-sure abiding-place for the blessed gods.”**
>
> — Hesiod, *Theogony*

3.1. Introduction to the Uranian system

Uranus is the 7th planet of the solar system, discovered by William Herschel on the 13 March 1781. It is the third largest planet in the solar system with a mean radius of $25,266\text{km}$ ($\sim 3.97\text{R}_\text{E}$). As it is a rotating gas giant, it shows an oblateness (i.e. flattening) of 0.02293 with its equatorial radius being $25,559\text{km}$ ($\sim 4.01\text{R}_\text{E}$) and its polar radius being $25,362\text{km}$ ($\sim 3.93\text{R}_\text{E}$). It is speculated to have a rocky core, above that the mantle is mainly made of a hot dense fluid of ‘icy’ materials, such as water, methane, and ammonia, and the upper atmosphere consists of a gaseous hydrogen/helium mixture. With a bulk density of $1270\text{kg}\cdot\text{m}^{-3}$ ($0.23\rho_\text{E}$) it is the second least dense planet in the solar system after Saturn. The atmosphere is made mainly of molecular hydrogen, helium, and methane - the latter also gives the planet its blue-green colour. At some parts of the atmosphere it shows the lowest temperature of the solar system planets with 49K ($-224°\text{C}$) [Williams, 2024f, Davis and Carney].

It is located at a mean distance of $\sim 19.19\text{AU}$ from the Sun, orbiting the star once every ~ 84 Earth years. Its orbit is inclined to the ecliptic by $0.04°$ and has an eccentricity of 0.047. The rotation axis is tilted by $97.77°$ to the orbital axis, i.e. the line perpendicular to the orbital plane, and it rotates once every ~ 17.24 hours [Williams, 2024f]. This great tilt creates a configuration where, during the Uranian solstices, the Sun illuminates an

entire hemisphere, while the other hemisphere is almost completely in darkness.

Uranus has 5 major moons: Miranda, Ariel, Umbriel, Titania, and Oberon. Their size, mass, and orbital distance are presented in table 3.1 (data from Thomas [1988], Jacobson et al. [1992], Williams [2023c]). For comparison the radius of the (Earth's) Moon is ~ 1737km and its mass is $\sim 734.6 \cdot 10^{20}$kg [Williams, 2024b].

Moon	Radius [km]	Mass [10^{20}kg]	Orbital distance [R_U]
Miranda	~ 236	0.7	5.1
Ariel	~ 579	12.9	7.5
Umbriel	585	12.2	10.5
Titania	588	34.2	17.2
Ariel	761	28.8	23

Table 3.1: Size, mass, and orbital distance for the major Uranian moons. As Miranda and Ariel are not spherical, their radius was taken as the average of their length on each axis on an orthogonal system. Data from Thomas [1988], Jacobson et al. [1992], Williams [2023c]

Miranda mainly consists of ice, while the rest are made of almost equal amounts of rocks and ice [Hussmann et al., 2006]. Despite their icy consistency, and especially their high amount of surface ice, they have a quite low geometric albedo, i.e. the ratio of their actual brightness to that if they were an idealised flat, fully reflecting, diffusively scattering disc with the same cross-section as the moon, which is between $30\% - 50\%$ [Karkoschka, 2001]. This is caused by a surface layer of ice mixed with a low-albedo component (e.g. Soifer et al. [1981], Brown and Cruikshank [1983]), which, while it has not yet been fully identified spectral modelling suggests that it is likely a carbon-rich material (e.g. Clark and Lucey [1984]), such as darkening and polymerization of methane and other organic substances [Cheng and Lanzerotti, 1978, Johnson et al., 1984]; this is also backed up by observations (e.g. Cartwright et al. [2015]).

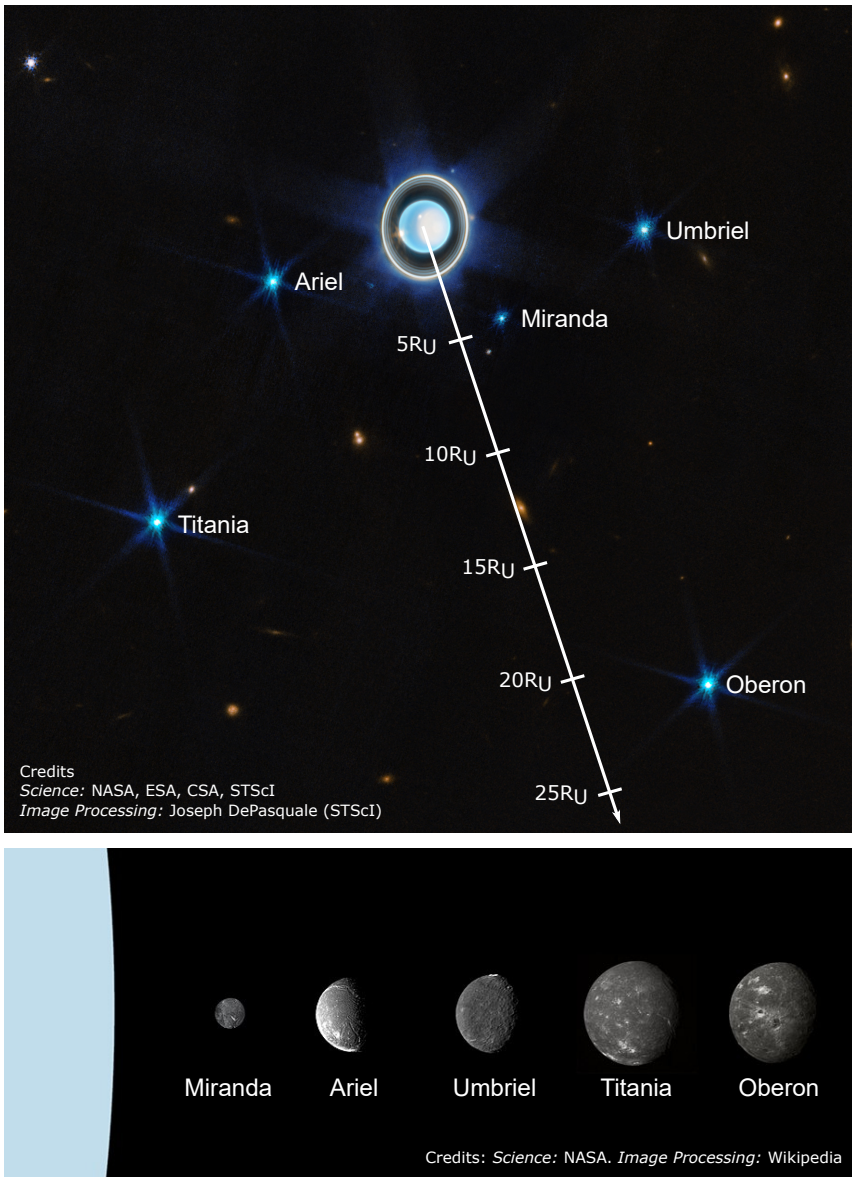

Figure 3.1: The Uranian inner magnetosphere with the relative size of the moons. *Top*: Uranus with the major moons, labelled. Figure adapted from NASA et al. [2023]. *Bottom*: The relative size of the major moons of Uranus, compared to the planet (on the left). Figure adapted from NASA and Wikipedia [2022].

3.2. Uranian magnetosphere

Before the Voyager 2 encounter it was unclear whether Uranus had a magnetosphere. While there were indications of a magnetosphere based on (possibly) Uranian auroral

UV emissions [Durrance and Moos, 1982, Durrance and Clarke, 1984], these conclusions were challenged by Yelle and Sandel [1986] who suggested that they were sourced by the interstellar wind, indicating an absence of magnetosphere. Eventually the existence of a magnetosphere was confirmed by Voyager 2 with the detection of radio bursts [Gurnett et al., 1986], radio emissions [Warwick et al., 1986], and in situ measurements of the magnetic field [Ness et al., 1986]. Uranus' magnetosphere has a unique configuration, where the magnetic axis has a 60° difference from the rotation axis, and a $0.3R_U$ offset from the centre of the planet [Ness et al., 1986].

The configuration of a magnetosphere can be described with the *solar wind attack angle*, α, (e.g. Lepping [1994]) which is the angle between the solar wind and the magnetic dipole axis; $\alpha = 0$ means that the dipole is pointing directly into the solar wind. For example, for Earth $\alpha \approx 60° - 120°$, meaning that the dipole is more or less perpendicular to the incoming solar wind flow. α for Uranus varies greatly, not only due to the great magnetic axis tilt, but also due to the rotation axis tilt to the orbital axis. This variation can be seen on the top graph of 3.2 (image adapted from Arridge and Eggington [2021]): there are periods where $\alpha = 120°$ going from $0° - 120°$ but also from $60° - 180°$, while in other periods it varies as little about 20° around 60° or 120°. The insets are showing the diurnal variation of the attack angle while it is in the minimum value, in 1986, (A) and the maximum value, in 2015 (B).

The following 4 snapshots show the orientation and configuration of the Uranian system for the time of the two inlets (top for A and bottom for B), half a planetary rotation apart (left column to right column). The orange arrow is the sunward direction, the green is the orbital path of Uranus, the dark red vector is the rotation axis, and the blue is the magnetic dipole. It is clear how the magnetic dipole varies diurnally, and the 'drift' of the rotation axis from pointing to the Sun to pointing the orbital path of the planet creates the seasonal variation of the magnetic field. Snapshots from Ikuchi [Arridge et al., 2020].

This variation is expected to create a plethora of phenomena, such as an open-closed magnetosphere [Cao and Paty, 2017], a helical magnetotail (e.g. Behannon et al. [1987], Arridge [2015]), and possibly a plasma full-depleted magnetosphere strongly dependent on season (e.g. Selesnick and Richardson [1986], Arridge and Paty [2021]), despite the low

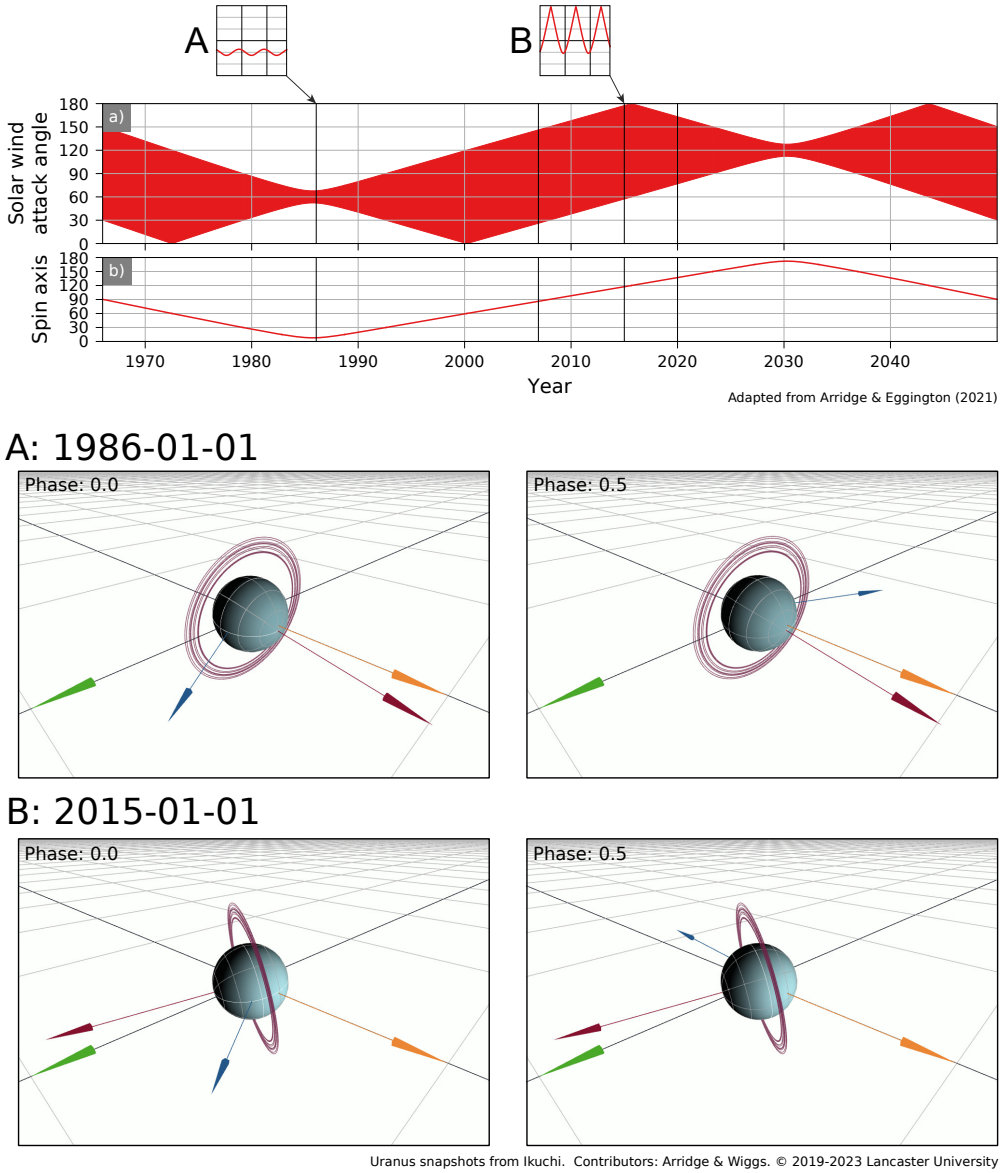

Figure 3.2: *Top graph*: Solar wind attack angle. *Bottom graph*: Angle between the Uranian spin axis and the solar wind. Inlets are showing the diurnal variation of the attack angle for minimum (A) and maximum (B) diurnal variation. The next 4 snapshots are showing the configuration of Uranus for those periods, half a rotation apart (left to right column), along with the sunward vector (orange), orbital path (green), rotation axis (dark red), and magnetic dipole (blue). It is clear that the attack angle changes over two timescales: diurnally and seasonally. (Graphs adapted from Arridge and Eggington [2021]. Snapshots from Ikuchi [Arridge et al., 2020]).

plasma β, measured to be at most ~ 0.1 at $L \lesssim 15$ [Krimigis et al., 1986]. The observed β is around an order of magnitude less than it was observed at Jupiter and Saturn [Krimigis et al., 1979, 1983].

3.3. Uranus' water-product torus

The main plasma source of the Uranian magnetosphere it is thought to be the Uranian atmosphere, mostly due to diffusion, where the energy of some particles allows them to escape the atmosphere. There is, though, potential contribution from the icy major moons, but so far no concrete evidence of the contribution has been found.

Bridge et al. [1986], reported, using Plasma Science (PLS) instrument data during the Voyager 2 flyby, that the detected magnetospheric ion plasma had two components: a warm component, with density up to 2 protons per cm^{-3} and temperature between $4 - 50\mathrm{eV}$, and a hot component, with density up to 0.1 proton per cm^{-3} and temperature a few keV. The warm component was observed everywhere in the magnetosphere, while the hot component was observed only outside $L = 5$. McNutt et al. [1987] constrain the core temperature of the warm component between $5 - 10\mathrm{eV}$, and the hot component less than 5keV; they also mention that the hot component is not Maxwellian. Sittler et al. [1987], also using PLS data, found that the magnetospheric electrons had also two components: a cold and a non-Maxwellian hot. In the inner magnetosphere only the cold component was present, with a density between $0.02 - 1\mathrm{cm}^{-3}$ and a temperature between $\sim 10 - 100\mathrm{eV}$. Farther away, closer to the terminator (i.e. at $L = 6.7$) and the magnetosheath, both components were present. The cold component had energies between $7 - 30\mathrm{eV}$, and the hot component that had a density less than $0.01\mathrm{cm}^{-3}$ and energies between $20\mathrm{eV} - 2\mathrm{keV}$. A density for the cold component could not be calculated, due to a spacecraft charging event while in this region: the spacecraft charged negatively to potentials exceeding the mean energy of the cold component, essentially repelling the cold electrons. Lastly, Krimigis et al. [1986], using data from the Low-Energy Charged-Particle (LECP) instrument, which is able to sample much higher energy particles, reported that the magnetospheric particle population consists mainly of protons and electrons, with energies to at least 4MeV and 1.2MeV for each species respectively. In general the electron

density exceeds the proton densities for any given energy. Also the ions have a Maxwellian distribution at low energies ions (less than $\sim$ 200keV) and a power-law distribution at higher energies (over $\sim$ 590keV). Lastly, in energies between $0.6 - 1$MeV/nucleon, the ion plasma is dominated by protons, with a small fraction (around 10^{-3}) being hydrogen. The observations from both instruments showed no hard evidence of any heavy ions.

A recent study though showed that this empty, compared to the rest of the gas giants, magnetosphere could be a result of Voyager 2 arriving at Uranus right after a solar wind event that massively compressed the magnetosphere, and in combination with its orientation, resulted to be depleted of almost all the plasma. [Jasinski et al., 2024]

The processes for creating plasma were described in section 1.7. As the Uranian system chemistry is similar to the Kronian, due to both planets having significant sources of water, the first approaches to characterise the magnetosphere plasma environment at Uranus were based to the moons being a significant plasma source, as was done by Cheng [1984]. Ip and Voigt [1985] carried this idea and assumed that internal sources can fill the magnetosphere in a homogenous manner, hence a plasma ring could be created on the pole-on epoch, if the magnetic dipole was aligned with the rotation axis. This would also be the configuration during the flyby of Voyager 2 from the planet.

Eviatar and Richardson [1986] also modelled the Uranian plasma assuming that the moons are significant plasma sources, but they explored not only the plasma contribution from each moon but also their composition. They argue that if a magnetosphere is empty of plasma it will start 'self-creating' it: a neutral torus will be created as a thin disk on the moon's rotational plane. Since it is unknown whether the Uranian moons are geologically active, they assume the neutrals initially will be released by external factors (vaporization by micrometeoroid impact, photosputtering, or sputtering by energetic particles). The neutral torus will then get ionised firstly through photoionisation and later by electron impact, and as it starts corotating the ions will impact the moons, releasing more and more neutrals. If the incident corotation energy of the ions is sufficiently large, so that the sputtering yield significantly exceeds unity (i.e. each incident ion releases more than one neutral), the plasma torus will be self-supporting.

A factor on the sustainability of the ion plasma population is that all moons, including

the innermost Miranda, orbiting at $\sim 5.08R_U$ [Williams, 2023c], are farther than the radial distance where rigid corotation and escape velocities are equal, which for Uranus is at $\sim 4.1R_U$ [Williams, 2024f]. Therefore any neutralisation of the ions, i.e. a charge exchange turning an ion to a neutral, close to that distance will result to the neutral escaping the Uranian magnetosphere. So if any neutralisation rate is higher than the ionisation rate the Uranian magnetosphere will be depleted of plasma.

For comparison the distance where rigid corotation and escape velocity are equal on Jupiter is at $\sim 2.88R_J$ and the closest major moon is Io at $\sim 5.91R_J$, and for Saturn it is at $\sim 2.42R_S$ and the closest major moon is Mimas at $\sim 3.08R_S$. For Neptune though the distance is at $\sim 4.27R_N$ and there are 6 major moons inside this distance: Naiad (at $\sim 1.95R_N$), Thalassa ($\sim 2.02R_N$), Despina ($\sim 2.12R_N$), Galatea ($\sim 2.5R_N$), Larissa ($\sim 2.97R_N$), and Hippocamp ($\sim 4.25R_N$). Therefore if any of those moons is a major contribution of magnetospheric neutrals, the recombination of the ionised neutrals in those distances will keep the neutrals in the Neptunian magnetosphere. (Data from Williams [2024a, 2023a, 2024e, 2023b, 2024c,d])

The Eviatar and Richardson [1986] model is treating all 5 icy moons separately. It considers atomic and molecular species of H, O, OH, H_2, H_2O, O_2, and a plasma-free magnetosphere as initial conditions, with the following mechanisms:

1. Photosputtering: UV sputtering gives H and OH, with total source flux of $10^6 \text{cm}^{-2}\text{s}^{-1}$. This value is based on the methodology of Harrison and Schoen [1967]. For the low temperatures in the vicinity of Uranus, the sublimation is considered negligible.

2. Sputtering by corotating ions: relatively minor role at Uranus. The incident corotation ion energies range from 2eV at Miranda to 192eV at Oberon, and their produced yield will be relatively small compared to photosputtering. This process though will affect the composition of the plasma, as the process ejecta are H, H_2, H_2O, O_2 [Bar-Nun et al., 1985], compared to the produced H and OH from photosputtering; the authors do not provide a flux estimate though.

3. Sputtering by energetic particles: no indication of existence of Uranian radiation belts. They calculated a maximum value of $5 \cdot 10^6 \text{cm}^{-2}\text{s}^{-1}$ with a drop off as L^{-3} at

Miranda. Although, modern approaches mention strong radiation belts on Uranus (e.g. Mauk and Fox [2010], Cohen et al. [2020])

4. Vaporization by micrometeoroids: Haff and Eviatar [1985] reported that in situations of weak charged particle sputtering the source might be significant. Estimates of their flux range over two orders of magnitude: from $2 \cdot 10^{-15}$g cm^{-2}s^{-1} based on observations of the atmosphere of Saturns' rings [Morfill et al., 1983] to $2 \cdot 10^{-17}$g cm^{-2}s^{-1}, which is consistent with the CO2 abundance in the atmosphere of Titan [Samuelson et al., 1983].

Those processes will release neutral particles, which will then get ionised by photoionisation, electron impact, or charge exchange processes. The particles though can be lost due to dissociation by solar UV radiation, or recombination. They claim that a steady state magnetosphere will be achieved in one Uranian year, and while there is the potential problem of the attack angle changing dramatically over this period, creating states of even a diurnal open-closed magnetosphere, they argue that since the transport by magnetospheric oscillations or atmospheric tides in their model is negligible in a pole-on magnetosphere, and all processes do not depend on the orientation of the magnetic field, their model should work. Hence, since the transport times are long, even a weak source can create a torus, and a steady state is achieved by the source rate and residence time.

Eventually two values of torus are being presented: one for maximum torus case (radiation belts are as intense as Earth's, and micrometeoroid flux is estimated by [Morfill et al., 1983]) and one for minimum torus case (no radiation belts, and the micrometeoroid flux is zero). Also they argue that heavy ions ($16 - 18$amu) densities are high enough and able to be detected by the PLS instrument, especially for Miranda where they can be detectable for the minimum torus case.

The Voyager 2 fly-by not only revealed the great angle between the magnetic and rotation axes [Ness et al., 1986], but also a nearly pure proton plasma composition [Bridge et al., 1986], with no traces of heavy ions - including water products. While the physics behind the Eviatar and Richardson [1986] model was solid, it was made before any in-situ plasma measurements of the Uranian magnetosphere, relying on assumptions of the planet's magnetic configuration, and often comparing the Uranian system to Earth,

Jupiter, or Saturn. As things are more complicated at Uranus than originally thought, these assumptions and comparisons lead to discrepancies between the model and the observations.

With the new data from Voyager 2, Cheng [1987] revised Eviatar and Richardson [1986] model for the Uranian magnetosphere. The Cheng [1987] model includes the great tilt of Uranus, and argues that the neutral sources (micrometeoroid impact, photosputtering and charged particle spattering) can be as high as $10^7 \mathrm{cm}^{-2}\mathrm{s}^{-1}$ for water surfaces. As the moons are covered by a dark substance, their low albedo of the moons can bring that number down, so a production rate of $10^6 \mathrm{cm}^{-2}\mathrm{s}^{-1}$ is nominal. The Cheng [1987] did not account for the compressed state of the Uranian magnetosphere during the Voyager 2 flyby [Jasinski et al., 2024].

For this model of water products each moon creates a torus with the inner limit,r_-, the outer, r_+, and a half-thickness, ΔZ. The orbital apsides (the points that the moons are closest or furthest away from Uranus) for molecules ejected parallel or antiparallel to the orbital velocity can be described with the equation:

$$\frac{r_\pm}{r_0} = \left[2\left(\frac{u_0}{u_0 \pm u_e}\right) - 1\right]^{-1} \tag{3.1}$$

where r_0 is the moon's orbital distance, u_0 is the Keplerian orbit speed, and u_e is the particles ejection speed (ejected parallel or antiparallel) to the orbital velocity. Cheng [1987] also notes that the velocity distribution of photosputtered neutrals is not well understood at the time they were creating the model. The torus' half thickness can be described as:

$$\Delta Z = \frac{r_0 u_e}{2u_0} \tag{3.2}$$

Also the average number density generated by each moon is:

$$n_n = \frac{R_m^2 \phi \tau_n}{2\Delta Z\left(r_+^2 - r_-^2\right)} \tag{3.3}$$

where R_m is the moon radius, ϕ is the nominal heavy neutral source strength (equal to $10^6 \mathrm{cm}^{-2}\mathrm{s}^{-1}$) and τ_n is the ionisation lifetime. The ionisation processes are the solar UV radiation, electron impact, and charge exchange with protons – same as in Eviatar and Richardson [1986]. Rates of ionisation and recombination are given in their paper. Also only the tori of the 3 innermost moons contribute to this model. Titania and Oberon

tori extend well beyond the magnetopause, and most of the neutrals they eject will never enter the magnetosphere. They will rapidly get ionised, as the solar wind will become an additional ionisation source.

This torus model also takes into account the efficiency of the processes over the distance: the nominal distance for electron impact and proton charge exchange is at $4.6 \lesssim L \lesssim 5.5$, where the denser proton plasma was detected [Bridge et al., 1986, McNutt et al., 1987]. At larger L-values the plasma density is rapidly reduced and the photoionisation becomes dominant. So for Miranda (orbiting at a distance of $\sim 5.1\mathrm{R_U}$) the values for electron impact and charge exchange are fully applied , for Ariel (orbiting at $\sim 7.5\mathrm{R_U}$) the same values were used but halved – as it is in a region where the plasma is not that thick – and for the rest of the moons solely photoionisation was used.

Cheng [1987] then estimated a steady state ion density for the Uranian inner magnetosphere. They assumed that the heavy ions source is the heavy neutrals torus, and the hydrogen ion (i.e. proton) sources are the ionisation of Uranus atomic hydrogen corona (e.g. Bridge et al. [1986], Krimigis et al. [1986]), and ionospheric protons driven by photoelectron escape. They also took into account that the heavy neutral ions are generated from a thin torus around Uranus, while the protons are expelled uniformly around the planet, following flux tubes towards the magnetosphere. The heavy neutral torus occupies a significantly smaller volume than Uranus, which is the source of the protons, therefore, if the ionisation rates between the two are comparable the heavy ions number density is expected to be much smaller than the protons.

The heavy ion loss rate is dominated by charge-exchange with the Uranian corona atomic hydrogen. Dissociative recombination losses are relatively small compared to rest of processes. Proton loss rate is dominated by charge exchange with heavy neutrals.

The model predicts a heavy ion to proton density of $\sim 1.3 \cdot 10^{-4}$. PLS observed a proton density $n_p \sim 1\mathrm{cm}^{-3}$ and placed an upper limit of heavy ion density $< 0.01\mathrm{cm}^{-3}$ ($n_p/n_i \approx 10^{-2}$) for energies $\lesssim 6\mathrm{keV}$ per charge. LECP set an upper limit of $n_p/n_i \approx 10^{-4}$ for energies $\mathcal{O}(MeV)$. Both of the instruments agree with the model findings that any heavy ions plasma would have been too low density to be observed by the Voyager 2 flyby. The LECP model though might not give an accurate ratio, as in these energies might be

connected to a thermal plasma, as it was used in the model. The model also calculated the plasma residence time to be ~ 30 days for the thermal proton density.

Fig. 3.3 shows the Uranus neutral torus distribution over the radial distance using the values given by Cheng [1987]. Of course this is a simplified view of the magnetospheric neutral torus, just to get a general idea of the expected densities. Additional factors need to be taken into consideration in order to have a full view of the Uranian neutral and plasma populations. A major factor is the moon activeness on geological processes: there are evidence of cryovolcanic resurfacing on the moons (e.g. Croft and Soderblom [1991]), tectonic activity (e.g. Titania is less cratered and more faulted than Oberon), and furthermore identified impact craters, and mass wasting features on Ariel [Cartwright et al., 2020]. There are also models predicting subsurface oceans for Titania and Oberon [Hussmann et al., 2006], which could expel water into the Uranian magnetosphere, similar to Enceladus for the Kronian system. Moreover, the unique orientation of the magnetic axis and the seasonal variation of the attack angle could also lead to seasonal variations of the magnetospheric plasma. When the Uranian rotation axis is perpendicular to the solar wind flow, the conditions are such that a plasmasphere (i.e. region in the magnetosphere consisting of low energy plasma) can be created with trapped particles that also can escape, but when the rotation axis is parallel to the solar wind flow no plasmasphere can be created [Selesnick and Richardson, 1986]. As shown in fig. 3.2 (second panel) this angle for Uranus takes all values from 0° to 180°, creating conditions that a plasmasphere can be created seasonally.

3.4. Scope of the project

So far two models of a Uranian neutral torus have been presented: the Eviatar and Richardson [1986] model that, despite the solid physics behind it, does not agree with what Voyager 2 found during the flyby, and the Cheng [1987] model that was adjusted based on the findings. These models can be considered only an indirect diagnostic of the neutral cloud and neutral production processes at the moons. For example the ion composition that Voyager 2 measured can be matched by either having a negligible neutral cloud, or by having a very dense neutral cloud with lots of ionisation, hence really high losses. In

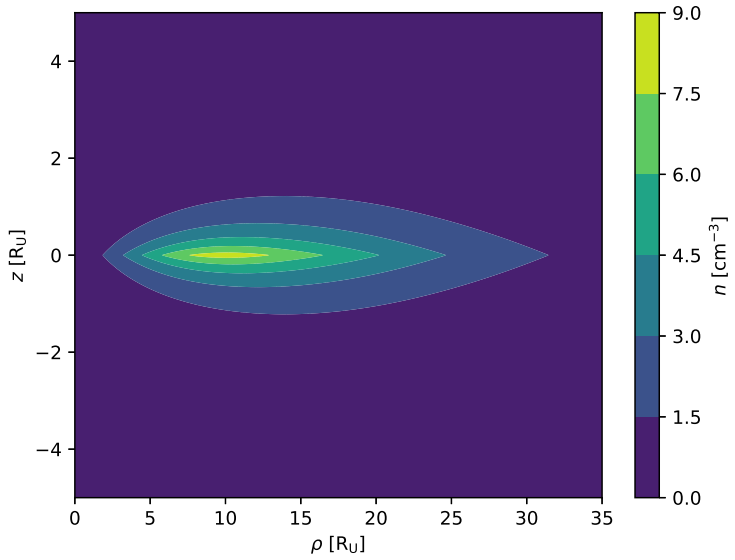

Figure 3.3: The neutrals density over the radial distance and equatorial height, using [Cheng, 1987] model. Fig. provided by Arridge [2022].

order to have a full model of the heavy neutral cloud there are many more parameters that need to be taken into consideration, such as both the diurnal and seasonal variations of the Uranian magnetosphere and how they affect the neutral torus losses, the accuracy of the rates for neutrals production and losses etc. So there are questions that the models can't answer.

Uranus' neutral cloud can be potentially directly measured remotely. At Saturn the Enceladus neutral water torus has been studied by Hartogh et al. [2011], using the Herschel/HIFI instrument [de Graauw et al., 2010]. The telescope operates in the far infrared (FIR) part of the electromagnetic spectrum, and there were multiple frequencies of water lines in the HIFI observations of Saturn. They found that the water was excited dynamically due to molecular collisions, and had a calculated a column density (i.e. the sum of the number density on the line-of-sight) of $\sim 4 \cdot 10^{13}\mathrm{cm}^{-2}$, with a $\lesssim 0.85\mathrm{R_S}$ vertical scale height.

For this project I will search for a Uranian neutral water torus using observations from Herschel/HIFI. My goal is to search for evidence of a torus at Uranus, investigate the

processes that generate it and attempt to place upper limits on the torus density.

3.5. HIFI data and analysis

3.5.1. Observations overview

The orientation of the Uranian system is shown on the left panel of 3.4, while the right shows the expected column density based on the values of Cheng [1987] (fig. 3.3). There were two observations of Uranus from HIFI, taken on 2010-06-15. Uranus size in the time of the observations is ~ 3.464" (arcseconds) and the dashed circle is the HIFI field-of-view for the 556.936GHz cy (for ease, it is rounded here to 557GHz), which is ~ 40". Also, as the observing time was ~ 4 hours the moons obviously moved, but this movement does not throw off the values of the neutral torus densities - at least not in such degree that will change the system dramatically. As an example: the innermost moon, Miranda, has an orbital period of ~ 34h, so the observation time was around 12% of its period, which is not enough to cause any dramatic changes in the neutral torus. As the rest of the moons are farther away than Miranda this number only goes down for them: Ariel moved about 1% on its orbit and the rest moved less than 1%.

Both the observations were taken on 2010-06-15, at 01:46:50UTC (observation ID: 1342198318) and 04:08:43UTC (observation ID: 1342198319), and both were observing in the region around 557GHz. Within this region lies the fundamental rotational 1_{10}–1_{01} line of ortho-H_2O.

Any molecule has three moments of inertia, I_A, I_B, and I_C, for each of its orthogonal axis, with the origin being on the centre of mass of the molecule. The water molecule is an *asymmetric top*, meaning that it has three independent moments of inertia, $I_A \neq I_B \neq I_C$. Besides the movement of the hydrogens with respect to the entire molecule, that can bend or stretch symmetrically and asymmetrically, the molecule rotation around an axis affects its inertia. The energy the water molecule absorbs (or emits) due to its rotation produces an absorption (or emission) line on the infrared part of the spectrum [Banwell and McCash, 1994]. The molecule's rotational energy state can be described as $J_{(K_A,K_C)}$, where J is the total angular momentum quantic number for the entire molecule, and K_A or K_C show the angular momentum along the A or C axes [Atkins and Friedman, 2010]. Lastly, water

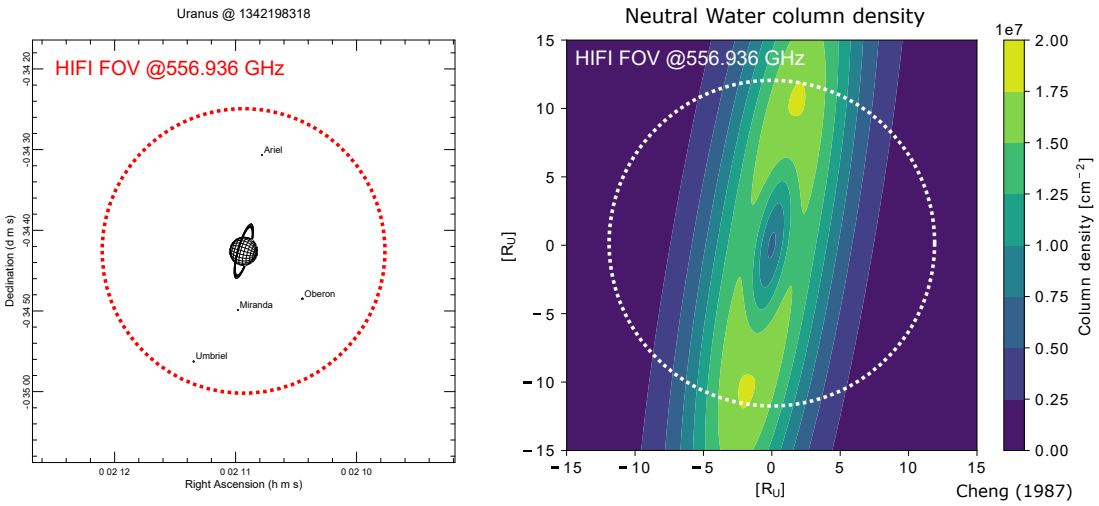

Figure 3.4: *Left*: The orientation of the system during HIFI observations. *Right*: the column density of the neutral torus, based on values of Cheng [1987], as seen from Herschel; fig. provided by Arridge [2022]. The circles are the HIFI FOV at the 557GHz line.

molecules can be found either in *ortho* or *para* state, meaning that the protons in the hydrogen nucleus can have parallel or antiparallel spin, respectively. The 557GHz water line is being produced when the nucleus oscillates between the states 1_{10} and 1_{01}.

While in the observations for Saturn HIFI took data for the 556.93GHz, 987.93GHz (para-2_{02}–1_{11}), 1097.36GHz (ortho-3_{12}–3_{03}), 1113.34GHz (para-1_{11}–0_{00}), and 1669.9GHz (ortho-2_{12}–1_{01}) water lines, for Uranus only a single frequency, the 557GHz was observed.

Fig. 3.5 shows the WBS raw data for both observations. The observation ID, the start and end of the observing time (in Zulu time, i.e UTC), and the direction the telescope was observing (right ascension and declination) are given on the top of each graph. The different colours of each graph correspond to different mixers on HIFI. The left panel for each observation shows the horizontal and vertical polarisations of the data are shown in the left and right panels respectively. The red dashed box on the first panel shows the location of the 557GHz water line emission. As explained in section 2.3.2 the produced spectrum is a combination of two spectrums around the frequency of the LO (fig. 2.10). One of the spectrum, the USB, is higher than the LO frequency and the other, the LSB,

is lower. Hence, each of the presented spectrums has two frequency ranges: one for the LSB on the top, and one for the USB on the bottom. Since we know that the emission line is at 557GHz we see that it belongs to the USB, so we are focusing on this part of the observations. The vertical axis show the antenna temperature for each frequency. As discussed in section 2.3.3 the telescope is essentially a bolometer, detecting temperature, and it operates almost the same way as an optical telescope, but instead of optical photons it uses the photons thermal energy to create a spectrum. The sinusoidal patterns (the rapid oscillation and the 'wave' across the entire spectrum) are a result of combination of standing waves and background noise on the signal. They seem to be more prominent on the left panel than the right, but this is simply because the maximum detected temperature of the emitted line is lower than the left panel; if both panels had the same maximum detected temperature, the oscillations too would be similar. They will be addressed and discussed later in the chapter.

3.5.2. Data reduction & error analysis

The data reduction process is described below – all the steps can be performed automatically using HIPE. The first step is defringing the signal, i.e. the removal of the sine standing waves. We chose to remove 3 standing waves, as the observations usually have up to 3 major standing waves; if we chose less we would have risked missing a major standing wave, while if we chose more there would have been a risk of removing any major features, such as actual spectral lines. Table 3.2 show the frequencies for each mode and observations.

The emission comes from the atmosphere of the entire planet, where polarisation mechanisms can be considered insignificant. The magnetic and electric fields are too weak to produce a considerable polarization through Zeeman and Stark effects respectively, and the random movement of the atmospheric particles does not allow for any large-scale anisotropy to develop. Any polarisation of the torus can be considered insignificant: while it can potentially polarise the absorption via scattering of the emission line with the torus particles, it needs a sufficiently high particle density to take place, and also it is visible from specific angles. Therefore, at this stage, of the first approach of the problem, and

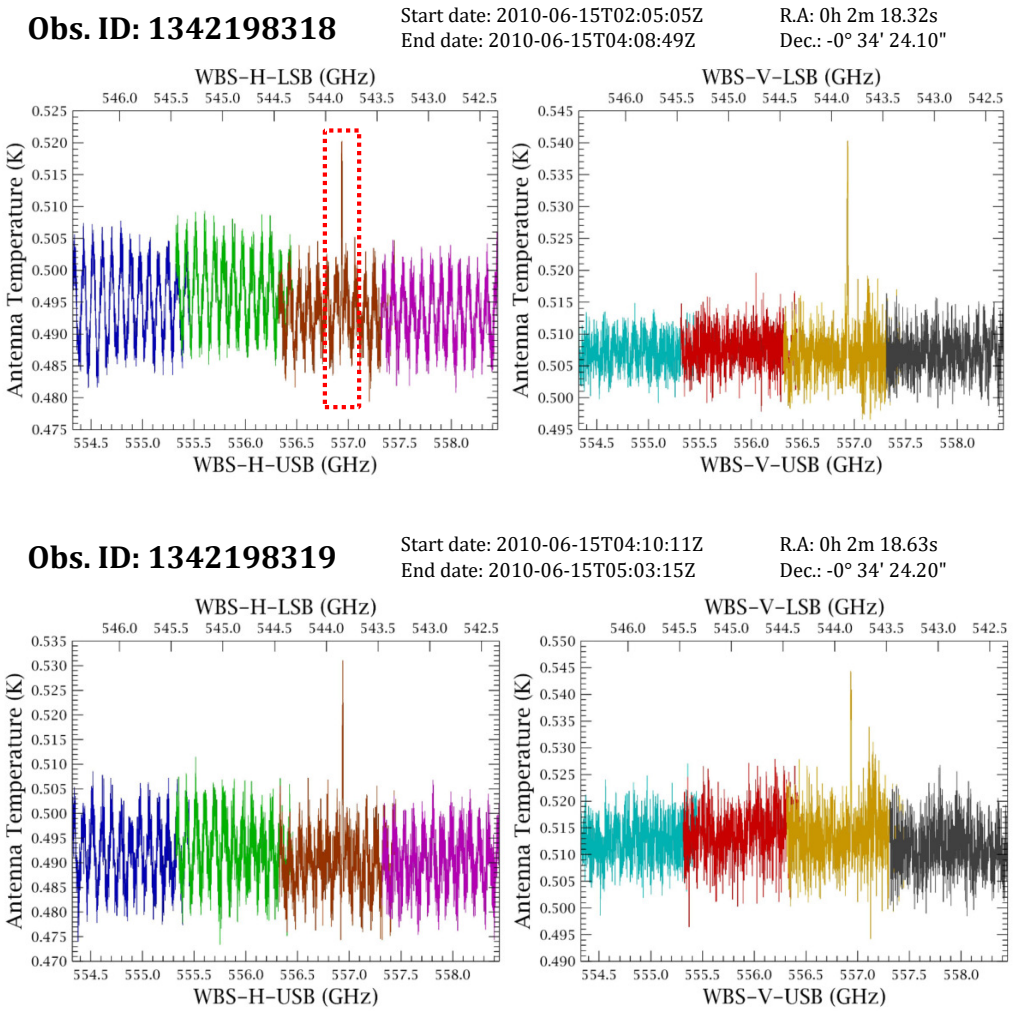

Figure 3.5: Raw data of the WBS for both Uranus observations: observation ID 1342198318 on the *top* and observation ID 1342198319 *bottom*. Some parameters of the observations are given next to the observation ID. The *left* panel of each observation shows the horizontal polarisation and the *right* shows the vertical polarisation. The red dashed box shows the location of the spectral line of interest, the 557GHz water line. The colours correspond to different bands of HIFI.

having only four hours of observations, we can consider that any introduced polarisation is weak. With this in mind we can combine the two polarised spectra in order to have a stronger and more accurate signal, but also to minimise the random noise. We can then

Mode - Polarisation	Obs-ID: 1342198318 Standing waves [GHz]	Obs-ID: 1342198319 Standing waves [GHz]
WBS-H	89.309, 91.242, 97.501	89.161, 91.253, 97.558
WBS-V	89.924, 91.971, 97.470	89.860, 92.240, 97.554
HRS-H	80.357, 94.442, 139.865	80.357, 95.367, 141.565
HRS-V	80.357, 139.722, 200.000	88.090, 120.736, 178.789

Table 3.2: Standing waves for each of the observations, mode, and polarisations, given in GHz.

calculate the new background noise and its Root Mean Square (RMS) across all wavelengths. The combined spectra is essentially a sum of the intensities of the USB and LSB spectra for each frequency, hence the background noise is double the real one. Table 3.3 shows the real noise for each polarisation alone and accumulated (H and V combined), for each observation. Note that the error in the accumulated spectrum is significantly lower than the other two spectra, as expected, since there are twice as many data. In general, the calculation of the background noise can be considered a diagnostic tool that provides information on the data quality. So it can be applied multiple times, at any stage of the processing, as a quick glance of the data quality.

Obs. ID:	1342198318		1342198319	
Mode	WBS	HRS	WBS	HRS
Mean H	0.247 ± 0.001	0.243 ± 0.006	0.246 ± 0.002	0.241 ± 0.009
Mean V	0.254 ± 0.001	0.253 ± 0.006	0.256 ± 0.002	0.255 ± 0.008
Mean Accumul.	0.250 ± 0.001	0.248 ± 0.004	0.251 ± 0.001	0.248 ± 0.007

Table 3.3: The background noise level, in K, for each spectrum in each polarisation channel and the accumulated of them.

3.5.3. Spectra presentation

As a first approach we can combine the two observations, as we are not expecting the system to have any great variations within the 3 hours in-between the observations. Combining the two spectra and recalculating the background noise, the new noise for the WBS mode is 0.2507 ± 0.0010 and for the HRS it is 0.248 ± 0.004. The final spectrum can be presented *subtracted*, i.e. with the actual intensity, where the lines will be above/below (above in our case) of the background noise, or *divided*, i.e. normalised, where the background level will be at 1, and any features will be above/below the baseline. Fig. 3.6 shows the combined spectra for both modes: the WBS on the left, and the HRS on the right. For the HRS the orange line is the individual data, while the blue line is the averaged data, every 4 datapoints. As seen in the figure there is a strong, wide emission water line, but also there is a hint of an absorption line, both centred around 557GHz.

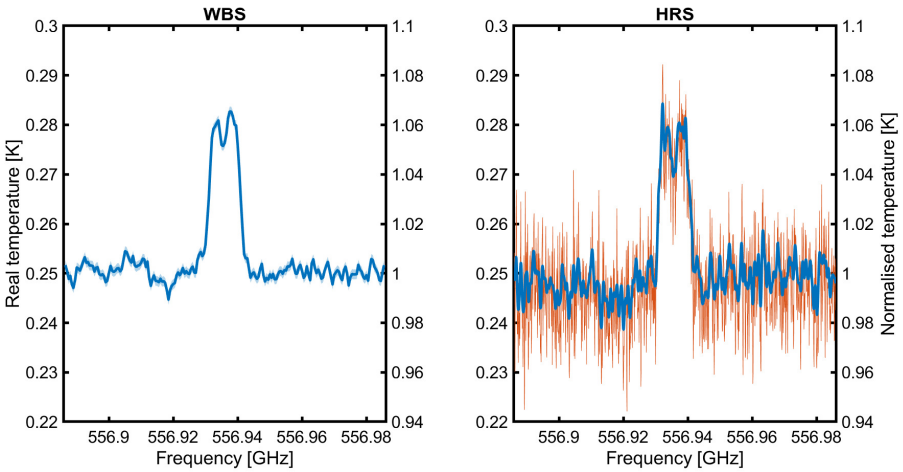

Figure 3.6: Combined spectra for each mode: WBS (left) and HRS (right). The left axis of each plot is the real temperature in K, and the right axis is the normalised temperature. For the HRS the red line is the individual measurements, and the thicker blue line is the averaged every 4 bins.

Both spectra show the background error in light blue around the main dark blue line, but the error is too small to see. As the noise is random and can be described by a Gaussian distribution with a mean value of zero, which is a valid assumption for radio astronomy,

a more useful assessment of the values during a measurements is calculating the standard deviation, σ, which shows the percentage of the values of a normal distribution that lie within an interval: 68% of the values lie within 1σ, 95% lie within 2σ, and 99.7% lie within 3σ. This can be seen as a probabilistic measure of the predictability of a measurement [Teyssier]. In radio astronomy we are assuming that the noise is Gaussian so this is the typical approximation that is done to set a threshold on the detection level. Applying this in spectroscopy: if we had a spectrum with only background noise signal, 95% of the datapoints would lie within 2σ, 99.7% of the datapoints would lie within 3σ from the background level etc. In astronomical observations the 3σ threshold is commonly used to distinguish a real signal from background noise [Miller et al., 2001]. This threshold is also applied to HIFI observations, as demonstrated in studies such as Gupta et al. [2010] and Persson et al. [2010]. Therefore, for a feature, i.e. an emission or absorption line, to be considered significant it needs to be over 3σ 'away' from the background level. In this case the probability for any of the lines' datapoints to still be noise and be mistakenly taken as the line would be 0.3%, which is a very small percentage. Assuming that the line has n datapoints lying outside the 3σ, the probability of all datapoints to be noise is 0.3^n, which is extremely small. Hence, if a line is 3σ 'away' from the background level, it is almost certain a line produced by a physical process, and not simply noise.

The σ is calculated as the background level divided by the RMS. Eq. 3.4 and 3.5 show the σ values for the WBS and HRS respectively. The Herschel engineers require a 3σ limit for a spectral feature to be considered real, which, for WBS is at 0.012K and for the HRS it is at 0.048K.

$$\sigma_{WBS} = \frac{\text{BKG.}_{WBS}}{\text{RMS}_{WBS}} = 0.004\text{K} \tag{3.4}$$

$$\sigma_{HRS} = \frac{\text{BKG.}_{HRS}}{\text{RMS}_{HRS}} = 0.016\text{K} \tag{3.5}$$

Therefore the emission line is clearly over the 3σ limit for the WBS, but not for the HRS, and the absorption line is below the 3σ limit for both instruments. One can argue that most the emission line is most probably real, and the absorption line is most probably not real, but those results will be discussed further in the next section.

3.5.4. Doppler analysis

For this work, and because of the limiting sample of our data, we assume that Uranus emits water in its upper atmosphere isotropically. Its rotation though will cause *Doppler broadening* to the line, i.e. the emission line will become wider due to Doppler effect. This is the case during the HIFI observations, as Uranus was almost edge-on (left panel of fig. 3.4), meaning that the effect will be observable in the data.

An example of the Doppler broadening is presented in fig. 3.7. The top panels (A) shows an example of emission from a non-rotating planet. In this case there will be a narrow emission line around the emitted frequency. Some broadening is happening naturally, hence, the line does not have the shape of a δ function. The middle panels (B) show the example of Uranus as seen from above, where its rotation shifts the frequency of the emitted line. The line has lower intensity that the non-rotating case, and it is much wider. The frequency corresponding to the full width at half maximum (FWHM) of the intensity is the maximum frequency the line blueshifted or redshifted. The bottom panels (C) show the results of Teanby et al. [2022] synthetic (modelled) emission spectrum, based on the orientation of Uranus during the observations. For their work they calculated the water abundance and vertical profile of Uranus using the same data as this project. On the left is the rotation rate of Uranus, assuming a solid-body rotation and based on rotation rates of Helled et al. [2010]. On the right is the synthetic spectrum based on the water emission during the observations period. The expected spectrum shows a plateau on the maximum intensity. They also calculated a Doppler broadening of the water line of $\sim$ 0.01GHz, based on the same data used for this work.

Teanby et al. [2022] used the emission line coming from the Uranian stratosphere to calculate a water column abundance of the Uranian stratosphere (uppermost atmosphere) of $\approx 0.54 \cdot 10^{-14}\text{cm}^{-2}$. They also reported that the planetary rotation affects significantly the shape of the observed emission lines. Their results helps rule out the emitted line being a product of a water torus. Moreover this constrains the flux dilution factor, K, which accounts for the temperature reduction when the beam does not fully cover the source (discussed in section 2.3.3), to be equal to 1, as the emitting body, i.e. Uranus, is fully inside the beam, regardless of the predicted torus span not being fully inside the

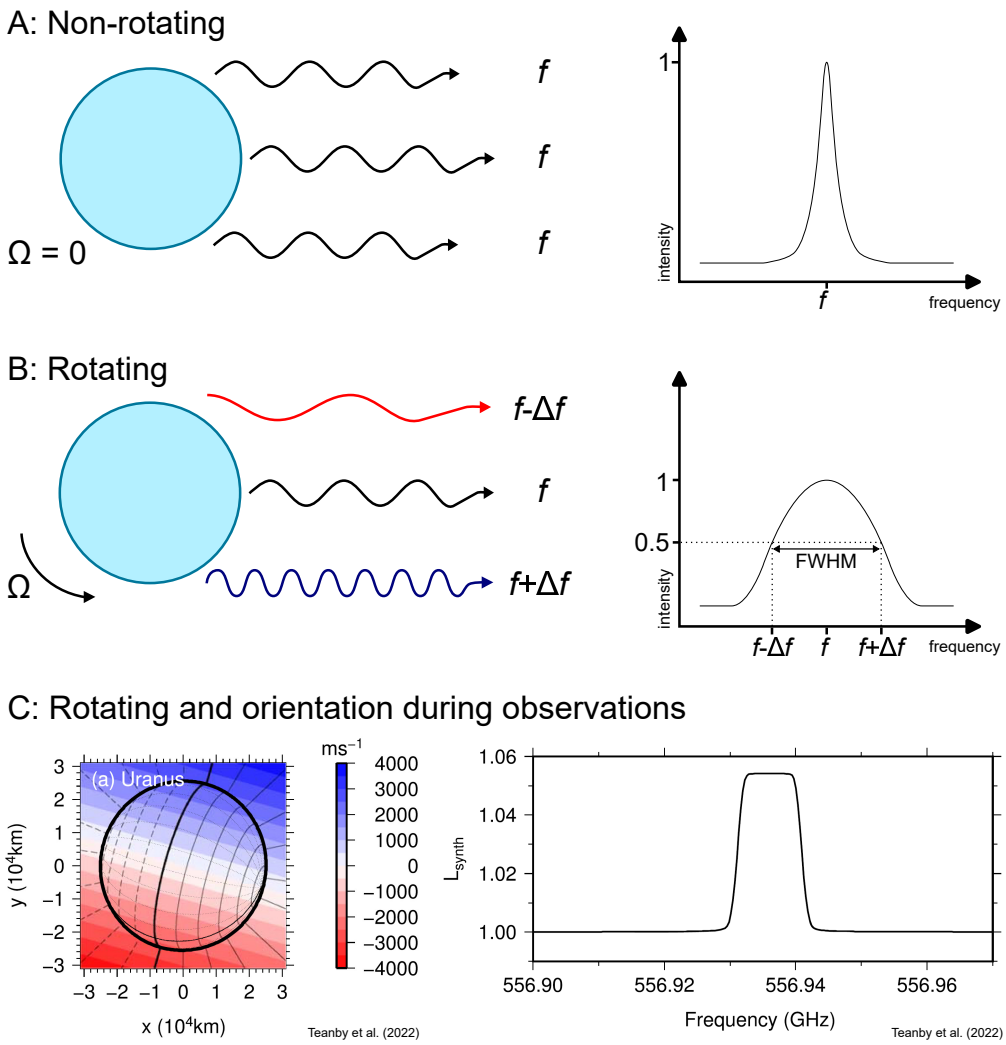

Figure 3.7: Example of Doppler broadening of a spectral line. *Top panels (A)*: example of a non-rotating planet. The emitted spectral line has almost no broadening. *Middle panels (B)*: example of rotating planet. The emitted line is less intense and broader. The FWHM intersects the spectral line at the frequency shift (Δf) that was added (or subtracted) from the line caused by the rotation of the planet. *Bottom panels (C)*: modelled emission spectrum for the time of observations, based on Teanby et al. [2022]. The model assumes a solid-body rotation. The expected spectrum shows a plateau on the maximum intensity Bottom panels reproduced by permission of the American Astronomical Society (AAS).

beam.

By converting the spectrum frequency, f, to relative velocity, u, around a reference line, f_0, any Doppler shifts of lines can be identified. For example, if the emitted water line is expected to be found at 557GHz and by applying the conversion it is found at -5km/s, it means that the body emitted the line is moving 5km/s away from the telescope. The frequency can be converted to relative velocity using the following equation

$$u = c\left(\frac{f_0 - f}{f_0}\right) \tag{3.6}$$

where c is the speed of light. This conversion is particularly important on defining the movement of objects that produced the lines, but also defining the source of the lines, as it will be shown later.

Lastly, in order to have a general idea of how much energy is radiated by Uranus at each frequency, the emitted intensity can be converted to spectral flux density, S, using the equation

$$S = \frac{326.9}{\eta_A} T_A \tag{3.7}$$

where η_A is the aperture efficiency of the telescope, and T_A is the antenna temperature. The variables and constants of eq. 3.7 is tied to Herschel and HIFI, and $\eta_A = 0.65$ for the frequency range of the observations Teyssier [2018]. This conversion gives the flux in Janskys (Jy), where $1\text{Jy} = 10^{-26}\text{W m}^{-2}\text{Hz}^{-1} = 1\text{J m}^{-2}$.

Fig. 3.8 show the spectrum velocity around the 557GHz water line for both instruments: WBS in dark blue and HRS in light blue. The scale on the left shows the subtracted (absolute) temperature (in K) and the scale on the right shows the spectral flux density (in Jy). The two scales are linearly connected to each other - they only differ by a multiplication factor. We see that the FWHM of the emission line is around 2.59km/s, which is the equatorial rotation speed of Uranus, denoting that the emission line is generated by the planet.

Focusing on the intensity for each feature, i.e. the emission and absorption lines, and using the standard deviations for each line as discussed in section 3.5.3 we see the following for each line:

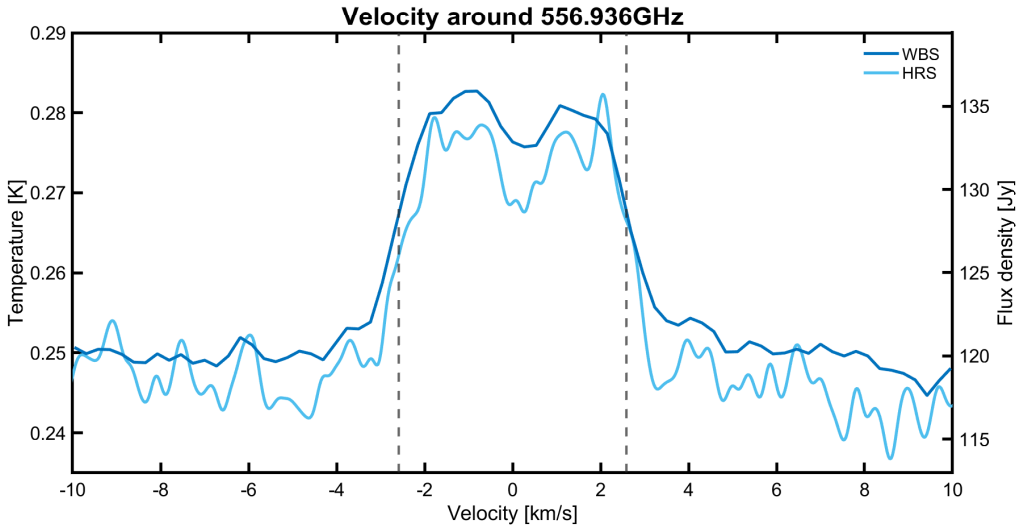

Figure 3.8: Spectrum velocity around the 557GHz water line. The dashed lines mark the equatorial rotation speed of Uranus. As the FWHM is around that speed it shows that the emission line comes from the planet.

Emission line

The emission line intensity is ~ 0.03K, which is beyond the 3σ limit for WBS (0.012K), but not for the 3σ limit for HRS (0.048K). One could challenge that the line could be product of noise, but it can be confidently said that the line is produced by the Uranus emission due to:

- HRS noise: the HRS data are very noisy, i.e. highly variable, as seen in fig. 3.8. Even if a lot of noise removal processes have been applied to the spectrum, it is impossible to remove all the noise. The high noise is also reflected to the error of the background noise calculation (i.e. RMS, in table 3.3): the HRS error is consistently much higher than the WBS error.

- σ: while the line from the HRS data is not over 3σ, it is around 2σ, which gives a confidence level of 95% of the feature being real. Spectroscopy uses the limit 3σ is as an adequate level of trusting the result being real, while, for example, in particle physics this limit is beyond 5σ ($> 99.999\%$). Therefore the 2σ for spectroscopy can be translated as the feature most probably being real and statistically confirmed.

- FWHM: As the FWHM is at the rotation speed of Uranus, it shows that the line is emitted by Uranus.
- past studies: Teanby et al. [2022] used the same data, along with line emission modelling, and confirmed that the line is emitted by Uranus.

Absorption line / feature

The absorption feature in the middle of the emitted line, at the relative speed of 0km/s, has an intensity decrease of ~ 0.005K. For WBS is close to 1σ (0.004K), while for HRS is well below 1σ (0.016K). It would be safer to focus on the WBS data, for the reasons mentioned above, but also the variation on the HRS background data is comparable to the feature. Even though this feature does not exceed the 3σ limit, it is still at 68% probability of being an actual absorption line, hence, it worth investigating whether the feature is indeed noise or if it is absorption by a water mass in front of the emitting Uranus.

Fig. 3.9 shows two possible cases of water masses in front of the emitting Uranus that could produce the absorption feature: very high altitude cold clouds in the Uranian stratosphere, that are above the emitting water (left), and part of the water torus being in front of the planet (right). Although, as the stratosphere follows the planetary rotation, any stratospheric clouds will also move. Due to the limited observations time it is hard to create a detailed emission map over the Uranian longitude, for variations to be identified, but even the slightest movement will be mapped at the absorption line. However, as shown in fig. 3.4 if a water torus exists, part of the torus is expected to be in front of Uranus. Also the fact that the feature is not moving towards or away from the telescope supports the idea of the absorption feature being created by a thin water torus: as the torus is rotating around the planet, it will be observed in the closest approach to the observer, hence, its relative speed towards the observer would be zero. This will also be true if the absorption feature is created by the Uranian water-rich rings, as they are on the same plane as the torus, and during the observations part of them is in front of the planet.

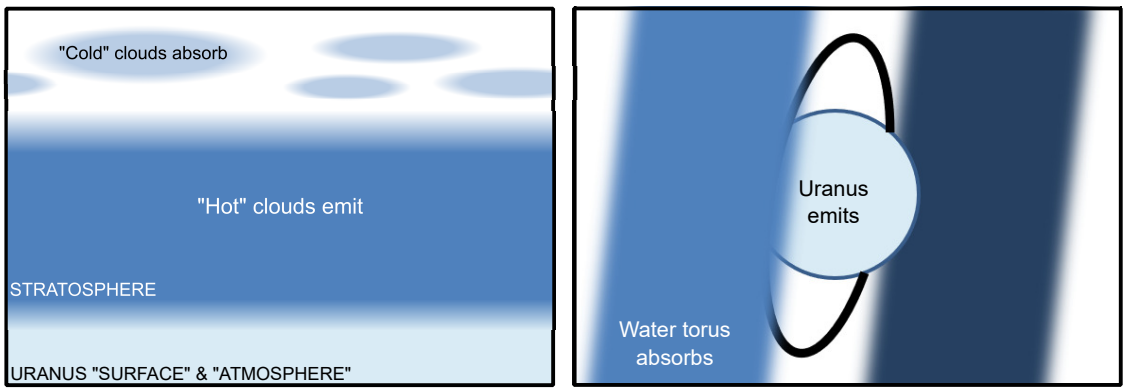

Figure 3.9: Cases of possible water absorption. *Left*: a colder layer of clouds over the emission cloud layer. *Right*: part of a water torus partially covers Uranus.

3.6. Conclusions & Future work

In this chapter I have demonstrated how I searched for a neutral water torus around Uranus, using data from Herschel/HIFI. Despite the fact that only two observations were available, the spectrum showed a clear water emission line, coming from the planet, and an absorption feature that, while it was not over the statistical significant level, it was visible in all observations.

An aspect of this project that can be beneficial to focus on is the polarisations of the beam. There are astronomical sources that emit polarised radiation, such as active galactic nuclei (where the strong magnetic field aligns the particles along the jet axis), scattering in reflection nebulae (where light is polarised when it interacts with gas, dust or other particles in the nebula) etc. There are no processes on the Uranian system that could polarise the emitting signal, so the vertical polarisation should be identical with the horizontal. In our data though the two are not exactly similar, as the vertically polarised spectrum is more intense than the horizontally. Hence, it worth investigating what causes this.

The absorption feature can also be approached statistically, in order to evaluate whether it is randomly created or not. One test that can be applied is assuming that the datapoints are normally distributed and calculating the probability of a $2-3\sigma$ fluctuation appearing. Also, a statistical significance test of the two features appearing simultaneously can also

add to the evaluation: if the combined probability of both the emission line and the absorption feature occurring at these locations by random chance is very low, it will show that they are not created by chance.

Another aspect that could improve this project is of course the use of models. A neutrals model of higher accuracy, with the additional feature of adding or removing sources, and adjusting each source's neutral density can be very useful on presenting the expected column density in the HIFI beam width. This can be combined with a model of an absorption line: either by modelling the required density to create such an absorption feature, or by modelling the line that our model density will produce. The result will give the minimum detectable column density. In addition, as the feature can be created by the water-rich rings, comparing the amount of rings material that was in front of the planet during the observations would help evaluating whether the feature is produced by them.

Lastly, including the option of changing the orientation of the neutrals model, but also the beam width and shape it could make the model a useful tool for other missions and observations.

4. Saturn

> **"He put these thoughts behind him, as the golden crescent of Saturn rose in the sky ahead. In all history, he was the only man to have seen this sight. To all other eyes, Saturn had always shown its whole illuminated disk turned full toward the Sun. Now it was a delicate bow, with the rings forming a thin line across it - like an arrow about to be loosed, into the face of the Sun itself."**
>
> — Arthur C. Clarke, *2001: A Space Odyssey*

4.1. Introduction to the Kronian system

Saturn is the 6th planet of the solar system, know since the ancient times. It's the second largest planet in the solar system with a mean radius of $58,232$km ($\sim 9.14\mathrm{R_E}$), and it shows an oblateness (flattening) of 0.09796: its equatorial radius is $60,268$km ($\sim 9.45\mathrm{R_E}$) while its polar radius is $54,362$km ($\sim 8.55\mathrm{R_E}$). It has a small rocky core surrounded by metallic hydrogen (i.e. hydrogen, where, under the extreme pressure it behaves like an electrical conductor) and helium [Guillot et al., 2009], while the rest of the planet is made of a helium-saturated molecular hydrogen, transitioning from liquid closer to the core to gas towards the outer layers [Faure and Mensing, 2007]. It is the least dense planet of the solar system, with a bulk density of $687\mathrm{kg}\cdot\mathrm{m}^{-3}$ – and, as it is usual to be said about Saturn, if you had a bathtub full with water big enough to fit Saturn, it would float, as it is the only planet whose bulk density is less than water. Its atmosphere is made mostly of molecular hydrogen and helium, with small parts of methane, ammonia, hydrogen deuteride, and ethene, and its temperature at the 1 bar level is around 134K ($-139°$C) [Williams, 2024e].

Saturn is located at a mean distance of ~ 9.5AU from the Sun, with a Kronian year lasting 29.45 earth years. Its orbit is inclined by $\sim 2.5\,$deg to the ecliptic and it has an eccentricity of 0.05. The rotation axis is tilted by $26.73°$ to its orbital plane, with a day duration of ~ 10.66 hours. This axial tilt creates seasons on Saturn, similar to Earth's.

It is also the only planet in the solar system with easily visible rings, because they

are significantly more massive than any other ring system and, despite other rings, they are mainly made from ice, a highly reflective material. Saturn's axial tilt of 27° causes their brightness to vary over a Kronian year as seen from Earth: their minimum apparent magnitude is +1.17, and their maximum apparent magnitude is −0.55; as a comparison Sirius has an apparent magnitude of −1. Recent research suggests that they were created in the last hundreds of million years [Kempf et al., 2023], making them considerably younger than Saturn itself, which is thought to be formed soon after the creation of the solar system, ~ 4.5 billion years ago. Fig. 4.1 shows the four main rings, named D, C, B, and A (arranged in order of proximity to the planet, from closest to farthest, as seen in fig. 4.2), followed by the narrow F ring, and the G and E rings. The tenuous Janus/Epimetheus, located between the G and E rings, cannot be seen in the figure. Also, far beyond the coverage of the figure, there is the largest of Saturn's rings, the Phoebe ring, extending from $128R_S$ to $207R_S$ [Verbiscer et al., 2009]. While the main rings are visible from the Earth, the rest of the rings are not visible either due to them being narrow, or due to them being made by non-reflecting material, e.g. the Phoebe ring is made by dust and particles from the surface of Saturn's moon, Phoebe. Table 4.1 shows the distances of each ring and gap (based on data from Williams [2022], Tiscareno, Verbiscer et al. [2009]). Any features appearing within a ring (gaps, or the division of the ring in regions) are directly underneath the main ring, starting with a dash. Besides the largest features presented above, there are many more gaps and ringlets that in some cases are no larger than tens of kilometres, e.g. the Bond ringlet in the C ring is $\sim$ 15km wide. The moons can gravitationally distort the rings' material creating gaps (e.g. Pan and Daphnis are orbiting in the Encke and Keeler gaps respectively), creating ringlets (e.g. Titan is responsible for the Titan ringlet, with a width of $\sim$ 23km in C ring), or even shape rings (e.g. Prometheus and Pandora are shaping the narrow F ring, Mimas is in resonance with the outer edge of the B ring). While some gaps are associated to a moon that created them, others remain unexplained.

The Kronian system in the inner magnetosphere, shown in fig. 4.2, which stretches up to $\sim 10R_S$ around the planet, contains some of the major moons: Mimas, Enceladus, Tethys, Dione, and Rhea. Enceladus, though, is the most important moon for the inner magnetosphere. The jets of ice coming from its south-polar region is the main provider of

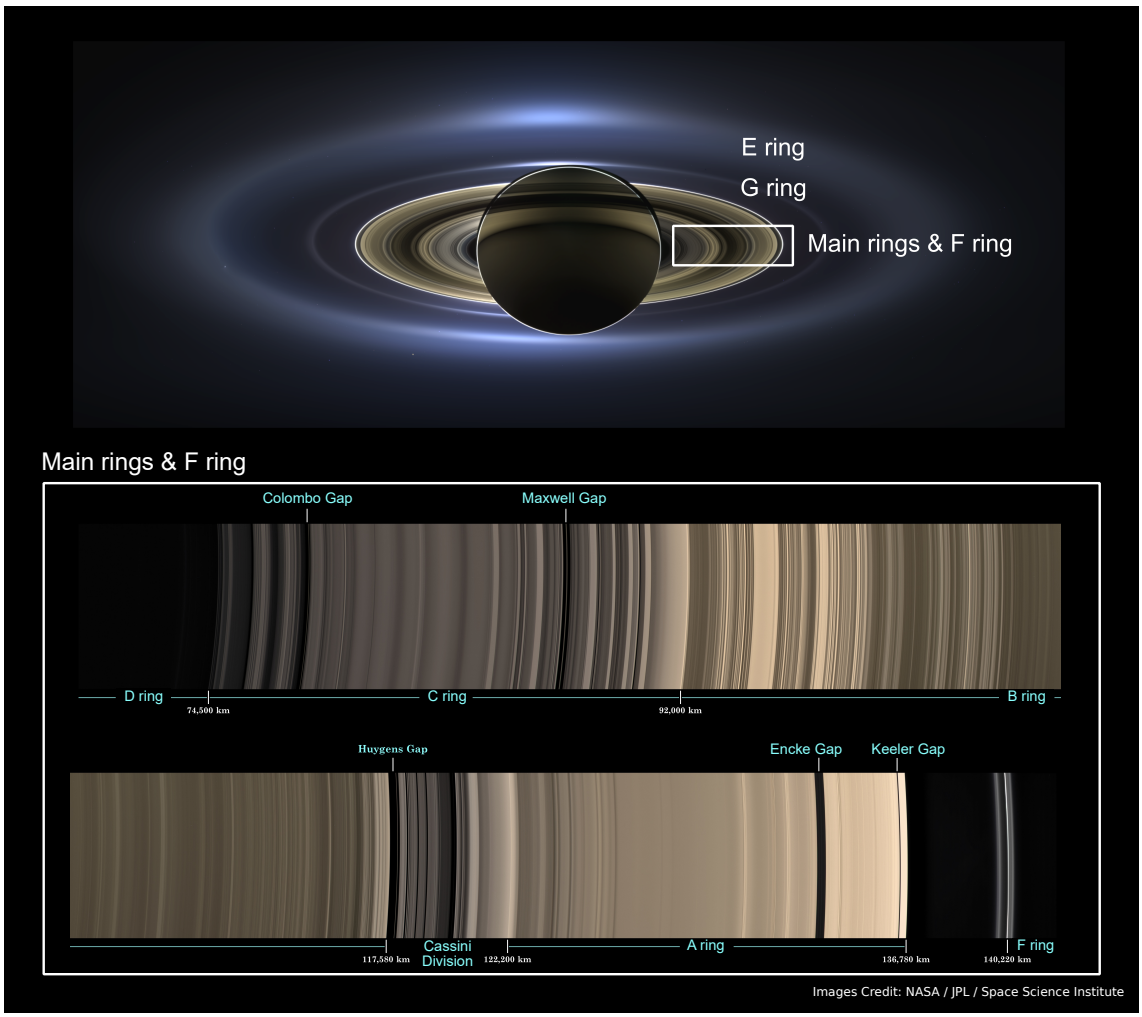

Figure 4.1: Saturn's rings. *Top*: a view of Saturn up to $\sim 5R_S$, along with labels for the visible rings. *Bottom*: close-up on Saturn's main rings, along with their distances from the centre of Saturn (bottom tags), and some of their features (top tags). Images credits: NASA et al. [2007, 2013]

the inner magnetospheric plasma (e.g. Burger et al. [2007]). The process of the creation of the plasma was described in section 1.7. Hence the Kronian plasma is mostly made from hydrogen and water-products (O^+,HO^+,H_2O^+) (e.g. Felici et al. [2018]). An additional plasma source is the rings (e.g. Persoon et al. [2020]), but they do not contribute as much as Enceladus.

To date, 146 of Saturns' moons have been discovered [NASA/JPL et al., 2023], and it

Region	Distance [km]	Distance [R_S]
D ring	$66,900 - 74,510$	$1.11 - 1.24$
C ring	$74,658 - 91,975$	$1.24 - 1.53$
- Colombo gap	$77,748 - 77,926$	~ 1.29
- Maxwell gap	$87,343 - 87,610$	~ 1.45
B ring	$91,975 - 117,507$	$1.53 - 1.95$
- B1 region	$91,975 - 99,000$	$1.53 - 1.64$
- B2 region	$99,000 - 104,000$	$1.64 - 1.73$
- B3 region	$104,000 - 110,000$	$1.73 - 1.83$
- B4 region	$110,000 - 116,500$	$1.83 - 1.93$
- B5 region	$116,500 - 117,507$	$1.93 - 1.95$
Cassini Division	$117,507 - 122,340$	$1.95 - 2.03$
- Huygens Gap	$117,507 - 117,930$	$1.95 - 1.96$
A ring	$122,340 - 136,780$	$2.03 - 2.27$
- Encke gap	$133,423 - 133,745$	~ 2.21
- Keeler gap	$136,487 - 136,522$	~ 2.26
F ring	$139,826 - 140,612$	$2.32 - 2.33$
Janus/Epimetheus ring	$149,000 - 154,000$	$2.47 - 2.56$
G ring	$166,000 - 173,200$	$2.75 - 2.87$
E ring	$180,000 - 480,000$	$2.99 - 7.96$
Phoebe ring	$< 7,722,240 - > 12,488,310$	$< 128 - > 207$

Table 4.1: Saturn's main rings and features distances from Saturn's centre, over the Kronian equatorial level.

is estimated that there are 100 ± 30 more that are larger than 2km in diameter [Ashton et al., 2021]. Only 24 are regular moons, i.e. they have prograde orbits and are not greatly inclined to Saturn's equatorial plane. Amongst those are the 7 major moons: Mimas, Enceladus, Tethys, Dione, Rhea, Titan, and Iapetus. All of the 7 major moons have a diameter larger than 300km, with Titan being the largest amongst them and the second largest in the solar system at its surface, with a radius of ~ 2575km ($\sim 1.48 r_{Moon}$).

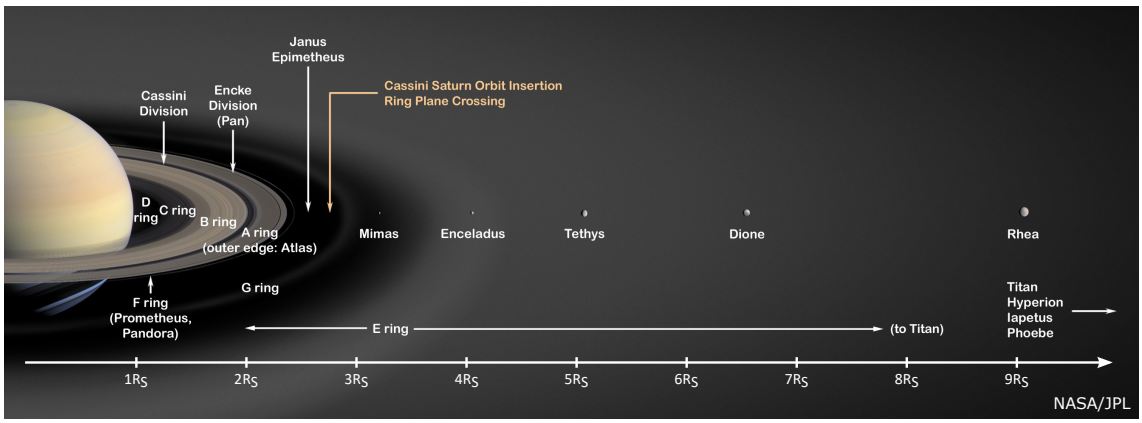

Figure 4.2: Saturn's rings and moons in the inner magnetosphere. The distance and names of the rings and moons are also marked. Image credits: NASA/JPL [2005].

It is also the only known moon with a substantial atmosphere.

To this date the mechanisms and timing of formation of these 3 components, i.e. Saturn, its rings, and its moons, are major topics of research.

4.2. Saturn's inner magnetospheric plasma and measurements

The Kronian magnetosphere is the second largest in the solar system, stretching to $\sim 20 R_S$ towards the stagnation point and hundreds of R_S towards the magnetotail. The strength of the magnetic dipole is $0.215 \text{Gauss} - {R_S}^3$, or equivalently $21.5 \mu\text{T} - {R_S}^3$ in SI units (a bit lower than $0.306 \text{Gauss} - {R_E}^3$, or $30,6 \mu\text{T} - {R_E}^3$, for the Earth), and its magnetic dipole is almost perfectly parallel to the rotation axis, as it is tilted by less than 0.007° and it is offset northward by $\sim 0.047 R_S$ [Cao et al., 2020]. It also has quadrupole and octupole moments with intensities $\sim 7\%$ and $\sim 13\%$ of the dipole moment respectively (e.g. Smith et al. [1980], Acuña et al. [1983]). These terms are stronger than those of Earths', which have intensities $\sim 6\%$ and $\sim 2\%$ respectively (e.g. Langel and Estes [1982]), but weaker than those of Jupiters', which have intensities $\sim 6\%$ and $\sim 2\%$ respectively (e.g. Acuña and Ness [1976]).

Cassini had three instruments/techniques able to measure the cold plasma: the CAPS, the LP, both of which could measure electrons and ions properties, and using the upper hybrid resonance frequency (f_{UHR}) from plasma waves measured by the RPWS, which

could measure only the electron density. Each instrument had a region for optimal operation, presented in fig. 4.3, with the solid colour. On the same figure, the striped colour shows regions where the instrument could still work, but its operation was not optimal. CAPS inside $\sim 5R_S$ was suffering from penetrating radiation, i.e. the intense radiation from Saturn would penetrate the walls of the instrument and reach the detectors producing wrong results. The LP could not accurately measure beyond $\sim 7R_S$ due to the plasma becoming hotter than the instrument's energy upper threshold of 10eV. The f_{UHR} could not be isolated from the plasma cyclotron frequency harmonics closer than $\sim 5R_S$, where the magnetic field was becoming strong and the f_{UHR} would collide on the electron cyclotron harmonics (example on fig. 2a in Menietti et al. [2017]), and it could not be detected beyond $\sim 10R_S$ [Persoon et al., 2020]. Ideally, since each instrument can measure accurately density over a restricted radial range, measurements from all three instruments should be used to create a full density map of Saturn's inner magnetosphere.

Persoon et al. [2020] created a diffusive equilibrium model for the inner magnetospheric plasma, using measurements from the three instruments: the electron properties from the RPWS (f_{UHR} for density, and the quasi-thermal noise spectroscopy (QTN) method for temperature) and the LP (that provided both density and temperature), and the ion properties from CAPS detectors combined with a 3D forward model fit. Fig. 4.4 shows the results of the Persoon et al. [2020] density model for three populations: water product ions (left panel), hydrogen ions (middle panel) and electrons (right panel). The heavier water products are more confined around the equatorial plane, where their density drops below $1cm^{-3}$ at $< 2R_S$ away from the Kronian equatorial plane, while the density of the hydrogen ions drops under $1cm^{-3}$ at around $3R_S$. There are two density peaks for the water products ions: at $\sim 4.5R_S$ with a density of $\sim 50cm^{-3}$ and $\sim 2R_S$ with a density of $\sim 30cm^{-3}$. The hydrogen ions also have the two peaks on the same radial distances, but with much less densities: $\sim 10cm^{-3}$ and $\sim 5cm^{-3}$ respectively. The electron density follows the water product ions with the same densities at the same distances. The abundance of the water products ions over the hydrogen ions, at the radial distances close to Enceladus and at the end of the main rings supports the accepted hypothesis: Enceladus and the rings are the two main plasma sources of the Kronian inner magnetosphere.

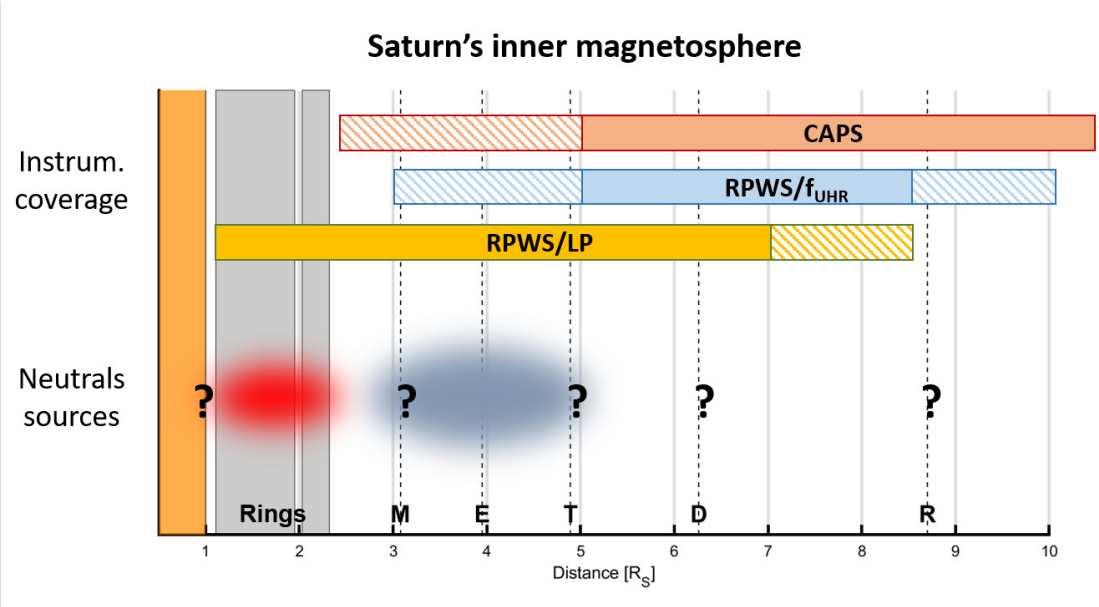

Figure 4.3: Saturn's inner magnetosphere with the Cassini instruments/experiments able to measure the plasma parameters, and the neutral sources, that will eventually become plasma. The dashed vertical lines are the orbital distances of Saturn's moons. The solid colour rectangular of each instrument is the region where the instrument operates nominally, while the striped is the region where it can still operate, but the operation is not nominal.

Also, electron density measurements confirmed the Persoon et al. [2020] model results for the electrons (fig. 13, panels (a) and (b) respectively, in Persoon et al. [2020]). The electron density following closely the heavy water products, shows that the region is in an almost quasi-neutrality state, as has already been assumed in the Persoon et al. [2020] model. Any deviations from the quasi-neutrality though between the model and the observations could be due to the rapid movement of the (lighter) electrons compared to the (heavier) ions, which makes them more susceptible in following the magnetic lines faster. For the same reason they are more spread away from the equatorial level than the water products: their density reaches 1cm^{-3} at around 3R_S compared to 1.5R_S for the water products.

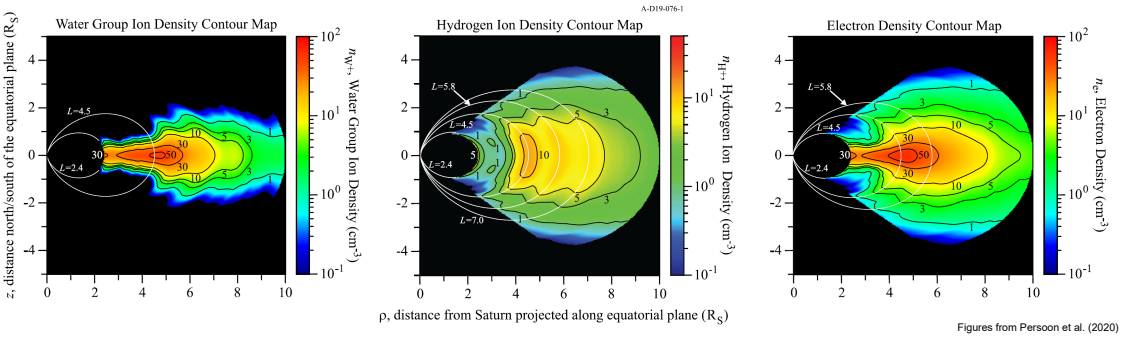

Figure 4.4: The plasma distribution for the Kronian inner magnetosphere, as calculated by Persoon et al. [2020]. *Left*: water-product ions. *Middle*: hydrogen ions. *Right*: electrons. Close to Enceladus distance the water-group ions density is significantly higher than the hydrogen distance, which supports the hypothesis that the moon a main plasma source of the Kronian magnetosphere. The water group ions density is also higher close to the main rings, which also supports that the rings, too, are a main plasma source, although not as strong as Enceladus.

4.3. Variations in inner magnetospheric plasma measurements between instruments

Persoon et al. [2020] also showed some disagreement between the electron density measurements from the f_{UHR} and the LP, shown in fig. 4.5. The left panel shows electron density from both the f_{UHR} (black dots) and the LP (red dots), for the whole $\sim$ 1800 measurements of the study. During this data sample Cassini was conducting high latitude orbits, going from the north hemisphere to the south hemisphere. The offset distance from the Kronian equatorial level is given in the x-axis. While the density calculated from the f_{UHR} seems to increase the closer to the equator Cassini approaches, there is a 'plateau' of LP 10cm^{-3} density measurements that expands perpendicular to the equatorial level, and at some regions reaching up to one order of magnitude smaller than the f_{UHR} measurements. Moreover, this variation between the measurements of the two instruments can be seen even in the same orbit, shown in the panel on the right: as Cassini moves across the equator, the LP measurements at ~ -0.4R$_S$ are higher than those of the f_{UHR}

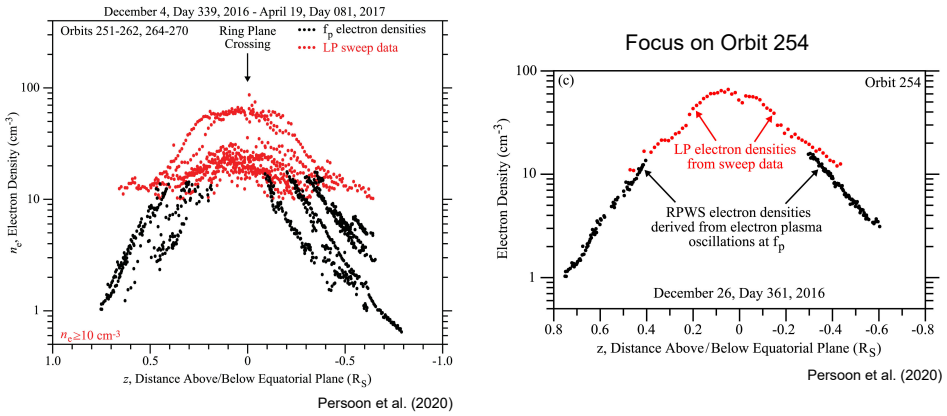

Figure 4.5: Differences in measurements between LP (red) and f_{UHR} (black). *Left*: data from Cassini high-latitude orbits. While the density calculated from the f_{UHR} seems to increase the closer to the equator Cassini is, there is a 'plateau' of LP density measurements at around 10cm^{-}3. *Right*: Data from Orbit 254, which again show that this variation between between LP and f_{UHR} densities is happening even in the same orbit. Figures from Persoon et al. [2020].

These variations denote that there are parameters that are affecting each instrument differently, that still remain unquantified. In order to study those parameters, including the photoelectrons impact, I focused on the LP equatorial electron plasma and compared them to the previous studies of Persoon et al. [2013] and Persoon et al. [2015]. I fitted the LP electron density measurements to the hybrid power-law model that predicts the electron density distribution on the equatorial plane, as described by Persoon et al. [2013]:

$$n^*_{e,eq} = \frac{n_0}{0.5\left[\left(\frac{r_0}{r}\right)^m + \left(\frac{r}{r_0}\right)^n\right]} \tag{4.1}$$

where $n^*_{n,eq}$ is the model equatorial electron density, n_0 is the density at the peak of the distribution, r_0 is the radial distance of the peak, and m and n are the radial dependencies of the plasma distribution inwards and outwards the peak density, respectively.

The data for this work covered a period from 2004-07-01 to 2017-09-09. In order to follow similar restrictions as Persoon et al. [2013] and Persoon et al. [2015] I selected only the data that were within $\pm 0.1 R_S$ from the equatorial level. In total there were 31517 datapoints. I then binned the datapoints over the radial distance from the planet in $0.2 R_S$

width bins, and I calculated the median. For the binning and fitting I used only data beyond L-shell 2.4, as inside that distance the data were few, sparse and very skewed. The LP electron data are presented in fig. 4.6. The top panel shows the raw data (light blue dots) with the median and standard deviation of the values in each bin (dark blue lines, where the central x mark is the median value), and the eq. 4.1 fitting (red line). The parameters of the fitted model are presented on the top right corner of the plot. The second panel shows again the binned values with the fitting results of the model using LP data (red), and additionally it presents the fitting results of Persoon et al. [2013] and Persoon et al. [2015] works. The third panel shows the skewness of the LP data for each bin. The skewness shows how symmetric the distribution of the data is around the median value. If it is equal to zero the data are perfectly distributed around a median, while the larger the skewness, the more spread the data are either above or below the median value. The data used here show that there are areas that the skewness is quite high, e.g. at L-shells ~ 2.4, ~ 5, and beyond 7. This might be caused by the density difference between the inbound and outbound phase of each orbit (example on fig. 8 in Xystouris [2016]), or even by the northern-southern asymmetry, caused by Enceladus south-facing plumes (examples in fig. 4.5).

Persoon et al. [2013] used data from the f_{UHR}, covering a period from 2004-10-28 to 2011-11-07, and they calculated the following model fitting parameters: $n_0 = 72\text{cm}^{-3}$, $r_0 = 4.6\text{R}_\text{S}$, $m = 4$ and $n = -4.8$. Persoon et al. [2015] repeated the same process with data covering a wider period, from 2004-07-01 to 2013-05-21, and while they calculated the same fitting parameters for n_0, r_0, and n, they calculated $m = 3$. The calculated parameters of the model using the LP data are $n_0 = 60.72\text{cm}^{-3}$, $r_0 = 4.22\text{R}_\text{S}$, $m = 2.73$ and $n = -4.89$. The R squared (R^2) was also calculated, which value (0.96) denotes that the model almost accurately predicts the density[1]. Comparing the LP fitting parameters with the f_{UHR} fitting parameters, the LP data fitting shows a lower maximum density ($\sim 61\text{cm}^{-3}$ compared to 72cm^{-3}) closer to the planet (4.2R_S compared to 4.6R_S). The outwards density decrease exponent for the LP data fitting is about the same as the one

[1]The R^2 can take a value between 0 and 1, where if 0 it means that the model does not predict the outcome at all, while if 1 it means that the model predicts the outcome perfectly. Hence the closer to 1 the value is, the better the prediction of the outcome

for the f_{UHR} data ($\sim$ 4.9 compared to 4.8); it also agrees with the previous publications of Persoon et al. [2005], Gurnett et al. [2007] on the equatorial electron density. The exponent for the inwards decrease though is even smaller than the other models ($\sim$ 2.7 compared to 3 and 4).

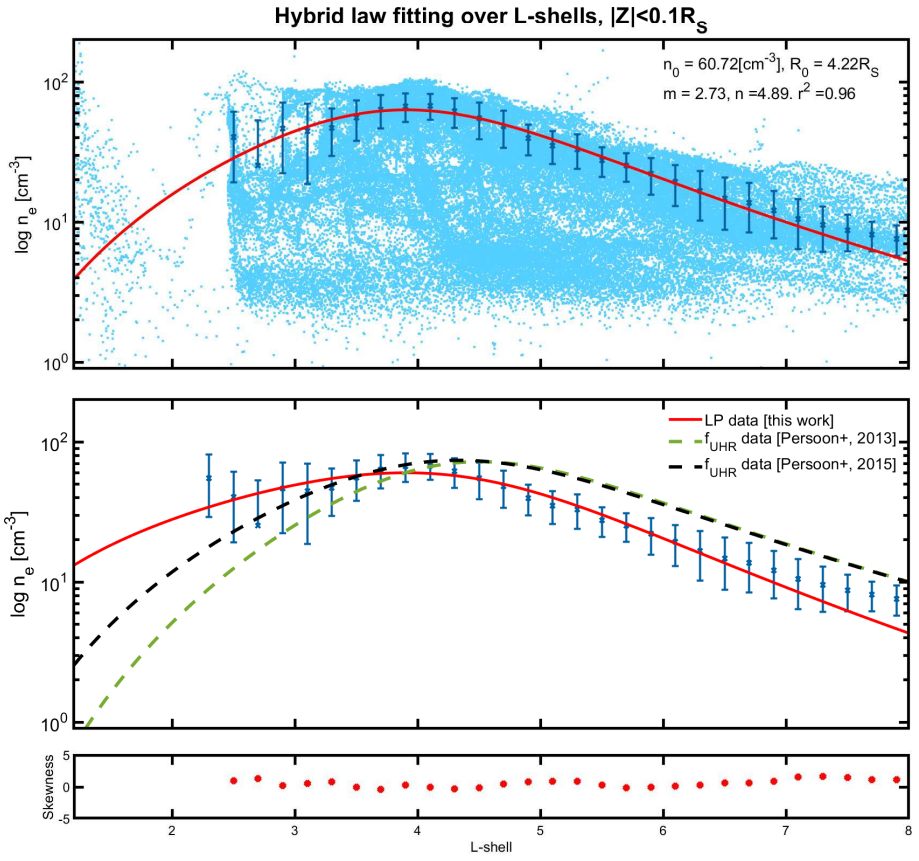

Figure 4.6: Plot of the LP electron density data and comparison with the f_{UHR} data. *Top*: the full LP data (light blue dots), binned data with the median (dark blue x) and the standard deviation as error (dark blue lines), and the density hybrid model fit (red line). The model values are presented on the top right of the panel. *Middle*: comparison of the model fitting for the LP data (red solid line), and two studies with f_{UHR} data (green and black dashed lines). *Bottom*: the skewness of the binned data - a perfectly symmetrical distribution has a skewness of zero. The interesting thing is the discrepancies of the fit inside $\sim 5R_S$ using different data from different periods or/and instruments.

There are several possible reasons for the inward shift and lower peak density the LP data show. As the LP being better on operating in closer distances to Saturn, it could be the instrument that gives the best result. Gurnett et al. [2005] also identified strong variations on the rings: a large density depletion over the main rings, and an increase of 2 orders of magnitude at the outer edge of the A ring. Persoon et al. [2015] mention that those variations could be a result of the of electron density variation inside the Enceladus orbit in late 2011 / early 2012. They also show a high density just beyond the A ring ($\sim 2.4\mathrm{R_S}$ to $\sim 2.7\mathrm{R_S}$) that was measured during the Saturn Orbit Insertion (SOI). These variations were shown also in my MSc thesis [Xystouris, 2016]. Lastly, the photoelectrons can also contribute to discrepancies between the two instruments/methods: any photoelectrons produced by the LP could potentially get re-captured by the instrument, while the f_{UHR} should - in theory - be produced solely by the magnetospheric plasma. As I was interested in studying the impact of the photoelectrons on an instruments' measurements, I focused on measurements of the LP and CAPS/ELS.

4.4. Searching for eclipses

The impact of the photoelectrons for the LP and CAPS was explained in section 2. To compare the impact on the measurements for each instrument I followed the very simple idea that when the spacecraft is an eclipse, i.e. in the shadow of a body, like the rings or Saturn, the generation of photoelectrons stops. Using the NAIF SPICE toolkit [Acton, 1996] function `cspice_gfoclt` (for MATLAB) I found the periods where Cassini goes into Saturn's shadow. In total, there were 118 total eclipses and no annular eclipses. The correctness of the calculated times was double-checked using the 3D visualization software NASA's Eyes [NASA and Bolles].

Additionally I found all the periods where Cassini was in the main rings' shadow by calculating the intersections of the Cassini - Sun vector on the Kronian equatorial plane and narrowing it to the periods with the appropriate geometry. I used the distances for each ring as presented in section 4.1. Overall, I found 161 solar eclipses by Saturn's main rings. In 73 instances there was an overlap of the eclipses caused by the two bodies: in 6 occasions the eclipse by the rings was totally in Saturn's shadow, while in 67 occasions

Cassini was already in the Ring's shadow while entering Saturn's shadow, or vice-versa. Fig. 4.7 shows an example of each case. A full table with all the eclipses can be found in the appendix A

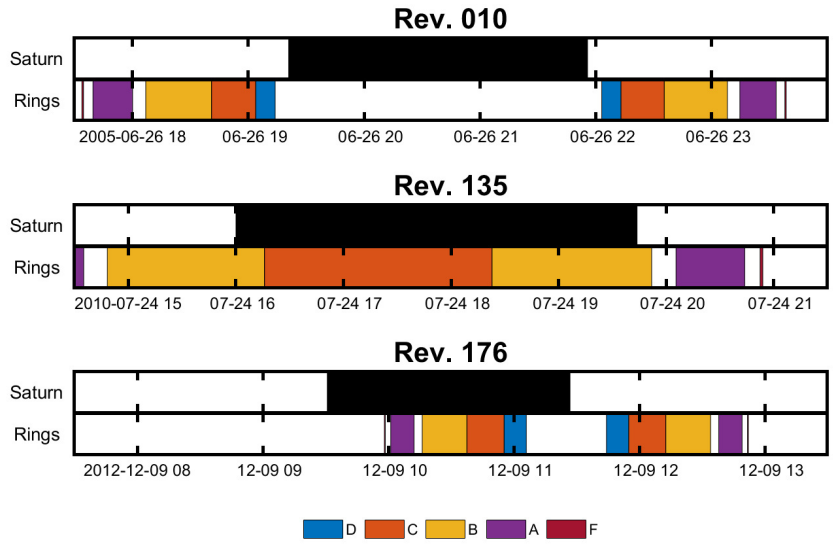

Figure 4.7: Schematic of the eclipse type. The first panel shows a case when the eclipse by the two bodies is completely separated (rev. 010 example), the second panel shows a case where the eclipse by Saturn occurs during an ongoing eclipse by the rings (rev. 135 example), and the third panel shows a 'hidden' eclipse of the rings that occurred during an on-going eclipse by Saturn (rev. 176 example).

It must also be noted that: (1) The rings can reflect and scatter sunlight in Saturn's shadow. In the works of this thesis I treat the rings as solid, non-reflecting bodies, ignoring any reflected and diffracted sunlight. (2) During Cassini's Grand Finale in Rev 270-286 Cassini was being shadowed by the rings twice in each orbit, due to the orbit geometry. (3) I did not use any data during the Grand Finale orbits as Cassini was too close to the ionosphere of the planet, affecting the measurements of the LP in a non-consistent way. E.g. while in some orbits during a ring eclipse the I_- part of the LP spectrum was dropping to the noise level (similar to fig. 4.15), in other orbits - or even in parts of the same orbit - the I_- part of the spectrum was dropping to the noise level, contradicting the expected reduction of the photoelectrons. Additionally there were orbits that the

spectrum showed no change at all during the eclipses.

4.5. Photoelectrons impact on the LP and CAPS measurements

While 118 total eclipses were identified, even in that distance, the size of sun was considerably big to create a 'partial' eclipse, i.e. the transition of Cassini from being sunlit to Saturn's shadow was not happening instantly, but there was a period where the sun was being partially covered. Such a partial eclipses could potentially affect the dataset, as, during the partial eclipse, Cassini is not fully illuminated by the sun, nor fully in the shadow, so the photoelectrons would vary depending on the amount of the sunlight that would reach Cassini. While the majority of them lasted less than one minute, and any effect they would have it would be insignificant (e.g. during low resolution mode the LP takes measurements every $\sim$ 5min, and there are only 17 instances where the LP was in the high resolution, $\sim$ 30s measurements mode), for this study we only used data while Cassini was in total eclipses.

I also attempted to study any photoelectrons variations while Cassini was not in a body's shadow but the LP was in Cassini's shadow. Those periods though are rare: there are only 10 orbits in which only the LP was at some point in Cassini's shadow and almost none of them has good, useable data - if any data exist they were either sparse, or the LP was not in the shadow long enough to take more than a couple of datapoints.

4.5.1. Overview of eclipses on photoionisation

I picked three eclipses-cases that were vastly different from each other. The criteria for selecting those eclipses were the distance from Saturn (L-shell), whether Cassini was conducting an equatorial or high latitude orbit, the angle of the Sun to the dipole equator, whether there was an ongoing eclipse by the rings or not, and how deep was the eclipse, i.e. how well the Sun - Saturn and Saturn - Cassini vectors were aligned. The first eclipse was on 2007-06-20, during Rev. 46, the second was on 2007-10-24, during Rev. 51, and the third was on 2010-06-19, during Rev. 133. Table 4.2 shows the characteristics for each eclipse.

I then focused on the actual measurements of the LP and ELS during each eclipse. An

Case #	Rev	Sun angle [°]	Rings eclipse?	Comments
1	46	12	Y	High latitude orbit Deep eclipse Close to Saturn
2	51	10	N	Equatorial orbit Shallow eclipse Close to Saturn Close to case #1
3	155	-4.8	N	Equatorial orbit Deep eclipse Far from Saturn

Table 4.2: Characteristics of each eclipse for the case study of photoelectrons. All three eclipses have different characteristics from each other.

example of the measurements is presented in fig. 4.8. The first panel shows the periods where Cassini was in the shadow of Saturn or the rings; each period is colour-coded. The second panel shows the L-shell (in blue) and the distance from the equator (in orange). The third panel shows the electron current of the, i.e. the current that the LP collected while positive bias was applied to the instrument. The fourth panel shows the total electron density (blue x's), and the density of each population (in coloured lines), calculated based on the methodology described in section 2.2.1. The final panel shows the CAPS counts spectrum for all energies, with the dashed line at $10eV$ showing the top energy threshold of the LP.

Some things that should be noted on this figure: ELS measurements seem to have a periodic variation. This is caused by the rotation of CAPS (more on the CAPS operation in section 2.2.4). In order to get the best representative sample of the plasma electrons I made sure to take measurements around the maximum count rate during each rotation. Also, there is an increase in the counts when Cassini gets inside the L shell 4 (marked with a black dashed circle). This is caused by the penetrating radiation: Cassini is close to the radiation belts of the planet, where the radiation is so strong (i.e. the electrons have a very high energy) that penetrates the instrument's walls, saturating the measurements. The effects of penetrating radiation are visible by comparing the left side of the plot (around 20:00UT) where it does not 'suffer' from penetrating radiation, with the right (marked with a black dashed line): on the regions without penetrating radiation there are visible, well-defined structures over all energies, with a clear separation in energies lower than $\sim$ 30eV (1.5 in logarithmic scale), while on the right, where the penetrating radiation is prominent, no structures can be identified, and the separation of the lower energy counts is not that clear. In general, high-energy ($\sim$ MeV) electrons exist everywhere in the magnetosphere, and penetrate constantly the walls of CAPS, but they are not enough to give a strong background signal.

The change in the measurements of both of the instruments when Cassini enters into Saturn's shadow is clear: for ELS the counts drop, while for the LP signal appears when a negative bias is applied to the probe. In theory this is not expected to happen, as the negative bias will repel the electrons. The registered current though is on the noise level

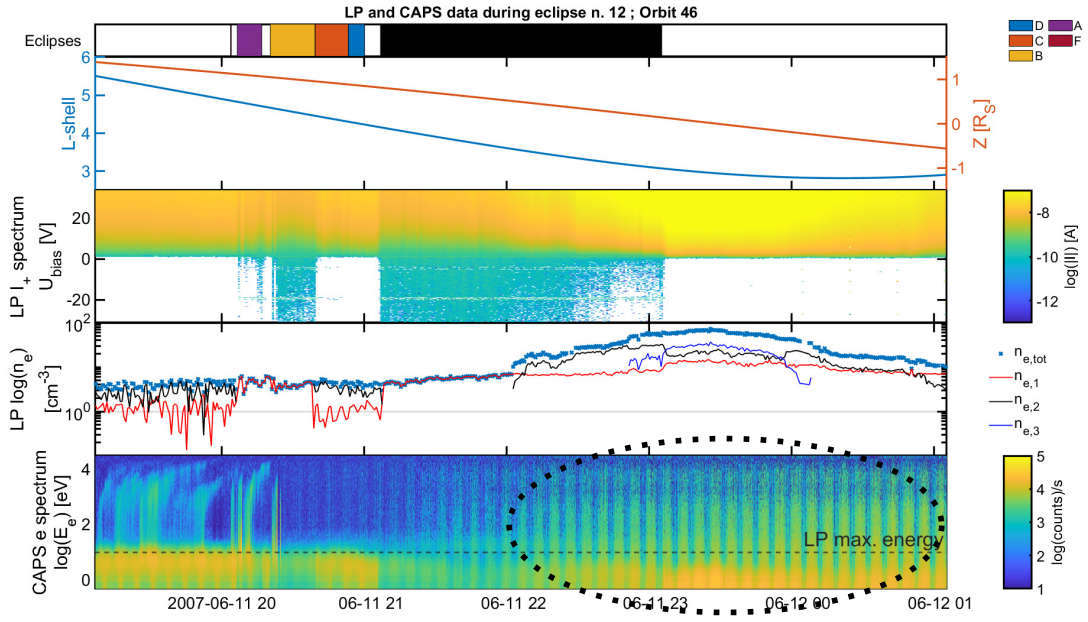

Figure 4.8: Example of LP and ELS data during an eclipse, along with spatial information of the spacecraft. *First panel*: the body in whose shadow Cassini was located. Black indicates a Saturn eclipse, and each colour denotes an eclipse of a specific ring, following the legend on the right of the panel. *Second panel*: Cassini's distance from the planet and the equator. *Third panel*: the LP ions spectrum, along with the current intensity colourbar (in logarithmic scale). *Fourth panel*: the calculated electron density with different colour for each electron population, and blue x's for the total density. *Fifth panel*: ELS counts spectrum, along with the counts colourbar (in logarithmic scale). The black dashed circle shows the region where penetrating radiation is affecting ELS measurements. The change in the measurements of both instruments is clear when Cassini goes into the shadow of Saturn. There are also changes in the measurements while Cassini is in the shadow of some of the rings; a further study on this will be presented in section 4.6.

of the instrument, meaning that it could be a result of thermal noise from the instrument electronics (explained in section 2.2.1). Therefore, we can safely say that a change did indeed happen, but we cannot extract any safe conclusions about the intensity of the current. There are also visible changes in the measurements of the instruments while Cassini was in the shadow of some of the rings. A further study on this will be presented in section 4.6.

The data for all three cases of this study are presented in fig. 4.9. Each case is marked on the left. The plots in the left column show data from two hours before the full eclipse to two hours after. The ELS measurements affected by penetrating radiation was marked with a black circle in each case. The right column show the region where I focused on for this study. In order to study the variability on the measurements due to the change of the photoelectrons density I focused on a region for each eclipse where there were good data from both instruments, i.e. there were no artefacts or unusual behaviour from the LP and there were good data, free from penetrating radiation from CAPS. Note that the colourcode for the CAPS measurements changes between each zoomed example, for the differences to be more visibly prominent.

To find any changes introduced by the eclipses I compared measurements for both instruments outside the eclipses to measurements inside the eclipses. The time for each measurement in each case is marked on fig. 4.9 with a red line, labelled 'Out' if it is outside the eclipse, or 'In' if it is inside the eclipse. In case there are multiple times inside or outside an eclipse, those are numbered, e.g. 'Out 1'. For the first eclipse I took one set of measurements outside the eclipse and two inside the eclipse, close to the beginning of the eclipse. As the penetrating radiation was quite strong during this case I chose not to take any sets in the middle of the eclipse, where they could have been affected by the radiation. I was also careful for the set outside the eclipse to be cleared of any eclipses by any ring. For the second eclipse I took two sets outside the eclipse, one before and one after the eclipse, and two set inside the eclipse, one right at the beginning of the eclipse and one in the middle of it. Lastly, for the third eclipse I took one set outside the eclipse and two sets inside the eclipse, close to the beginning and in the middle of the eclipse.

Fig. 4.10, 4.11, and 4.12 show the measurements for each case. Each figure has four

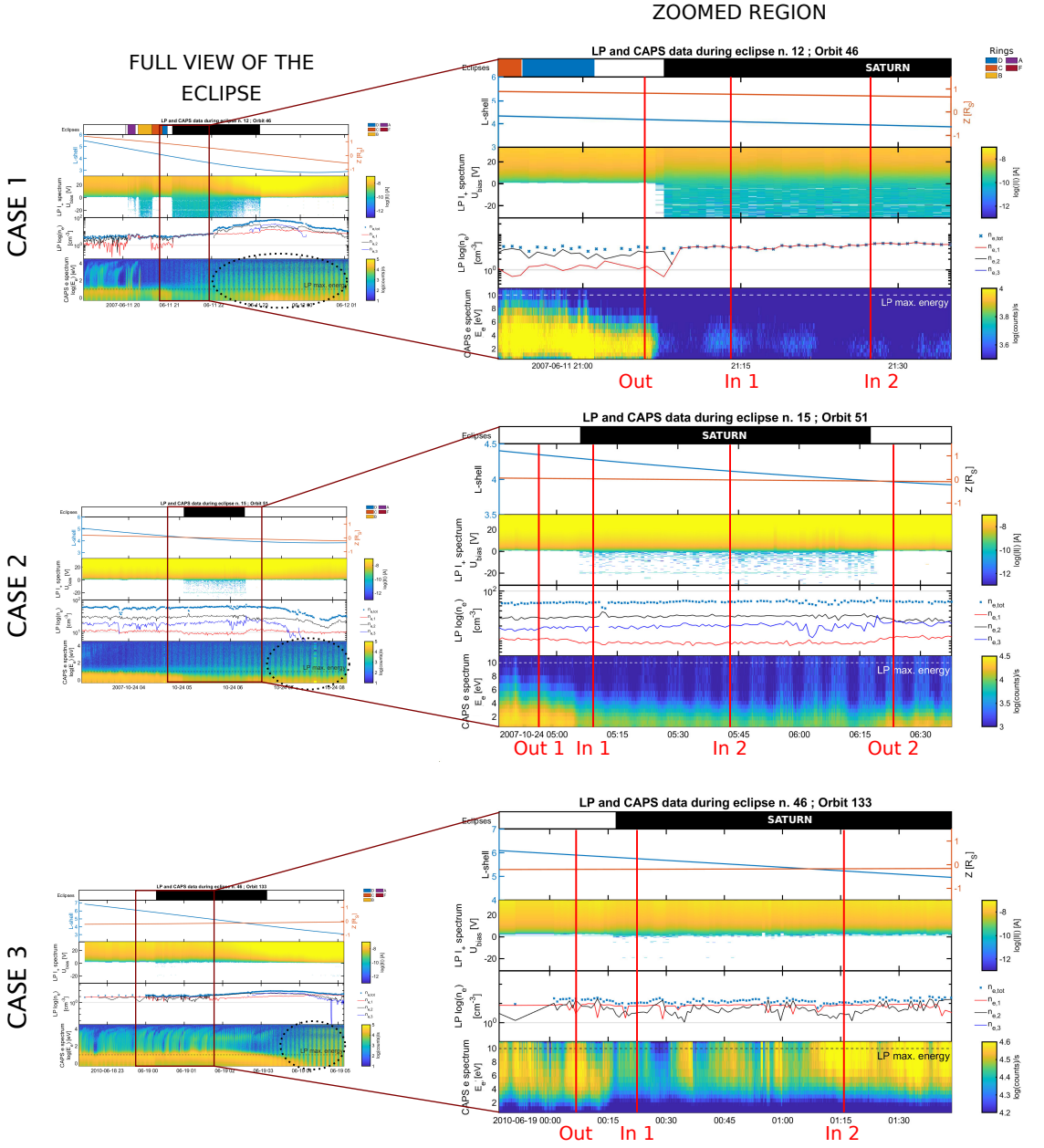

Figure 4.9: LP and ELS data for all the eclipses-cases of the study. On the *left* all the data around the eclipse are presented, while on the *right* there are the region for each eclipse I focused on for this study. The red vertical lines show the exact time of the compared data.

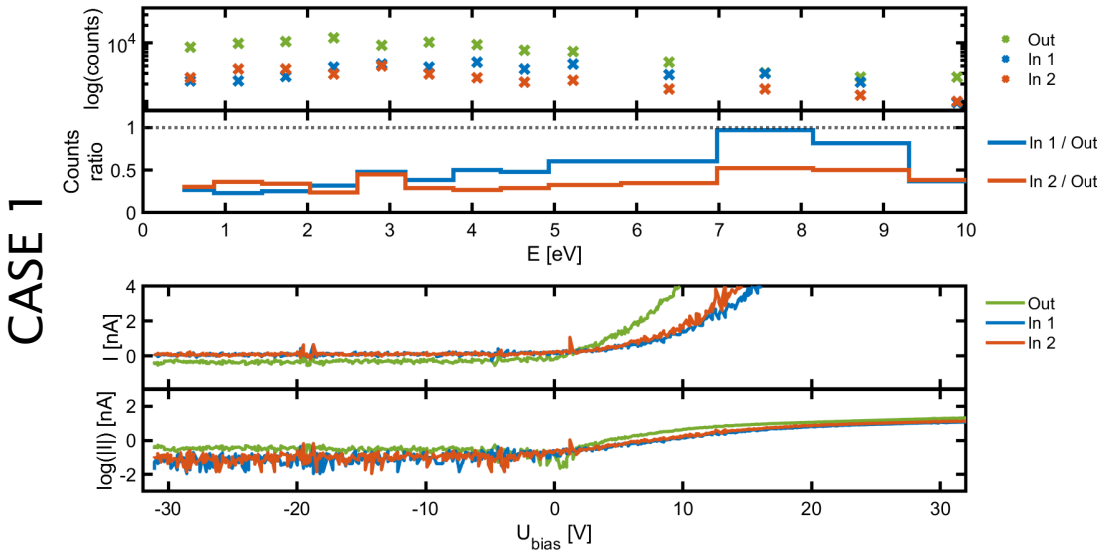

Figure 4.10: Comparison of CAPS and LP measurements inside and outside of an eclipse for the first case. For CAPS the ratio of the measurements is an indicator of how much the measurements changed due to the variation of the photoelectrons; a ratio of 1 (dashed line) shows no change in electrons number, and a ratio less than 1 show a decrease of the electrons during the eclipse. For the LP this is mapped on the decrease of the current where $U_{bias} < U_{fl}$, where it drop to the detectable current noise level (100pA).

panels. The top two panels are for ELS measurements, showing the counts logarithmic scale and the counts ratio (outside to inside the eclipse) over the energy range. The counts ratio can show changes in the measurements during an eclipse: a ratio of 1, presented with the dashed line, shows that there was no change in the measurements, a signal less than 1 shows a decrease of the electrons during an eclipse, and a signal over 1 shows an increase of electrons during an eclipse (which would be a surprising discovery!). The bottom two panels of each eclipse show the LP measurements: the measured current and the logarithm of the current magnitude over the applied bias voltage. As the photocurrent affects, in theory, both the ion and electron current (as discussed in sections 2.2.1 and 2.2.5), differences are expected to exist in both.

The ELS measurements during the eclipses showed a counts decrease (ratios under 1)

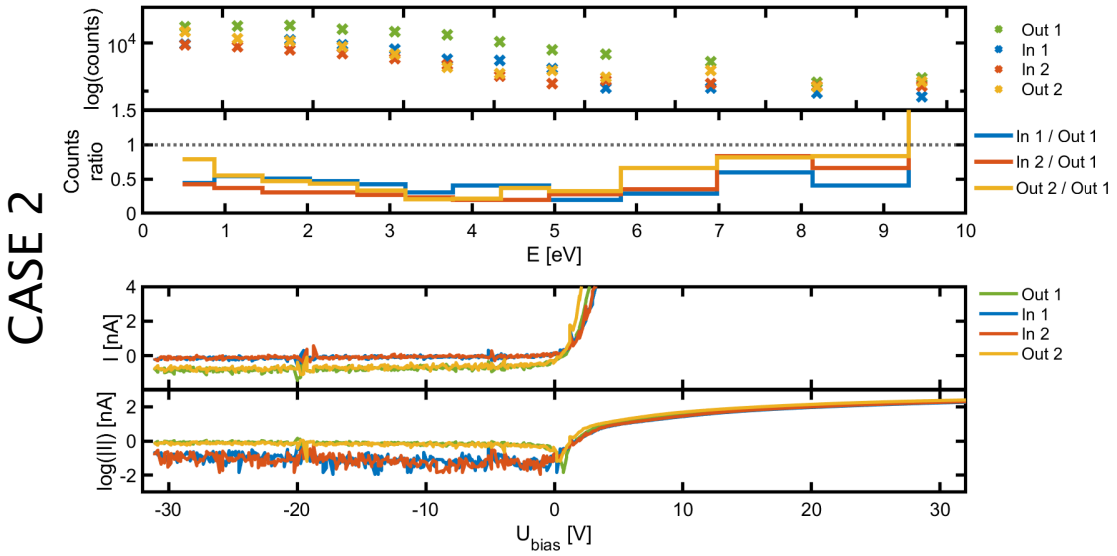

Figure 4.11: Same as fig. 4.10 for case 2.

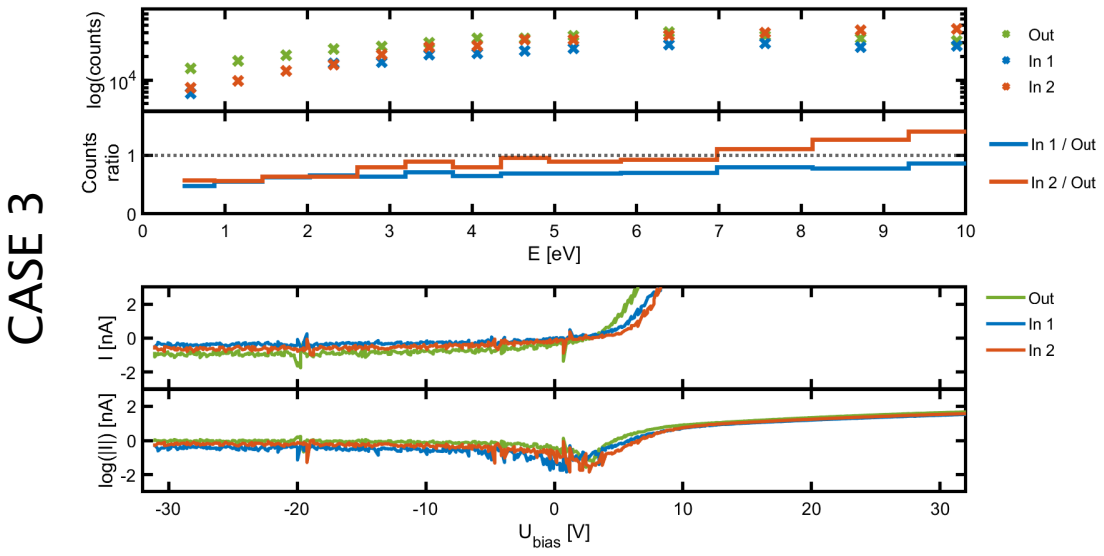

Figure 4.12: Same as fig. 4.10 case 3.

in the low energies for all eclipses. For the first and second cases the counts decrease was visible up to $\sim$ 7eV, while for the third the counts were strongly decreased up to $\sim$ 3eV, while they were slightly decreased or stable from $\sim$ 3eV to $\sim$ 7eV. It is unclear why the decrease of the third case did not span in higher energies, but a possible reason is that the produced photoelectrons were generated by different surface with a different work function each. As the photon lost a different amount of energy in the two surfaces, the photoelectrons produced with the remaining energy of the photon, will have different energies.

For the LP the ion-side current, I_{-}, (current for applied bias voltage $< U_{fl}$) for all three cases dropped to the 100pA noise level, denoting that the photocurrent generation stopped. Also, for the first eclipse it seemed that an electron population disappeared when Cassini entered into Saturn's shadow, that could indicate a decrease in the electron density caused by the halt in the production of photoelectrons. The fact though that the total electron density though did not decrease that much in combination with this decrease not seen in the rest of the cases does not allow us to safely connect the electron population decrease with the lack of photoelectrons.

4.5.2. Initial investigation of spacecraft potential changes

During this work I supervised an undergraduate student for a 4-week summer project. The goal was for them, as an undergraduate, to follow the process of researching a problem (i.e. identify and understand the problem, develop strategy of to study it, and develop critical thinking on interpreting the results) and assist to an ongoing research project, which was the project mentioned above. Their contribution was to apply different filters of removing the noise in the ELS data (i.e. removing the highest energy counts, or the average of 3 highest energies counts, or the counts median) and provide the final data for ELS. They also calculated the change of potential of the spacecraft between sunlit and eclipse periods using Liouville mapping, i.e. tracking the changes in the electrons phase space distribution, based on the fact that the phase space density must be conserved. They reported that for the cases studied above the spacecraft potential did not change much. This is an interesting result, as, having a more accurate view of the spacecraft

potential variation during eclipses can be beneficial in instruments that are affected by those changes, like, e.g. the LP.

The preliminary results for the project described here were presented by me in the American Geophysical Union Fall Meeting 2022 [Xystouris et al., 2022]. The student's work showed that it is a good avenue to go down in the future, as it can give valuable results on how the photoelectrons affect multiple instruments. Further on the future work that can be done on this project is discussed in section 4.8.

4.6. Photoelectrons variations & Saturn's main rings optical depth

In this section I present my study where, using the LP measurements I calculated the opacity of Saturn's Main Rings by measuring the variations of the photocurrent; the study is published in Monthly Notices of the Royal Astronomical Society (MNRAS) [Xystouris et al., 2023a]. As shown in fig. 4.8 there are changes in the measurements of both the LP and CAPS while Cassini travels through the shadow of the main rings. These change in measurements are connected to the variation of the photocurrent of the instrument, which variations are linked to the transparency of each of the main rings.

The study of the photoelectrons can also lead to discoveries in different areas than strictly studying the impact of the photoelectron variations on an instrument. Such an example is Brace et al. [1988] where, using the photoemission variations of the LP on the Pioneer Venus Orbiter they estimated the solar irradiance in EUV over time. In the same way I focused on the photoelectron variations on the LP measurements while Cassini was in a body's shadow (Saturn's or the rings') to calculate the opacity of Saturns' Main Rings.

Also in this section fig. 4.14 was provided by my supervisor, Dr C. Arridge, as a means of understanding the LP surface photoemission when we were first discussing the project.

4.6.1. Past studies on Saturn's main rings optical depth

The ring opacity can provide information about the size of the rings particles. Maxwell [1859] was the first to hypothesise that Saturn's rings are not single solid objects, but each one consists of smaller particles. The different distribution of the particles in each ring will block a different amount of sunlight - or, equivalently, will let a different amount of

sunlight to pass through the ring. Therefore, by measuring the opacity of a ring, we can extract information about the particles size distribution and number density.

One of the first studies on ring opacity was from Esposito et al. [1983], where, using stellar occultations from the ultraviolet (UV) spectrometer of the photopolarimeter system (PPS) onboard Voyager 2 during its flyby of Saturn they calculated the optical depth of the rings in the ultraviolet C (UV-C) range ($100 - 280nm$); this is presented in fig. 4.13. The D ring appeared tenuous, with optical depth, τ, approximately 0; the C ring had a quite low normal optical depth with $\tau \sim 0.1$; the B ring was the most opaque one, with τ from 0.6 to well over 2.6; the Cassini Division had a C-like opacity, and the A ring was opaque with $\tau \sim 0.5$.

Later studies used data from the Cassini era, so a larger amount of data were available. Colwell et al. [2009, 2010], using data from Cassini's Ultraviolet Imaging Spectrograph (UVIS) (operating in the $115 - 190nm$ spectral range), showed that the optical depth for the A ring was between 0.5 and 1 without large variations, but the B ring was well above 1 and varying significantly over distance, sometimes reaching values up to 5; these variations are connected with the difference of the particles sizes and number densities over the regions of the B ring. The optical depths for the C ring and Cassini Division were similar and closer to 0, at around 0.1. This 'division' between the A–B rings and C–D rings was reported in other wavelengths too, e.g. by Hedman et al. [2013] where, using data from Cassini's Visual and Infrared Mapping Spectrometer (VIMS; operating in two different spectral ranges at $350 - 1050nm$ and $850 - 5200nm$) they reported a uniform distribution of a visible and near-UV absorbers across the A ring, the Cassini Division, and the outer B ring, that increases towards the inner B ring and stays high over the C ring - hence the higher reflectivity of the A and B rings.

Farrell et al. [2017], using RPWS data from Saturn Orbit Insertion, reported an inverse correlation between ring electron plasma density and ring opacity from the A ring to C ring, including the Cassini Division, with the density of the B ring found to be the highest, as it is the most optically thick. A series of studies, using the LP data, studied the properties of Saturn's ionosphere in and out of shadow to examine the effects of attenuated light on photochemical processes and observed changes connected to the opacity of the

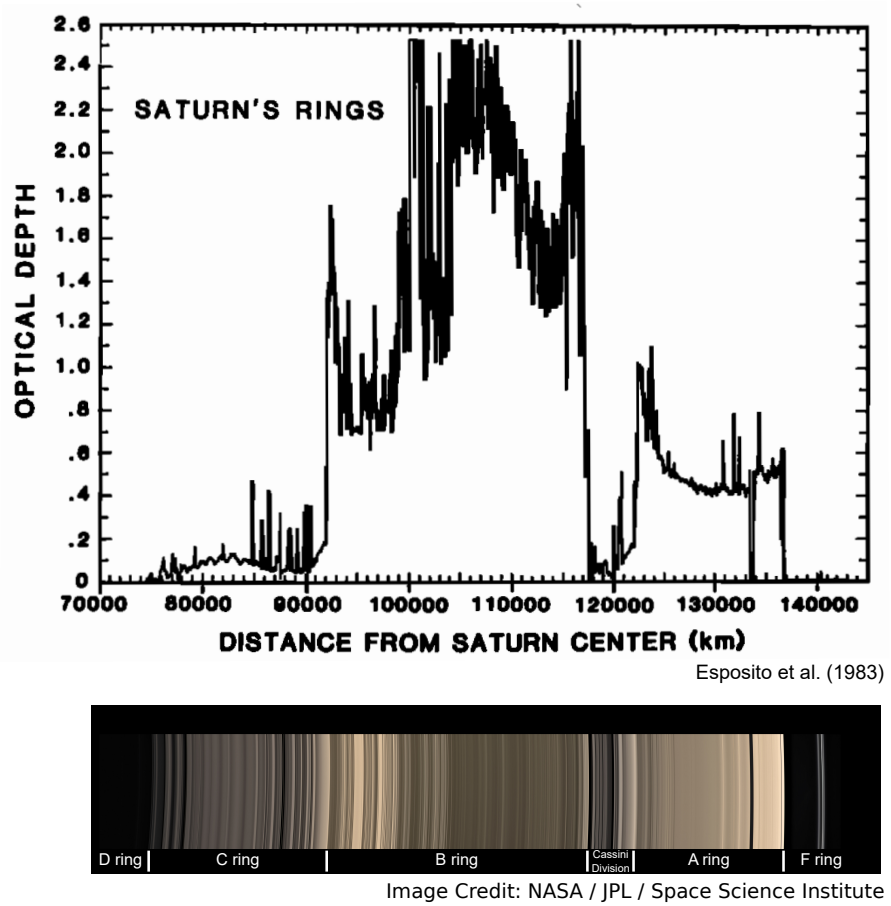

Figure 4.13: *Top*: Saturn main rings optical depth in UV, as measured from Voyager 2 Photopolarimeter System (PPS) (from Esposito et al. [1983].). The D ring appeared tenuous, the C ring had a quite low optical depth, the B ring was the most opaque, the Cassini Division had a C-like opacity, and the A ring was opaque. *Bottom*: a photo of the rings taken in the visible part of the spectrum by Cassini Imaging Science Subsystem (ISS), as an aid of the optical depth interpretation (Image credits: NASA et al. [2007]). The exact rings distances are presented in table 4.1.

rings. Wahlund et al. [2018] used LP data during the Grand Finale orbits - where the spacecraft conducted a series of orbits passing in-between Saturn the D ring - and, based on the photoionization of Saturn's ionosphere, reported that the A and most of the B ring are opaque to solar extreme ultraviolet (EUV), as there was very little plasma within

the regions of the rings' shadows. The Cassini Division was found to be less opaque to EUV, and the C and D rings are transparent to EUV, as no plasma changes were reported in their shadows. Hadid et al. [2018], using the same instrument and for the same period, also reported that while the A ring shows a somewhat uniform opacity in EUV throughout the entire extent of the ring, the B ring has a non-uniform EUV opacity that is probably connected with the reported altitude-latitude variation of the proximal orbits (e.g. Wahlund et al. [2018], Persoon et al. [2019]).

4.6.2. Definition of optical depth using LP measurements

The optical depth, τ, is defined as the ratio of the incident radian flux, Φ_e^i to the transmitted radiant flux, Φ_e^t:

$$\tau = \ln \frac{\Phi_e^i}{\Phi_e^t} \tag{4.2}$$

where the radiant flux is a wavelength integral of the spectral radiant flux, $\Phi_{e,\lambda}$ [McCluney, 2014]:

$$\Phi_e = \int_0^\infty \Phi_{e,\lambda} d\lambda \tag{4.3}$$

This logic can be applied to the LP, where the photoemission current can be given as:

$$I_{ph} = A_{LP} j_{ph} = \pi r_{LP}^2 j_{ph} \tag{4.4}$$

where j_{ph} is the photoemission current density, and A_{LP} is the probe area that receives sunlight. The photoemission current density is

$$j_{ph} = e \int_0^\infty Y(\lambda) H(\lambda) d\lambda \tag{4.5}$$

where e is the electron charge, $Y(\lambda)$ is the yield of photoelectrons, and $H(\lambda)$ is the flux of photons per unit wavelength.

The spectral flux density, $E_{e,\lambda}$ is the energy flux per unit wavelength, and it is related to $H(\lambda)$ by the energy of a photon at a particular wavelength:

$$H(\lambda) = E_{e,\lambda} \frac{\lambda}{hc} \tag{4.6}$$

Gathering equations 4.4, 4.4, and 4.6 we have:

$$I_{ph} = \frac{A_{LP} e}{hc} \int_0^\infty Y(\lambda)\, E_{e,\lambda} \lambda \, d\lambda \tag{4.7}$$

The integrand of 4.7 is presented in fig. 4.14. The first panel shows the photoelectron yield of the annealed titanium nitride [Diaz-Aguado et al., 2018], which is the material the LP is coated with. The second panel shows the solar spectrum [Huebner et al., 1992]. If we multiply the first by the second panel we get the LP photoelectron spectrum, which is shown in the third panel. The total photoemission is $\sim 33{\cdot}10^9 e_{ph}$ cm^{-2} s^{-1}. The dominant emission frequency is at Lyman-α, which emits $\sim 60\%$ of the total photoelectrons, while the rest of the Lyman series emit $\sim 10\%$, and the Lyman continuum $\sim 6\%$, hence the LP photoemission takes place on the EUV part of the electromagnetic spectrum.

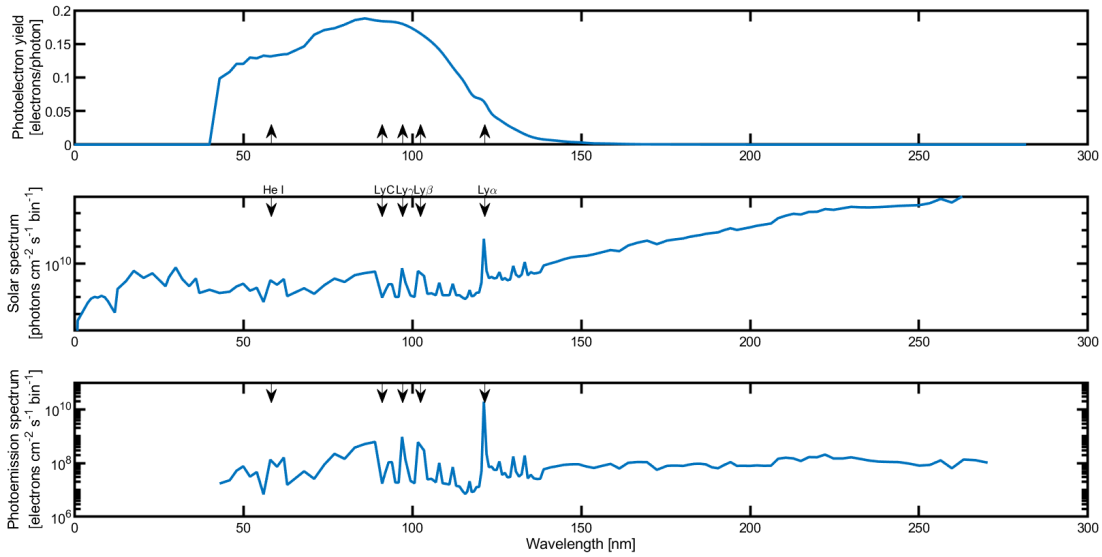

Figure 4.14: The photoemission spectrum of the Cassini LP at Saturn. *Top*: The photoelectron yield of titanium nitride matching the coating for the LP. *Middle*: The solar spectrum. *Bottom*: A multiplication of the two gives the photoemission spectrum for the LP. The majority of the photoelectrons are generated in Lyman-α.

Besides the solar radiation, interstellar radiation is an additional source of radiation that could affect the LP photoemission. Focusing around the wavelength for Lyman-α at

$\sim$ 121.6nm - as the dominant contributor frequency of photoelectrons - the photoelectrons emitted by the sunlight are $\sim 2 \cdot 10^{10} e_{ph}\ cm^{-2} s^{-1} \text{bin}^{-1}$, and as the bin width is about 0.75nm(= 7.5Å) the solar radiation photoelectron flux is $\sim 2.7 \cdot 10^{9} e_{ph}$ $\text{cm}^{-2}\text{s}^{-1}\text{Å}^{-1}$. For the background radiation Henry [2002] showed that the maximum flux for the Lyman-α wavelength in the (unrealistic) case where no radiation is lost due to any process (i.e. all the scattered radiation remains part of the interstellar radiation field, and the interstellar grain is fully reflective) is $\sim 1.3 \cdot 10^{6} e_{ph}$ $\text{cm}^{-2}\text{s}^{-1}\text{Å}^{-1}$, which is three orders of magnitude smaller than the solar flux. Hence any contribution from the interstellar radiation can be neglected.

Eq. 4.7 is similar to equations used in optical remote sensing, where the measured pixel intensity is an integration of an instrument response function over a signal as a function of wavelength. Let $R(\lambda) = Y(\lambda)\,\lambda$, as a response function for how much current is produced per unit wavelength for a given spectral radiant flux $\Phi_{e,\lambda}$. The ratio of the photoemission current out of the eclipse (incident current), I^i_{pe} to that in an eclipse (transmitted current), I^t_{pe} is

$$\frac{I^i_{pe}}{I^t_{pe}} = \frac{\int_0^\infty R(\lambda)\,\Phi^i_{e,\lambda} d\lambda}{\int_0^\infty R(\lambda)\,\Phi^t_{e,\lambda} d\lambda} \tag{4.8}$$

Combining equations 4.2, 4.3, and 4.8, the optical depth for the LP currents is given as:

$$\tau = \ln \frac{\Phi^i_e}{\Phi^t_e} = \ln \frac{I^i_{pe}}{I^t_{pe}} \tag{4.9}$$

Therefore by simply taking the ratio of the measured incident current to the measured transmitted current the optical depth can be calculated. The methodology described above also mirrors the methodology used in other studies that determined the optical depth of Saturns' rings, e.g. Colwell et al. [2010], where they took measurements of stars while they were not occulted by the rings, and them with the measurements of the same stars while they were occulted by rings.

4.6.3. Data examples

I focused on data during ring eclipses, described in 4.4. As there were many combinations of types of eclipses (with / without rings and / or Saturn), and the LP mode was changing

from eclipse to eclipse, the type of the eclipses and the operation mode of the LP is summarised on table 4.3.

Description	Number of eclipses of Saturn	Number of overlapping Saturn-Rings eclipses	Number of eclipses of Rings
HR LP data	11	6	24
LR LP data	25	5	19
MR LP data	25	—	7
No LP data	25	53	33
Inconclusive data	—	73*	88

Table 4.3: Eclipse summary accompanied with the data description. The LP operates either in a high-resolution rate, or a low-resolution rate. The inconclusive data are orbits that either had too sparse datapoints, or data of low quality. The note (*) on the overlapping eclipses is for the 6 eclipses by the rings that were totally in Saturn's shadow (behind the planet); while they are acknowledged, they are not used in the analysis.

Fig. 4.15 shows an example of the LP data during the eclipse in rev. 046. It is the 12th eclipse by Saturn, and it lasted for 119 minutes. The top three plots show the spacecraft's orbit in KSMAG: the unit vector of the z-axis, $\hat{\boldsymbol{e_z}}$, is pointing along the Kronian magnetic dipole axis, $\hat{\boldsymbol{e_y}} = \hat{\boldsymbol{e_z}} \times \hat{\boldsymbol{e_{Sun}}}$, and $\hat{\boldsymbol{e_x}}$ lies in the Kronian equator completing the right-handed orthogonal system. The time goes from blue to red. The middle plot shows the LP spectrum and the calculated electron densities and temperatures, along with the location of Cassini, in which body's shadow it was, and the eclipse depth for Saturn. The bottom two plots show the I-V curves on the times A and B of the spectrum.

The spectrum shows the measured current as a function of the applied bias voltage in time; the current magnitude is shows at the colourbar. The horizontal lines around -3V and -17V are caused by interference from another instrument. It is clear that the spectrum changes when Cassini enters into a body's shadow, as the current is reaching almost the noise level (100pA). This can be seen comparing the two I-V curves on the bottom (the top panel for each shows the current in linear scale and the bottom shows it

in logarithmic scale): curve A is a sweep outside the eclipse, while curve B is during an eclipse by Saturn. The ion current outside the eclipse is around -1nA, while inside the eclipse is less than ± 100pA, which is the threshold of the electronic noise of the instrument (explained in section 2.2.1). This change is connected to the lack of photoemission while the spacecraft is in the shadow. As mentioned in section 2.2.1 the ion-side current, I_- is the sum of the photoemission current and the ion current - the cold plasma electrons do not contribute here, as they are repelled due to the negative bias voltage in this region. Hence as the photoemission goes to near zero and the ion current is very small and does not change dramatically, the ion-side current is a near-zero current during the eclipses. Also, another noticeable feature between the two sweeps is while the floating potential, U_{fl} is clearly identifiable by the inflection in the current magnitude when Cassini is outside of an eclipse, it is that not clearly noticeable inside the eclipse.

Focusing on the period where Cassini was going through the main rings shadow (identified by the colour of the bars at the top) it is clear that each ring has a different impact on the measurements. The A and B rings have similar behaviour as if Cassini was eclipsed by Saturn, while the C and D rings show a behaviour as if Cassini was not eclipsed at all. Focusing on the A, B, and C rings, we see that all three show some kind of structure on the ion current. The A ring has the more intense changes, as in some regions that the ion current drops to zero, while in others the spectrum looks very similar to that being outside the shadow. The B ring has more subtle changes, with the ion current on the outer inner B ring to be more time closer to zero than that on the inner B ring. Lastly, there are some subtle changes on the ion current intensity in the middle the C ring.

Another interesting feature is the variation of the electron population number during the eclipses (seen in the fourth panel of fig. 4.15). As mentioned the electron plasma density is given by a multiple electron population model, and the total density is the sum of the density of the individual populations. In this example as Cassini approaches the rings shadow the best fit is a two-population density, but as it enters the shadow of the A ring the best fit model is an one-population density, which changes back to two as Cassini transits from the shadow of the B ring to the C ring. As Cassini enters into Saturn's shadow the density drops down to a single population, mid-way through the

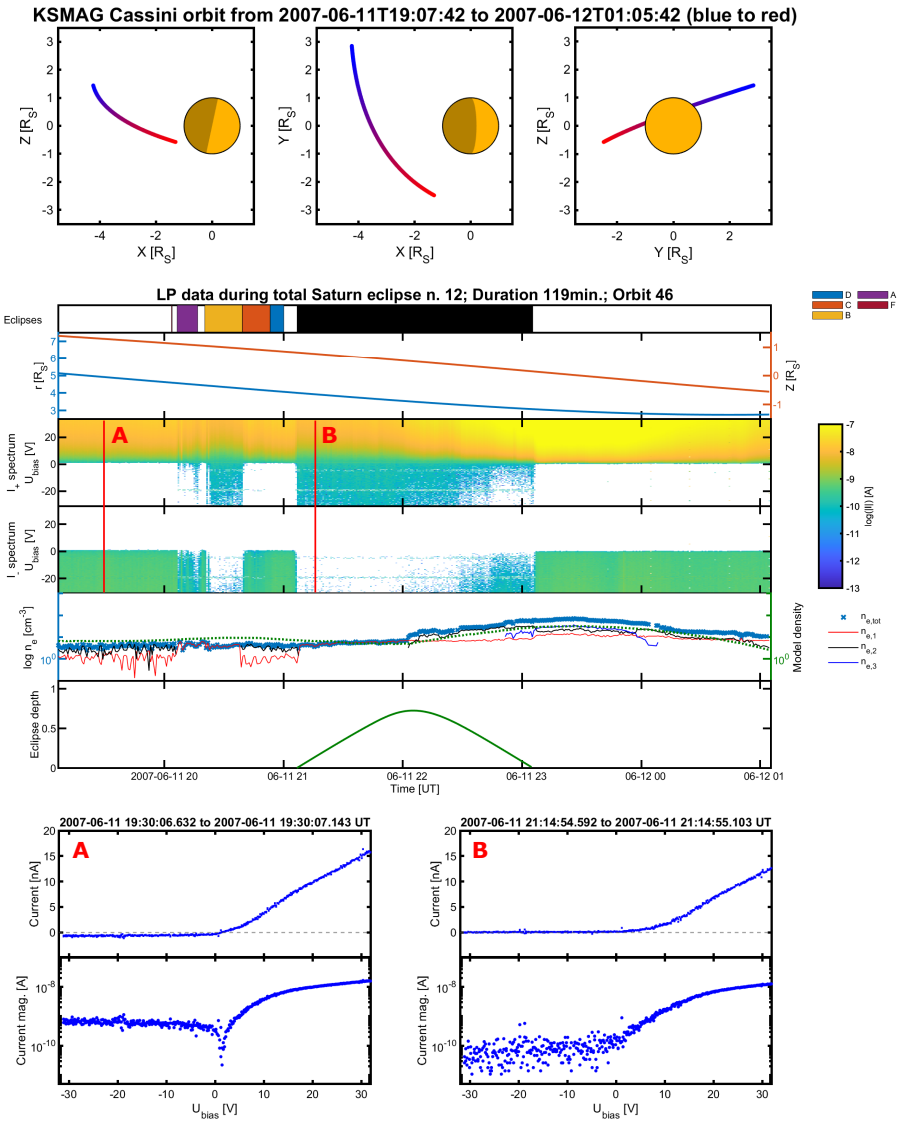

Figure 4.15: Example of 'good' LP data during an eclipse. The top three panels show Cassini's orbit. The figure in the middle show which body eclipses Cassini at a specific time, Cassini's distance from the planet and the equator, the LP spectrum for electrons and ions, the calculated electron density, and the eclipse depth. The last two panels show a sweep outside (A) and inside (B) a Saturn eclipse. This is a dataset where the data are clear and well-structured, as the changes in the LP spectrum are visible when Cassini goes into the shadow of Saturn, or rings with high optical depth.

eclipse a second electron population appears, and just before the eclipse by Saturn ends a third one appears. These changes are mostly consistent with one of the populations being the photoelectrons, disappearing while Cassini passes behind optically thick rings or enters into Saturn's shadow. While the appearance of a population mid-way the eclipse by Saturn is not supported by a variation of the photoelectrons, it can be supported by Cassini going into an area with denser plasma, as at the time the population appears ($\sim$ 2200UT) it gets close to the equatorial plane in a radial distance of $\sim 4\mathrm{R_S}$, which is the orbital distance of Enceladus, which is a plasma source.

Lastly, a last feature that should be mentioned is the increase of the ion current towards the end of the eclipse ($\sim$ 2230UT), which could denote Cassini entering a region of energetic electron plasma, with photoelectrons generated due to scattered sunlight, or a region where the ion currents become more important, due to Cassini entering a region of higher density. Such spectra that change dramatically during the Saturn eclipse are quite rare in our dataset.

While an example with good-looking data was presented, it must be acknowledged that not all of the data are that well-structure. Such an example is presented in fig. 4.16 for eclipse n. 46, during rev. 133. One can notice that while the LP spectrum changes while Cassini is in Saturn's shadow the negative bias current does not cross zero, opposed to the example in fig. 4.15. A possible reason for this is Cassini being in a high-density plasma where the ion current is higher than the instrument thermal noise, hence it is non-negligible. Also if the spacecraft is in a high-energy electrons region, they can potentially overpass the potential and collide with the LP, producing, falsely, ion current. There are about 20 eclipses of this type, which is a small number compared to the sample, so it can confidently be said that the results are not affected by those cases.

Taking a closer look on fig. 4.15 on the periods where Cassini was in the shadow of the rings, the rapid change of the current compared to the motion of the spacecraft rules out the changes to be caused by a change in the surrounding ion density, or the secondary electron current, as the energetic ions/electrons impact rates are usually negligible in these regions (e.g. Thomsen et al. [2016]), and strengthens the idea of the photoelectron being the major driving force. As the changes in I_- are more prominent in the A and B rings,

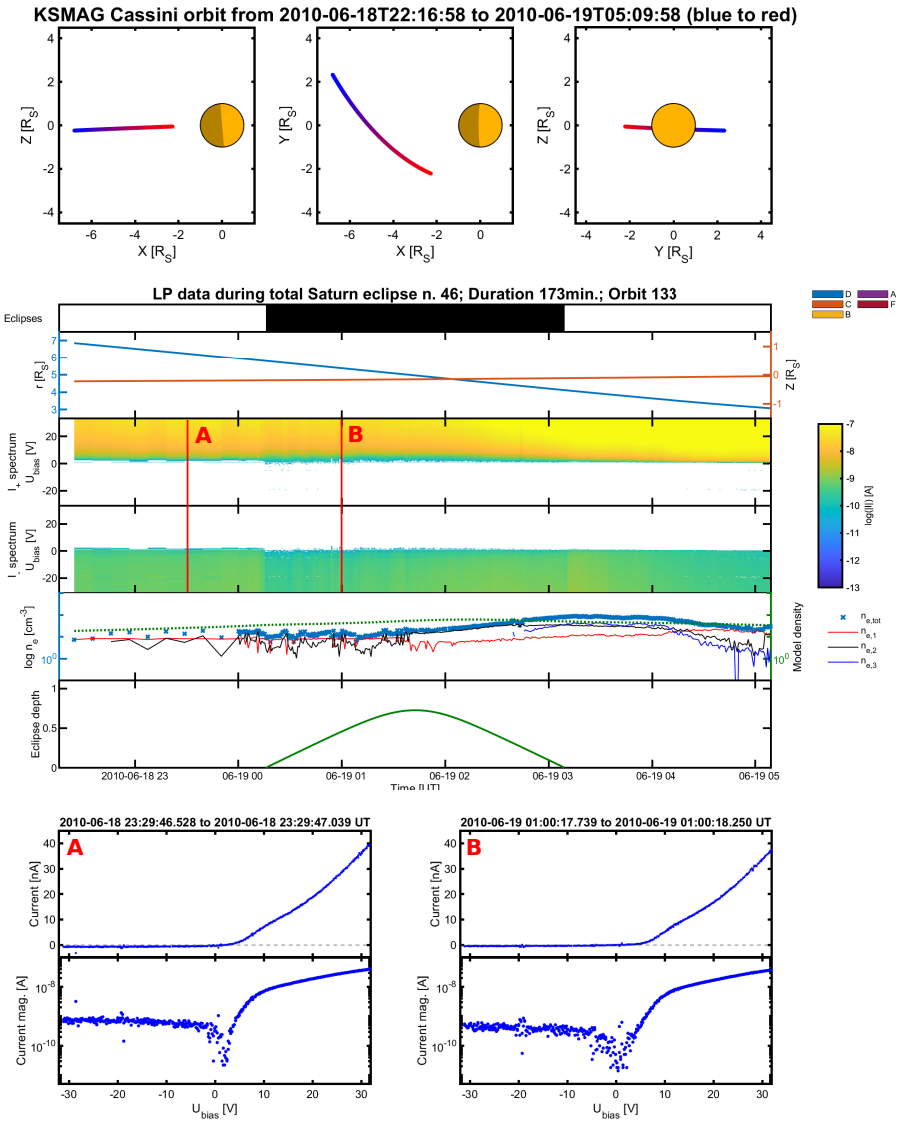

Figure 4.16: Example of 'bad' LP data during an eclipse. Same structure as fig. 4.15. In this dataset, while one can see some changes in the LP spectrum when Cassini goes into the shadow of Saturn, they are not that prominent.

which also are the most optically thick in quite a few wavelengths, they could be linked with the difference in the optical depth in the part of the spectrum that the LP is more sensitive to, which is the EUV as it will be shown in the next section.

4.6.4. System geometry and rings structure

There are two major factors that can affect the path of the sunlight through the rings. The first one is the angle in which the incident sunlight crosses the rings plane, and the second is the fine structures of the rings.

Incident sunlight angle

As the rings material absorbs the incident sunlight, the distance the sunlight travelled through the rings is important: the longer the distance, the more sunlight will get absorbed. We can 'standardise' the distance by introducing a "viewing factor", ξ, that adjust the path of the incident sunlight to be perpendicular to the rings plane. As seen in fig. 4.17 ξ can be defined as the cosine between Cassini and the ring plane normal vector, i.e. $\xi = \cos\theta$; while the figure is a two-dimensional representation ξ can be easily calculated in three dimensions. The angle θ though is affected by the Kronian seasons, as, due to Saturn's 26.73° inclination on the orbital plane it can take maximum and minimum values. Therefore during Saturn's equinoxes the sunlight comes parallel to the ring plane, hence $\theta = 90°$ and $\xi = \xi_{max} = 1$, while during the solstices the sunlight incident angle is $\theta = 63.17°$ and $\xi = \xi_{min} \approx 0.45$. As the dataset is covering a period of about 13 years, the incident Sun angle was varying. Therefore, based the time periods where eclipses were possible and the available data, the dataset was divided in four angle groups depending the angle of the Sun: smaller than 75°, between 75° and 80°, between 80° and 84°, and over 84°.

Rings fine structures

It has been observed, in various wavelength (e.g. Dunn et al. [2004], Nicholson et al. [2005]), that in A and B rings there are bar-like structured, with spaces in-between. This is a result of the self gravity of the ring particles, where azimuthal density wakes are being

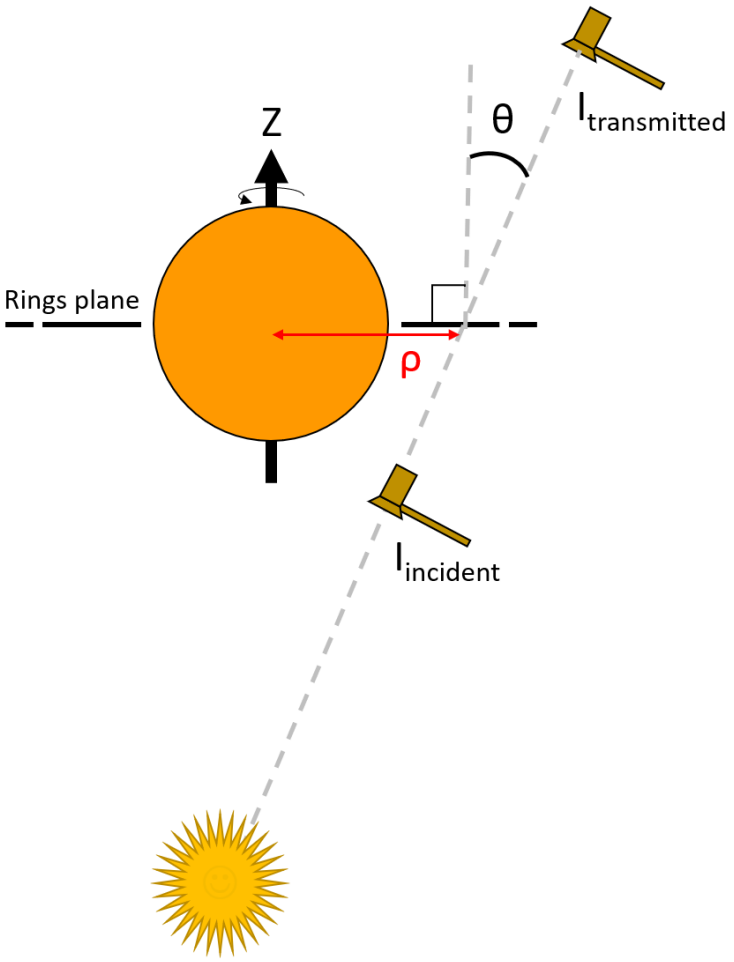

Figure 4.17: A graphic representation of the transmitted and incident currents, and the normalization angle.

created (e.g. Colombo et al. [1976], Cuzzi et al. [2002], Salo et al. [2004], Colwell et al. [2006]), grouping ring particles into these structures. These structures can be seen in fig. 4.1, intensified in the B ring. A close-up view of the B ring outer edge is presented in fig. 4.18, where self-gravity wakes clearly are visible in both the B ring (left half, lighter grey colours) and the Cassini Division (right half, darker grey colours). The image maps an approximate square area, about $\sim$ 1500km edge long, which shows that the width of the wakes can be as narrow as $\sim$ 1km.

As the self-gravity waves result from matter that has 'clumped' together, the sunlight cannot pass through them. The sunlight though passes through the gaps in-between the wakes. Therefore, if we want to calculate the optical depth of an area with self-gravity wakes we need to take into consideration the geometry of the wakes, and essentially average

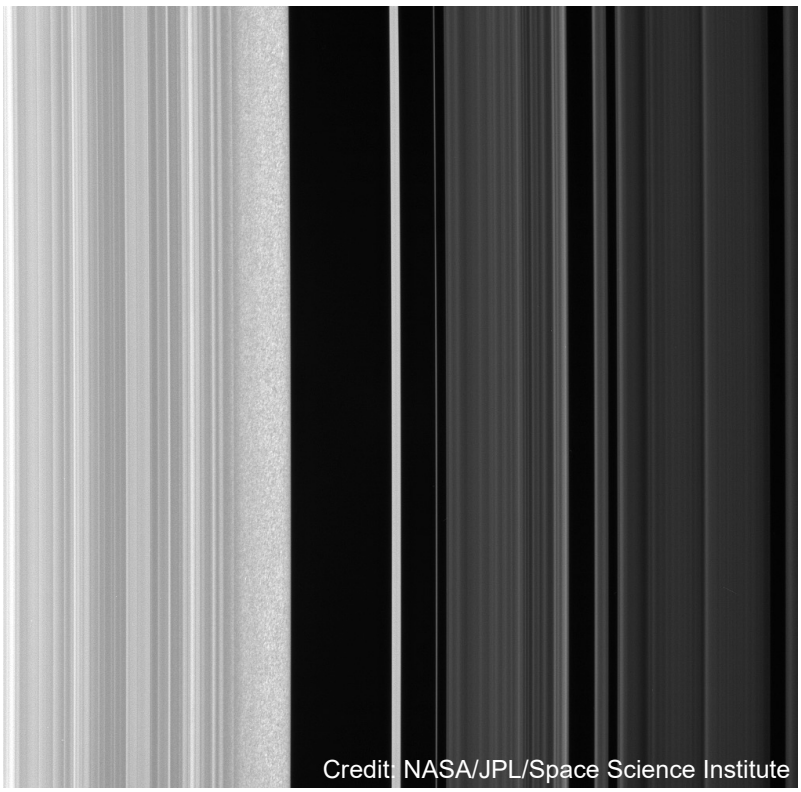

Figure 4.18: The B ring edge (left half) and the Cassini Division (right half). Many ringlets and wakes are visible, some of which are a result self-gravity of the rings matter. Image credit: NASA et al. [2008]

the calculated optical depth over the entire area, in order to include the wakes structures.

There are two main models calculating the optical depth of rings with self-gravity wakes, presented in fig. 4.19. Each model is using data of a different instrument and assumes a different wake geometry. The *Pasta model* [Hedman et al., 2007] describes the wakes as infinitely long opaque tubes with ellipsoidal cross-section, and was developed using data from the Cassini's VIMS, and (as Jerousek et al. [2016] said 'in keeping the culinary naming theme') the *Granola Bar* model [Colwell et al., 2006] describes the wakes as infinitely long rectangular slabs, and was developed using data from Cassini's UVIS.

The opaque wakes totally block any incident sunlight, hence the transmitted sunlight that is observed is essentially whatever amount of sunlight passed through the gaps in-between the wakes. A straight-up measurement of the optical depth will give the optical

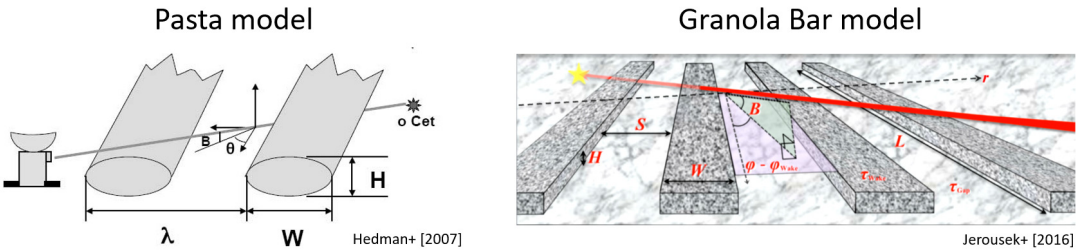

Figure 4.19: The two models for the geometry of the self-gravity wakes in A and B rings. *Left*: the "Pasta model", as described in Hedman et al. [2007], where also this figure is taken from. *Right*: the "Granola Bar" model, as described in Colwell et al. [2006] - the figure is taken from Jerousek et al. [2016]. The main difference between the two models is the shape of the wakes.

depth of the gaps in-between the structures, τ_G, but it is essential to include any effects from the geometry of the wakes; if the effects are not included, given that the space between the wakes is mostly depleted of any particles, a much lower optical depth would be calculated.

Both models are parametrizing similar physical properties of the wakes. The Pasta model is parametrised in terms of the width (W) and height (H) of each structure, and the separation (G) between the structures. The separation and width are summed to give the characteristic wavelength ($\lambda = G + W$) of the structure and gap. The model also uses the ratios G/λ and H/λ ratios [Nicholson and Hedman, 2010]. The Granola Bar model is parametrised in terms of the ratios of the height (H) and separation (S) of the wakes with respect to their width (W), H/W and S/W [Colwell et al., 2006, 2007].

Both models also use two the ring plane azimuth angle, ϕ, and the wake angle, ϕ_w, presented in schematically in fig. 4.20. The ring plane azimuth angle, ϕ, measured from the outward radial direction from Saturn to the ring plane projection of the line-of-sight from Cassini to the star, which is the Sun in our case. The wake angle, ϕ_w, measured counter-clockwise from the radial direction outward from Saturn, towards the trailing orbital direction [Jerousek et al., 2016]. The values of ϕ_w differ not only between the two rings, but also on the method of observation. For the B ring Colwell et al. [2007] calculated

a range of 69 deg −70 deg. For the A ring Salo et al. [2004] calculated an angle of ∼ 69 deg using numerical simulations, Hedman et al. [2007] calculated an angle of 63 deg −73 deg using VIMS observations, Colwell et al. [2006] calculated an angle of 45 deg −80 deg using UVIS observations, while Ferrari et al. [2009] calculated an angle of ∼ 70 deg and Nicholson et al. [2005] calculated an angle of ∼ 67 deg, both using radar observations. For this work $\phi_w = 70$ deg was used, as it was the same average value used in Jerousek et al. [2016].

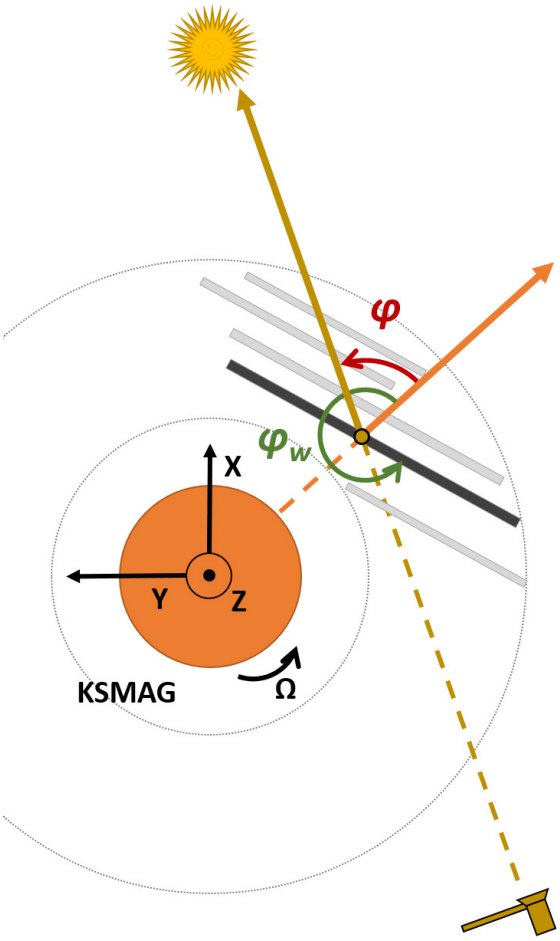

Figure 4.20: A graphic representation of the ϕ and ϕ_{wake} angles. The two grey circles show the extend of the rings plane, and the parallel rectangles show the wakes. This figure is not an accurate representation of the Kronian rings system (as wakes exist only in A and B rings, and they are not as big as they are presented), but it helps the reader understand the definition of the two angles.

The returned values of the optical depth calculated by the two models are difficult to compare directly for two reasons: there are differences in the assumed geometry of the wakes, and UVIS and VIMS are operating in different wavelengths. Jerousek et al. [2016] combined observations from UVIS and VIMS, and using a modified self-gravity wake model they found that the structure of the wakes are different in the two rings. The A ring has

wakes that are clearly separated with relatively empty gaps between them with an optical depth of ~ 0.1, while the B ring the gaps are not that well-defined, with higher optical depth. They also found that the angle θ plays bigger role on calculating the optical depth than the observing wavelength. In the limit where the angle $\theta \approx 90\,\text{deg}$, i.e. the source and the observer are almost parallel to the rings plane, the two models diverge to the same result: the rings transparency is calculated to be around zero, which is expected, as in this geometry no sunlight can penetrate through the rings disk.

In this study for the A and B rings the Granola bar model [Colwell et al., 2007] was used, as it was developed using observations of similar wavelengths to this study (in the EUV region). The parameters used were from Jerousek et al. [2016], as they took into consideration the observations from both UVIS and VIMS. For the C and D rings, as there are no self-gravity waves in those rings, we simply corrected the light path using ξ. Equation eq. 4.10 presents the optical depth calculations required for each ring.

$$\tau_n = \begin{cases} \tau_G - \ln\left(\frac{S/W - H/W|\sin(\phi-\phi_W)|\cot(90-\theta)}{S/W+1}\right)\xi & \text{A, B rings} \\ \tau_G \xi & \text{C, D rings} \end{cases} \tag{4.10}$$

The values of S/W and H/W were calculated from Jerousek et al. [2016]. For the A ring a linear fit was fitted on their model values over the radial distance (see their fig. 7), ρ, getting the equations $S/W = 0.751\rho - 1.421$ and $H/W = 8.035\rho - 15.703$ for the two ratios. For the B ring we took the average of each region (see their fig. 8); the values are presented in 4.4

Region	S/W	H/W
B1	1.125	0.1
B2	0.188	0.038
B3	0.094	0
B4	0.125	0.019
B5	1.125	0.15

Table 4.4: Average values of the S/W and H/W ratios for each region of the B ring based on visual averages of the data in fig. 8 of Jerousek et al. [2016].

I, of course acknowledge that this is not the most accurate method in obtaining and calculating the values of the two parameters. To evaluate the impact of the method I used on the calculations accuracy I calculated the optical depth for the B1 region, where the two ratios varied the most, using two extreme values: 0.5 and 1.5. The optical depth between them changes about 10%, which is well within the statistical variation of our data as we will show later (4.23). Therefore for the purposes of this study the approach is adequate.

4.6.5. Calculation of rings' optical depth

To apply eq. 4.10 we need measurements of the photoemission current. The LP measures the current as a function of the applied bias voltage, so a selection of an appropriate voltage is required. The current should be measured in negative bias, sufficiently far from the floating potential, and also avoiding known instrumental interference (see section 4.6.3). We chose to take an average from from $U_{bias} = -8$V to $U_{bias} = -14$V, centred on $U_{bias} = -11$V. In order to overlook any extreme values caused by random noise or interference from other instruments the median was used rather than the average. Also the data were limited to periods where Cassini was only in the rings's shadow, but not in both the rings and Saturn's shadow.

Moreover, I calculated the spatial resolution and error introduced by the movement of Cassini. During a sweep the LP needs 46ms to measure the current between -14V and -8V and Cassini moved a maximum of around 950m in this duration. This is the theoretical maximum limit for any detectable structures on the rings, i.e. any structures smaller than 950m cannot be resolved no matter how many data points we have. In practice though we need to take into consideration the sampling rate of the LP and the sample size of our data. As mentioned in section 2.2.1 the LP has two operation modes, sampling every 10min or 10s, and during those times Cassini moves about 13000km or 210km respectively. But, as there are data from multiple orbits, the data fill the gaps between the distances, and as we will show later (e.g. 4.23) the average radial resolution of our study is around 1000km. This of course depends on the number of data points for each radial distance from Saturn, e.g. some areas in B1 region have more datapoints than

in B3. For comparison, the archived data for UVIS are binned in 1km and 10km - and Colwell et al. [2007] used a spatial resolution of $\sim$ 10m - and VIMS spatial resolution was $\sim$ 200m to $\sim$ 3km.

Fig. 4.21 shows the transmitted current, i.e. the current that passed through the rings, over the distance where the Cassini - Sun vector intersects Saturn's equatorial level. In total we had 1331 datapoints, presented in the top panel; the lines show continuous sets of measurements, while the points show point measurements. For the statistical analysis the data were binned over the distance, which were generated by recursively subdividing the spatial range into smaller and smaller bins until the data were distributed in bins with minimum of 20 datapoints per bin. This is presented in the bottom panel. This technique gives the best spatial resolution whilst maintaining a statistically meaningful number of data points in a bin. The bins could have been subdivided to a smaller number of datapoints, e.g. 10 or 15 per bin, which would provide a higher resolution and allowed to see more structure, e.g. to partially resolve the Colombo gap, but it would also introduced a higher uncertainty due to smaller sample sizes in each bin.

Similar to what was deduced from fig. 4.15, fig. 4.21 shows that the measured current is different over each ring. Over A and B rings the current is almost at the noise level ($\pm 100n$A, which is ± 1 on the scale of fig. 4.21), over the D ring it is at the background (i.e. outside of any ring's shadow) level, and over the C ring is in an intermediate state between A/B rings and the C ring. As previously discussed when I_- is close to the noise level denotes that the photoemission is negligible, so we can conclude that A and B rings are the most optically thick (B being the most optically thick since the current is the closest to the noise level), D ring is the least optically thick, and C ring is intermediate between these extrema. The largest of the ring gaps, Maxwell and Encke, are clearly identifiable as inflections in the measured current at those locations. There are hints of the Colombo gap in the raw data, but it is being smoothed out during the binning. For similar reasons we cannot extract any useful conclusions for the F ring.

In order to estimate the incident sunlight (numerator in eq. 4.9) we calculated the extension of the Sun - Cassini vector while Cassini was between Saturn and the Sun (see fig. 4.17). In total our sample was 2562 datapoints, shown in fig. 4.22; we followed a similar

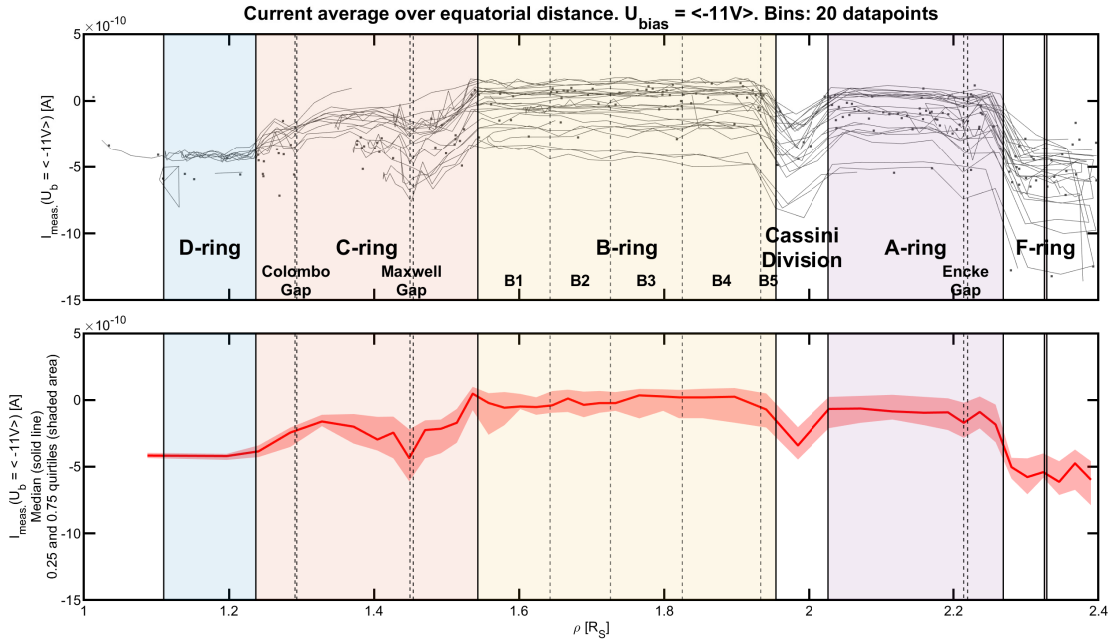

Figure 4.21: The measured current around$U_{bias} = -11$V over the Kronian equatorial distance. *Top*: raw data (the lines show continuous sets of measurements, while the points show point measurements). *Bottom*: median (solid line) and the 0.25 and 0.75 quartiles (shaded area). The vertically coloured areas show each ring and the dashed line show some features of the rings: the gaps, or the regions of the B ring

process as in fig. 4.21. On the top panel one can distinguish two groups of measurements: one closer to 0μA, and one closer to -0.5μA. The near-zero measurements are from Cassini's Rev. 249 (day 320/2016 to day 328/2016) and 253–259 (day 350/2016 to day 34/2017). While the origin for these anomalously low currents is not clear, potential reasons could be the change of the instrument's operation in August 2008, or Cassini being in larger L-shells, where the ion current is negligible and the I_- is just photoemission.

The current in fig. 4.22 seems to be almost constant over the radial distance, with a mean value of $\overline{I_{inc.}} = -0.04471\mu$A and a standard deviation of $\sigma_{I_{inc.}} = 0.0022\mu$A. The current uncertainty can be described with the standard error, $\alpha_{I_{inc.}} = 0.00025\mu$A. Hence the current from the incident light is $I_{inc.} = -0.0447 \pm 0.0003\mu$A. The analysis will not be affected from the differentiation between the two groups of the incident current (one close

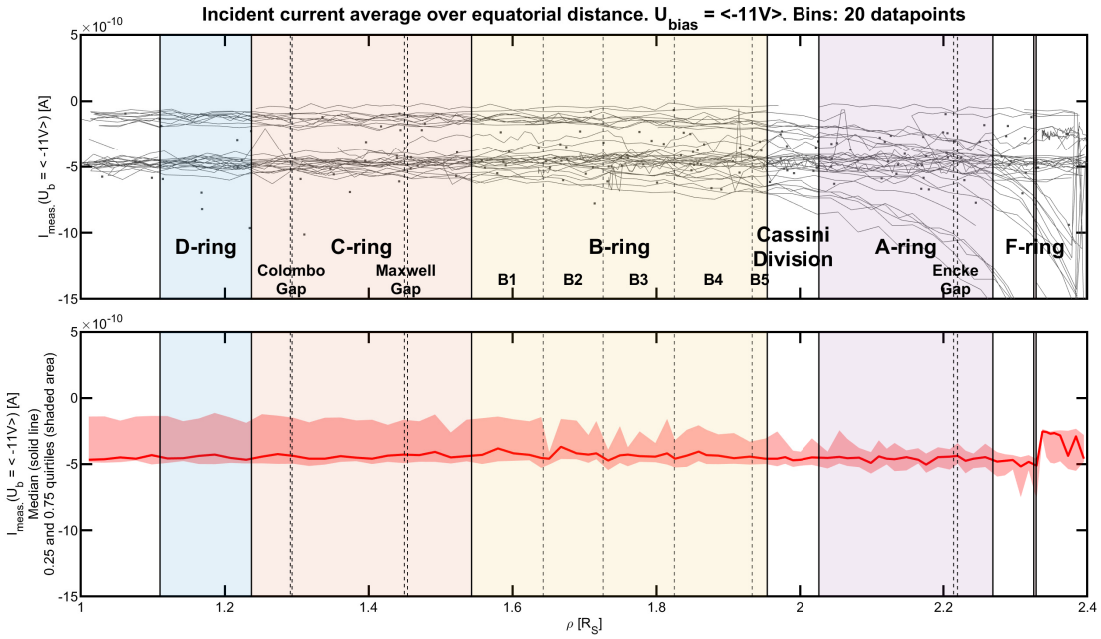

Figure 4.22: The incident current. The fig. format is the same as fig. 4.21

to 0μA and one close to -0.05μA) as the standard error narrowed down the uncertainty, despite the seemingly big difference between the 0.25 and 0.75 quartiles.

Using eq. 4.10 the optical depth can be calculated by taking the natural logarithm of the incident to transmitted current ratio, plus the extra factor for the A and B rings. But here rises a problem: while the incident current is negative, some of the transmitted current is positive, making the ratio negative, whose natural logarithm cannot be defined. This positive transmission is within the random electronic (Johnson-Nyquist) noise value, which is also the main reason for the current being positive and not zero. Also other possible reasons can be interference by other instruments and the change of the spacecraft charge. This issue is addressed by removing those measurements. Also, a maximum optical depth can be calculated, following a method similar to Colwell et al. [2010], where they defined a maximum optical depth, τ_{max}, based on the minimum number of counts they could measure. For this work the minimum current corresponds to the noise level of 100pA, so the minimum measurable current is the standard error of the measurements for the incident current. Hence the maximum optical depth that can be calculated with the LP

data is

$$\tau_{max} = \ln \frac{|I_{inc.}|}{\alpha_{I_{inc.}}} \approx 5.17 \tag{4.11}$$

The normal optical depth of the rings can be calculated using eq. 4.10 that takes into consideration all the factors affecting the optical depth (the angle of the Sun and the properties of the self-gravity wakes in A and B rings), and it is presented on fig. 4.23. Similarly to fig. 4.21 and fig. 4.22 the top panel shows the individual datapoints, and the bottom the median with the 0.25/0.75 quartiles. The statistical maximum depth (eq. 4.11) is also shown as the dashed horizontal lines for each ring/region. The four angle groups are presented colour-coded: data in angles smaller than 75° are in blue dots, between 75° and 80° are in orange crosses, between 80° and 84° are in green triangles, and angles over 84° are in purple x's. The theoretical maximum optical depth for each angle group follows the respective colour.

The normal optical depth of the D ring is very close to 0, for the C ring it is around 0.1, for the B ring it is the highest of all with its median varying from over one to almost two, and lastly for the it is A ring from under two on the inner edge to around one on the outer edge. The Maxwell Gap is visible in our measurements, but it look like the optical depth is at the limit of what can be seen as the optical depth falls close to 0, i.e. there is not that much absorbent matter in the area; the Colombo Gap was not visible. The Encke Gap though is not as clear as in fig. 4.21 but this most probably is a result of: (1) the binning, where even though the data were binned in 10-datapoints bins to maximize the resolution without losing information, it seems that the bin was simply too big and it just smoothed out the gap, and (2) the correction factor that the Granola Bar model introduced for the A and B rings (eq. 4.10), where, while there are no wake structures in the gaps, the factor was still applied giving a much higher optical depth than what really is. Also, the couple of data points that seemingly are over the τ_{max} are safely assumed to be not real: this can happen when the current is positive, but smaller than the statistical error of the measurements used for eq. 4.11.

As discussed in section 4.6.2 the LP is sensitive in the EUV wavelengths: mainly the Lyman-α line, with some contributions from shorter wavelengths. The High Speed Photometer (HSP) in UVIS has a range from $\sim$ 115nm to $\sim$ 190nm (mentioned in section

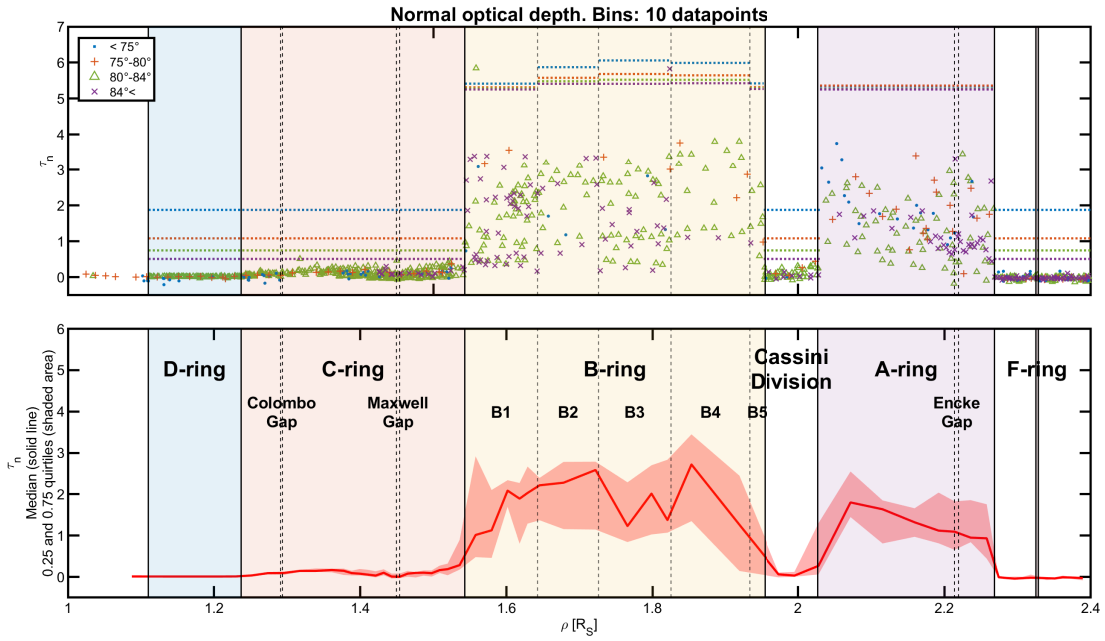

.

Figure 4.23: Normal optical depth for our dataset. *Top*: raw data, divided into 4 angle groups, colour-coded, based on the legend on the top left. The symbols show the datapoints where the logarithm was positive, while the dashed line shows the maximum optical depth, τ_{max}, for each group. *Bottom*: the median of the positive datapoints (red line) with the corresponding 0.25 and 0.75 quartiles (shaded area) – same format to bottom of fig. 4.21

4.6.1). Fig. 4.24 shows the range of the instruments close to the EUV. The LP range is marked in different shades of blue according to the contribution of each region: the highest contributor, Lyman-α, is in dark blue, the Lyman series is in lighter blue, and the Lyman continuum is in light blue. UVIS spectral range is in green, and the Voyager 2 PPS frequency at 264nm is in dark red. On the top of the plot each wavelength region is marked: EUV, Far UV (F-UV), and Middle UV (M-UV). Even if the LP wavelength range overlaps only partially with UVIS range, the results of this study can still be compared to those of Colwell et al. [2006, 2007, 2010]; this is shown in table 4.5. The optical depth this study calculated for the D ring is very close to zero and for the C ring it was ~ 0.1; they both agree with the mentioned previous studies. For the B1 region this study showed an

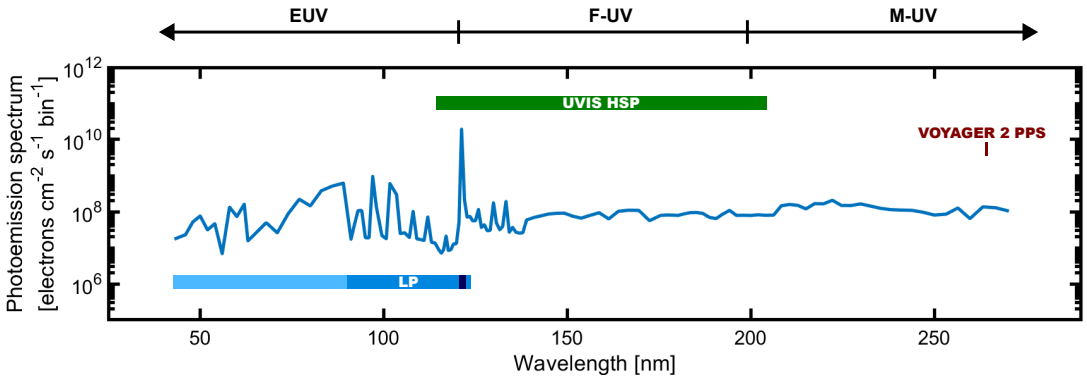

.

Figure 4.24: Photoemission spectrum of the LP from fig. 4.14, showing the wavelength ranges of the LP, UVIS, and Voyager 2 PPS. Each colour of the LP range correspond to different emission frequencies, as described in section 4.6.2: the dark blue is the Lyman-α, the lighter blue is where the rest of the Lyman series emit, and the lightest (sky) blue is the Lyman continuum. There is some overlaps between the LP and UVIS wavelengths, which allow for some comparison of the results of the two instruments.

increased optical depth to ~ 2, which agrees to ~ 1 to ~ 2 of the previous studies, for B2 this study found ~ 2 which also agrees with the previous studies, and for B3 it was ~ 1.5 which again agrees with what the previous studies calculated. For B4 this study found a drop from ~ 2 to ~ 1 as the distance increases, which does marginally agree with the optical depth of greater or equal to 2 reported by previous studies; the small number of datapoints in this region though does allow to extract a safe result. The same applies for B5, where the calculated optical depth of ~ 1.75 came from only a handful of datapoints, while previous studies had a significantly greater optical depth of over two, or even around three, but with a much larger sample. For the Cassini Division this study calculated an optical depth of ~ 0.1 that increases to ~ 0.5 as approaching the A ring, agreeing with previous studies that found the same 'pattern'. Lastly, for the A ring the values from this work were a bit higher than past studies: ~ 1 compared to ~ 0.5. Overall though the results are in good agreement, which was somewhat expected, as both instruments operate in the same wavelength range and the same way, i.e. by observing the variations

of light (in the LP case the Sun, in UVIS case a star) when it goes through the material of the rings. This is also an exciting result, as it not only validates the methodology and approach to the optical depth calculation, but also demonstrates a unique way of using the LP, which is essentially a plasma instrument.

Ring / Region	This study	Previous studies [Colwell et al., 2006, 2007, 2010]
D	~ 0	~ 0
C	~ 0.1	~ 0.1
B1	~ 2	~ 1 to ~ 2
B2	~ 2	$\gtrsim 2$
B3	~ 1.5	~ 1.5
B4	~ 1 to ~ 2	≥ 2
B5	~ 1.75	~ 1 to ~ 3
Cassini Division	~ 0.1 to ~ 0.5	~ 0.1 to ~ 0.4
A	~ 1	~ 0.5

Table 4.5: Comparison of the normal optical depth of this study with previous studies of Colwell et al. [2006, 2007, 2010]. The only regions that do not agree are B4 and B5, but this could be due to the limited datapoints of this study.

It is estimated that the main reasons for the discrepancies are:

1. The limited dataset of this study compared to the previous studies. Only 2200 datapoints were used here compared to tens of thousands of Colwell et al. [2010] for example. This did not give a high-enough resolution radially compared to the rest of the studies

2. High energy electrons that impact the LP will generate secondary electrons that are not accounted for in this study. The measurements are mostly inside the reported mean $L = 6.2$ boundary for energetic electrons [Thomsen et al., 2016], so it is estimated that their impact will be minimal. But this may affect some measurements, hence should be investigated in future studies.

3. The rings are mainly made of ice, a highly reflective material, but also have fine structures, e.g. the self-gravitational wakes for the A and B rings. Sunlight can be reflected and/or diffracted, reaching Cassini from areas that are not on Cassini's line of sight with the Sun (example of fig. 4.25), generating extra photoelectrons. Also, while in this analysis the self-gravitational wakes for the A and B rings were taken into consideration, Colwell et al. [2021] reported non-axisymmetric narrow features, named *phantoms*, in the regions B2 and B3, with a size of less than 100m. Even if these phantoms width is much smaller than the theoretical minimum location error of around one kilometre for the LP, they could potentially affect the results as the light will behave the same way it does with the self-gravitational wakes. This feature could potentially help in defining the optical depth of the B3 region – a region that many studies struggle with due to the lack of data.

4. Saturn's Planetary Period Oscillations (PPOs). It was found that the PPOs affect the Kronian system (e.g. on the ionospheric diffusive layer modulation [Provan et al., 2021]), at the Saturn Kilometric Radiation low-frequency extension events (e.g. Bradley et al. [2020]), hence it worth studying any possible connection of the fluctuation of the magnetospheric plasma density or appearance / disappearance of the electron populations with the PPOs. In addition, works that argue for an electron density asymmetry (e.g. Gurnett et al. [2007]) need to be taken into consideration.

4.7. Discussion on photoelectrons and LP data analysis in eclipses

The methodology of Fahleson [1967] for calculating the ion parameters uses a slightly negative spacecraft potential, but during eclipses the spacecraft potential is expected to become very negative, hence the LP data during the eclipses might need to be recalibrated. This does not mean that all the previous studies that used LP data need to be revised: the LP database has almost 77,000 datapoints for the entire mission, out of which Cassini was in the shadow of Saturn or its rings in only 4215 of them (2263 for the rings and 1952 for Saturn) – that's about 0.5% of the entire database. Moreover, it is not known how negative the spacecraft potential becomes during the eclipses, making it hard to take that factor into consideration for our analysis.

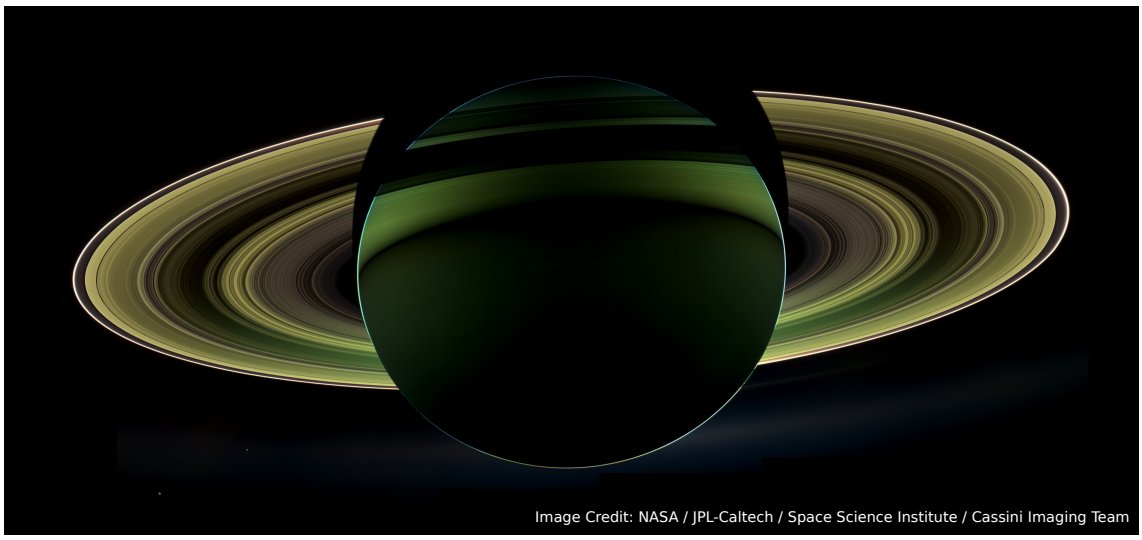

.

Figure 4.25: A beautiful view of a solar eclipse from Saturn taken by the Imaging Science Subsystem. The image is a combination of images in the infrared, red, and violet spectral filters. Even if Cassini is in the night side, the shadow of the rings is still visible on the planet. As the rings are highly reflective, the y reflect the sunlight even in the shadow of the planet. In our work, we treat the rings as solid, non-reflecting bodies, ignoring any reflected sunlight. Image credit: NASA/JPL-Caltech/Space Science Institute [2012]

Even though the photoemission current stops when Cassini enters into an eclipse, and begins when it exits from an eclipse, no consistent change on the number of electron populations was observed. While there were some occasions that a population appears or disappears close to when Cassini enters/exits a Saturn eclipse or an eclipse by the optically thick rings, in the vast majority of the Saturn's shadow crossings or crossings between the rings there was no change in the population number. This could possibly denote that the photoelectrons are not tied to a specific population. It must be mentioned that the cold electron number density changes spatially around Saturn, as shown in Persoon et al. [2020], which could affect the change of the populations number

As Cassini's design gave the LP the unfortunate position of being directly opposite the radiators for VIMS and Composite Infrared Spectrometer (CIRS) [Matson et al., 2002],

and the radiators needed to be shielded from the sunlight meant that the LP would have been constantly in the sunlight. This meant that it is impossible to study any variations on the LP measurements while the instrument is in the spacecraft's shadow, i.e. only the LP is in the shadow while Cassini is in sunlight. There were only 10 occasions where the LP was in Cassini's shadow and almost none of them had useable data. There are also many instances that the LP operation was switched from high-resolution mode to a low-resolution mode for the duration of the eclipse for the necessities of other instruments. This resulted to a series of eclipses to be practically unusable for this study, as there was not a clear passing from the light to the darkness and vice-versa.

4.8. Future work

There is some interesting work that can be done on the project where I compared the ELS and LP data during the eclipses. As the main target of the project is to study any photoelectron variations as a result of Cassini going into Saturn's shadow, comparing the electron density variation of both instruments could reveal if any part of the measured density corresponds to photoelectrons. As ELS covers a much wider energy range than the LP (around $0.6 - 28$eV and around $0 - 10$eV respectively) in order to have similar datasets we can calculate the ELS electron density for energies up to ~ 10eV. Also, as we used only 3 cases, a beneficial step would be to use the data from the entire available dataset: there are 54 eclipses in the entire duration that CAPS was operating (from the beginning of the mission to June 2011, and from March to May 2012), so there are many eclipses that both instruments are operating and have good, useable data.

Furthermore, using ELS data to study the spacecraft potential changes during eclipses will help us having a better understanding on the spacecraft charging, and the role of photoelectrons. As seen in section 2.2.5 the LP floating potential is connected to the spacecraft potential, which is connected to the photoemission; hence knowing how the latter varies could ultimately help with defining in higher accuracy the floating potential.

Regarding the calculation of the main rings optical depth, a future aspect that would be beneficial to the project is to study the impact of the high-energy electrons: as they can overcome the negative potential of the LP and their impact on the probe can create

secondary electrons, which will be (wrongly) counted as magnetospheric plasma electrons.

I consider the rings and the planet non-reflective objects, but that might not be the case, as there might be diffraction or reflection effects. If such effects exist it means that sunlight can reach the probe while it is expected not to. E.g. in my analysis for the A and B rings I assume that the incident sunlight towards the gaps was transmitted through them and measured, but the incident sunlight towards the self-gravity waves was absorbed/lost by them. If there are any diffraction effects due to the light passing through an opening, or reflection effects due to the highly reflective ice (after all the rings are visible from the Earth), they could redirect light to regions where Cassini is in the 'shadow' of the wake. This will result to the light reaching the LP measuring while expecting no light to pass passing through the rings, therefore giving a lower optical depth in some regions. Models of refraction and reflection can be made to further study any possible impact of those effects on the measurements.

A study of the Cassini parameters and conditions (location, plasma density, etc.) when the negative-bias current, I_{-}, surpasses zero during eclipses would provide a deeper understanding of the instrument operation. It was also mentioned that the PPOs affect the Kronian system, hence a possible connection of PPOs with either the plasma density fluctuations or the appearance/disappearance of electron populations could be studied.

As there are orbits with discrepancies between each other, a study using data from other Cassini instruments that have the capability to measure the cold electron plasma, CAPS or the f_{UHR} from RPWS, could be beneficial to determine the nature and source those discrepancies. This can be combined with the data combination of the first project mentioned in this chapter.

Lastly, it also worth investigating the idea of a 'relaxation time' of the photoelectron cloud, readjusting to any changes in the spacecraft charge. If the relaxation time is not short enough, for the cloud to adjust to the new conditions before new measurement is taken, it can affect the future measurements, e.g. if Cassini goes into Saturn's shadow the first measurements in the shadow will have have 'leftover' photoelectrons, therefore they will not be respond to the new conditions. In such case Cassini's spatial resolution might need to be reconsidered, and adjusted to the relaxation time: in section 4.6.5 it was

mentioned that the resolution of the optical depth is $\sim$ 1000km, but if the photoelectron cloud adjusts in a time that Cassini travelled more than $\sim$ 1000km the resolution should follow the relaxation time and have the measurements properly grouped.

5. Fields of view and spacecraft-vector intersections

> **"Mere data makes a man. A and C and T and G. The alphabet of you. All from four symbols. I am only two: 1 and 0."**
>
> — Niander Wallace, *Blade Runner 2049*. (Based on Philip K. Dick novel *Do Androids Dream of Electric Sheep?*)

5.1. Introduction to the problem

Measurements with instruments onboard a spacecraft are often affected by the presence of the spacecraft platform and other components attached to the spacecraft bus, such as antennas, booms, thrusters, solar panels, radiators and also other instruments. This applies to scientific instruments and any instruments that are used for operations, such as star trackers or other cameras. These effects include occluding the fields-of-view (FOV) of instruments (e.g. Szita et al. [2001], Young et al. [2004]), partly shielding instruments from cosmic rays and other radiation sources (e.g. Arridge et al. [2009]), and shadowing that can lead to differential spacecraft charging (e.g. Whipple [1981]) . Some of these effects depend on the orientation of the spacecraft. For example, the platform may shadow an instrument from sunlight or from an ambient plasma flow, thus placing the instrument into a plasma wake (e.g. Samir et al. [1980], Hastings [1995]). Such shadowing may be dynamic in short spacecraft-time-scales, such as a spacecraft rotation for a spin-stabilisation or an altitude change on a three-axis stabilised spacecraft for placing some target in an instrument's FOV. Those situations may affect the measurements, often negatively, and need to be identified and accounted for in the data. Here, a simple and fast method is presented to calculate any kind of shadowing, as well as define a FOV for an instrument onboard a spacecraft, using a triangulated mesh (e.g., Hughes et al. [2013]) 3D model. The models are freely available, and they are typically composed during the spacecraft design and assembly stage, usually prior to the launch, making the presented method robust and accessible to everyone.

Mathematically, the problem of calculating a FOV, or a spacecraft wake or shadow can be approached with ray tracing, modelling light transport in the spacecraft frame-

of-reference. The basics of this modelling works by checking whether the ray of light originating from a point intersects with a surface on the spacecraft (bus, booms, antennas, instruments etc.). For a simple case of an intersection between a spherical surface and a ray, the problem is easily reduced to an intersection between the ray and a cross-section of a sphere containing the ray. However, spacecrafts are rarely spherical. Because of the complex geometry of a typical spacecraft and the need for precision, CAD models often use Constructive Solid Geometry (CSG) involving applying Boolean operations to simple solid objects to produce more complicated shapes. By utilizing the capabilities of modern computers, CSG models can be converted into mesh-based models that can have a higher precision.

In this section I will present the work I have done on (1) calculating an instrument's field-of-view (FOV) that has already been installed on a spacecraft, and (2) searching for any intersections of a vector with the spacecraft. This section has been published in the RAS Techniques and Instruments [Xystouris et al., 2024]. My contribution to this project was providing the script for the splitting of the faces in section 5.3.2, conducting the entire work in section 5.4.2, and providing the vectors in section 5.4.3.

5.2. Method

Fig. 5.1 shows the mesh of a sphere. The top panel shows the sphere as drawn in the 3D modelling software Blender, while the bottom panel shows the mesh for this sphere, i.e. a 'web' of polygons - in this case triangles. The higher the number of polygons used in the mesh, the more detailed the shape will be, as seen in the figure, where the resolution increases from left to right.

Since 3D meshes are commonly built out of triangles, the method reduces to finding intersections of a given ray with each triangle. There are several alternative ways of mathematically approaching this; the chosen approach for this work is a simple "all on same-side" technique, described below for reader's convenience.

Let a ray originating from a point with position vector $\boldsymbol{O}$, and propagating in the direction vector $\boldsymbol{D}$. The coordinate vector of an arbitrary point $\boldsymbol{P}$ on the path of the ray

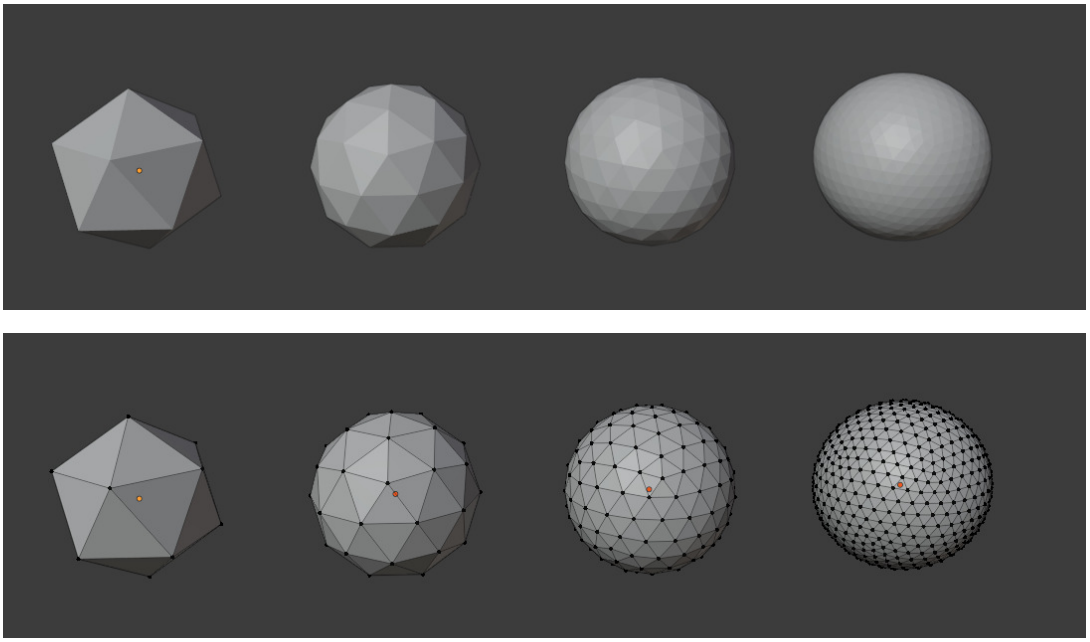

Figure 5.1: Example of mesh of a sphere. *Top*: the sphere, drawn in the 3D modelling software Blender. *Bottom*: the mesh of each sphere. The higher number of polygons used, the more detailed the model.

is

$$\boldsymbol{P} = \boldsymbol{O} + t\boldsymbol{D} \tag{5.1}$$

where t is a scalar distance along $\boldsymbol{D}$ measured from $\boldsymbol{O}$.

Any plane can be described by a vector $\boldsymbol{N}$ normal to the plane, and a point $\boldsymbol{Q}$ on the plane. The plane equation relates to these quantities to some other arbitrary point in the plane $\boldsymbol{R}$

$$(\boldsymbol{R} - \boldsymbol{Q}) \cdot N = \boldsymbol{R} \cdot \boldsymbol{N} - \boldsymbol{Q} \cdot \boldsymbol{N} = 0 \tag{5.2}$$

where $\boldsymbol{N}$ is the (unit) normal of the plane and $\boldsymbol{Q} \cdot \boldsymbol{N} = d$ is the shortest distance from the origin to a point on the plane, and is constant for all points on the plane. Setting $\boldsymbol{P} = \boldsymbol{R}$ and combining the two equations we get

$$t = \frac{d - \boldsymbol{N} \cdot \boldsymbol{O}}{\boldsymbol{N} \cdot \boldsymbol{D}} \tag{5.3}$$

Since t defines the distance along the ray, only the points with $t > 0$ are towards the plane from $\boldsymbol{O}$. In case of a ray being parallel to the plane then there will be no intersection, hence $\boldsymbol{N} \cdot \boldsymbol{D} = 0$, and t has no solution (e.g. [Marsden and Tromba, 2011]).

Let a triangle lying on the plane, with vertices $\boldsymbol{V_1}$, $\boldsymbol{V_2}$ and $\boldsymbol{V_3}$. The intersection point, $\boldsymbol{P}$, on the plane of the triangle can be on either side of each of its edges. If it is on the same side of all three edge then it is inside the triangle and the ray intersects it. In order to formulate this, each edge of the triangle is treated as a vector, going from one vertex to another: $(\boldsymbol{V_j} - \boldsymbol{V_i})$. Then the cross product of the edge with the vertex-point vector is calculated: $(\boldsymbol{V_j} - \boldsymbol{V_i}) \times (\boldsymbol{P} - \boldsymbol{V_i})$. The triangle vectors must be in a continuous closed loop, $\boldsymbol{V_1V_2} \rightarrow \boldsymbol{V_2V_3} \rightarrow \boldsymbol{V_3V_1}$ for the sign of the cross products $(\boldsymbol{V_j} - \boldsymbol{V_i}) \times (\boldsymbol{V_k} - \boldsymbol{V_i})$ and $(\boldsymbol{V_j} - \boldsymbol{V_i}) \times (\boldsymbol{P} - \boldsymbol{V_i})$ to be consistent. Therefore, if the sign of the cross products is the same for all three tests for each edge the intersection point $\boldsymbol{P}$ is inside the triangle, while if even one of the signs is different the intersection point is outside the triangle. This is presented schematically in fig. 5.2, and it is effectively the *winding number algorithm* (e.g. Hormann and Agathos [2001]).

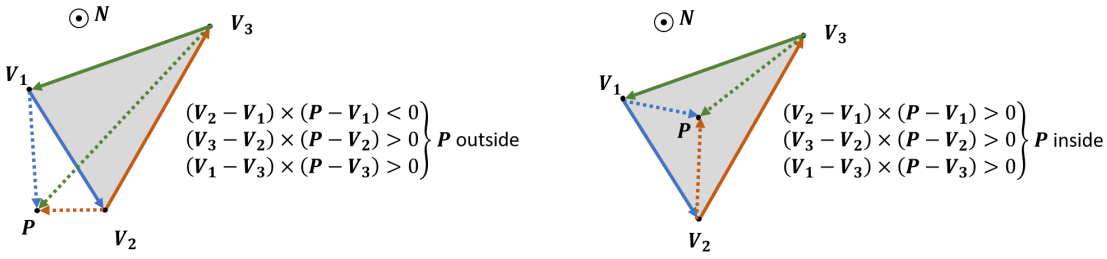

Figure 5.2: Sketch of winding number algorithm. *Left*: a point outside a triangle. *Right*: a point inside a triangle. The cross product $(\boldsymbol{V_j} - \boldsymbol{V_i}) \times (\boldsymbol{P} - \boldsymbol{V_i})$ changes sign depending on whether the point is outside or inside the triangle.

While the described method works perfectly, the iteration for checking every face individually for an intersection is $\mathcal{O}(3m)$ where m is the number of triangles in the model. A faster method is merging the projections of the model faces and treating them as a single shape. This is very useful for conducting the check through a big dataset, as only the contour of the spacecraft needs to be calculated, and thus the algorithm becomes $\mathcal{O}(3n)$

where n is the number of points in the projected single shape and generally $n \ll 3m$. The method is described in detail in the following section.

5.3. MATLAB implementation

5.3.1. Simplest model formats: STL & OBJ

Firstly, the method requires a set of triangular faces representing the model spacecraft which are available from most 3D model file formats. For example stereolithography (STL, .stl extension) or wavefront OBJ (.obj extension) files are suitable, which are also commonly used for 3D printing and computer graphics. Those files can be loaded into MATLAB as faces and vertices of the model; an STL file can be loaded into using the routine by Johnson [2011], while an OBJ file can be imported using the Geometry Process Toolbox by Jacobsen and others [2021]. The result for both of the files is a n-by-3 matrix containing the three coordinates for each vertex, n being the number of vertices, and an m-by-3 array containing the indices of each vertex that make up a polygon face, i.e. a triangle in this case. As an example, the triangle of fig. 5.2 will be loaded as a 3-by-3 vertices array (showing the unique position for each vertex position on the x, y, and z planes), and the face array will simply be a 1-by-3 array containing the vertices $[V_1, V_2, V_3]$. Both the STL and OBJ files are effectively unitless, so if one wants to have the model in physical distances a scaling factor may be required, as well as translation of the model to align the origin with the desired coordinate system.

Of course, these are not the only tools and routines able to process mesh files – any routine that creates a mesh of triangles is adequate for this methodology. Also, other 3D formats can be used if they are converted into a mesh representation, which may be trivially achieved by the importing routine, or converting the file to .obj or .stl using a 3D modelling software, such as Blender.

5.3.2. Unified polygons method

The next step is to shift (translate) the coordinates so that the origin is the viewing point of the instrument of interest. The instruments are normally not point-like and a choice of a 'centre' of the instrument is necessary, like for instance a mean of the detector's cross-

section coordinates. The only caveat is that the origin must be outside the model – if it is inside, the surfaces of the instrument will be blocking its view. Using the Cassini spacecraft as an example, the detector of the Radio and Plasma Wave Science Langmuir Probe (RPWS/LP) is a sphere, while the Cassini Plasma Spectrometer (CAPS) not only has sensors, each with a specific FOV, but also the entire instrument rotates. While the LP can be well approximated as a point, calculating the FOV for CAPS is a more complex procedure and requires defining a separate FOV and direction for each orientation, pixel, and sensor (CAPS is further described in section 5.4.2). The reader will see that the FOV for only one of the CAPS sensors was calculated, but following the same steps FOV for the other two can also be calculated.

After shifting the origin to the viewing point, a projection of the FOV onto a spherical 'sky' is done trivially by converting to spherical coordinates. The angular coordinates (azimuth, ϕ, and elevation, θ) are sufficient to uniquely define any direction from the viewing point, thus reducing the problem to two dimensions. Here, though, one must be careful on faces that cross a discontinuity in azimuth, e.g., if the azimuth range is $[-\pi, +\pi]$ then there will be a discontinuity if one vertex has an azimuth near $+pi$ and another near $-pi$, and will be incorrectly mapped. As an example, let the azimuth range be $[0, 2\pi]$. If a face has two vertices in azimuth at $+30^\circ$ and one at -30° then it is clear that their angular separation is 30°, yet it will be incorrectly calculated as 330°.

The solution for this was to split these faces into smaller faces that have all their vertices on the same side of the azimuthal discontinuity. For this example let a face with edges $\boldsymbol{A}$, $\boldsymbol{B}$, and $\boldsymbol{C}$, and the azimuthal range to span from $[0, +2\pi]$. The first step is to connect the azimuthal discontinuity with the Cartesian coordinates. The Cartesian coordinates are connected to the azimuth, ϕ, of the spherical coordinates as follows:

$$\begin{aligned} x &= f\,(r, \theta) \cos\phi \\ y &= f\,(r, \theta) \sin\phi \end{aligned} \tag{5.4}$$

At the discontinuity eq. 5.4 gives:

$$\begin{aligned} x\,(0 \text{ or } 2\pi) &\neq 0 \\ y\,(0 \text{ or } 2\pi) &= 0 \end{aligned} \tag{5.5}$$

Hence the discontinuity lies on the $y = 0$ line. In general this result depends the azimuth of the discontinuity. Also the elevation-dependent Cartesian elements can be ignored, as the discontinuity is mapped only on the azimuth.

Then the discontinuity side that each edges lies must be identified. There will always be one edge on one side of the discontinuity and two edges on the other. Let the one that is alone to be $\boldsymbol{A}$ and the other two $\boldsymbol{B}$ and $\boldsymbol{C}$. We can define two vectors going from $\boldsymbol{A}$ to $\boldsymbol{B}$, and from $\boldsymbol{A}$ to $\boldsymbol{C}$ parametrically as follows

$$\boldsymbol{A} \rightarrow \boldsymbol{B} = \begin{cases} \boldsymbol{x_{A \rightarrow B}}\left(t_1\right) = \left(\boldsymbol{x_B} - \boldsymbol{x_A}\right) t_1 + \boldsymbol{x_A} \\ \boldsymbol{y_{A \rightarrow B}}\left(t_1\right) = \left(\boldsymbol{y_B} - \boldsymbol{y_A}\right) t_1 + \boldsymbol{y_A} \\ \boldsymbol{z_{A \rightarrow B}}\left(t_1\right) = \left(\boldsymbol{z_B} - \boldsymbol{z_A}\right) t_1 + \boldsymbol{z_A} \end{cases} \tag{5.6}$$

$$\boldsymbol{A} \rightarrow \boldsymbol{C} = \begin{cases} \boldsymbol{x_{A \rightarrow C}}\left(t_2\right) = \left(\boldsymbol{x_C} - \boldsymbol{x_A}\right) t_2 + \boldsymbol{x_A} \\ \boldsymbol{y_{A \rightarrow C}}\left(t_2\right) = \left(\boldsymbol{y_C} - \boldsymbol{y_A}\right) t_2 + \boldsymbol{y_A} \\ \boldsymbol{z_{A \rightarrow C}}\left(t_2\right) = \left(\boldsymbol{z_C} - \boldsymbol{z_A}\right) t_2 + \boldsymbol{z_A} \end{cases} \tag{5.7}$$

There is exactly one point on each line segment $\boldsymbol{y_{A \rightarrow B}}$ and $\boldsymbol{y_{A \rightarrow C}}$ that crosses the discontinuity at $y = 0$. Let this points be $\boldsymbol{S_1}$ and $\boldsymbol{S_2}$ for the $\boldsymbol{x_{A \rightarrow B}}$ and $\boldsymbol{x_{A \rightarrow C}}$ vectors respectively. The value of the parameters t_1 and t_2 on the discontinuity can be found by simply setting the y-element of eq. 5.6 and eq. 5.7 equal to zero:

$$\boldsymbol{y_{A \rightarrow B}}\left(t_1\right) = 0 \Rightarrow t_{\boldsymbol{S_1}} \triangleq t_1\left(\boldsymbol{y_{A \rightarrow B}} = 0\right) = -\frac{\boldsymbol{y_A}}{\boldsymbol{y_B} - \boldsymbol{y_B}} \tag{5.8}$$

$$\boldsymbol{y_{A \rightarrow C}}\left(t_2\right) = 0 \Rightarrow t_{\boldsymbol{S_2}} \triangleq t_2\left(\boldsymbol{y_{A \rightarrow C}} = 0\right) = -\frac{\boldsymbol{y_A}}{\boldsymbol{y_C} - \boldsymbol{y_B}} \tag{5.9}$$

Note that t_1 and t_2 are simply abstract parameters, while $t_{\boldsymbol{S_1}}$ and $t_{\boldsymbol{S_2}}$ have a specific, unique value. By replacing eq. 5.6 and eq. 5.7 with the $t_{\boldsymbol{S_1}}$ from eq. 5.8 and $t_{\boldsymbol{S_2}}$ from eq. 5.9 respectively, we get the spacial coordinates (x, y, z) for S_1 and S_2, i.e. the point

on the two vectors that lie on the discontinuity

$$\boldsymbol{S_1} = \begin{cases} \boldsymbol{x_{S_1}} = (\boldsymbol{x_B} - \boldsymbol{x_A})\, t_{\boldsymbol{S_1}} + \boldsymbol{x_A} \\ \boldsymbol{y_{S_1}} = (\boldsymbol{y_B} - \boldsymbol{y_A})\, t_{\boldsymbol{S_1}} + \boldsymbol{y_A} \\ \boldsymbol{z_{S_1}} = (\boldsymbol{z_B} - \boldsymbol{z_A})\, t_{\boldsymbol{S_1}} + \boldsymbol{z_A} \end{cases} \tag{5.10}$$

$$\boldsymbol{S_2} = \begin{cases} \boldsymbol{x_{S_2}} = (\boldsymbol{x_B} - \boldsymbol{x_A})\, t_{\boldsymbol{S_2}} + \boldsymbol{x_A} \\ \boldsymbol{y_{S_2}} = (\boldsymbol{y_B} - \boldsymbol{y_A})\, t_{\boldsymbol{S_2}} + \boldsymbol{y_A} \\ \boldsymbol{z_{S_2}} = (\boldsymbol{z_B} - \boldsymbol{z_A})\, t_{\boldsymbol{S_2}} + \boldsymbol{z_A} \end{cases} \tag{5.11}$$

Now it is a simple matter of simply splitting the original face, $\boldsymbol{ABC}$, to smaller, $\boldsymbol{AS_1S_2}$, $\boldsymbol{S_1BC}$ and $\boldsymbol{S_1CS_2}$, that are on the same side of the discontinuity. This is presented schematically in fig. 5.3. The original, grey, face on the left is split in three coloured on the right.

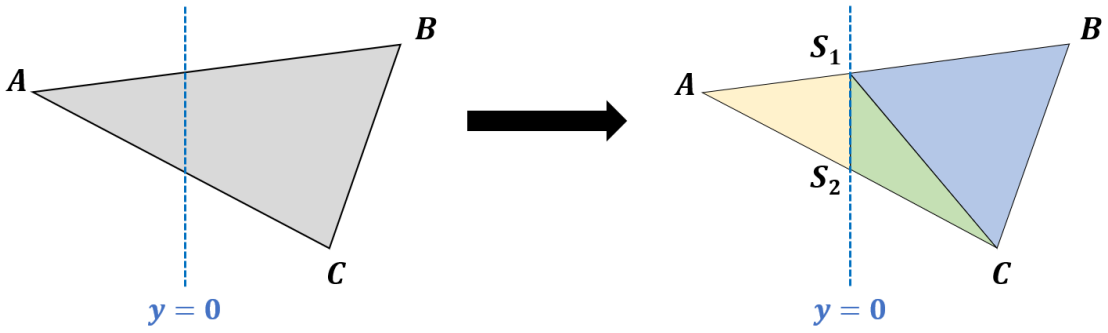

Figure 5.3: Sketch of the face splitting around the discontinuity at $y = 0$. The original grey face on the left is split in three smaller, each with different colour, on the right.

MATLAB has a function for generalised polygon objects, called `polyshape`. Since the STL geometry is composed of triangles, converting them to polyshapes is necessary. This requires looping through each triangle and passing their vertex coordinates $[\phi, \theta]$ to the `polyshape` function. Afterwards, the triangle polyshapes can be trivially united by the `union` function, resulting in a spacecraft contour in angular space that also includes any voids in the spacecraft structure as seen from the viewing point. Because of the looping,

this process requires $\mathcal{O}(m)$ steps, hence it is computationally consuming (proportional to the 3D model polygon count), but it needs to be done only once per viewing point.

With a unified spacecraft contour defined in the angular space it is now easy to check whether a vector, such as the incident sunlight, the plasma ram vector, or the neutral corotation vector, intersects with any part of the spacecraft by simply checking whether the $[\phi, \theta]$ of the direction vector is inside the polyshape contour; for MATLAB it is done by using MATLAB's `isinterior` function.

5.4. Applications: Cassini example

5.4.1. The model

Cassini is being used as an example of this methodology. Fig. 5.4 is the 3D model of Cassini from NASA Visualization Technology Applications And Development (VTAD) [2023]. The three plots in fig. 5.4 show the structure of the model (model, mesh, and close-up mesh); the screenshots are from the computer graphics software Blender.

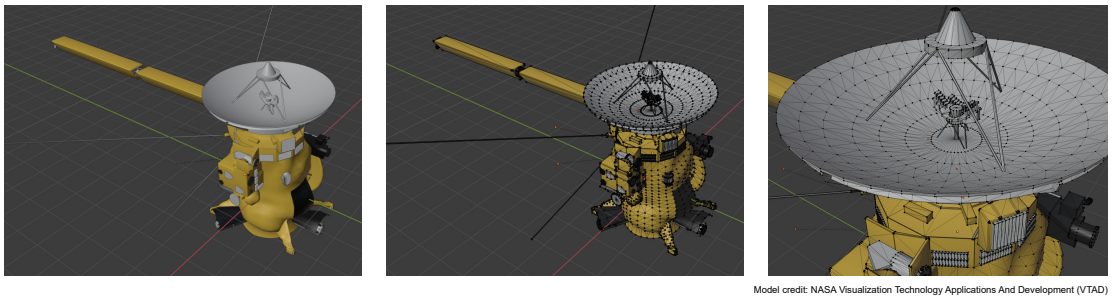

Figure 5.4: Cassini's 3D model. *Left*: the model of the spacecraft. *Middle*: the mesh of the model. *Right*: a close-up on the faces of the model.

5.4.2. CAPS FOV

As described above, this methodology can give the FOV of an instrument. This was tested by calculating the FOV of the Cassini Plasma Spectrometer (CAPS) Ion Mass Spectrometer (IMS) and then comparing it with the FOV given in the instrument's technical paper [Young et al., 2004]. A description of CAPS was presented in section 2.2.4. Fig. 5.5 shows the CAPS position onboard Cassini (highlighted by a red dashed circle).

Figure 5.5: The position of CAPS on the Cassini spacecraft, marked with a red dashed circle.

Using the methodology described above, the IMS FOV of the instrument was computed, for the azimuths of $-80°$, $-60°$, $-30°$, $0°$, $+30°$, $+60°$, $+90°$ and $+104°$. This was done by first rotating CAPS to the desired azimuth in Blender and then loading the model in MATLAB. Also, in order to have the best possible picture of the FOV two models of Cassini were used: with and without the Huygens probe. The results are shown in fig. 5.6, where the IMS IFOV is the dashed box in the middle of each panel. To help with a better understanding of the FOV and how it changes while CAPS is rotating several elements of Cassini were labelled on the figures: the High Gain Antenna (HGA), the Low-Energy Magnetospheric Measurement System (LEMMS) which has a cylindrical shape, the Ion and Neutral Mass Spectrometer (INMS) which has an angled and narrow tube-like shape, the walls of Ion Beam Spectrometer (IBS) which is part of CAPS, the LP, the Radioisotope Thermoelectric Generator (RTG) shield, the Huygens Probe and its mount, and the spacecraft thrusters. Also all plots have the -x, -y and +x-axis on the spacecraft coordinates.

The FOVs show a highly detailed contour of the spacecraft that one can easily identify elements and instruments that could obscure the IMS FOV for certain detectors. For example, at $\phi = -80°$ the view is obstructed at elevation angles between $-80°$ to $-20°$ and $60°$ to $80°$, hence blocking the corresponding detectors. Also differences of the FOV

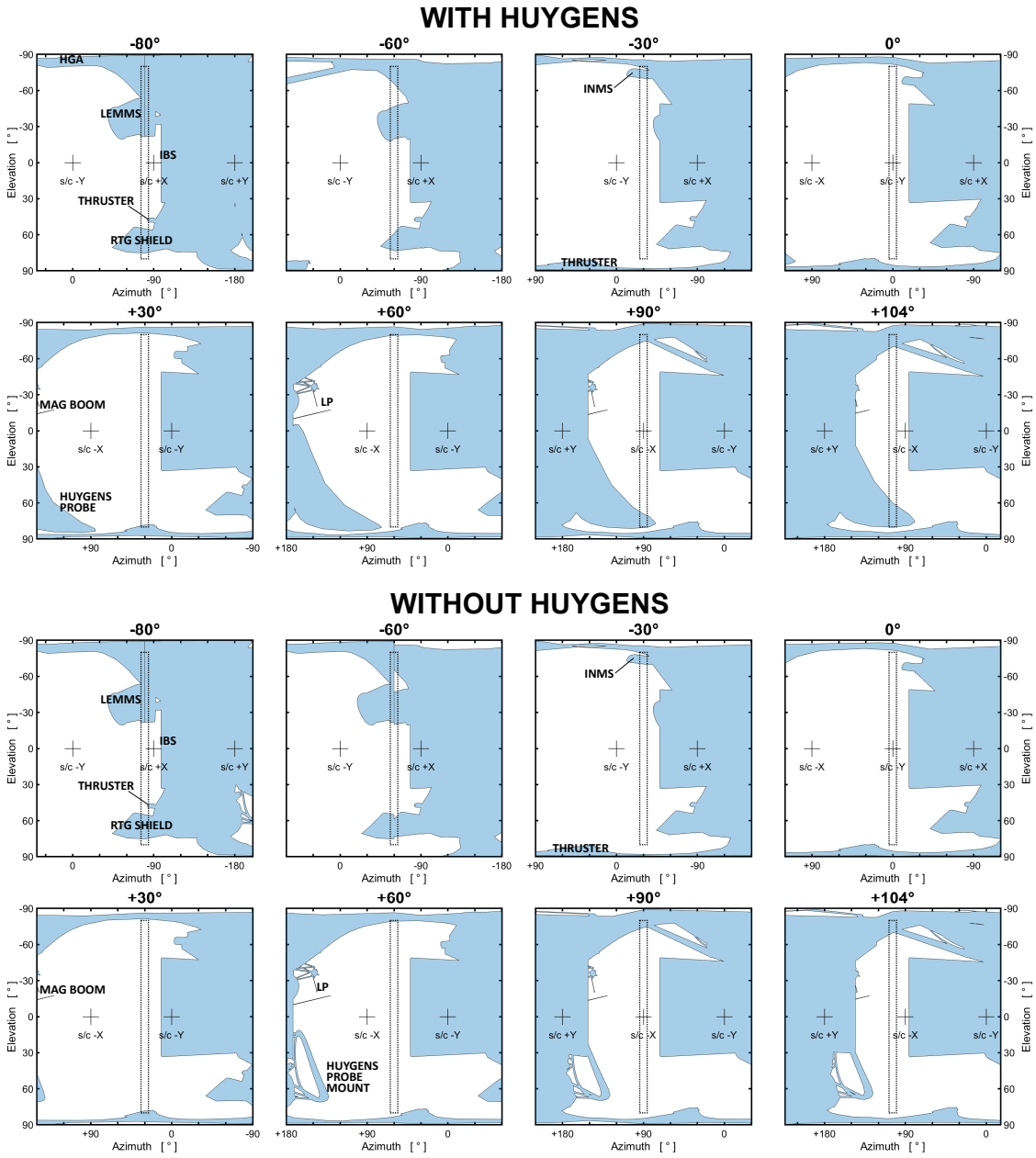

Figure 5.6: IFOV of IMS for multiple azimuths. The top panels are calculated for the period prior Huygens release, while the bottoms are after the release of Huygens.

due to Huygens release can be identified: while Huygens was attached to Cassini the view of the detector at elevation angles between 60° to 80° for azimuths over $\sim 85°$ was blocked, and this changed after the release of Huygens.

In fig. 5.7 the results of this methodology are compared with the IMS FOV as was presented in Young et al. [2004]. Panel (a) shows the FOV as presented in Young et al. [2004] for the entire rotation range of CAPS, $180° \times 160°$. One can think of it like a 'rolling' IFOV as the actuator moves. The x-axis shows the azimuth the actuator points at. The red dashed boxes at azimuths around $+30°$, $-30°$, and $-80°$ are three IFOV to focus on in order to compare the results of the methodology described here with the Young et al. [2004]; they are presented in panels (b), (c), and (d) respectively. Those three IFOV were specifically chosen as they are the most different on the area that is obscured by the spacecraft than Young et al. [2004]. The Fields and Particles Pallet (FPP) was also labelled, to follow the notation of panel (a). Unfortunately, the authors of Young et al. [2004] do not specify how the FOV was calculated; they do mention though that all three CAPS sensors (ELS, IMS, and IBS) give similar results.

Comparing the FOV at $+30°$ one can see that while Young et al. [2004] FOV shows that there is some blockage by the HGA and the thruster, our FOV shows that there is only a minimal obscuration by the thruster. At $-30°$ Young et al. [2004] FOV shows the FPP obscuring the FOV from $\theta = -80°$ to $\theta = -50°$ but our methodology showed that the obscuration is until around $-70°$, and it also specified that INMS is responsible for this. Lastly, at $-80°$ Young et al. [2004] FOV shows that the unobscured part is only between $\theta = -20°$ to $\theta = -30°$, while our methodology showed a much wider unobscured part between $\theta = -20°$ to $\theta = +60°$. Hence for CAPS a more detailed FOV can be crucial on understanding the data collected by a specific anode.

5.4.3. Cassini LP FOV, and applications: illumination and plasma flow

As an additional example of calculating the FOV of an instrument the FOV of the RPWS/LP was also calculated. The position of the RPWS/LP on Cassini is marked in fig. 5.8 with a red dashed circle (screenshot from the software Blender), and the RPWS/LP FOV is presented in fig. 5.9. As before parts of Cassini were marked, including the Cosmic Dust Analyser (CDA), to help with the understanding of the FOV. The LP is somewhat different to CAPS since the LP consists of a spherical probe that measures electric currents to the probe as a function of an applied voltage. For example, currents are generated

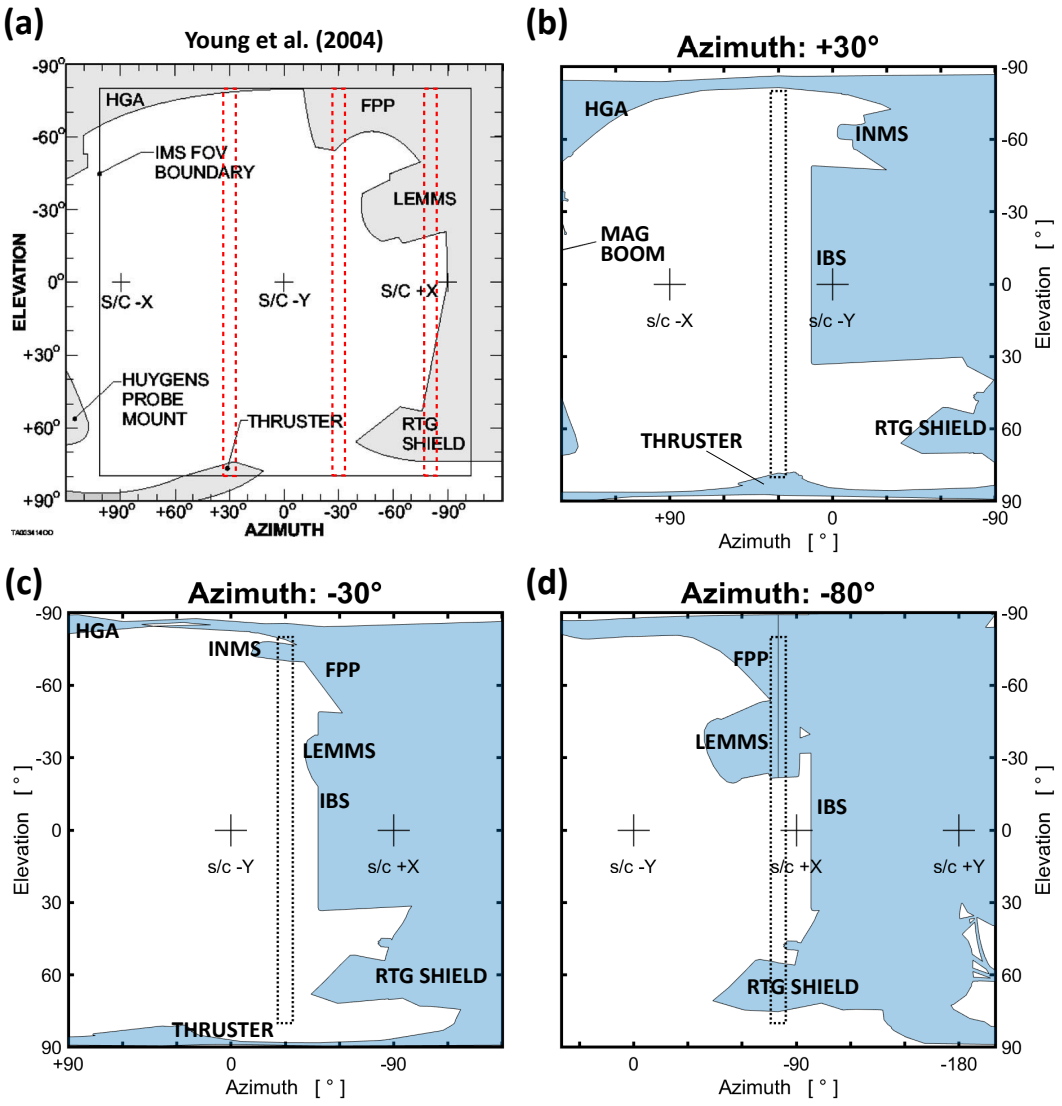

Figure 5.7: Comparison of IMS FOVs with the one in CAPS technical paper [Young et al., 2004], shown in *panel (a)*. *Panels (b) to (d)* show the FOV for the specific azimuths ($+104°$, $-30°$, and $-80°$). These azimuths are also marked in panel (a) with the red dashed boxes. Comparing the FOV of this work with Young et al. [2004] one can find quite some differences, which shows the higher accuracy of FOVs this work can offer.

when the plasma flow around the spacecraft reaches the probe, or when sunlight hits the spherical probe surface. As such, the analysed FOV here demonstrates in what directions

certain sources of electric current may be affected by the presence of different parts of the spacecraft.

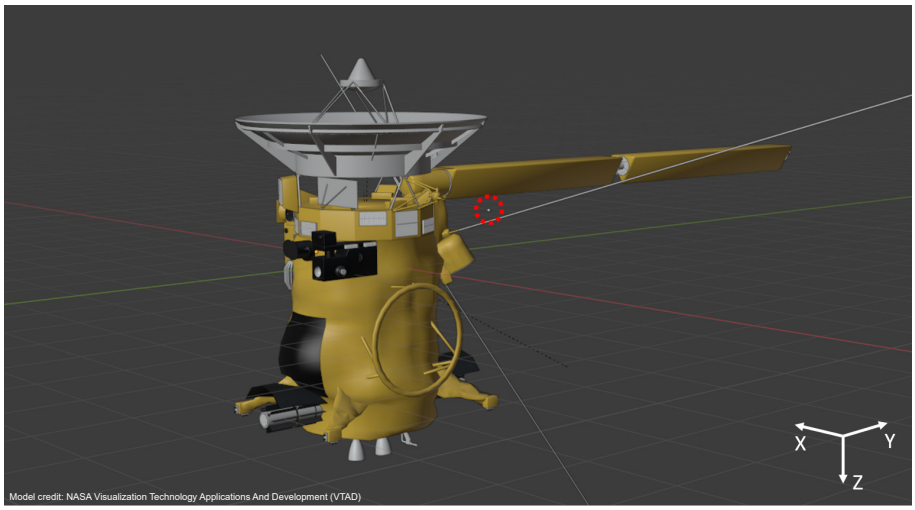

Figure 5.8: The position of the RPWS/LP on the Cassini spacecraft is marked with a red dashed circle.

Additionally, an application of how to implement the FOV with a vector of interest was presented, using the NASA's Navigation and Ancillary Information Facility (NAIF) SPICE toolkit [Acton, 1996]. The NAIF SPICE toolkit is a tool that provides ancillary data to missions, and support to space science mission design, planning of observations, and data analysis. It is especially useful in calculating spacecraft positions and the orientation of instruments.

Here it is demonstrated how one can find the direction of incoming sunlight and plasma flow, as seen from the RPWS/LP onboard Cassini. The example below is in the KSMAG coordinate system with $\hat{\boldsymbol{e_z}}$ along Saturn's magnetic dipole axis, $\hat{\boldsymbol{e_y}} = \hat{\boldsymbol{e_z}} \times \hat{\boldsymbol{e_{Sun}}}$, and $\hat{\boldsymbol{e_x}}$ in Saturn's equator, completing the right-handed orthogonal system. Any suitable coordinate system can be used, however.

For sunlight the approach is straight-forward: the function `cspice_spkpos` calculates the position of the Sun as seen from the RPWS/LP in the spacecraft coordinate system. Then, as described in section 5.3, the spacecraft faces were projected from Cartesian to spherical coordinates and lastly it was tested if the sunward direction is inside the projected

contour.

For the plasma flow though, both the corotational plasma motion around Saturn and the spacecraft motion and orientation are important. The plasma velocity vector $\boldsymbol{u_{pl}}$ at the spacecraft position $\boldsymbol{r_{s/c}}$ is given by

$$\boldsymbol{u_{pl}} = \boldsymbol{\Omega} \times \boldsymbol{r_{s/c}} \tag{5.12}$$

where $\boldsymbol{\Omega}$ is Saturn's angular velocity. Since in KSMAG the rotation axis is parallel to the magnetic dipole, $\boldsymbol{\Omega} = (0, 0, \Omega_z)$, and the plasma velocity vector becomes

$$\boldsymbol{u_{pl}} = -\Omega_z r_{pl,y} \hat{\boldsymbol{e_x}} + \Omega_z r_{pl,x} \hat{\boldsymbol{e_y}} \tag{5.13}$$

where $\hat{\boldsymbol{e_x}}$ and $\hat{\boldsymbol{e_y}}$ are the unit vectors in the x and y directions respectively.

To include the movement of Cassini, $\boldsymbol{v_{s/c}}$, a simple Galilean velocity transformation can be used

$$\boldsymbol{u_{pl'}} = \boldsymbol{u_{pl}} + \boldsymbol{v_{s/c}} \tag{5.14}$$

where $\boldsymbol{u_{pl'}}$ is the plasma velocity as seen from Cassini. Lastly, the function `cspice_sxform` gives the state rotation matrix from KSMAG to the spacecraft frame, and with that the plasma velocity in the spacecraft frame.

This methodology was applied on the LP during part of Cassini's orbit 046 (from 2007-06-11 22:00UTC to 2007-06-12 01:10UTC). The top left of fig. 5.9 shows the direction of the incident sunlight, with the LP FOV for the entire sky, and top right of the same figure shows the magnetospheric plasma flow direction, also with the LP FOV. Additionally the plots on the bottom panel show the LP data during that period. The first row shows the duration of the eclipse by Saturn, the second row shows Cassini's orbital parameters (radial distance, r and distance from the equator, Z), the third row show the LP ion current along with the logarithm of its intensity colourcoded, and the last plot shows both vectors - the plasma wake (blue), and the sunshine (red), and the moments where the LP was in the shadow, or in the plasma wake. The two top panels show that the spacecraft did not block any of the sunlight for this period, but the HGA did block the plasma flow in some periods (marked with the black X over the initial datapoints, and presented in the last plot of the bottom panel). The interesting thing though is that when the LP was

in the plasma wake, the ion current intensity seemingly dropped. This correlation of the decrease ion current with the LP being in the plasma wake definitely needs more study.

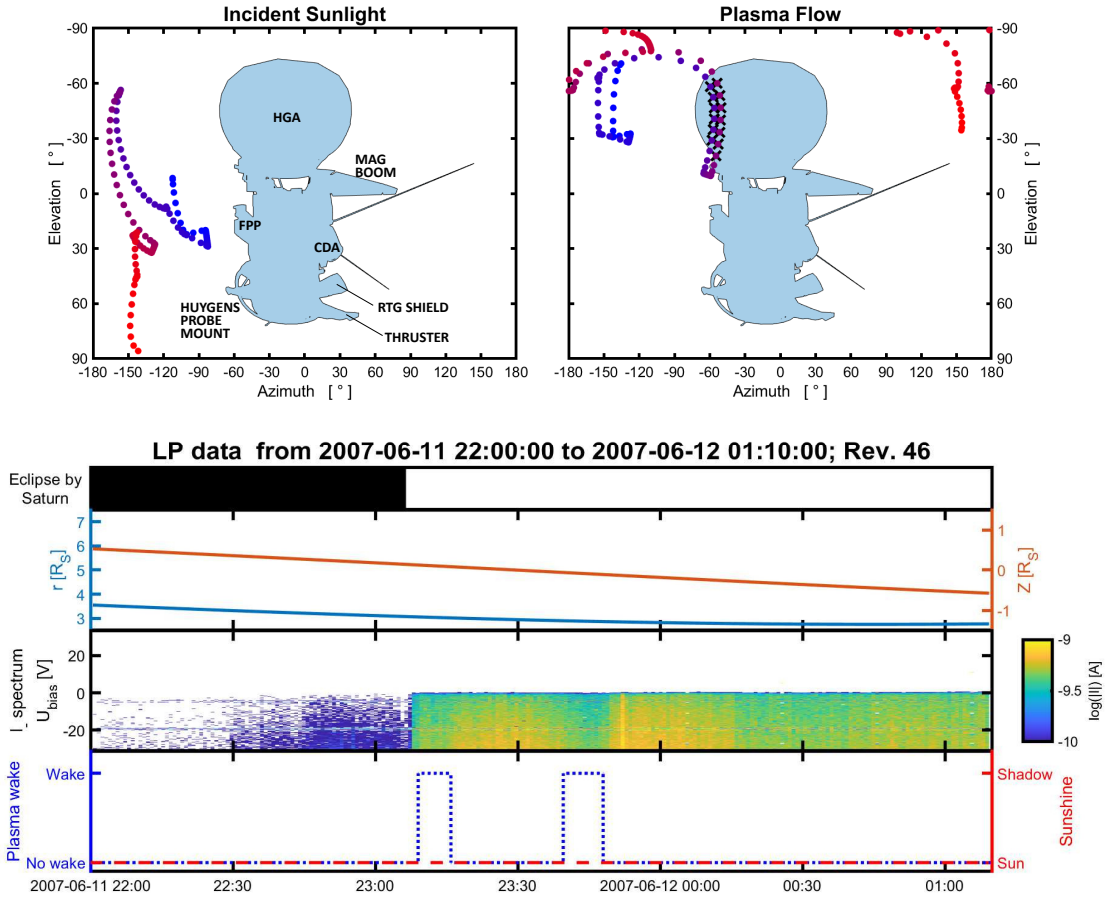

Figure 5.9: Surface-vector intersection example, along with the instrument's data. Data are from 2007-06-11 22:00UTC to 2007-06-12 01:10UTC. Panel (a): sunlight. Panel (b): plasma flow direction. The vectors intersecting with the spacecraft are marked with the black X. Time goes from blue to red with a resolution of one minute. Panel (c): the LP data for this period, showing the duration of the eclipse by Saturn (first row), Cassini's orbital parameters (second row), the LP ion current (third row), and a plot with both vectors - the plasma wake (blue), and the sunshine (red). There are hints in the data that the plasma wakes are correlated with decreases in the LP ion current.

5.5. Discussion & conclusions

This work demonstrates how, using simple scripts, an accurate and high-detailed FOV of an instrument can be computed, based on its position on the spacecraft, which can be useful and important for instruments with an array of detectors, like CAPS. Additionally it was shown how to determine whether a vector (e.g. sunlight, plasma velocity) intersects a surface of a spacecraft using basic computational geometry. This is especially important for instruments which must correct for the photoelectric effect, like the RPWS/LP onboard Cassini (e.g. Jacobsen et al. [2009], Holmberg et al. [2012], Shebanits et al. [2017], Xystouris et al. [2023a]). The major advantages of this work are the high-detailed FOVs that take into consideration every surface of the spacecraft and its payload, but also how easily a new FOV can be computed during any changes on the spacecraft during its mission, e.g. the release of Huygens probe during the Cassini mission.

The code used for this project is available in the Git-Hub repository `https://github.com/geo-xst/spacecraft-vector-intersection` [Xystouris et al., 2023b], along with some examples.

The spacecraft 3D model required for this test can often be found online, as the responsible agencies (e.g. NASA, ESA, JAXA) provide free access to these resources. In case a model is not available it may be easily built with a free 3D design/CAD software like Blender, Tinkercad, or FreeCAD. This should also be useful at the spacecraft design stage for any future spacecraft.

As a future work for this project a feature that can isolate and control individual instruments on a spacecraft can be useful. In this CAPS needed to first be rotated manually on Blender and then the new model to be loaded in MATLAB. With the mentioned feature one would have skipped the need for a manual manipulation of the model.

In conclusion, the advantage of this methodology is both its simplicity and versatility: it can be used for any spacecraft 3D model, it uses basic calculation principles and basic model formats, it uses free or institutionally supplied software, it is relatively easily translatable to almost any programming language and it provides an excellent educational platform for future generations of space enthusiasts.

6. Summary & Future work

"HAIL SCIENCE!"

— Professor Farnsworth, *Futurama (S07E20 - "Calculon 2.0")*

6.1. Overview

This thesis focused on the creation and distribution of the cold magnetospheric plasma in the magnetospheres of Saturn and Uranus. I chose those two planets as they have some similarities: they both have a magnetic field similar in overall field strength, but still lower than the strong field of Jupiter. They also both have icy moons that can create a water-rich plasma, which is different than the nitrogen-rich plasma in Neptune. Of course, their vastly different magnetic field and rotation axis configuration does not allow a direct comparison. Saturn's magnetic field is almost perfectly aligned with its rotation axis and its axial tilt is $\sim 27^\circ$ from its orbital plane, while Uranus' magnetic field is tilted by $\sim 60^\circ$ from its rotation axis and the rotation axis is tilted almost 100° to its orbital plane. Nevertheless, with the Cassini mission, exploring the Kronian system for over 13 years, useful knowledge can be obtained from the Kronian system that could be applied to the (hopefully) upcoming mission to Uranus in the early 2030s.

In this chapter I will first give a summary of my projects and work I did for this thesis, and then I will discuss how each study can be expanded and improved.

6.2. Uranus

For Uranus I focused on detecting a neutral torus around the planet Xystouris et al. [in preparation]. The process of plasma generation, as discussed in section 1.7, starts with a source, in this case the Uranian icy moons, that deposit neutrals in the magnetosphere. The neutrals then get ionised and create the magnetospheric plasma. As Uranus has moons that are covered with ice it is expected to have a water torus on the moons orbital distance, hence a water-rich magnetospheric plasma. During Voyager 2 flyby in 1986 no plasma was detected, except for some high energy ions. Even today this is puzzling the scientific community. Arridge and Eggington [2021] have shown that the unique orientation

of the axes of the planet creates an environment where the magnetic dipole angle towards the flowing solar wind changes not only seasonally, but also diurnally. Therefore Voyager could simply had the flyby in a period where the plasma was instantly depleted due to the configuration and direction of the magnetosphere. A new study by Jasinski et al. [2024] report that the intense solar activity greatly compressed the Uranian magnetosphere, depleting it from any the magnetospheric plasma.

For my study I searched for a neutral water torus around the planet using data from the Herschel space telescope, taken in 2010. During that time Uranus had a completely different orientation than the period of Voyager's flyby: in 1986 the summer solstice on the planet's northern hemisphere, and 2010 was the equinox. The Herschel observations revealed a broad emission line from Uranus and within this I found evidence of a possible weak absorption line. However, the strength of the line compared to the noise level meant that this didn't reach the level of significance normally required by the Herschel team. Despite this it can still be considered as an absorption line candidate.

There are quite a few things that could be done for continuing the project on the search for a water torus on Uranus. The first part to focus on is to further study the candidate absorption feature and assert whether it is real or not. This can be done by first calculating the probability of the feature being produced randomly or not. As seen, the background fluctuates quite strongly, which one can argue that the feature is a product by this fluctuation. Therefore an assumption can be made that every datapoint is an individual test, hence by knowing how many of them are outside the 2σ and 3σ area, where the feature currently lies, the realness of the feature can be asserted.

The second part is to focus on the observations polarisation: the observations were taken in two different polarisations, 90° apart from each other. In theory, as mentioned in section 3.5.2, there are no processes on the Uranian system that could polarise the signal, hence the two polarisations should be identical. The data though show some differences, as the signal in the vertical polarisation looks stronger than the one in the horizontal. Therefore it worth investigating why is so.

The use of models will also be useful. A forward line model would hugely benefit this project: by modelling the existing absorption line, the density and temperature of water

the creating it can be defined, and upper limits can be set on the observed torus water column density. Additionally, combining the forward line model with a neutrals torus model can help with asserting which of the moons contribute to the torus density - as discussed in section 3.3 it is currently believed that Titania and Oberon do not contribute to the torus density. The process above can also be inverted, and starting with a given density by each moon an absorption line can be calculated. This can be especially useful to assert noise levels in the observations, e.g. if the absorption line is expected to be stronger than it currently is, it means that the noisy spectrum is causing the line not reaching the required significance level. Also, as Uranus has water-type rings, the modelling for this project will also help assert whether the absorption feature is being created by them or not.

By allowing some flexibility in the neutrals model, such as changing the orientation of the system for different times (e.g. equinox, solstice), changing the location of the observer (e.g. on Earth, at L2), and changing the size of the area for the calculated column density - i.e. essentially modifying it to generate a neutral column at arbitrary times, from arbitrary viewing directions and with arbitrary FOVs - can be helpful for using the model for other missions or observations.

Additional water observations from other missions can also be used. One of them is the James Webb Space Telescope (JWST). While its range ($\sim$ 10.5THz to $\sim$ 500THz [NASA and SCScI]) is outside the water emission range, it does include some OH lines, e.g. at 12.87GHz and 15.7GHz. As the OH is part the water-products group, i.e. it can be produced in the existence of water, detecting OH could denote the existence of a water torus.

6.3. Saturn

For Saturn I used data from LP and CAPS, and I focused on the parameters that could affect the measurements of cold plasma, and specifically the photoelectrons, i.e. electrons produced by any sunlit metallic surface of the spacecraft or instrument. The photoelectrons are unavoidable almost all the time, as Cassini is in sunlight almost constantly. But as there are periods that Cassini goes into solar eclipses by Saturn (i.e. goes into Saturn's

shadow), I followed the simple logic that the photoelectron generation should cease when there is no sunlight, and I used the data in those periods to search for any measurements variations due to the decrease of the photoelectrons number. In all of the projects connected with the measurements variations during eclipses, I found that both instruments' measurements show variations connected to the change in photoelectrons number. Also, these variations can be tied to the optical depth of the medium the sunlight goes through.

As the LP measurements showed variations not only when Cassini was in the shadow of Saturn, but also when it was in the shadow of different rings, I also focused on periods where Cassini was in the main ring's shadow. The definition of photoemission current depends on the intensity of sunlight and how the probe surface material responds to photons of different wavelengths. I was able to show that these factors allow us to measure the optical depth of the rings [Xystouris et al., 2023a]. I also took into consideration both the angle of the Sun with respect to the ring plane, and the self-gravity waves in A and B rings. My results were in agreement with other studies that also measured the main rings optical depth around the same wavelengths as the LP (Colwell et al. [2006, 2007, 2010]). The novelty of this study was that: (1) the LP, which is a plasma instrument, was used to measure the transparency of the optical depth, and (2) the results of LP and UVIS are in agreement, despite the spatial resolution of the LP being two orders of magnitude lower ($\sim$ 1000km compared to a maximum 10km respectively). It was really exciting that this study was highlighted with press releases and mentions from several websites, including the Royal Astronomical Society [Massey R. for the Royal Astronomical Society (RAS), 2023], Lancaster University [Lancaster University], space.com [Feehly C. for space.com, 2023], phys.org [phys.org, provided by Lancaster University, 2023], and Forbes [Carter J. for Forbes, 2023].

While this is a complete published work there are several aspects that can take the project a step further. One of them is the impact of the high-energy electrons, as they can overcome the negative potential of the LP and create secondary electrons, which will be (wrongly) counted as magnetospheric plasma electrons. Even though their contribution is not expected to be significant (Thomsen et al. [2016] reported a mean boundary at $L = 6.2$, and the spacecraft is inside that distance for most of the measurements), it worth

investigating their impact.

The highly reflectivity of the rings' ice, but also the diffracting nature of the light was something that was not considered in this study. Fig. 4.25 shows some parts of the dark side of Saturn being lit by sunlight, denoting that such reflection and refraction effects do exist. If they are intense enough they can potentially affect the LP measurements, by redirecting sunlight to the LP while Cassini is in the shadow. The extra light will falsely give a higher transparency to the ring. Models of refraction and reflection can be made to further study any possible impact of those effects in the measurements.

A study of the Cassini parameters and conditions (location, plasma density, etc.) when the negative-bias current, I_{-}, surpasses zero during eclipses would provide a deeper understanding of the instrument operation. It was also mentioned that the Planetary Period Oscillations (PPOs) affect the Kronian system, hence a possible connection of PPOs with either the plasma density fluctuations or the appearance/disappearance of electron populations could be studied.

As there are orbits with discrepancies between each other, a study using data from other Cassini instruments that have the capability to measure the cold electron plasma, CAPS or the f_{UHR} from the RPWS, could be beneficial to determine the nature and source those discrepancies.

Moreover, it also worth investigating the idea of a 'relaxation time' of the photoelectron cloud, i.e. the time required for the spacecraft to readjust to any changes in the spacecraft charge. If the relaxation time is not short enough for the cloud to adjust to the new conditions before a new measurement is taken, the measurements resolution should be re-evaluated. Currently every measurement is treated as a single datapoint, assuming that during each measurement the spacecraft potential is already readjusted from any variations of the photoelectrons. If the readjustment time is longer than the time for two consecutive measurements, an average time and location of Cassini might need to be reconsidered.

The next step was to include data from CAPS and investigate whether they also vary in periods where Cassini goes into a body's shadow, and if so how they are compared to the variations in the LP data. For this I conducted a 'case' study, focused on three

eclipses that (1) had different characteristics from each other regarding the distance from Saturn, type of orbit, whether there was an eclipse by the rings etc. and (2) had data from both instruments that were of good quality. Table 4.2 shows the full characteristics of the eclipses.

While Cassini was in Saturn's shadow both instruments measurements showed variations caused by the variation of the photocurrent: the LP ion-side IV current, I_{-}, dropped to almost the instrument's noise level, which denotes a reduction of photoelectrons, and the CAPS the electron counts dropped, which also denotes that the local electron density was reduced. As this change was consistent to all three eclipses the moment Cassini was entering Saturn's shadow, the only reason that this could happen is if there was a drop in the photoelectrons number during eclipses. Some preliminary results were presented by me in the American Geophysical Union Fall Meeting 2022 [Xystouris et al., 2022], and while this is not a complete project yet, the results are promising to show how the photoelectrons affect multiple instruments.

As the measurements variations are not the same in all three cases, e.g. CAPS counts drop in energies below $\sim$ 7eV in two cases and $\sim$ 3eV in the third, a study using data from other Cassini instruments that have the capability to measure the cold electron plasma, CAPS, LP, and the f_{UHR} from RPWS, could be beneficial to determine the nature and source those discrepancies, but also to quantify the photoelectron density variations.

Also a good contribution on this project will be to calculate the electron density from the ELS measurements by 'capping' the energy at 10eV, which is the LP maximum detectable energy; the densities from the two instruments then can be compared directly. In theory both instruments should show approximately the same density, as they are in the same region. If there are discrepancies it would be interesting to investigate the reasons for them. A possible reason would be the spacecraft not being evenly charged, due to the plasma flow, or sunlight, where in both cases negative charges are being added (or removed) only from some of the spacecraft faces.

It would also be useful to study the spacecraft potential changes using ELS measurements: the electrons require a specific energy (i.e. work function) to 'escape' from a surface, but this can change based on the charge of the surface. Therefore based on the

energy up to which the ELS electrons counts drop, which is connected to the energy distribution of the photoelectrons, the spacecraft potential, $U_{s/c}$ can be calculated. Moreover, as the spacecraft potential is connected to the LP floating potential, $U_{fl.}$ calculating $U_{s/c}$ will allow us to study further the connection between $U_{s/c}$ and $U_{fl.}$.

Moreover a seasonal analysis could also be useful, as to investigate any changes introduces by the variations of the UV sunlight over a solar cycle. Lastly one can introduce simulations of measurements, or spacecraft potential, inside and outside eclipses based on the LP and CAPS data. For the latter the use of the Spacecraft Plasma Interaction System (SPIS) [Roussel et al., 2008], a spacecraft-plasma interaction modelling tool, can also be integrated.

6.4. Instruments & spacecraft

Both of the planets were studied from an instrumentation point of view, as I was mostly interested on the operation ot the instruments, and how measurements can be taken using with in situ, or remote observations. The multiple instruments on Cassini that are able to measure the cold plasma in Saturn operate in different ways, and ideally by combining their observations one can have the most complete picture of the cold plasma spatial and temperature distribution. There are challenges though on the calibration of an instrument, as, while it can be well-calibrated before flight, it is often impossible to predict and recreate the conditions the instrument will meet at the planet during the mission, e.g. CAPS was affected by penetrating radiation while in the Kronian radiation belts, and, as discussed above, the LP is affected by sunlight.

Another factor is the placement of the instrument on the spacecraft. If the instrument is an imager, or it has a narrow field of view, a detailed field of view (FOV) would be beneficial the right interpretation of the data, e.g. as shown in fig. 5.6 parts of the FOV of CAPS is blocked for specific angle, therefore the data from those sensors should be used with caution. Also the requirements of some instruments might give unfortunate positions on an instrument, e.g. as the LP was placed opposite the radiators for VIMS and CIRS, where they needed to be in the shadow constantly, meant that the LP was in sunlight constantly hence the photoelectrons produced by the instrument were very difficult to be

separated from the cold magnetospheric plasma measurements.

For addressing the issues mentioned above I created algorithms and scripts where, using a 3D model of a spacecraft, can: (1) calculate the FOV of an instrument, and (2) find if a vector is intersecting any part of the spacecraft, e.g. the sunlight towards the LP is blocked by Cassini [Xystouris et al., 2024]. These features can be particularly important for some instruments, and can help with an instrument's calibration.

An aspect that can be improved in this project is introducing a feature that can isolate and control individual instruments on a spacecraft. For the published work CAPS needed to first be rotated manually on Blender, and then the new model to be loaded in MATLAB. With the mentioned feature one would have skipped the need for a manual manipulation of the model.

Also a feature on tracking multiple specific parts of the spacecraft, and showing a combined FOV with different colours for each selected part could also improve the project. For example one could plot the ELS, IMS, and LEMMS FOVs if they are interested in further study the directionality of an event.

This project is made in such a way that it is highly adaptable to any spacecraft with a 3D model of a spacecraft. It can also be used for future mission, on deciding the placement of instruments, as it relatively easily to create a spacecraft model. The code for this project is available at: `https://github.com/geo-xst/spacecraft-vector-intersection` [Xystouris et al., 2023b].

A. Appendices

A. Full eclipses catalogue

In this appendix tables with all the data of the eclipses by Saturn and the rings that were used in chapter 4 are provided. The Saturn eclipses were acquired using the NAIF SPICE toolkit Acton [1996] function `cspice_gfoclt` (for MATLAB). The rings eclipses were calculating by finding the intersections of the Cassini - Sun vector on the Kronian equatorial plane, and narrowing it to the periods where: (i) Cassini was behind the rings, and (ii) the intersection was in the radial distance of a ring; the satisfaction of both conditions meant that Cassini was in the shadow of a ring. The distances of each ring are based on Williams [2022].

The given times are in Barycentric Dynamical Time (TDB), a time scale that takes into account relativistic effects that affect the time, such as the rotation of the Earth and the gravity of the planets. The difference between TDB and UTC is ~ 32.18s, which includes the sum of leap seconds since TDB was introduced and any relativistic effects (whose contribution though in the order of $\sim$ ms).

Table A.1 shows the solar eclipses of Saturn, table A.2 shows the periods overlapping eclipses by the rings and Saturn, and table A.3 shows the eclipses by rings that did not overlap with an eclipse by Saturn. For better understanding on the overlapping eclipses a schematic of the interaction between the eclipses by Saturn and by the rings is presented in fig. 4.7.

In rev. 271–286 there were two eclipses by the rings: one close to the periapsis and one close to the apoapsis; they are marked as “a” and “b”, e.g. 271a and 271b.

Ecl. #	Rev.	Start time [TDB]	Duration [min]	Low/High resolution	Interaction with eclipse by rings?
1	7	2005-05-03 05:10:44	152.48	L	—
2	8	2005-05-21 09:33:02	153.30	L	—
3	9	2005-06-08 14:10:19	154.05	L	—
4	10	2005-06-26 19:20:44	155.13	L	—
5	11	2005-07-15 01:52:27	156.03	L	—

Ecl. #	Rev.	Start time [TDB]	Duration [min]	Low/High resolution	Interaction with eclipse by rings?
6	12	2005-08-02 09:32:50	156.64	L	—
7	13	2005-08-20 15:01:21	157.08	L	—
8	14	2005-09-05 14:37:26	135.57	L	Y
9	28	2006-09-15 08:45:17	865.50	no data	Y
10	44	2007-05-10 15:22:12	134.32	L	Y
11	45	2007-05-26 19:39:26	136.53	H	Y
12	46	2007-06-11 21:07:42	118.77	H	—
13	47	2007-06-27 22:10:12	89.85	L	—
14	50	2007-09-30 07:16:04	53.88	H	—
15	51	2007-10-24 05:05:49	71.88	H	—
16	52	2007-11-17 05:02:21	75.64	L	—
17	53	2007-12-03 06:10:05	82.77	L	Y
18	54	2007-12-19 03:06:50	75.03	mixed	Y
19	56	2008-01-15 20:33:58	59.40	L	Y
20	57	2008-01-27 18:47:17	56.35	mixed	Y
21	58	2008-02-08 17:23:46	58.94	H	Y
22	59	2008-02-20 17:25:33	55.92	H	Y
23	68	2008-05-17 22:44:06	28.53	L	—
24	69	2008-05-25 21:59:47	21.88	L	Y
25	70	2008-06-01 21:53:30	52.74	L	Y*
26	71	2008-06-09 01:12:50	50.91	mixed	Y*
27	72	2008-06-16 04:20:03	49.55	mixed	Y*
28	73	2008-06-23 07:26:26	47.70	L	Y*
29	74	2008-06-30 08:17:44	45.84	L	Y*
30	75	2008-07-07 09:07:41	43.83	L	Y*
31	76	2008-07-14 09:58:08	41.51	L	—
32	77	2008-07-21 10:53:24	39.03	L	Y
33	78	2008-07-28 11:53:20	36.30	L	Y

Ecl. #	Rev.	Start time [TDB]	Duration [min]	Low/High resolution	Interaction with eclipse by rings?
34	119	2009-10-13 14:58:38	275.15	no data	—
35	120	2009-11-01 14:35:34	270.13	L	—
36	121	2009-11-20 15:19:42	265.87	L	—
37	122	2009-12-09 16:19:34	260.90	L	—
38	123	2009-12-25 20:42:06	209.83	H	—
39	125	2010-01-26 19:15:29	211.96	L	—
40	126	2010-02-13 05:58:25	220.59	L	—
41	127	2010-03-02 19:12:07	216.37	H	—
42	128	2010-03-20 10:34:05	211.09	no data	—
43	129	2010-04-07 00:56:00	198.98	no data	—
44	130	2010-04-27 09:49:57	197.03	L	—
45	131	2010-05-17 20:57:04	181.72	no data	—
46	133	2010-06-19 00:16:58	173.24	H	—
47	135	2010-07-24 15:59:51	224.10	no data	Y
48	136	2010-08-13 13:55:03	220.74	mixed	Y
49	137	2010-09-02 14:36:04	217.43	no data	Y
50	138	2010-09-22 13:04:59	213.34	L	—
51	139	2010-10-16 03:21:19	189.72	no data	—
52	140	2010-11-09 04:00:37	173.32	no data	—
53	141	2010-11-29 23:59:46	65.66	L	—
54	142	2010-12-20 13:39:09	30.13	L	—
55	150	2011-07-10 12:12:04	55.64	H	—
56	151	2011-08-01 04:31:41	47.43	L	—
57	152	2011-08-23 00:23:36	37.88	L	—
58	153	2011-09-13 19:42:15	72.53	L	—
59	154	2011-10-01 13:35:01	70.34	H	—
60	155	2011-10-19 09:08:07	66.82	H	—
61	156	2011-11-06 04:45:49	63.40	H	—

Ecl. #	Rev.	Start time [TDB]	Duration [min]	Low/High resolution	Interaction with eclipse by rings?
62	157	2011-11-24 01:22:20	60.35	H	—
63	158	2011-12-11 22:55:10	57.56	L	—
64	167	2012-06-05 00:29:47	114.90	L	Y
65	168	2012-06-28 13:08:03	142.73	no data	Y
66	169	2012-07-22 11:56:45	125.32	no data	Y
67	170	2012-08-12 11:01:57	211.47	no data	Y
68	171	2012-09-02 17:18:00	207.07	no data	Y
69	172	2012-09-24 00:48:16	201.00	no data	Y
70	173	2012-10-17 05:15:48	274.20	no data	Y
71	174	2012-11-10 03:52:59	274.13	no data	Y
72	175	2012-11-26 08:57:31	198.23	no data	Y
73	176	2012-12-09 09:30:41	116.37	no data	—
74	177	2012-12-22 15:38:35	138.85	no data	—
75	178	2013-01-04 22:09:58	156.44	no data	Y
76	179	2013-01-18 05:09:05	170.92	no data	Y
77	180	2013-01-31 12:22:01	182.34	no data	Y
78	181	2013-02-13 19:39:26	191.00	no data	Y
79	182	2013-02-25 11:06:32	158.97	no data	Y
80	183	2013-03-09 10:11:42	171.31	no data	Y
81	184	2013-03-21 09:11:18	182.28	no data	Y
82	185	2013-04-02 08:11:34	190.44	no data	Y
83	186	2013-04-12 03:48:20	147.28	no data	Y
84	187	2013-04-21 17:28:48	151.28	no data	Y
85	188	2013-05-01 07:09:56	154.42	no data	Y
86	189	2013-05-10 20:47:45	157.30	no data	Y
87	190	2013-05-20 10:32:17	159.87	L	Y
88	191	2013-05-31 06:01:43	231.36	no data	Y
89	192	2013-06-12 04:57:18	235.82	no data	Y

Ecl. #	Rev.	Start time [TDB]	Duration [min]	Low/High resolution	Interaction with eclipse by rings?
90	193	2013-06-24 04:07:20	238.57	no data	—
91	194	2013-07-06 03:10:48	239.21	no data	—
92	195	2013-07-19 22:12:34	284.05	no data	Y
93	237	2016-06-30 03:25:20	252.53	no data	Y
94	238	2016-07-24 02:19:14	245.60	no data	Y
95	239	2016-08-08 22:46:01	225.00	no data	Y
96	242	2016-09-13 18:52:23	28.93	no data	Y
97	243	2016-09-25 17:22:02	114.34	no data	Y
98	256	2017-01-10 02:18:37	46.33	no data	Y
99	257	2017-01-17 05:35:33	135.71	no data	Y
100	258	2017-01-24 09:14:31	182.40	no data	Y
101	259	2017-01-31 13:02:03	220.89	no data	Y
102	260	2017-02-07 17:22:32	255.04	no data	Y
103	261	2017-02-14 21:50:02	280.71	no data	Y
104	262	2017-02-22 01:38:45	305.38	no data	Y
105	263	2017-03-01 05:44:51	323.72	no data	Y
106	264	2017-03-08 09:39:30	339.45	no data	Y
107	265	2017-03-15 13:35:17	352.79	no data	Y
108	266	2017-03-22 17:29:05	364.70	no data	Y
109	267	2017-03-29 21:22:49	374.27	no data	Y
110	268	2017-04-06 01:18:35	382.90	no data	Y
111	269	2017-04-13 05:23:54	389.32	no data	Y
112	270	2017-04-20 09:33:50	394.09	no data	Y
113	271	2017-04-26 14:33:36	398.76	no data	Y
114	272	2017-05-03 01:24:55	391.16	no data	Y
115	273	2017-05-09 12:12:20	374.51	no data	Y
116	274	2017-05-15 23:00:07	346.55	no data	Y
117	275	2017-05-22 09:56:12	300.15	no data	Y

Ecl. #	Rev.	Start time [TDB]	Duration [min]	Low/High resolution	Interaction with eclipse by rings?
118	276	2017-05-28 22:02:21	206.97	no data	Y

Table A.1: Full table with all the eclipses by Saturn. The first column shows the number of the eclipse. The second column shows the rev. number in which the eclipse took place. The third column shows the time the eclipse started, in UT (rounded to the closest minute). The fourth column shows the duration of the eclipse in minutes. The fifth column shows the data resolution type: "L" is for low-resolution data, i.e. when the LP was conducting one sweep every $\sim$ 10min, "H" is for high-resolution data, i.e. the LP was conducting one sweep every $\sim 30s$, "mixed" is when the LP sweeping rate changed during the eclipse and there are both high- and low-resolution data, and "no data" is for the eclipses without data. The sixth column denotes whether there was an interaction with an eclipse by the rings during the eclipse by Saturn, i.e. when Cassini was already in the rings' shadow while it was entering in Saturn's shadow. The asterisk for rev. 70–75 denotes that these eclipses by the rings were totally in Saturn's shadow, i.e. Cassini was already in Saturn's shadow.

#	Rev.	Res.
1	14	L
2	28	no data
3	44	L
4	45	H
5	53	inconcl.
6	54	H
7	56	L
8	57	H
9	58	H
10	59	H

#	Rev.	Res.
26	170	no data
27	171	no data
28	172	no data
29	173	no data
30	174	no data
31	175	no data
32	178	no data
33	179	no data
34	180	no data
35	181	no data

#	Rev.	Res.
50	239	no data
51	242	no data
52	243	no data
53	256	no data
54	257	no data
55	258	no data
56	259	no data
57	260	no data
58	261	no data
59	262	no data

#	Rev.	Res.
11	69	inconcl.
12	70	blocked
13	71	blocked
14	72	blocked
15	73	blocked
16	74	blocked
17	75	blocked
18	77	no data
19	78	no data
20	135	L
21	136	H
22	137	no data
23	167	L
24	168	no data
25	169	no data
36	182	no data
37	183	no data
38	184	no data
39	185	no data
40	186	no data
41	187	no data
42	188	no data
43	189	no data
44	190	inconcl.
45	191	no data
46	192	no data
47	195	no data
48	237	no data
49	238	no data
60	263	no data
61	264	no data
62	265	no data
63	266	no data
64	267	no data
65	268	no data
66	269	no data
67	270	no data
68	271b	no data
69	272b	no data
70	273b	no data
71	274b	no data
72	275b	no data
73	276b	no data

Table A.2: Simultaneous eclipses by both Saturn and the rings. The first column shows the number of the eclipse. The second column shows the rev. number in which the eclipse took place. The third column shows the eclipse data type. "L" is for low resolution data, i.e. when the LP was conducting one sweep every $\sim$ 10min, "H" is for high resolution data, i.e. the LP was conducting one sweep every $\sim$ 30s, "inconcl." is when the data are not well structured so it is inconclusive on what type of data they are (e.g. when there are gaps longer than 10 minutes in the data), "no data" is when the LP had no data during the eclipse, and "blocked" is when the eclipse by the rings took place in an ongoing eclipse by Saturn, hence it is blocked (only for rev. 70-75).

#	Rev.	Res.
1	6	L
30	87	H
59	274a	mixed

#	Rev.	Res.
2	7	L
3	8	L
4	9	L
5	10	L
6	11	L
7	12	L
8	13	L
9	43	no data
10	46	H
11	55	mixed
12	60	H
13	61	no data
14	62	H
15	63	H
16	64	H
17	65	H
18	66	H
19	67	H
20	68	L
21	76	no data
22	79	L
23	80	H
24	81	L
25	82	mixed
26	83	L
27	84	L
28	85	L
29	86	L

#	Rev.	Res.
31	88	H
32	89	inconcl.
33	90	L
34	91	mixed
35	92	L
36	93	L
37	94	L
38	95	inconcl.
39	176	no data
40	177	no data
41	236	no data
42	240	no data
43	241	no data
44	244	no data
45	245	no data
46	246	no data
47	247	no data
48	248	no data
49	249	no data
50	250	no data
51	251	no data
52	252	no data
53	253	no data
54	254	no data
55	255	no data
56	271a	H
57	272a	H
58	273a	H

#	Rev.	Res.
60	275a	mixed
61	276a	mixed
62	277a	H
63	277b	no data
64	278a	H
65	278b	no data
66	279a	H
67	279b	no data
68	280a	inconcl.
69	280b	no data
70	281a	no data
71	281b	no data
72	282a	H
73	282b	no data
74	283a	H
75	283b	no data
76	284a	H
77	284b	no data
78	285a	no data
79	285b	no data
80	286a	no data
81	286b	no data
82	287	H
83	288	inconcl.
84	289	H
85	290	H
86	291	inconcl.
87	292	H

#	Rev.	Res.	#	Rev.	Res.	#	Rev.	Res.

Table A.3: Eclipses by the rings without an overlapping eclipse by Saturn. The columns are the same as in table A.2, with the addition of "mixed" on the data type, denoting that the LP sweeping rate changed during the eclipse and there are both high- and low-resolution data.

Abbreviations

ASI	**A**genzia **S**paziale **I**taliana (Italian Space Agency)
AU	**A**stronomical **U**nit
CAPS	**C**assini **P**lasma **S**pectrometer
CAD	**C**omputer-**A**ided **D**esign
CDA	**C**osmic **D**ust **A**nalyser
CIRS	**C**omposite **I**nfra**r**ed **S**pectrometer
CSG	**C**onstructive **S**olid **G**eometry
DSB	**D**ouble **S**ide**b**and
ELS	**EL**ectron **S**pectrometer
ESA	**E**uropean **S**pace **A**gency
EUV	**E**xtreme **U**ltra**v**iolet
FIR	**F**ar **I**nfra**r**ed
F-UV	**F**ar **U**ltra**v**iolet
FOV	**F**ield-**O**f-**V**iew
FPC	**F**ocal **P**lane **C**hopper
FPP	**F**ields and **P**articles **P**allet
FWHM	**F**ull **W**idth at **H**alf **M**aximum
HGA	**H**igh **G**ain **A**ntenna
HIFI	**H**eterodyne **I**nstrument for the **F**ar **I**nfrared
HIPE	**H**erschel **I**nteractive **P**rocessing **E**nvironment
HRS	**H**igh **R**esolution autocorrelation **S**pectrometer
HSP	**H**igh-**S**peed **P**hotometer
IBS	**I**on **B**eam **S**pectrometer
IMF	**I**nterplanetary **M**agnetic **F**ield
IF	**I**ntermediate **F**requency
IFOV	**I**nstanteneous **F**ield **O**f **V**iew
IMF	**I**nterplanetary **M**agnetic **F**ield
IMS	**I**on **M**ass **S**pectrometer

INMS	**I**on and **N**eutral **M**ass **S**pectrometer
ISS	**I**maging **S**cience **S**ubsystem
JAXA	**J**apanese **A**erospace E**x**ploration **A**gency
JWST	**J**ames **W**ebb **S**pace **T**elescope
LECP	**L**ow-**E**nergy **C**harged-**P**article
LEMMS	**L**ow-**E**nergy **M**agnetospheric **M**easurement **S**ystem
LO	**L**ocal **O**scillator
LP	**L**angmuir **P**robe
LSB	**L**ower **S**ide**b**and
M-UV	**M**iddle **U**ltra**v**iolet
NASA	**N**ational **A**eronautics and **S**pace **A**dministration
NAIF	**N**avigation and **A**ncillary **I**nformation **F**acility
N-UV	**N**ear-**U**ltra**v**iolet
OML	**O**rbital **M**otion **L**imiting
PLS	**Pl**asma **S**cience
PPO	**P**lanetary **P**eriod **O**scillation
PPS	**P**hoto**p**olarimeter **S**system
RAS	**R**oyal **A**stronomical **S**ociety
RMS	**R**oot **M**ean **S**quare
RPWS	**R**adio and **P**lasma **W**aves **S**cience
RTG	**R**adioisotope **T**hermoelectric **G**enerator
SOI	**S**aturn **I**nsertion **O**rbit
SPICE	**S**pacecraft **P**lanet **I**nstrument **C**-matrix **E**vents
SSB	**S**ingle **S**ide**b**and
TDB	**T**emps **D**ynamique **B**arycentrique (Barycentric Dynamical Time)
UHR	**U**pper **H**ybrid **R**sonance
USB	**U**pper **S**ide**b**and
UV	**U**ltra**v**iolet
UV-C	**U**ltra**v**iolet **C**
UVIS	**U**ltra**V**iolet **I**maging **S**pectrograph

VIMS **V**isual and **I**nfrared **M**apping **S**pectrometer

WBS **W**ide-**B**and acousto-optical **S**pectrometer

References

N. Achilleos, P. Guio, F. Hardy, C. Paranicas, and A. M. Sorba. The Magnetodisk Regions of Jupiter and Saturn. In R. Maggiolo, N. André, H. Hasegawa, and D. T. Welling, editors, *Magnetospheres in the Solar System*, volume 2, page 455, May 2021. doi: 10.1002/9781119815624.ch29.

C. H. Acton. Ancillary data services of NASA's Navigation and Ancillary Information Facility. *Planet. Space Sci.*, 44(1):65–70, Jan. 1996. doi: 10.1016/0032-0633(95)00107-7.

M. H. Acuñna and N. F. Ness. The main magnetic field of Jupiter. *J. Geophys. Res.*, 81 (16):2917, June 1976. doi: 10.1029/JA081i016p02917.

M. H. Acuñna, J. E. P. Connerney, and N. F. Ness. The Z_3 Zonal Harmonic Model of Saturn's Magnetic Field: Analyses and Implications. *J. Geophys. Res.*, 88(A11): 8771–8778, Nov. 1983. doi: 10.1029/JA088iA11p08771.

C. Arridge. ELS operation diagram. Courtesy of C. Arridge. Used with permission.

C. Arridge. Uranus neutral torus model density. Courtesy of C. Arridge. Used with permission, 2022.

C. Arridge, J. Wiggs, and Lancaster University. Ikuchi. URL `https://github.com/chrisarridge/Ikuchi`, 2020. doi: 10.5281/zenodo.3451443.

C. S. Arridge. Magnetotails of Uranus and Neptune. In *Magnetotails in the Solar System*, volume 207, pages 119–133, Jan. 2015. doi: 10.1002/9781118842324.ch7.

C. S. Arridge and J. W. B. Eggington. Electromagnetic induction in the icy satellites of Uranus. *Icar.*, 367:114562, Oct. 2021. doi: 10.1016/j.icarus.2021.114562.

C. S. Arridge and C. Paty. Asymmetrical Magnetospheres: Uranus and Neptune. In R. Maggiolo, N. André, H. Hasegawa, and D. T. Welling, editors, *Magnetospheres in the Solar System*, volume 2, page 515, May 2021. doi: 10.1002/9781119815624.ch33.

C. S. Arridge, K. K. Khurana, C. T. Russell, D. J. Southwood, N. Achilleos, M. K. Dougherty, A. J. Coates, and H. K. Leinweber. Warping of Saturn's magnetospheric

and magnetotail current sheets. *Journal of Geophysical Research (Space Physics)*, 113: A08217, Aug. 2008. doi: 10.1029/2007JA012963.

C. S. Arridge, L. K. Gilbert, G. R. Lewis, E. C. Sittler, G. H. Jones, D. O. Kataria, A. J. Coates, and D. T. Young. The effect of spacecraft radiation sources on electron moments from the Cassini CAPS electron spectrometer. *Planet. Space Sci.*, 57(7):854–869, June 2009. doi: 10.1016/j.pss.2009.02.011.

C. S. Arridge, G. Xystouris, C. Cochrane, I. Cohen, G. DiBraccio, P. Kollmann, L. Lamy, A. Masters, C. Paty, A. Solomonidou, et al. Fundamental Space Physics in Uranus' Magnetosphere. In *Bulletin of the American Astronomical Society*, volume 55, page 018, July 2023. doi: 10.3847/25c2cfeb.15e9f2c8.

E. Ashton, B. Gladman, and M. Beaudoin. Evidence for a Recent Collision in Saturn's Irregular Moon Population. *Planet. Sci. J.*, 2(4):158, Aug. 2021. doi: 10.3847/PSJ/ac0979.

P. W. Atkins and R. S. Friedman. *Molecular Quantum Mechanics (5th ed.)*. Oxford University Press, Nov. 2010. ISBN 9780199541423.

F. Bagenal and S. Bartlett. Jupiter's Magnetosphere. URL `https://lasp.colorado.edu/mop/files/2012/04/JupMag-8.jpg`. (Accessed: 21 Mar. 2024).

F. Bagenal and P. A. Delamere. Flow of mass and energy in the magnetospheres of Jupiter and Saturn. *Journal of Geophysical Research (Space Physics)*, 116(A5):A05209, May 2011. doi: 10.1029/2010JA016294.

C. N. Banwell and E. M. McCash. *Fundamentals of Molecular Spectroscopy (4th ed.)*. McGraw-Hill Publishing Company, London, England, 1994. ISBN 0077079760.

A. Bar-Nun, G. Herman, M. L. Rappaport, and Y. Mekler. Ejection of H_2O, O_2, H_2 and H from water ice by 0.5-6 keV H^+ and Ne^+ ion bombardment. *Applied Surface Science*, 150:143–156, Jan. 1985.

W. Baumjohann and R. A. Treumann. *Basic space plasma physics (3rd ed.)*. World Scientific Publishing Co, 2022. ISBN 978-981-12-5405-5. doi: 10.1142/p015.

K. W. Behannon, R. P. Lepping, J. Sittler, E. C., N. F. Ness, B. H. Mauk, S. M. Krimigis, and R. L. McNutt. The magnetotail of Uranus. *J. Geophys. Res.*, 92(A13):15354–15366, Dec. 1987. doi: 10.1029/JA092iA13p15354.

M. Blanc, S. Bolton, J. Bradley, M. Burton, T. E. Cravens, I. Dandouras, M. K. Dougherty, M. C. Festou, J. Feynman, et al. Magnetospheric and Plasma Science with Cassini-Huygens. *Space Sci. Rev.*, 104(1):253–346, July 2002. doi: 10.1023/A:1023605110711.

L. H. Brace, W. R. Hoegy, and R. F. Theis. Solar EUV measurements at Venus based on photoelectron emission from the Pioneer Venus Langmuir probe. *J. Geophys. Res.*, 93 (A7):7282–7296, July 1988. doi: 10.1029/JA093iA07p07282.

T. J. Bradley, S. W. H. Cowley, E. J. Bunce, H. Melin, G. Provan, J. D. Nichols, M. K. Dougherty, E. Roussos, N. Krupp, C. Tao, et al. Saturn's Nightside Dynamics During Cassini's F Ring and Proximal Orbits: Response to Solar Wind and Planetary Period Oscillation Modulations. *Journal of Geophysical Research (Space Physics)*, 125(9): e27907, Sept. 2020. doi: 10.1029/2020JA027907.

S. A. Brands, A. de Koter, J. M. Bestenlehner, P. A. Crowther, J. O. Sundqvist, J. Puls, S. M. Caballero-Nieves, M. Abdul-Masih, F. A. Driessen, M. García, S. Geen, G. Gräfener, C. Hawcroft, L. Kaper, Z. Keszthelyi, N. Langer, H. Sana, F. R. N. Schneider, T. Shenar, and J. S. Vink. The R136 star cluster dissected with Hubble Space Telescope/STIS. III. The most massive stars and their clumped winds. *Astron. Astroph.*, 663:A36, July 2022. doi: 10.1051/0004-6361/202142742.

H. S. Bridge, J. W. Belcher, B. Coppi, A. J. Lazarus, R. L. McNutt, S. Olbert, J. D. Richardson, M. R. Sands, R. S. Selesnick, J. D. Sullivan, et al. Plasma Observations near Uranus: Initial Results from Voyager 2. *Science*, 233(4759):89–93, July 1986. doi: 10.1126/science.233.4759.89.

R. H. Brown and D. P. Cruikshank. The Uranian satellites: Surface compositions and opposition brightness surges. *Icar.*, 55(1):83–92, July 1983. doi: 10.1016/0019-1035(83)90052-0.

M. H. Burger, E. C. Sittler, R. E. Johnson, H. T. Smith, O. J. Tucker, and V. I. Shematovich. Understanding the escape of water from Enceladus. *Journal of Geophysical Research (Space Physics)*, 112(A6):A06219, June 2007. doi: 10.1029/2006JA012086.

H. Cao, M. K. Dougherty, G. J. Hunt, G. Provan, S. W. H. Cowley, E. J. Bunce, S. Kellock, and D. J. Stevenson. The landscape of Saturn's internal magnetic field from the Cassini Grand Finale. *Icar.*, 344:113541, July 2020. doi: 10.1016/j.icarus.2019.113541.

X. Cao and C. Paty. Diurnal and seasonal variability of Uranus's magnetosphere. *Journal of Geophysical Research (Space Physics)*, 122(6):6318–6331, June 2017. doi: 10.1002/2017JA024063.

C. W. Carlson, D. W. Curtis, G. Paschmann, and W. Michael. An instrument for rapidly measuring plasma distribution functions with high resolution. *Advances in Space Research*, 2(7):67–70, Jan. 1982. doi: 10.1016/0273-1177(82)90151-X.

Carter J. for Forbes. How Solar Eclipses At Saturn Just Revealed Secrets About Its Rings, November 2023. URL `https://www.forbes.com/sites/jamiecartereurope/2023/11/20/how-solar-eclipses-at-saturn-just-revealed-secrets-about-its-rings/`. (Accessed: 19 Feb. 2024).

R. J. Cartwright, J. P. Emery, A. S. Rivkin, D. E. Trilling, and N. Pinilla-Alonso. Distribution of CO_2 ice on the large moons of Uranus and evidence for compositional stratification of their near-surfaces. *Icar.*, 257:428–456, Sept. 2015. doi: 10.1016/j.icarus.2015.05.020.

R. J. Cartwright, C. B. Beddingfield, T. A. Nordheim, J. Roser, W. M. Grundy, K. P. Hand, J. P. Emery, D. P. Cruikshank, and F. Scipioni. Evidence for Ammonia-bearing Species on the Uranian Satellite Ariel Supports Recent Geologic Activity. *Astrophys. J. Lett.*, 898(1):L22, July 2020. doi: 10.3847/2041-8213/aba27f.

A. F. Cheng. Magnetosphere, rings, and moons of Uranus. In J. T. Bergstralh, editor, *NASA Conference Publication*, volume 2330 of *NASA Conference Publication*, pages 541–556, Oct. 1984.

A. F. Cheng. Proton and oxygen plasmas at Uranus. *J. Geophys. Res.*, 92(A13):15309–15314, Dec. 1987. doi: 10.1029/JA092iA13p15309.

A. F. Cheng and L. J. Lanzerotti. Ice sputtering by radiation belt protons and the rings of Saturn and Uranus. *J. Geophys. Res.*, 83(A6):2597–2602, June 1978. doi: 10.1029/JA083iA06p02597.

A. F. Cheng, P. K. Haff, R. E. Johnson, and L. J. Lanzerotti. Interactions of planetary magnetospheres with icy satellite surfaces. In J. A. Burns and M. S. Matthews, editors, *IAU Colloq. 77: Some Background about Satellites*, pages 403–436. 1986.

R. N. Clark and P. G. Lucey. Spectral properties of ice-particulate mixtures and implications for remote sensing. 1. Intimate mixtures. *J. Geophys. Res.*, 89:6341–6348, July 1984. doi: 10.1029/JB089iB07p06341.

I. J. Cohen, B. H. Mauk, P. Kollmann, G. B. Clark, M. Gkioulidou, A. Y. Ukhorskiy, R. L. McNutt, H. T. Smith, A. M. Rymer, P. C. Brandt, and D. L. Turner. The Ice Giant Radiation Belts. In *51st Annual Lunar and Planetary Science Conference*, Lunar and Planetary Science Conference, page 1431, Mar. 2020.

G. Colombo, P. Goldreich, and A. W. Harris. Spiral structure as an explanation for the asymmetric brightness of Saturn's A ring. *Nature*, 264:344, Nov. 1976. doi: 10.1038/264344a0.

J. Colwell, M. Brooks, R. Jerousek, C. Coleman, K. Lina, A. Rothermich, and L. Esposito. Phantoms in the Dark: Mesoscale Openings in the Core of Saturn's B Ring. In *European Planetary Science Congress*, pages EPSC2021–858, Sept. 2021. doi: 10.5194/epsc2021-858.

J. E. Colwell, L. W. Esposito, and M. Sremčević. Self-gravity wakes in Saturn's A ring measured by stellar occultations from Cassini. *Geophys. Res. Lett.*, 33(7):L07201, Apr. 2006. doi: 10.1029/2005GL025163.

J. E. Colwell, L. W. Esposito, M. Sremčević, G. R. Stewart, and W. E. McClintock. Self-

gravity wakes and radial structure of Saturn's B ring. *Icar.*, 190(1):127–144, Sept. 2007. doi: 10.1016/j.icarus.2007.03.018.

J. E. Colwell, P. D. Nicholson, M. S. Tiscareno, C. D. Murray, R. G. French, and E. A. Marouf. *The Structure of Saturn's Rings*, page 375. 2009. doi: 10.1007/978-1-4020-9217-6_13.

J. E. Colwell, L. W. Esposito, R. G. Jerousek, M. Sremčević, D. Pettis, and E. T. Bradley. Cassini UVIS Stellar Occultation Observations of Saturn's Rings. *Astroph. J.*, 140(6): 1569–1578, Dec. 2010. doi: 10.1088/0004-6256/140/6/1569.

J. E. P. Connerney. Magnetic fields of the outer planets. *J. Geophys. Res.*, 98(E10): 18659–18680, Oct. 1993. doi: 10.1029/93JE00980.

J. E. P. Connerney, M. H. Acuñna, and N. F. Ness. The magnetic field of Uranus. *J. Geophys. Res.*, 92(A13):15329–15336, Dec. 1987. doi: 10.1029/JA092iA13p15329.

J. E. P. Connerney, M. H. Acuñna, and N. F. Ness. The magnetic field of Neptune. *J. Geophys. Res.*, 96:19023–19042, Oct. 1991. doi: 10.1029/91JA01165.

S. K. Croft and L. A. Soderblom. Geology of the Uranian satellites. In J. T. Bergstralh, E. D. Miner, and M. S. Matthews, editors, *Uranus*, pages 561–628. 1991.

S. A. Curtis and N. F. Ness. Are Uranus' rings black because they are in the solar wind? *Geophys. Res. Lett.*, 12(12):855–858, Dec. 1985. doi: 10.1029/GL012i012p00855.

J. N. Cuzzi, J. E. Colwell, L. W. Esposito, C. C. Porco, C. D. Murray, P. D. Nicholson, L. J. Spilker, E. A. Marouf, R. C. French, et al. Saturn's Rings: pre-Cassini Status and Mission Goals, July 2002.

P. Davis and S. Carney. Uranus Facts. URL `https://solarsystem.nasa.gov/planets/uranus/in-depth/`. (Accessed: 13 Aug. 2023).

T. de Graauw, F. P. Helmich, T. G. Phillips, J. Stutzki, E. Caux, N. D. Whyborn, P. Dieleman, P. R. Roelfsema, H. Aarts, et al. The Herschel-Heterodyne Instrument for the Far-Infrared (HIFI). *Astron. Astroph.*, 518:L6, July 2010. doi: 10.1051/0004-6361/201014698.

M. F. Diaz-Aguado, J. W. Bonnell, S. J. Rezvani, K. Koshmak, A. Giglia, S. Nannarone, and M. Gruntman. Experimental Investigation of Total Photoemission Yield from New Satellite Surface Materials. *J. Spacecr. Rockets*, 56, Oct. 2018. doi: 10.2514/1.A34245.

J. W. Dungey. Interplanetary Magnetic Field and the Auroral Zones. *Phys. Rev. Lett.*, 6 (2):47–48, Jan. 1961. doi: 10.1103/PhysRevLett.6.47.

D. E. Dunn, L. A. Molnar, J. T. Niehof, I. de Pater, and J. J. Lissauer. Microwave observations of Saturn's rings: anisotropy in directly transmitted and scattered saturnian thermal emission. *Icar.*, 171(1):183–198, Sept. 2004. doi: 10.1016/j.icarus.2004.04.008.

S. T. Durrance and J. T. Clarke. Lyman-alpha aurora. In J. T. Bergstralh, editor, *NASA Conference Publication*, volume 2330 of *NASA Conference Publication*, pages 559–572, Oct. 1984.

S. T. Durrance and H. W. Moos. Intense Lyα emission from Uranus. *Nature*, 299(5882): 428–429, Sept. 1982. doi: 10.1038/299428a0.

Encyclopædia Brittanica. Herschel Space Observatory photo, 2019. URL `https://www.britannica.com/topic/Herschel-space-telescope`. (Accessed: 19 Jul. 2023).

ESA. Herschel Publishing Rules and Guidelines. URL `https://www.cosmos.esa.int/web/herschel/publishing-rules-guidelines`. (Accessed: 13 Feb. 2024).

ESA. Herschel's Instruments, 2007a. URL `https://www.esa.int/ESA_Multimedia/Images/2007/09/Herschel_s_instruments`. (Accessed: 19 Jul. 2023).

ESA. Heterodyne Instrument for Far Infrared (HIFI) beam sketch, 2007b. URL `https://sci.esa.int/s/AMKB3lW`. (Accessed: 20 Jul. 2023).

L. W. Esposito, M. Ocallaghan, K. E. Simmons, C. W. Hord, R. A. West, A. L. Lane, R. B. Pomphrey, D. L. Coffeen, and M. Sato. Voyager Photopolarimeter Stellar Occulation of Saturn's Rings. *J. Geophys. Res.*, 88(A11):8643–8649, Nov. 1983. doi: 10.1029/JA088iA11p08643.

A. Eviatar and J. D. Richardson. Predicted Satellite Plasma Tori in the Magnetosphere of Uranus. *Astrophys. J. Lett.*, 300:L99, Jan. 1986. doi: 10.1086/184611.

U. Fahleson. Theory of Electric Field Measurements conducted in the Magnetosphere with Electric Probes. *Space Sci. Rev.*, 7:238–262, Oct. 1967. doi: 10.1007/BF00215600.

W. M. Farrell, W. S. Kurth, D. A. Gurnett, A. M. Persoon, and R. J. MacDowall. Saturn's rings and associated ring plasma cavity: Evidence for slow ring erosion. *Icar.*, 292:48–53, Aug. 2017. doi: 10.1016/j.icarus.2017.03.022.

G. Faure and T. M. Mensing. *Introduction to Planetary Science: The Geological Perspective*. Springer Dordrecht, Apr. 2007. doi: 10.1007/978-1-4020-5544-7.

Feehly C. for space.com. Solar eclipses seen by long-dead Cassini spacecraft shed new light on Saturn's rings, November 2023. URL `https://www.space.com/saturn-rings-transparency-cassini-eclipse-data`. (Accessed: 19 Feb. 2024).

M. Felici, C. S. Arridge, R. J. Wilson, A. J. Coates, M. Thomsen, and D. Reisenfeld. Survey of Thermal Plasma Composition in Saturn's Magnetosphere Using Time-of-Flight Data From Cassini/CAPS. *Journal of Geophysical Research (Space Physics)*, 123(8):6494–6513, Aug. 2018. doi: 10.1029/2017JA025085.

C. Ferrari, S. Brooks, S. Edgington, C. Leyrat, S. Pilorz, and L. Spilker. Structure of self-gravity wakes in Saturn's A ring as measured by Cassini CIRS. *Icar.*, 199(1):145–153, Jan. 2009. doi: 10.1016/j.icarus.2008.09.001.

D. J. Fixsen. The Temperature of the Cosmic Microwave Background. *Astrophys. J.*, 707 (2):916–920, Dec. 2009. doi: 10.1088/0004-637X/707/2/916.

P. Gibbon. Introduction to Plasma Physics. *arXiv e-prints*, art. arXiv:2007.04783, July 2020. doi: 10.48550/arXiv.2007.04783.

J. A. Gledhill. Magnetosphere of Jupiter. *Nature*, 214(5084):155–156, Apr. 1967. doi: 10.1038/214155a0.

R. J. L. Grard. Properties of the satellite photoelectron sheath derived from photoemission laboratory measurements. *J. Geophys. Res.*, 78(16):2885–2906, June 1973. doi: 10.1029/JA078i016p02885.

R. L. Gray. *Remote sensing of Jupiter's magnetospheric dynamics*. PhD thesis, Lancaster University, UK, Jan. 2018.

M. J. Griffin, A. Abergel, A. Abreu, P. A. R. Ade, P. André, J. L. Augueres, T. Babbedge, Y. Bae, T. Baillie, et al. The Herschel-SPIRE instrument and its in-flight performance. *Astron. Astroph.*, 518:L3, July 2010. doi: 10.1051/0004-6361/201014519.

T. Guillot, S. Atreya, S. Charnoz, M. K. Dougherty, and P. Read. Saturn's Exploration Beyond Cassini-Huygens. In M. K. Dougherty, L. W. Esposito, and S. M. Krimigis, editors, *Saturn from Cassini-Huygens*, page 745. 2009. doi: 10.1007/978-1-4020-9217-6{\uderscore}23.

H. Gupta, P. Rimmer, J. C. Pearson, S. Yu, E. Herbst, N. Harada, E. A. Bergin, D. A. Neufeld, G. J. Melnick, et al. Detection of OH^+ and H_2O^+ towards Orion KL. *Astron. Astroph.*, 521:L47, Oct. 2010. doi: 10.1051/0004-6361/201015117.

D. A. Gurnett, W. S. Kurth, F. L. Scarf, and R. L. Poynter. First Plasma Wave Observations at Uranus. *Science*, 233(4759):106–109, July 1986. doi: 10.1126/science.233.4759.106.

D. A. Gurnett, W. S. Kurth, D. L. Kirchner, G. B. Hospodarsky, T. F. Averkamp, P. Zarka, A. Lecacheux, R. Manning, A. Roux, et al. The Cassini Radio and Plasma Wave Investigation. *Space Sci. Rev.*, 114(1-4):395–463, Sept. 2004. doi: 10.1007/s11214-004-1434-0.

D. A. Gurnett, W. S. Kurth, G. B. Hospodarsky, A. M. Persoon, T. F. Averkamp, B. Cecconi, A. Lecacheux, P. Zarka, P. Canu, et al. Radio and Plasma Wave Observations at Saturn from Cassini's Approach and First Orbit. *Science*, 307:1255–1259, Feb. 2005. doi: 10.1126/science.1105356.

D. A. Gurnett, A. M. Persoon, W. S. Kurth, J. B. Groene, T. F. Averkamp, M. K. Dougherty, and D. J. Southwood. The Variable Rotation Period of the Inner Region of Saturn's Plasma Disk. *Science*, 316:442, Apr. 2007. doi: 10.1126/science.1138562.

G. Gustafsson and J.-E. Wahlund. Electron temperatures in Saturn's plasma disc. *Planet. Space Sci.*, 58:1018–1025, June 2010. doi: 10.1016/j.pss.2010.03.007.

L. Z. Hadid, M. W. Morooka, J.-E. Wahlund, L. Moore, T. E. Cravens, M. M. Hedman, N. J. T. Edberg, E. Vigren, J. H. Waite Jr., et al. Ring Shadowing Effects on Saturn's Ionosphere: Implications for Ring Opacity and Plasma Transport. *Geophys. Res. Lett.*, 45(19):10,084–10,092, Oct. 2018. doi: https://doi.org/10.1029/2018GL079150.

P. K. Haff and A. Eviatar. Plasma production by meteoroid impact. In NASA, Washington Repts. of Planetary Geol. and Geophys. Program, 1984 p 50-51 (SEE N85-23474 13-91), Apr. 1985.

P. K. Haff and A. Eviatar. Micrometeoroid impact on planetary satellites as a magnetospheric mass source. *Icar.*, 66(2):258–269, May 1986. doi: 10.1016/0019-1035(86)90156-9.

D. A. Hamlin, R. Karplus, R. C. Vik, and K. M. Watson. Mirror and Azimuthal Drift Frequencies for Geomagnetically Trapped Particles. *J. Geophys. Res.*, 66(1):1–4, Jan. 1961. doi: 10.1029/JZ066i001p00001.

C. J. Hansen, L. Esposito, A. I. F. Stewart, J. Colwell, A. Hendrix, W. Pryor, D. Shemansky, and R. West. Enceladus' Water Vapor Plume. *Science*, 311:1422–1425, Mar. 2006. doi: 10.1126/science.1121254.

H. Harrison and R. I. Schoen. Evaporation of Ice in Space: Saturn's Rings. *Science*, 157 (3793):1175–1176, Sept. 1967. doi: 10.1126/science.157.3793.1175.

P. Hartogh, E. Lellouch, R. Moreno, D. Bockelée-Morvan, N. Biver, T. Cassidy, M. Rengel, C. Jarchow, T. Cavalié, et al. Direct detection of the Enceladus water torus with Herschel. *Astron. Astroph.*, 532:L2, Aug. 2011. doi: 10.1051/0004-6361/201117377.

D. E. Hastings. A review of plasma interactions with spacecraft in low Earth orbit. *J. Geophys. Res.*, 100(A8):14457–14484, Aug. 1995. doi: 10.1029/94JA03358.

M. M. Hedman, P. D. Nicholson, H. Salo, B. D. Wallis, B. J. Buratti, K. H. Baines, R. H. Brown, and R. N. Clark. Self-Gravity Wake Structures in Saturn's A Ring Revealed by Cassini VIMS. *Astroph. J.*, 133(6):2624–2629, June 2007. doi: 10.1086/516828.

M. M. Hedman, P. D. Nicholson, J. N. Cuzzi, R. N. Clark, G. Filacchione, F. Capaccioni, and M. Ciarniello. Connections between spectra and structure in Saturn's main rings based on Cassini VIMS data. *Icar.*, 223(1):105–130, Mar. 2013. doi: 10.1016/j.icarus.2012.10.014.

R. Helled, J. D. Anderson, and G. Schubert. Uranus and Neptune: Shape and rotation. *Icar.*, 210(1):446–454, Nov. 2010. doi: 10.1016/j.icarus.2010.06.037.

R. C. Henry. The Local Interstellar Ultraviolet Radiation Field. *Astrophys. J.*, 570(2): 697–707, May 2002. doi: 10.1086/339623.

D. R. Higgins. *Advanced optical calibration of the Herschel HIFI heterodyne spectrometer.* PhD thesis, Department of Experimental Physics, National University of Ireland Maynooth, 2011.

R. D. Higgins and J. W. Kooi. Electrical standing waves in the HIFI HEB mixer amplifier chain. In K. J. Linden, L. P. Sadwick, and C. M. O'Sullivan, editors, *Terahertz Technology and Applications II*, volume 7215 of *Society of Photo-Optical Instrumentation Engineers (SPIE) Conference Series*, page 72150L, Feb. 2009. doi: 10.1117/12.811127.

H. E. Hinteregger, K. R. Damon, and L. A. Hall. Analysis of Photoelectrons from Solar Extreme Ultraviolet. *J. Geophys. Res.*, 64(8):961–969, Aug. 1959. doi: 10.1029/JZ064i008p00961.

W. R. Hoegy and L. H. Brace. Use of Langmuir probes in non-Maxwellian space plasmas. *Review of Scientific Instruments*, 70(7):3015–3024, July 1999. doi: 10.1063/1.1149862.

M. K. G. Holmberg, J. E. Wahlund, M. W. Morooka, and A. M. Persoon. Ion densities and velocities in the inner plasma torus of Saturn. *Planet. Space Sci.*, 73(1):151–160, Dec. 2012. doi: 10.1016/j.pss.2012.09.016.

K. Hormann and A. Agathos. The point in polygon problem for arbitrary polygons. *Computational Geometry*, 20(3):131–144, 2001. ISSN 0925-7721. doi: https://doi.org/10.1016/S0925-7721(01)00012-8. URL `https://www.sciencedirect.com/science/article/pii/S0925772101000128`.

W. F. Huebner, J. J. Keady, and S. P. Lyon. Solar Photo Rates for Planetary Atmospheres and Atmospheric Pollutants. *Astrophys. Space Sci.*, 195(1):1–294, Sept. 1992. doi: 10.1007/BF00644558.

J. F. Hughes, A. van Dam, M. McGuire, D. F. Sklar, J. D. Foley, S. K. Feiner, and A. K. *Computer graphics: principles and practice (3rd ed.)*. Addison-Wesley Professional, Boston, MA, USA, July 2013. ISBN 0321399528.

H. Hussmann, F. Sohl, and T. Spohn. Subsurface oceans and deep interiors of medium-sized outer planet satellites and large trans-neptunian objects. *Icar.*, 185(1):258–273, Nov. 2006. doi: 10.1016/j.icarus.2006.06.005.

A. K. Ip and G. H. Voigt. Plasma-dominated magnetic field configurations for the magnetosphere of Uranus. *J. Geophys. Res.*, 90(A7):6287–6294, July 1985. doi: 10.1029/JA090iA07p06287.

A. Jacobsen and others. gptoolbox: Geometry Processing Toolbox, 2021. URL `https://github.com/alecjacobson/gptoolbox/`. (Accessed: 21 Feb. 2024).

K. S. Jacobsen, J.-E. Wahlund, and A. Pedersen. Cassini Langmuir probe measurements in the inner magnetosphere of Saturn. *Planet. Space Sci.*, 57:48–52, Jan. 2009. doi: 10.1016/j.pss.2008.10.012.

R. A. Jacobson, J. K. Campbell, A. H. Taylor, and S. P. Synnott. The Masses of Uranus and its Major Satellites From Voyager Tracking Data and Earth-Based Uranian Satellite Data. *Astroph. J.*, 103:2068, June 1992. doi: 10.1086/116211.

J. M. Jasinski, C. J. Cochrane, X. Jia, W. R. Dunn, E. Roussos, T. A. Nordheim, L. H. Regoli, N. Achilleos, N. Krupp, and N. Murphy. The anomalous state of Uranus' magnetosphere during the Voyager 2 flyby. *Nature Astron.*, Nov. 2024.

R. G. Jerousek, J. E. Colwell, L. W. Esposito, P. D. Nicholson, and M. M. Hedman. Small particles and self-gravity wakes in Saturn's rings from UVIS and VIMS stellar occultations. *Icar.*, 279:36–50, Nov. 2016. doi: 10.1016/j.icarus.2016.04.039.

X. Jia, M. G. Kivelson, K. K. Khurana, and R. J. Walker. Magnetic Fields of the Satellites of Jupiter and Saturn. *Space Sci. Rev.*, 152(1-4):271–305, May 2010. doi: 10.1007/s11214-009-9507-8.

E. Johnson. STL File Reader, MATLAB Central File Exchange, 2011. URL `https://www.mathworks.com/matlabcentral/fileexchange/22409-stl-file-reader`. (Accessed: 21 Feb. 2024).

R. E. Johnson, L. J. Lanzerotti, and W. L. Brown. Sputtering processes: Erosion and chemical change. *Advances in Space Research*, 4(9):41–51, Jan. 1984. doi: 10.1016/0273-1177(84)90007-3.

T. V. Johnson, C. M. Yeates, and R. Young. Space science reviews volume on Galileo Mission overview. *Space Sci. Rev.*, 60(1-4):3–21, May 1992. doi: 10.1007/BF00216848.

A. D. Johnstone, C. Alsop, S. Burge, P. J. Carter, A. J. Coates, A. J. Coker, A. N. Fazakerley, M. Grande, R. A. Gowen, et al. Peace: a Plasma Electron and Current Experiment. *Space Sci. Rev.*, 79:351–398, Jan. 1997. doi: 10.1023/A:1004938001388.

S. P. Joy, M. G. Kivelson, R. J. Walker, K. K. Khurana, C. T. Russell, and T. Ogino. Probabilistic models of the Jovian magnetopause and bow shock locations. *Journal of Geophysical Research (Space Physics)*, 107(A10):1309, Oct. 2002. doi: 10.1029/2001JA009146.

S. J. Kanani, C. S. Arridge, G. H. Jones, A. N. Fazakerley, H. J. McAndrews, N. Sergis, S. M. Krimigis, M. K. Dougherty, A. J. Coates, et al. A new form of Saturn's magnetopause using a dynamic pressure balance model, based on in situ, multi-instrument Cassini measurements. *Journal of Geophysical Research (Space Physics)*, 115(A6): A06207, June 2010. doi: 10.1029/2009JA014262.

E. Karkoschka. Comprehensive Photometry of the Rings and 16 Satellites of Uranus with the Hubble Space Telescope. *Icar.*, 151(1):51–68, May 2001. doi: 10.1006/icar.2001.6596.

S. Kempf, N. Altobelli, J. Schmidt, J. N. Cuzzi, P. R. Estrada, and R. Srama. Microm-

eteoroid infall onto Saturn's rings constrains theirage to no more than a few hundred millionyears. *Science Advances*, May 2023. doi: 10.1126/sciadv.adf8537.

D. Kester, I. Avruch, and D. Teyssier. Correction of electric standing waves. In *Bayesian Inference and Maximum Entropy Methods in Science and Engineering*, volume 1636 of *American Institute of Physics Conference Series*, pages 62–67, Dec. 2014. doi: 10.1063/1.4903711.

M. G. Kivelson. Planetary Magnetodiscs: Some Unanswered Questions. *Space Sci. Rev.*, 187(1-4):5–21, Apr. 2015. doi: 10.1007/s11214-014-0046-6.

M. G. Kivelson and C. T. Russell. *Introduction to Space Physics*. 1995. doi: 10.1017/9781139878296.

M. G. Kivelson, F. Bagenal, W. S. Kurth, F. M. Neubauer, C. Paranicas, and J. Saur. Magnetospheric interactions with satellites. In F. Bagenal, T. E. Dowling, and W. B. McKinnon, editors, *Jupiter. The Planet, Satellites and Magnetosphere*, volume 1, pages 513–536. 2004.

S. M. Krimigis. The magnetosphere of Neptune. *Planetary Report*, 12:10–13, Apr. 1992.

S. M. Krimigis, T. P. Armstrong, W. I. Axford, C. O. Bostrom, C. Y. Fan, G. Gloeckler, L. J. Lanzerotti, E. P. Keath, R. D. Zwicki, et al. Hot Plasma Environment at Jupiter: Voyager 2 Results. *Science*, 206(4421):977–984, Nov. 1979. doi: 10.1126/science.206.4421.977.

S. M. Krimigis, J. F. Carbary, E. P. Keath, T. P. Armstrong, L. J. Lanzerotti, and G. Gloeckler. General characteristics of hot plasma and energetic particles in the Saturnian magnetosphere - Results from the Voyager spacecraft. *J. Geophys. Res.*, 88:8871–8892, Nov. 1983. doi: 10.1029/JA088iA11p08871.

S. M. Krimigis, T. P. Armstrong, W. I. Axford, A. F. Cheng, G. Gloeckler, D. C. Hamilton, E. P. Keath, L. J. Lanzerotti, and B. H. Mauk. The Magnetosphere of Uranus: Hot Plasma and Radiation Environment. *Science*, 233(4759):97–102, July 1986. doi: 10.1126/science.233.4759.97.

M. L. Kutner and B. L. Ulich. Recommendations for calibration of millimeter-wavelength spectral line data. *Astrophys. J.*, 250:341–348, Nov. 1981. doi: 10.1086/159380.

J. G. Laframboise. *Theory of spherical and cylindrical Langmuir probes in a collisionless, Maxwellian plasma at rest.* PhD thesis, Toronto Univ. (Ontario). Inst. for Aerospace Studies, 1966.

Lancaster University. Using eclipses to calculate the transparency of Saturn's rings. URL `https://www.lancaster.ac.uk/news/using-eclipses-to-calculate-the-transparency-of-saturns-rings`. (Accessed: 19 Feb. 2024).

R. A. Langel and R. H. Estes. A geomagnetic field spectrum. *Geophys. Res. Lett.*, 9(4): 250–253, Apr. 1982. doi: 10.1029/GL009i004p00250.

J. P. Lebreton and D. L. Matson. An overview of the Cassini mission. *Nuovo Cimento C Geophysics Space Physics C*, 15(6):1137–1147, Dec. 1992. doi: 10.1007/BF02506708.

R. P. Lepping. Comparisons of the field configurations of the magnetotails of Uranus and Neptune. *Planet. Space Sci.*, 42(10):847–857, Oct. 1994. doi: 10.1016/0032-0633(94)90065-5.

J. S. Lew. Drift Rate in a Dipole Field. *J. Geophys. Res.*, 66(9):2681–2685, Sept. 1961. doi: 10.1029/JZ066i009p02681.

W. Li and M. K. Hudson. Earth's Van Allen Radiation Belts: From Discovery to the Van Allen Probes Era. *Journal of Geophysical Research (Space Physics)*, 124(11):8319–8351, Nov. 2019. doi: 10.1029/2018JA025940.

G. F. Lindal, J. R. Lyons, D. N. Sweetnam, V. R. Eshleman, D. P. Hinson, and G. L. Tyler. The atmosphere of Neptune: Results of radio occultation measurements with the Voyager 2 spacecraft. *Geophys. Res. Lett.*, 17(10):1733–1736, Sept. 1990. doi: 10.1029/GL017i010p01733.

J. E. Marsden and A. Tromba. *Vector Calculus (6th ed.)*. W. H. Freeman, 2011. ISBN 978-1-4292-1508-4.

Massey R. for the Royal Astronomical Society (RAS). Using eclipses to calculate the transparency of Saturn's rings, November 2023. URL `https://ras.ac.uk/news-and-press/news/using-eclipses-calculate-transparency-saturns-rings`. (Accessed: 19 Feb. 2024).

A. Masters, N. Achilleos, M. G. Kivelson, N. Sergis, M. K. Dougherty, M. F. Thomsen, C. S. Arridge, S. M. Krimigis, H. J. McAndrews, et al. Cassini observations of a Kelvin-Helmholtz vortex in Saturn's outer magnetosphere. *Journal of Geophysical Research (Space Physics)*, 115(A7):A07225, July 2010. doi: 10.1029/2010JA015351.

D. L. Matson, L. J. Spilker, and J.-P. Lebreton. The Cassini/Huygens Mission to the Saturnian System. *Space Sci. Rev.*, 104(1):1–58, July 2002. doi: 10.1023/A:1023609211620.

B. H. Mauk and N. J. Fox. Electron radiation belts of the solar system. *Journal of Geophysical Research (Space Physics)*, 115(A12):A12220, Dec. 2010. doi: 10.1029/2010JA015660.

B. H. Mauk, D. J. Williams, R. W. McEntire, K. K. Khurana, and J. G. Roederer. Storm-like dynamics of Jupiter's inner and middle magnetosphere. *J. Geophys. Res.*, 104(A10): 22759–22778, Oct. 1999. doi: 10.1029/1999JA900097.

B. H. Mauk, D. G. Mitchell, R. W. McEntire, C. P. Paranicas, E. C. Roelof, D. J. Williams, S. M. Krimigis, and A. Lagg. Energetic ion characteristics and neutral gas interactions in Jupiter's magnetosphere. *Journal of Geophysical Research (Space Physics)*, 109(A9): A09S12, Sept. 2004. doi: 10.1029/2003JA010270.

J. C. Maxwell. *On the stability of the motion of Saturn's rings.* Macmillan, Cambridge, 1859. doi: 10.3931/e-rara-244.

W. McCluney. *Introduction to Radiometry and Photometry (2nd ed.).* Artech House Publ., Boston, London, 2014.

W. B. McKinnon and R. L. Kirk. Triton. In T. Spohn, D. Breuer, and T. V. Johnson, editors, *Encyclopedia of the Solar System (Third Edition)*, pages 861–881. Elsevier, Boston, third edition edition, 2014. ISBN 978-0-12-415845-0. doi: https://doi.org/10.

1016/B978-0-12-415845-0.00040-2. URL https://www.sciencedirect.com/science/article/pii/B9780124158450000402.

R. L. McNutt, F. Bagenal, J. Belcher, H. Bridge, A. Eviatar, C. Goertz, A. J. Lazarus, K. Ogilvie, J. Richardson, et al. The low energy plasma in the Uranian magnetosphere. *Advances in Space Research*, 7(12):237–241, Jan. 1987. doi: 10.1016/0273-1177(87)90224-9.

J. D. Menietti, T. F. Averkamp, W. S. Kurth, S. Y. Ye, D. A. Gurnett, and B. Cecconi. Survey of Saturn electrostatic cyclotron harmonic wave intensity. *Journal of Geophysical Research (Space Physics)*, 122(8):8214–8227, Aug. 2017. doi: 10.1002/2017JA023929.

R. L. Merlino. Understanding Langmuir probe current-voltage characteristics. *Am. J. Phys.*, 75(12):1078–1085, 2007. doi: 10.1119/1.2772282. URL https://doi.org/10.1119/1.2772282.

C. J. Miller, R. C. Nichol, L. Wasserman, C. Genovese, A. Connolly, and A. Hopkins. What Does a Three-Sigma Detection Really Mean? In *American Astronomical Society Meeting Abstracts #198*, volume 198 of *American Astronomical Society Meeting Abstracts*, page 30.04, May 2001.

L. A. Morabito, S. P. Synnott, P. N. Kupferman, and S. A. Collins. Discovery of Currently Active Extraterrestrial Volcanism. *Science*, 204(4396):972, June 1979. doi: 10.1126/science.204.4396.972.

G. E. Morfill, H. Fechtig, E. Gruen, and C. K. Goertz. Some consequences of meteoroid impacts on Saturn's rings. *Icar.*, 55(3):439–447, Sept. 1983. doi: 10.1016/0019-1035(83)90114-8.

C. D. Motchenbacher and J. A. Connelly. *Fundamental Noise Mechanisms*. John Wiley & Sons; New York, August 1993. ISBN 978-0-471-57742-3.

H. M. Mott-Smith and I. Langmuir. The Theory of Collectors in Gaseous Discharges. *Phys. Rev.*, 28:727–763, Oct. 1926. doi: 10.1103/PhysRev.28.727.

NASA and D. Bolles. NASA's Eyes. URL https://science.nasa.gov/eyes/. (Accessed: 15 May 2024).

NASA and SCScI. Science Instruments. URL https://www.stsci.edu/jwst/instrumentation/instruments. (Accessed: 15 May 2024).

NASA and Wikipedia. Uranus Moons, 2022. URL https://commons.wikimedia.org/wiki/File:Uranus_moons.jpg. (Accessed: 29 Aug. 2023).

NASA, JPL, and Space Science Institute. Expanse of Ice, 2007. URL https://photojournal.jpl.nasa.gov/catalog/PIA08389. (Accessed: 13 May 2023).

NASA, JPL, and Space Science Institute. Inspecting the Edge, 2008. URL https://ciclops.org/view.php%3fid=4820.html. (Accessed: 15 May 2023).

NASA, JPL, and Space Science Institute. The Day the Earth Smiled, 2013. URL https://photojournal.jpl.nasa.gov/catalog/PIA17172. (Accessed: 05 Nov. 2024).

NASA, ESA, CSA, STScI, and J. DePasquale. Uranus (NIRCam Compass Image), 2023. URL https://webbtelescope.org/contents/media/images/2023/117/01GWQDSFM5JFT8D8D2GHCBEY23. (Accessed: 29 Aug. 2023).

NASA Visualization Technology Applications And Development (VTAD). Cassini 3D Model, 2023. URL https://solarsystem.nasa.gov/resources/2401/cassini-3d-model/. (Accessed: 05 Mar. 2023).

NASA/ESA and Hubble Heritage Team (STScI/AURA) and Clarke J. (University of Michigan). Jupiter's North Pole Aurora, 2001. URL https://www.jpl.nasa.gov/images/pia03155-satellite-footprints-seen-in-jupiter-aurora. (Accessed: 23 Mar. 2024).

NASA/JPL. PIA03550: Saturn's Rings (Artist's Concept), 2005. URL https://photojournal.jpl.nasa.gov/catalog/PIA03550. (Accessed: 27 Sep. 2023).

NASA/JPL, IAU WGPSN, IAUC/CBET, and MPEC. Planetary Satellite Discovery Circumstances, 2023. URL https://ssd.jpl.nasa.gov/sats/discovery.html. (Accessed: 24 Sep. 2023).

NASA/JPL-Caltech/Space Science Institute. PIA14934: A Splendor Seldom Seen, 2012. URL https://photojournal.jpl.nasa.gov/catalog/PIA14934. (Accessed: 28 Mar. 2024).

NASA's Jet Propulsion Laboratory (JPL). Cassini-Huygens mission overview, 2023. URL https://solarsystem.nasa.gov/missions/cassini/science/overview/. (Accessed: 23 Jul. 2023).

National Academies of Sciences, Engineering, and Medicine. *Origins, Worlds, and Life: A Decadal Strategy for Planetary Science and Astrobiology 2023-2032*. The National Academies Press, Washington, DC, 2023. ISBN 978-0-309-47578-5. doi: 10.17226/26522. URL https://nap.nationalacademies.org/catalog/26522/origins-worlds-and-life-a-decadal-strategy-for-planetary-science.

N. F. Ness, M. H. Acuñna, K. W. Behannon, L. F. Burlaga, J. E. P. Connerney, R. P. Lepping, and F. M. Neubauer. Magnetic Fields at Uranus. *Science*, 233(4759):85–89, July 1986. doi: 10.1126/science.233.4759.85.

P. D. Nicholson and M. M. Hedman. Self-gravity wake parameters in Saturn's A and B rings. *Icar.*, 206(2):410–423, Apr. 2010. doi: 10.1016/j.icarus.2009.07.028.

P. D. Nicholson, R. G. French, D. B. Campbell, J.-L. Margot, M. C. Nolan, G. J. Black, and H. J. Salo. Radar imaging of Saturn's rings. *Icar.*, 177(1):32–62, Sept. 2005. doi: 10.1016/j.icarus.2005.03.023.

V. Ossenkopf. The intensity calibration for HIFI. Technical Report ALMA Memo 442.1, SRON National Institute for Space Research, January 2003. URL https://www.cosmos.esa.int/documents/12133/996743/The+intensity+calibration+for+HIFI. (Accessed: 23 Jul. 2023).

S. Ott. The Herschel Data Processing System — HIPE and Pipelines — Up and Running Since the Start of the Mission. In Y. Mizumoto, K. I. Morita, and M. Ohishi, editors, *Astronomical Data Analysis Software and Systems XIX*, volume 434 of *Astronomical Society of the Pacific Conference Series*, page 139, Dec. 2010. doi: 10.48550/arXiv.1011.1209.

A. M. Persoon, D. A. Gurnett, W. S. Kurth, G. B. Hospodarsky, J. B. Groene, P. Canu, and M. K. Dougherty. Equatorial electron density measurements in Saturn's inner magnetosphere. *Geophys. Res. Lett.*, 32(23):L23105, Dec. 2005. doi: 10.1029/2005GL024294.

A. M. Persoon, D. A. Gurnett, J. S. Leisner, W. S. Kurth, J. B. Groene, and J. B. Faden. The plasma density distribution in the inner region of Saturn's magnetosphere. *Journal of Geophysical Research (Space Physics)*, 118:2970–2974, June 2013. doi: 10.1002/jgra.50182.

A. M. Persoon, D. A. Gurnett, W. S. Kurth, J. B. Groene, and J. B. Faden. Evidence for a seasonally dependent ring plasma in the region between Saturn's A Ring and Enceladus' orbit. *Journal of Geophysical Research (Space Physics)*, 120:6276–6285, Aug. 2015. doi: 10.1002/2015JA021180.

A. M. Persoon, W. S. Kurth, D. A. Gurnett, J. B. Groene, A. H. Sulaiman, J. E. Wahlund, M. W. Morooka, L. Z. Hadid, A. F. Nagy, et al. Electron Density Distributions in Saturn's Ionosphere. *Geophys. Res. Lett.*, 46(6):3061–3068, Mar. 2019. doi: 10.1029/2018GL078020.

A. M. Persoon, W. S. Kurth, D. A. Gurnett, J. B. Faden, J. B. Groene, M. W. Morooka, J. E. Wahlund, R. J. Wilson, and J. D. Menietti. Distribution in Saturn's Inner Magnetosphere From 2.4 to 10 R_S: A Diffusive Equilibrium Model. *Journal of Geophysical Research (Space Physics)*, 125(3):e27545, Mar. 2020. doi: 10.1029/2019JA027545.

C. M. Persson, J. H. Black, J. Cernicharo, J. R. Goicoechea, G. E. Hassel, E. Herbst, M. Gerin, M. de Luca, T. A. Bell, A. Coutens, et al. Nitrogen hydrides in interstellar gas. Herschel/HIFI observations towards G10.6-0.4 (W31C). *Astron. Astroph.*, 521:L45, Oct. 2010. doi: 10.1051/0004-6361/201015105.

phys.org, provided by Lancaster University. Using eclipses to calculate the transparency of Saturn's rings, November 2023. URL `https://phys.org/news/2023-11-eclipses-transparency-saturn.html`. (Accessed: 19 Feb. 2024).

G. L. Pilbratt, J. R. Riedinger, T. Passvogel, G. Crone, D. Doyle, U. Gageur, A. M. Heras, C. Jewell, L. Metcalfe, et al. Herschel Space Observatory. An ESA facility for

far-infrared and submillimetre astronomy. *Astron. Astroph.*, 518:L1, July 2010. doi: 10.1051/0004-6361/201014759.

A. Poglitsch, C. Waelkens, N. Geis, H. Feuchtgruber, B. Vandenbussche, L. Rodriguez, O. Krause, E. Renotte, C. van Hoof, et al. The Photodetector Array Camera and Spectrometer (PACS) on the Herschel Space Observatory. *Astron. Astroph.*, 518:L2, July 2010. doi: 10.1051/0004-6361/201014535.

G. Provan, S. W. H. Cowley, E. J. Bunce, S. E. Milan, A. M. Persoon, and D. A. Gurnett. Planetary Period Oscillations of Saturn's Dayside Equatorial Ionospheric Electron Density Observed on Cassini's Proximal Passes. *Journal of Geophysical Research (Space Physics)*, 126(9):e29332, Sept. 2021. doi: 10.1029/2021JA029332.

R. C. Rice, K. Nykyri, X. Ma, and B. L. Burkholder. Characteristics of Kelvin-Helmholtz Waves as Observed by the MMS From September 2015 to March 2020. *Journal of Geophysical Research (Space Physics)*, 127(3):e29685, Mar. 2022. doi: 10.1029/2021JA02968510.1002/essoar.10507334.2.

J. F. Roussel, F. Rogier, G. Dufour, J. C. Mateo-Velez, J. Forest, A. Hilgers, D. Rodgers, L. Girard, and D. Payan. SPIS Open-Source Code: Methods, Capabilities, Achievements, and Prospects. *IEEE Transactions on Plasma Science*, 36(5):2360–2368, Oct. 2008. doi: 10.1109/TPS.2008.2002327.

H. Salo, R. Karjalainen, and R. G. French. Photometric modeling of Saturn's rings. II. Azimuthal asymmetry in reflected and transmitted light. *Icar.*, 170(1):70–90, July 2004. doi: 10.1016/j.icarus.2004.03.012.

U. Samir, Y. J. Kaufman, L. H. Brace, and H. C. Brinton. The dependence of ion density in the wake of the AE-C satellite on the ration of body size to Debye length in an $[O^+]$-dominated plasma. *J. Geophys. Res.*, 85(A4):1769–1772, Apr. 1980. doi: 10.1029/JA085iA04p01769.

R. E. Samuelson, W. C. Maguire, R. A. Hanel, D. E. Jennings, Y. L. Yung, and A. C. Aikin. CO_2 o Titan. *J. Geophys. Res.*, 88(A11):8709–8715, Nov. 1983. doi: 10.1029/JA088iA11p08709.

R. S. Selesnick and J. D. Richardson. Plasmasphere formation in arbitrarily oriented magnetospheres. *Geophys. Res. Lett.*, 13(7):624–627, July 1986. doi: 10.1029/GL013i007p00624.

N. Sergis, S. M. Krimigis, D. G. Mitchell, D. C. Hamilton, N. Krupp, B. H. Mauk, E. C. Roelof, and M. K. Dougherty. Energetic particle pressure in Saturn's magnetosphere measured with the Magnetospheric Imaging Instrument on Cassini. *Journal of Geophysical Research (Space Physics)*, 114(A2):A02214, Feb. 2009. doi: 10.1029/2008JA013774.

O. Shebanits, E. Vigren, J. E. Wahlund, M. K. G. Holmberg, M. Morooka, N. J. T. Edberg, K. E. Mandt, and J. H. Waite. Titan's ionosphere: A survey of solar EUV influences. *Journal of Geophysical Research (Space Physics)*, 122(7):7491–7503, July 2017. doi: 10.1002/2017JA023987.

M. Shi, R. A. Baragiola, D. E. Grosjean, R. E. Johnson, S. Jurac, and J. Schou. Sputtering of water ice surfaces and the production of extended neutral atmospheres. *J. Geophys. Res.*, 100(E12):26387–26396, Jan. 1995. doi: 10.1029/95JE03099.

J. A. Simpson, T. S. Bastian, D. L. Chenette, G. A. Lentz, R. B. McKibben, K. R. Pyle, and A. J. Tuzzolino. Saturnian trapped radiation and its absorption by satellites and rings - The first results from Pioneer 11. *Science*, 207:411–415, Jan. 1980. doi: 10.1126/science.207.4429.411.

J. Sittler, Edward C., K. W. Ogilvie, and R. Selesnick. Survey of electrons in the Uranian magnetosphere: Voyager 2 observations. *J. Geophys. Res.*, 92(A13):15263–15281, Dec. 1987. doi: 10.1029/JA092iA13p15263.

E. J. Smith, J. Davis, L., D. E. Jones, J. Coleman, P. J., D. S. Colburn, P. Dyal, C. P. Sonett, and A. M. A. Frandsen. The planetary magnetic field and magnetosphere of Jupiter: Pioneer 10. *J. Geophys. Res.*, 79(25):3501, Jan. 1974. doi: 10.1029/JA079i025p03501.

E. J. Smith, L. Davis, D. E. Jones, P. J. Coleman, D. S. Colburn, P. Dyal, and C. P. Sonett. Saturn's Magnetic Field and Magnetosphere. *Science*, 207(4429):407–410, Jan. 1980. doi: 10.1126/science.207.4429.407.

B. T. Soifer, G. Neugebauer, and K. Matthews. Near-infrared spectrophotometry of the satellites and rings of Uranus. *Icar.*, 45(3):612–617, Mar. 1981. doi: 10.1016/0019-1035(81)90027-0.

Soutwest Research Institute (SwRI). Cassini Plasma Spectrometer (CAPS) photo. URL `https://www.swri.org/technology-today/article/cassinis-grand-finale`. (Accessed: 12 Feb. 2024).

SRON Netherlands Institute for Space Research. The HIFI focal plane unit, 2007. URL `https://sci.esa.int/s/AjGDMBw`. (Accessed: 20 Jul. 2023).

S. Szita, A. N. Fazakerley, P. J. Carter, A. M. James, P. Trávnícek, G. Watson, M. André, A. Eriksson, and K. Torkar. Cluster PEACE observations of electrons of spacecraft origin. *Annales Geophysicae*, 19(10):1721–1730, Oct. 2001. doi: 10.5194/angeo-19-1721-2001.

L. J. Tacconi, C. S. Arridge, A. Buonanno, M. Cruise, O. Grasset, A. Helmi, L. Iess, E. Komatsu, J. Leconte, J. Leenaarts, J. Martin-Pintado, R. Nakamura, and D. Watson. Voyage 2050: Final recommendations from the Voyage 2050 Senior Committee. Technical report, May 2001. URL `https://www.cosmos.esa.int/web/voyage-2050`. (Accessed: 08 Mar. 2023).

N. A. Teanby, P. G. J. Irwin, M. Sylvestre, C. A. Nixon, and M. A. Cordiner. Uranus's and Neptune's Stratospheric Water Abundance and Vertical Profile from Herschel-HIFI. *Planet. Sci. J.*, 3(4):96, Apr. 2022. doi: 10.3847/PSJ/ac650f.

D. Teyssier. Personal communication. 03 Dec. 2024.

D. Teyssier. Quick-start Guide to Herschel-HIFI. Technical Report HERSCHEL-HSC-DOC-2129, version 1.2, European Space Agency / European Space Astronomy Centre (ESA/ESAC), Jan. 2018. URL `https://www.cosmos.esa.int/documents/12133/996743/QUICK-START+GUIDE+TO+HERSCHEL-HIFI`. (Accessed: 20 Apr. 2024).

D. Teyssier, I. Avruch, S. Beaulieu, J. Braine, A. Marston, P. Morris, M. Olberg, M. Rengel, and R. Shipman. The Heterodyne Instrument for the Far Infrared (HIFI) Handbook.

Technical Report HERSCHEL-HSC-DOC-2097, version 2.1, European Space Agency / European Space Astronomy Centre (ESA/ESAC), December 2017. URL `https://www.cosmos.esa.int/web/herschel/legacy-documentation-hifi`. (Accessed: 12 Jun. 2023).

P. C. Thomas. Radii, shapes, and topography of the satellites of Uranus from limb coordinates. *Icar.*, 73(3):427–441, Mar. 1988. doi: 10.1016/0019-1035(88)90054-1.

M. F. Thomsen, A. J. Coates, E. Roussos, R. J. Wilson, K. C. Hansen, and G. R. Lewis. Suprathermal electron penetration into the inner magnetosphere of Saturn. *Journal of Geophysical Research (Space Physics)*, 121(6):5436–5448, June 2016. doi: 10.1002/2016JA022692.

M. Tiscareno. Vital Statistics for Saturn's Rings and Inner Satellites. URL `https://pds-rings.seti.org/saturn/saturn_tables.html`. (Accessed: 13 May 2023).

V. M. Vasyliūnas. *Plasma distribution and flow*, page 395–453. Cambridge Planetary Science Old. Cambridge University Press, 1983. doi: 10.1017/CBO9780511564574.013.

A. J. Verbiscer, M. F. Skrutskie, and D. P. Hamilton. Saturn's largest ring. *Nature*, 461 (7267):1098–1100, Oct. 2009. doi: 10.1038/nature08515.

M. F. Vogt, M. G. Kivelson, K. K. Khurana, R. J. Walker, M. Ashour-Abdalla, and E. J. Bunce. Simulating the effect of centrifugal forces in Jupiter's magnetosphere. *Journal of Geophysical Research (Space Physics)*, 119(3):1925–1950, Mar. 2014. doi: 10.1002/2013JA019381.

J. E. Wahlund, M. W. Morooka, L. Z. Hadid, A. M. Persoon, W. M. Farrell, D. A. Gurnett, G. Hospodarsky, W. S. Kurth, S. Y. Ye, et al. In situ measurements of Saturn's ionosphere show that it is dynamic and interacts with the rings. *Science*, 359 (6371):66–68, Jan. 2018. doi: 10.1126/science.aao4134.

J. W. Warwick, D. R. Evans, J. H. Romig, C. B. Sawyer, M. D. Desch, M. L. Kaiser, J. K. Alexander, T. D. Carr, D. H. Staelin, et al. Voyager 2 Radio Observations of Uranus. *Science*, 233(4759):102–106, July 1986. doi: 10.1126/science.233.4759.102.

E. C. Whipple. Potentials of surfaces in space. *Reports on Progress in Physics*, 44(11): 1197–1250, Nov. 1981. doi: 10.1088/0034-4885/44/11/002.

D. Williams. Saturnian Rings Fact Sheet, 2022. URL `https://nssdc.gsfc.nasa.gov/planetary/factsheet/satringfact.html`. (Accessed: 16 Dec. 2023).

D. Williams. Jovian Satellite Fact Sheet, 2023a. URL `https://nssdc.gsfc.nasa.gov/planetary/factsheet/joviansatfact.html`. (Accessed: 27 Apr. 2024).

D. Williams. Saturnian Satellite Fact Sheet, 2023b. URL `https://nssdc.gsfc.nasa.gov/planetary/factsheet/saturniansatfact.html`. (Accessed: 27 Apr. 2024).

D. Williams. Uranus Moons Fact Sheet, 2023c. URL `https://nssdc.gsfc.nasa.gov/planetary/factsheet/uraniansatfact.html`. (Accessed: 27 Apr. 2024).

D. Williams. Jupiter Fact Sheet, 2024a. URL `https://nssdc.gsfc.nasa.gov/planetary/factsheet/jupiterfact.html`. (Accessed: 27 Apr. 2024).

D. Williams. Moon Fact Sheet, 2024b. URL `https://nssdc.gsfc.nasa.gov/planetary/factsheet/moonfact.html`. (Accessed: 29 Aug. 2023).

D. Williams. Neptune Fact Sheet, 2024c. URL `https://nssdc.gsfc.nasa.gov/planetary/factsheet/neptunefact.html`. (Accessed: 27 Apr. 2024).

D. Williams. Neptunian Satellite Fact Sheett, 2024d. URL `https://nssdc.gsfc.nasa.gov/planetary/factsheet/neptuniansatfact.html`. (Accessed: 27 Apr. 2024).

D. Williams. Saturn Fact Sheet, 2024e. URL `https://nssdc.gsfc.nasa.gov/planetary/factsheet/saturnfact.html`. (Accessed: 27 Apr. 2024).

D. Williams. Uranus Fact Sheet, 2024f. URL `https://nssdc.gsfc.nasa.gov/planetary/factsheet/uranusfact.html`. (Accessed: 27 Apr. 2024).

G. Xystouris. Investigation of the electron density close to the rings of Saturn and Prediction of the F-ring plasma characteristics. Master's thesis, Uppsala University, Department of Physics and Astronomy, and Swedish Institute of Space Physics, Uppsala Division, 2016. urn:nbn:se:uu:diva-314112.

G. Xystouris, D. Teyssier, and C. Arridge. Searching for a neutral water torus at Uranus. in preparation.

G. Xystouris, C. S. Arridge, R. H. Wilson, M. W. Morooka, J.-E. Wahlund, A. J. Coates, and G. H. Jones. Comparison of Cassini Langmuir Probe and Cassini Plasma Spectrometer Observations During Solar Eclipses by Saturn and the Main Rings: Photoelectrons and Asymmetries. In *AGU Fall Meeting Abstracts*, volume 2022, pages SM45E–2281, Dec. 2022.

G. Xystouris, C. S. Arridge, M. M. Morooka, and J.-E. Wahlund. Estimating the optical depth of Saturn's main rings using the Cassini Langmuir Probe. *Mon. Not. of the R. Astron. Soc.*, 526(4):5839–5860, Dec. 2023a. doi: 10.1093/mnras/stad2793.

G. Xystouris, O. Shebanits, and C. S. Arridge. Spacecraft-Vector Intersection. URL `https://github.com/geo-xst/spacecraft-vector-intersection`, 2023b. doi: 10.5281/zenodo.13323604. (Accessed: 13 Nov. 2024).

G. Xystouris, O. Shebanits, and C. S. Arridge. A simple spacecraft - vector intersection methodology and applications. *RAS Techniques and Instruments*, 3(1):166–173, Jan. 2024. doi: 10.1093/rasti/rzae012.

R. V. Yelle and B. R. Sandel. Uranian H Ly-α emission: The interstellar wind source. *Geophys. Res. Lett.*, 13(2):89–92, Feb. 1986. doi: 10.1029/GL013i002p00089.

D. T. Young, J. J. Berthelier, M. Blanc, J. L. Burch, A. J. Coates, R. Goldstein, M. Grande, T. W. Hill, R. E. Johnson, V. Kelha, et al. Cassini Plasma Spectrometer Investigation. *Space Sci. Rev.*, 114(1-4):1–112, Sept. 2004. doi: 10.1007/s11214-004-1406-4.